

Advancing Knowledge of Mechanically-Fiber Reinforced Asphalt Concrete

by

Hossein Noorvand

A Dissertation Presented in Partial Fulfillment
of the Requirements for the Degree
Doctor of Philosophy

Approved July 2020 by the
Graduate Supervisory Committee:

Kamil Kaloush, Co-Chair
Shane Underwood, Co-Chair
Michael Mamlouk
Barzin Mobasher

ARIZONA STATE UNIVERSITY

August 2020

© 2020 Hossein Noorvand

All Rights Reserved

ABSTRACT

The use of reinforcing fibers in asphalt concrete (AC) has been documented in many studies. Published studies generally demonstrate positive benefits from using mechanically fiber reinforced asphalt concrete (M-FRAC); however, improvements generally vary with respect to the particular study. The widespread acceptance of fibers use in the asphalt industry is hindered by these inconsistencies. This study seeks to fulfill a critical knowledge gap by advancing knowledge of M-FRAC in order to better understand, interpret, and predict the behavior of these materials. The specific objectives of this dissertation are to; (a) evaluate the state of aramid fiber in AC and examine their impacts on the mechanical performance of asphalt mixtures; (b) evaluate the interaction of the reinforcement efficiency of fibers with compositions of asphalt mixtures; (c) evaluate tensile and fracture properties of M-FRAC; (d) evaluate the interfacial shear bond strength and critical fiber length in M-FRAC; and (e) propose micromechanical models for prediction of the tensile strength of M-FRAC. The research approach to achieve these objectives included experimental measurements and theoretical considerations. Throughout the study, the mechanical response of specimens with and without fibers are scrutinized using standard test methods including flow number (AASHTO T 378) and uniaxial fatigue (AASHTO TP 107), and non-standard test methods for fiber extraction, direct tension, semi-circular bending, and single fiber pull-out tests. Then, the fiber reinforcement mechanism is further examined by using the basic theories of viscoelasticity as well as micromechanical models.

The findings of this study suggest that fibers do serve as a reinforcement element in AC; however, their reinforcing effectiveness depends on the state of fibers in the mix,

temperature/ loading rate, properties of fiber (i.e. dosage, length), properties of mix type (gradation and binder content), and mechanical test type to characterize M-FRAC. The outcome of every single aforementioned elements identifies key reasons attributed to the fiber reinforcement efficiency in AC, which provides insights to justify the discrepancies in the literature and further recommends solutions to overcome the knowledge gaps. This improved insight will translate into the better deployment of existing fiber-based technologies; the development of new, and more effective fiber-based technologies in asphalt mixtures.

DEDICATION

To my beloved wife, Neda

To my kid, Nirvan

to my father, Yasoub

to my mother, Nasirn

to my brother, Hassan

for their support, reassurance, and love without which none of this would be possible.

I love you.

ACKNOWLEDGMENTS

I am indebted to many individuals and organizations for not only making this research possible but also shaping my professional academic life. First of all, I would like to express my sincere gratitude to my advisors Dr. Kamil Kaloush and Dr. Shane Underwood for their guidance and support throughout my PhD studies. Dr. Kaloush has continuously put trust in my initiatives, which has given me the confidence to grow in my field of study. Dr. Kaloush has been more than just an academic advisor for me; his positive attitude and excellent guidance have made these past five years a memorable fruitful working experience. His mentorship attitude is something that I aspire to achieve equally one day. Dr. Underwood has taught me many aspects of being a successful researcher including the importance of thoroughness and attentiveness while performing experiments and analyzing the test data. I am truly inspired to achieve his level of dedication and passion towards research. I am deeply grateful to my committee members Dr. Barzin Mobasher, and Dr. Michael Mamlouk for helping me shape my doctoral research more realistically by critically assessing my work. I would like to specially thank Dr. Hasan Ozer, Dr. Jeff Stempihar and Dr. Elham Fini who have provided valuable lessons and meaningful insights that have supported my research.

I would like to thank all my present, and past colleagues in the Advanced Pavement Laboratory, Samuel Castro Brockman, Jeff Stempihar, Jose Medina, Ramadan Salim, Dirk BeGell, Padmini Gudipudi, Ashraf Alrajhi, Akshay Gundla, Aswin Srinivasan, Janak Shah, Gurpreet Rai, Guru Karnati, Ali Zalghout, Jolina Karam, Seng Hkawn, Carlos Obando, Gonzalo Arredondo, Phani Kaligotla, and Xiao Zhang as well as Maryam Kazembeyki who have provided support throughout my research studies. My sincere appreciation to our

laboratory managers, Mr. Jeff Long and Mr. Peter Goguen for providing all technical support I needed to complete my experiments. Their presence, time and help have been truly invaluable.

On a separate note, I would like to thank Samuel Castro Brockman and Dirk BeGell for their significant contribution toward my research studies. I received tremendous assistance in carrying out my experiments from Samuel in the last couple of years and without his help many of my efforts would not have been accomplished. I am truly indebted to my friend Dirk for assisting and training me how to work with 3D-printers which enormously allowed me to develop a single fiber pull-out test for my research study. I would like to explicitly thank Jose Medina and Ramadan Salim for their friendship, company, and teaching me various aspects of asphalt concrete design and analysis. I benefited a lot by collaborating and interacting with them during my PhD study.

A special thanks to the entire FORTA Corporation team, specially Mr. Martin Doody, for the financial support and the faith they put in me that gave me the research freedom to drive the science without any constraints.

Finally, I want to express my most sincere gratitude to Dr. Nima Farzadnia, who has been my major driving force to be where I am today. He was the first who understood my research capabilities, strengthen my perspectives, and always encouraged me to pursue my passion.

TABLE OF CONTENTS

	Page
LIST OF TABLES.....	xiii
LIST OF FIGURES.....	xvii
CHAPTER	
1 INTRODUCTION	1
Background	1
Problem Statement	2
Objective	5
Dissertation Outline.....	6
2 LITERATURE REVIEW	10
Fiber Reinforced Composites.....	10
Fiber Technology	11
Fiber Reinforced Asphalt Concrete.....	12
Types of Reinforcing Fibers Used in Asphalt Mixtures	13
Characteristics of Aramid Fiber	16
Laboratory Study of Mechanically Fiber Reinforced Asphalt Concrete.....	16
Machinal Performance of Asphalt Concrete with Fibers	17
Machinal Performance of Asphalt Concrete with Synthetic Fibers	19
Fiber Mixing Methods.....	22
Effect of Fiber State on Mechanical Performance of FRAC	24
Understanding the Reinforcement Mechanism of Fibers in Composites.....	26
Fiber Bridging Mechanism.....	26

CHAPTER	Page
Shear Stress Transfer Mechanism	29
Micromechanical Models for Fiber Reinforced Composites	38
Summary	41
3 EFFECT OF THE FIBER STATE ON THE MECHANICAL PERFORMANCE OF FIBER REINFORCED ASPHALT CONCRETE	43
Introduction	43
Methodology	43
Materials	44
Fiber Mixing Method	46
Mechanical Characterization	47
Fiber State	50
Results	56
Mechanical Characterization	56
Fiber State	62
Summary and Discussion	70
4 EVALUATING INTERACTION OF FIBER REINFORCEMENT MECHANISM WITH MESOSTRUCTURE OF ASPHALT CONCRETE	73
Introduction	73
Experimental Program	74
Asphalt Mixture Selection	74
Materials	76
Fiber Mixing Methods	79

CHAPTER	Page
Laboratory Test Methods	82
Results	82
Optimum Fiber Mixing Method	82
State of Aramid Fibers in the Asphalt Mixes	84
Repeated Load Permanent Deformation Test.....	86
Dynamic Modulus Test	88
Uniaxial fatigue test.....	91
Interaction of Fiber Reinforcement Mechanism with Composition of Asphalt Concrete.....	94
Summary	106
 5 MECHANISM OF MECHANICALLY-FIBER REINFORCED ASPHALT CONCRETE IN TENSION	108
Introduction	108
Materials.....	109
Test Methods	110
Direct Tension Test	110
Semi-circular Bending Test.....	119
Design of Experiment.....	121
Results	123
State of Dispersed Aramid Fibers with Different Lengths and Dosages....	123
Fatigue Life of M-FRAC.....	124
Tensile capacity of M-FRAC	125

CHAPTER	Page
<u>E</u> valuation of Fracture Energy and Toughness of M-FRAC	130
Summary and Discussion.....	138
Effect of Test Type.....	138
Effect of Temperature/Loading Rate.....	140
Effect of Fiber Dosage and Length	143
Effect of Mix Type	145
6 EVALUATION OF INTERFACIAL SHEAR BOND STRENGTH AND CRITICAL FIBER LENGTH IN FIBER REINFORCED ASPHALT CONCRETE.....	147
Introduction	147
Objective	148
Experimental Program.....	149
Materials.....	149
Sample Preparation.....	150
Test Methods	152
Results	155
Pilot Study for Improvement of Data Quality	155
General Observation of Load-Displacement Data	158
Evaluation of Effective Fiber Diameter	160
The Effect of Fiber Dimension on the τ	162
The effect of Fiber Types on τ at Different Displacement Rates.....	164
Relationship Between Asphalt Mastic Stiffness and Shear Bond Strength	166

CHAPTER	Page
Relationship Between Matrix Stiffness and Theoretical Critical Fiber Embedded Length.....	171
Fiber Length Recommendations	176
7 DEVELOPMENT OF MICROMECHANICAL MODEL FOR PREDICTING THE TENSILE STRENGTH OF FIBER REINFORCED ASPHALT CONCRETE.	178
Introduction	178
Formulation of Micromechanical Model for FRAC	179
Voigt's and Reuss's Models.....	179
Modified Rule of Mixture	180
Hirsch Model	181
Cox Shear-Lag Model	181
Nairn's Modified Shear-Lag Model	182
Halpin-Tsai Model.....	183
Incorporation of Viscoelasticity	184
Incorporation of Efficiency Factors.....	188
Model Assumptions.....	195
Results and Discussion.....	197
Hirsch Model	198
Shear Lag Model	198
Generalized Micromechanical Models for Predicting Tensile Strength of FRAC.....	200

CHAPTER	Page
8 SUMMARY, CONCLUSIONS AND FUTURE WORK	208
Summary and Conclusions.....	208
Effect of Fiber State on Mechanical Performance of Fiber Reinforced Asphalt Concrete.....	208
Evaluating Interaction of Fiber Reinforcement Mechanism with Mesostructure of Asphalt Concrete	209
Mechanism of Mechanically-Fiber Reinforced Asphalt Concrete in Tension....	210
Evaluation of Interfacial Shear Bond Strength and Critical Fiber Length in Fiber Reinforced Asphalt Concrete	212
Development of Micromechanical Models for Predicting the Tensile Strength of FRAC.....	214
Industry Use and Implementation	215
Future Work	217
References.....	219
APPENDIX A.....	229
APPENDIX B.....	243
APPENDIX C.....	248

LIST OF TABLES

Table		Page
2-1.	Physical Properties of Some Fibers (Löfgren 2005).....	15
2-2.	Summary of Well-known Micromechanical Models Which Have Been the Basis for Other Developed Models in the Literature (Malekmohammadi 2014).....	39
3-1.	Measured Physical Properties of Fiber.	46
3-2.	Aramid Fiber Dispersion States.....	51
3-3.	Summary of Extracted Aramid Dosage and Fiber State.....	63
4-1.	Mix Design Information.	78
4-2.	Gradation and Basic Volumetric Properties of All the Mixes.....	78
4-3.	Summary of Extracted Aramid Dosage and Fiber State for Various Fiber Mixing Methods.....	84
4-4.	Summary of Extracted Aramid Dosage and Fiber State for Various Fiber Mixing Methods.....	86
5-1.	Design of Engineering Experiment for the Effect of Multiple Variables on the Mechanical Response of M-FRAC Mixtures.	122
5-2.	Relative Percentages of the Different Fiber Dispersion Categories by Weight After Extraction for Mixes C and F2 with Various Fiber Length and Dosage.	123
5-3.	Data Summary of Stress-Log Reduced Strain Rate Mastercurves for No Fiber Case	127
6-1.	Measured Physical Properties of Fibers Types.....	149
6-2.	Experimental Design Factors of Single Fiber Pull-out Test.	154

Table	Page
6-3. Theoretical Critical Embedded Length of a Single Aramid Fibers for Mastic and AC Specimens Tested at Different Temperatures and Displacement Rates.	175
6-4. Recommended Fiber Lengths for Different Pavement Distresses and Fiber Types to Ensure High Efficiency.....	177
7-1. Proposed Modified Micromechanical Models for Predicting the Tensile Strength of FRAC.	201
7-2. Properties of Recycled Plastic Fiber and Asphalt Concrete Matrix Used for This Study (Yoo and Al-Qadi 2014).....	206

LIST OF FIGURES

Figure	Page
1-1. Overview Summary of Proposed Research Plan.....	9
2-1. Composites Classified by Reinforcement Shape (Mobasher 2011).	10
2-2. Internal Atomic Defects in Bulk Materials (Mamlouk and Zaniewski 2006).....	11
2-3. Schematic Description of the Fracture Process in Uniaxial Tension and the.....	27
2-4. Schematic Representation of the Microfibers Effect on the Fracture Process in Uniaxial Tension (Löfgren 2005).	29
2-5. Profile of the (a) Tensile Stress in the Fiber and (b) Shear at the Interface From Cox Model.....	35
2-6. Distribution of Shear Stress Along Fibril Direction at Different Loading Rates	37
2-7. Schematic Overview of Various Well-known Micromechanics in Terms of Complexity and Computational Effort (Malekmohammadi 2014).	40
3-1. Comparison of Gradations for the Mixtures.....	45
3-2. Thermogravimetric analysis (TGA) of Aramid and Polyethylene Fibers Compared with the Measurement in the Literature.....	46
3-3. Fatigue Life Definition of a Typical Axial Fatigue Test.	50
3-4. Summary of Casting Method to Evaluate In-situ Fiber Distribution; (a) Tested Specimen, (b) Splitting Specimen Along the Diagonal, (c) Half Splitting Specimen, (d) Zoomed in Photo of Region Identified in (c), (e) Casting on Split Specimen, (f) Separated Asphalt Mixtures from Cast Specimen, and (g) Complete Separation of Asphalt Mixture from Cast Specimen.	53
3-5. Photo of Sample Prepreation for Horizontal Core.....	55

Figure	Page
3-6. Comparison of $ E^* $ Mastercurves in; (a) Semi-log and (b) Log-log Scale.	57
3-7. Accumulated Strain and Flow Number Results for Control (No Fiber), FA and FB Mixes.	58
3-8. Results of Fatigue Evaluation; (a) Damage Characteristic Curve and (b) Predicted Fatigue Life Relationships.	60
3-9. Accumulated Strain During Flow Number Test for No Fiber Specimens Cored Horizontally and Vertically.	61
3-10. Accumulated Strain During Flow Number Test for (a) Vertical and (b) Horizontal Fiber and No Fiber Specimens.	62
3-11. State of Extracted Aramid Fibers from a Single Sample of (a) FA and (b) FB.	64
3-12. Photos Taken from the Aramid Fibers Distributed on the Surface Fracture of Each FB Mix; (a) Overall View of Casting Surface and (b) Enlarged Photo of Central Section.	65
3-13. Photos Taken from the Aramid Fibers Distributed on the Surface Fracture of Each FB mix; (a) Overall View of Casting Surface and (b) Enlarged Photo of Central Section.	66
3-14. SEM Images of Aramid Fibers of FA mix at Different Conditions; (a) Original Bundles (Unagitated); (b) Extracted Agitated Bundles; (c) Extracted Clusters; and (d) Extracted Individual Fibers (all images at 500x magnification).	69
3-15. SEM Images of Extracted Aramid Fibers of FB Mix at Different Conditions; (a) Agitated Bundles; (b) Clusters; and (c) Individual Fibers (All Images at 500x Magnification).	69

Figure	Page
4-1. Summary of Trends with Respect to The Binder/Mix Type and Performance Based on LTPP Climatic Regions.	76
4-2. Average Accumulated Strain During Flow Number Test for Mixes (a) A, (b) B, (c) C, (d) D, (e) E, (f) F-1, (g) F-2, (h) F-3, and (i) G.....	88
4-3. Comparison of $ E^* $ Mastercurves for Mixes (a) A, (b) B, (c) C, (d) D, and (e) E in; Log-log Scale (Left Figures) and Semi-log Scale (Right Figures).....	90
4-4. Comparison of Damage Characteristic Curves (Left Figures) and Predicted Fatigue Life Relationship Based on Constant Strain (Right Figures) for Mixes (a) A, (b) B, (c) C, (d) D, (e) E, (f) F-1, (g) F-2, (h) F-3, and (i) G.	94
4-5. (a) FN and (B) N_f Simulated at 300 μs Level of All the Mixes With and Without Fibers.	95
4-6. Comparison of V_{be} Values with Enhanced Flow Number of Asphalt Mixtures Due to Fiber for All the Mixes.	99
4-7. Comparison of $FAMT(Index)$ with Enhanced N_f of Asphalt Mixtures Due to Fiber.	103
4-8. Schematic Representation of FAM Phase in M-FRAC.....	104
4-9. Surface Failure of Specimens After Fatigue Test for (a) Mix D and (b) Mix C. .	105
5-1. Close-up Image of the Vertically Cored Specimens (the part of Specimens Near the Edge Was Painted with Blue Color for Air Void Distribution Study).	112
5-2. Cylindrical Asphalt Concrete Specimen with a Symmetric External Annular Crack Subjected to Applied Tensile Load.	113
5-3. Direct Tension Test Setup and Gluing Jig.....	114

Figure	Page
5-4. Typical Deformation Behavior under Tensile Load for (a) Replicate 1 and (b) Replicate 2 of Mix D at 20°C and 0.6 mm/min.	116
5-5. Photo of Sample Failure and Crack Plane Under Direct Tension Test.	116
5-6. Comparison of Average of Four LVDTs for Each Replicate.	117
5-7. Analysis of Loading Rate in Mix C Specimens (a) at 10°C and 0.6 mm/min and (b) 20°C and 11 mm/min.	119
5-8. Schematic of SCB Sample Preparation.	120
5-9. SCB Test Fixture.	121
5-10. <i>Nf</i> of Mixes C, D, and F-2 for No Fiber and Fiber Specimens at 300 μ s.	124
5-11. Example of Time-Temperature Superposition Application to Shift (a) Maximum Stress-Log Strain Rate Data to (b) Construct Maximum Stress Mastercurves as a Function of Reduced Strain Rate for the No Fiber Case.	128
5-12. Stress-log Reduced Strain Rate Mastercurve for No fiber and Fibers Specimens of mix C and 19 mm fiber.	129
5-13. Fracture Toughness of DT Asphalt Concrete Specimens with and without Fibers for Different Mix Types and Fiber Length and Dosage at 20°C.	133
5-14. Fracture Toughness of Fiber and No Fiber Specimens from (a) DT Test and (b) SCB Test at 10°C and Strain Rate of 0.0012 Per S for Different Mix types, Fiber Length and Dosage.	135
5-15. Total Fracture Energy of Asphalt Concrete with/without Fibers at 10°C Based on DT and SCB tests for Different Fiber Dosage, Length and Mix Types.	137

Figure	Page
5-16. Schematic Representation of (a) Crack Growth Mechanism, (b) Typical Monotonic Tension Test, and (c) Uniaxial Cyclic Fatigue Test.	140
5-17. Strain Field Superimposed on the Aggregate Structure at (a) -12°C and 0.7 mm/min and (b) 25°C and 50 mm/min at Peak Load in Each Case. The Bottom Figures are the Corresponded Fracture Process Zone Estimation Using Thresholding the DIC-Measured Strain Fields. Also, the Strain Contour Color Scale is Shown Next to the Top Figures (Doll <i>et al.</i> 2017).	141
5-18. Stress Profile Along an Embedded Fiber in a Matrix as a Function of Fiber Length.	145
6-1. Measured Stress-Strain Relationship of Fibers.	149
6-2. Photos of (a) Laser Beam, Cup, and Alighmnet Gadget for Fiber Pull-out Test Set up and (b) the Close-up of the Alighmnet Gadget and the Cup.	151
6-3. Fiber Pull-out Test Set up.	153
6-4. The Alignment of (a) Front and (b) Sideview of Fiber vs. Grip in the Pull-out Test.	153
6-5. Matrix Failure Mode of Fiber Pull-out Test at 20°C and 0.1 mm/s Using PG 70-22 Binder for (a) Aramid fiber with $Le=10$ mm, (b) Aramid Fiber with $Le=20$ mm, and (c) Nylon Fiber with $Le=10$ mm.	156
6-6. Load Displacement Curves of Pull-out Test Performed at 20°C and 0.5 mm/s for Different Replicates of Nylon 1 in the Asphalt Mastic.	157
6-7. Example of Force Displacement Relationship of Fiber During Pulling from Asphalt Mastic at Different Displacement Rates.	158

Figure	Page
6-8. Fiber Pull-out Failure Modes.....	159
6-9. Example of Fiber Pull-out Load Displacement Curve for Different Le based on Aramid Fibers at 20°C and 0.5 mm/s.....	160
6-10. Example of Fiber Diameter Measurement from (a) the Conical Shape of Hole Left After Pulled-out Fiber and (b) the Diameter of Fiber Coated with Asphalt Mastic.	161
6-11. Bundles of Aramid Fibers Each Representing a Distinct Diameter.	162
6-12. Effect of Different (a) Embedded Length of Nylon 1 and (b) Diameter of Aramid Fiber on the τ and F at 20°C and Displacement Rate of 0.5 mm/s.	163
6-13. Example of the Effective Pull-out Volume for (a) Thin and Short Fibers (b) Thick and Long Fibers.....	164
6-14. Average Shear Bond Strength for Different Fiber Types at Different Displacement Rates.	166
6-15. Relationship Between Ea of Binders with the Measured τ from the Pull-out Experiment.....	169
6-16. Relationship Between Ea and τ for both Asphalt Concrete and Mastic Specimens.	171
6-17. Forces Applied on a Single Fiber at the Crack/Microcrack.	172
6-18. Optical Microscopy Images of Aramid Fiber (a) Before and (a) After Pull-out Test.	174
6-19. Theoretical Critical Length of Aramid Fiber vs. Shear Bond Strength.....	176
7-1. Schematic Drawing of a Fiber at an Angle Across an Aribtriray Crack Plane. ...	190

Figure	Page
7-2. Comparison of Empirically and Theoretically Measured Tensile Strength of FRAC at Different Fiber Volume Fractions.	197
7-3. Comparison of Predicted Theoretical Tensile Strength Values Using (a) Shear Lag and (b) Halpin-Tsai Models with Experimental Data of M-FRAC at Different Fiber Volume Fractions and 19 mm Fiber Length.....	202
7-4. Comparison of Predicted Theoretical Tensile Strength Values Using (a) Shear Lag and (b) Halpin-Tsai Models with Experimental Data of M-FRAC at Different Fiber Aspect Ratio and 0.15% Fiber Content.	203
7-5. Comparison of Predicted Theoretical Tensile Strength Values Using (a) Shear Lag and (b) Halpin-Tsai Models with Experimental Data of M-FRAC for Different Mixes (C, D, and F-2) at 19 mm Length and 0.15% Content.	204
7-6. Comparison of Predicted Theoretical Tensile Strength Values Using (a) Shear Lag and (b) Halpin-Tsai Models with Experimental Data of M-FRAC at Different Volume Fractions of Recycled Plastic Short Fiber and 30 mm Length.	207

CHAPTER 1

INTRODUCTION

1.1 Background

Roadway pavements are an essential constituent of the transportation infrastructure. Pavements built with asphalt concrete makeup roughly 90% of the paved roads in the U.S. and over 99% of paved roads globally (USDOT 2010). Asphalt concrete is the popular paving material thanks to its lower initial cost compared with other alternatives, availability, ease of constructability, and ability to be used at both low volume and high-volume traffic conditions with equal success. Still, these roadways are under ever growing demands to carry heavier traffic loads. With weathering and continued usage, asphalt pavements endure deterioration and need several maintenance activities during their designed service life. Production of better-performing asphalts may not always be feasible through refining and processing improvements. Hence, modification of the asphalt concrete by incorporating new additives either in the bitumen or in the asphalt mixture is one of the common strategies to enhance the service lifetime of asphalt pavements. To this end, there are different types of modifiers, including various resins, rubbers, polymers, sulfur, metal complexes, fibers and chemical agents (Park 2012).

Fibers have been used as reinforcement for asphalt materials for many years in various parts of the world. Fiber Reinforced Composites have been used in engineering applications where a conventional material cannot fulfill the particular set of engineering properties that are needed (Bentur *et al.* 2006). This research study particularly refers to fiber reinforcement by means of randomly distributed short or chopped fibers. If properly

used, the overall cost for incorporating fiber reinforcement is generally low since relatively small quantities are needed to realize major benefits and no modifications or only small modifications are needed in the existing production processes (Park 2012). In general, Fibers are into asphalt for one of three reasons: (1) to prevent draindown or raveling of porous asphalt (PA) and stone matrix asphalt (SMA) (McDaniel 2015), (2) to improve resistance to mechanical performance, i.e. cracking and rutting resistance (Abtahi *et al.* 2010, Slebi-Acevedo, Lastra-González, *et al.* 2019), and (3) to enable multifunctional applications (Park 2012). The potential use of fiber as a reinforcement material in asphalt concrete (AC) has been documented in many studies.

1.2 Problem Statement

While published studies generally demonstrate positive benefits from using FRAC, it is not always the case, and when improvements are found they vary with respect to the types of fibers, properties of fiber (length, dosage, state), mix type and the mechanical experiment. In some cases, no statistically significant improvement has been identified from using fibers into asphalt mixtures. Due to this inconsistency, the widespread acceptance of fibers use in asphalt industry is plagued. The current state of knowledge with respect to fiber-reinforcement in AC materials has been mainly driven by experimental basis, with little fundamental investigation.

It is commonly accepted that the primary effect of fibers is that they improve the cracking resistance of composite materials by simply additional bridging mechanism across cracks which exist in different characteristic sizes and natures. The main mechanism that dictate their effectiveness is attributed to the effectiveness of the load transfer across

the interface between fiber and asphalt matrix. This study identifies key reasons attributed to the reinforcement mechanism of fibers and further proposes solutions to justify and/or possibly overcome the discrepancies in the literature. The governing factors that has significant impact on the reinforcement efficiency of fibers in asphalt mixtures are briefly explained as follows:

- The effect of fiber state as the basic, fundamental mechanisms that govern the mechanical response of FRAC is an undeniable issue. Stated differently, the reinforcement efficiency of fibers in composite are strongly dependent on the fiber state, inclusive of how the fibers are dispersed (dispersion), where the fibers are located (distribution), how they are arranged (orientation) and surface morphology (Noorvand et al. 2018). Although these effects have been recognized in previous studies, little to no systematic study has been done to attempt to quantify and correlate the effect of fiber state to the mechanical properties and performance improvements.
- The reinforcement efficiency of fibers is linked to the gradation, binder content, binder types and other volumetric properties of asphalt mixtures. There is no systemic study to relate the efficiency of fiber reinforcement to the composition of asphalt concrete.
- Asphalt concrete is a viscoelastic material that shows time and temperature dependency and, except at low temperatures, viscoplastic non-recoverable strain. This means that the reinforcing effect of fibers on the tensile strength, toughening and fracture energy properties of asphalt might vary at different time (frequency, loading rate) and temperatures as well as fiber properties and mix types. There is

no study considering the synergic effect of mechanical testing type, mix design type, time-temperature dependency of asphalt, and dosage and length of fibers to study the tensile and fracture properties of M-FRAC.

- Interface between fibers and matrix including the shear bond characteristics as well as efficiency of load transfer govern the failure mechanism of fibers in the asphalt. Because of the viscoelastic nature of FRAC, the shear bond strength between the fibers and the asphalt matrix are affected by temperature and loading rate. So, there is a need to develop a relationship between the shear bond strength and the stiffness of asphalt binder, mastic or concrete in the mix. This can provide fundamental understanding on the mechanisms of shear bond strength with reference to how easily the fibers pull out from the asphalt mastic and how easily the fibers break. Moreover, since shear bond strength is a parameter used to determine the critical fiber embedded length, an established shear bond-asphalt modulus relationship allows one to propose a practical fiber critical length in the asphalt concrete.
- A full factorial experiment to study all above parameters, while needed, are time-consuming and costly. Alternatively, mathematical models can be used to similarly examine the relationships between the mentioned parameters to predict the mechanical properties of fiber reinforced composites. Despite its popularity in any fiber reinforced composites field which shed light to further understanding fibers reinforcement, its use in FRAC is surprisingly non-existent to the best knowledge of this author.

1.3 Objective

The objective of this study is to develop a framework and a generalized theory for evaluating the fundamental mechanism of fiber reinforced asphalt concrete using experimental and theoretical methods. The specific objectives of this research are as follows.

- To quantify the state of aramid fiber including their distribution, dispersion, morphology, and orientation in the asphalt mix, and then to examine the impacts of fiber state on laboratory modulus, rutting, and fatigue performance of asphalt mixtures.
- To evaluate the mechanical properties of various asphalt mix designs reinforced with and without aramid fibers; then identify and quantify the key factors in the composition of asphalt mixtures attributed to the reinforcement mechanism of fibers.
- To evaluate the synergic effect of temperature and loading rate, mix types, fiber dosage, and fiber length on the cracking resistance of asphalt concrete with and without fibers using different tensile tests.
- To develop an analytical framework to determine and correlate the empirical shear bond strength from pull out test to the modulus of asphalt mastic and asphalt concrete in the mix; and then recommend a practical fiber length as a function of temperature for use in asphalt concrete.
- To present a variety of micromechanical techniques that could be potentially instructive in predicting the tensile strength of mechanically-fiber reinforced asphalt concrete.

1.4 Dissertation Outline

This dissertation consists of six chapters.

Chapter 1: Introduction

This section provides an overall introduction and background of this study, the needs for this research as well as the research objectives.

Chapter 2: Literature Review

This chapter provided a review of topics related to fiber reinforced asphalt concrete (FRAC) technology, critical assessment of experimental work on the mechanical behavior of FRAC, reinforcement mechanism of fibers in the composites as well as asphalt, and an overview of existing micromechanical models used for prediction of fiber reinforced composites.

Chapter 3: Effect of Fiber State on Mechanical Performance of Fiber Reinforced Asphalt Concrete

This chapter investigates and quantifies the state of fibers (distribution, dispersion, morphology, and orientation) in the asphalt mix using different test methods. Then, it studies how the state of fibers would influence the mechanical properties of asphalt mixtures with respect to their laboratory modulus, rutting, and fatigue performance.

Chapter 4: Evaluating Interaction of Fiber Reinforcement Mechanism with Mesostructure of Asphalt Concrete

This chapter first develops an optimal laboratory mixing process of fibers in an effort to improve the dispersion of fibers in asphalt mix. Then, it evaluates the mechanical properties of various asphalt mix designs reinforced with and without aramid fibers. Finally, it identifies and quantifies the key factors in the composition of asphalt mixtures attributed to the reinforcement mechanism of fibers.

Chapter 5: Mechanism of Mechanically-Fiber Reinforced Asphalt Concrete in Tension

This chapter evaluates the effect of temperature and loading rate on the tensile property of M-FRAC using a time-temperature superposition principle. Then, it studies mechanical behavior of M-FRAC with respect to different mix design types, fiber dosage, and fiber length using uniaxial fatigue, direct tension, and semi-circular bending tests.

Chapter 6: Evaluation of Interfacial Shear Bond Strength and Critical Fiber Length in Fiber Reinforced Asphalt Concrete

This chapter describes the analysis of shear bond strength using the experimental pull-out test at different displacement rates. Then, it establishes a relationship between shear bond strength and apparent modulus of asphalt mastic using elastic-viscoelastic correspondence principle. Finally, it uses the relationship in combination with mechanical tensile testing from Chapter 5 to determine a temperature dependent critical fiber length.

Chapter 7: Development of Micromechanical Model for Predicting the Tensile Strength of Fiber Reinforced Asphalt Concrete

This chapter presents several well-established micromechanical models to predict the mechanical behavior of composites. These models are then modified with some efficiency factors which are based on both theoretical calculation and experimental parameter obtained from Chapters 3 and 4 of this study. The accuracy of predicted tensile strength from the models are compared with the experimental measurements obtained from Chapter 5 and another experimental study in the literature.

Chapter 8: Summary, Conclusions and Future Work

This chapter Provides summary of the findings and conclusions from this research and the needs for future work.

A summary of the proposed research plan is shown in Figure 1-1.

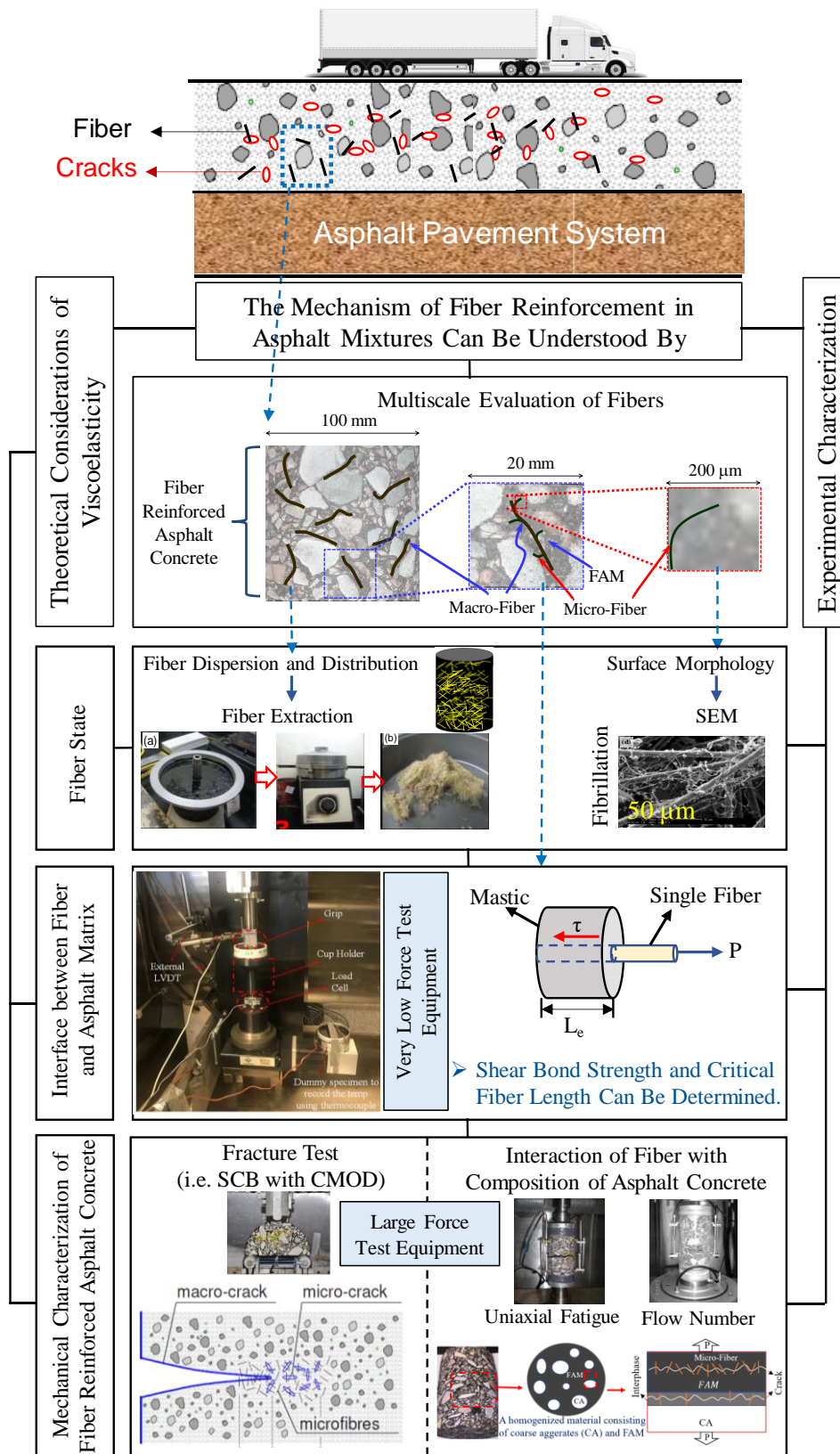


Figure 1-1. Overview Summary of Proposed Research Plan.

CHAPTER 2

LITERATURE REVIEW

2.1 Fiber Reinforced Composites

Fiber reinforced composites have been used in engineering applications where a pure material cannot fulfill the certain number of properties that are needed. Composites by definition refers to inclusion of one or more discontinuous phases (known as reinforcement) in a continuous phase which is a weaker material (known as matrix) (Clyne and Hull 2019). In any composite material, fibers are added to enhance the properties and behavior of the material. Four major types of matrices have been commonly used including polymers, metals, ceramic and carbon. Most of the composites used in the industry today are based on polymer matrices (Bentur and Mindess 2006, Gibson 2011).

Composites are classified by the shape or continuity of the reinforcement as shown in Figure 2-1, in which they are described as continuous or discontinuous relative to their continuity and as particulate or fiber relative to the shape of the reinforcement. The reinforcement is introduced in the form of long (continuous) or short (discontinuous) fibers, disks or plates, spheres, or ellipsoids. This research study particularly refers to fiber reinforcement by means of randomly distributed short fibers (Mobasher 2011).

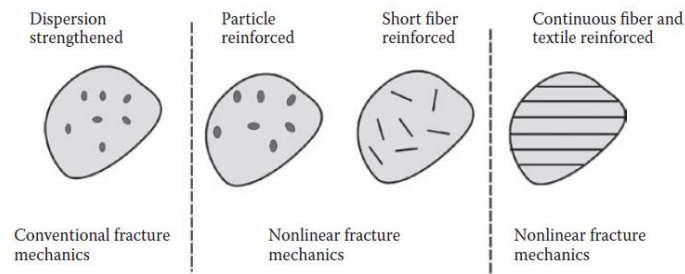


Figure 2-1. Composites Classified by Reinforcement Shape (Mobasher 2011).

2.2 Fiber Technology

Fibers are available in a variety of sizes, shapes, and materials. Fibers can be either natural or synthetic. Fibers have a very high strength-to-diameter ratio, with near crystal-sized diameters. In general, materials have several types of internal defects at the atomic scale, such as point defects, missing atoms and line defects, as shown in Figure 2-2. Fracture usually starts at the location of these defects. Since fibers have very small diameters, with near crystal-size, they have very few atomic defects. These minimal atomic defects make fibers very strong as compared to bulk materials. For example, a glass plate fractures at stresses of 10-20 kPa, yet glass fibers have strengths of 3-5 GPa or more (more than 300 times stronger) (Mamlouk and Zaniewski 2006).

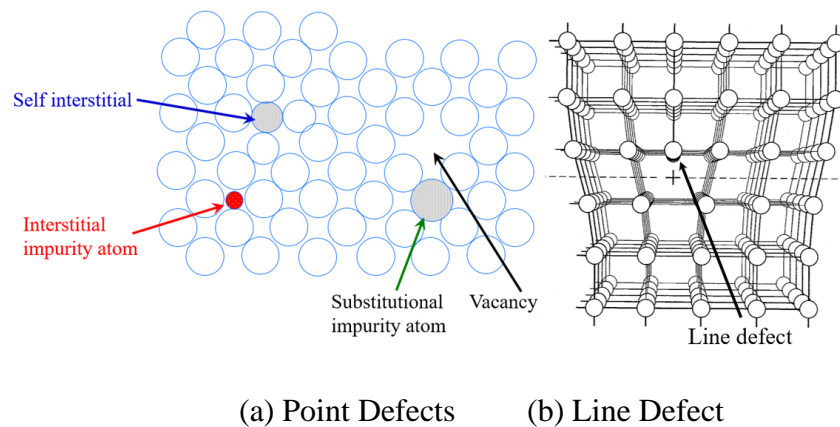


Figure 2-2. Internal Atomic Defects in Bulk Materials (Mamlouk and Zaniewski 2006).

Fibers are physically characterized by several important terms, definitions, parameters, and features, which are essentially dependent on fiber geometry rather than fiber type (i.e., metallic, polymeric, etc.). Some of these important relevant definitions are briefly mentioned as follows (Löfgren 2005, Mobasher 2011).

- *aspect ratio*: the ratio of length to diameter;
- *Filament*: a single and long continuous fiber with a largely circular shape
- *Yarns (or filament yarns)*: bundle of fibers consisting of several hundreds or thousands of filaments of microfibers;
- *Denier*: a unit of fiber fineness defined by the weight in grams of 9000 m of yarn. For example, 1 denier equals to 1 g/9000 m.
- *Chopped strand*: fibers chopped to different lengths;
- *Fibrillated*: the continuous networks of fiber, in which the individual fibers have branching fibrils
- *Monofilament*: a large-diameter continuous fiber, typically with a diameter larger than 100 μm ;
- *Multifilament*, a yarn consisting of many continuous filaments or strands.

2.3 Fiber Reinforced Asphalt Concrete

Fibers have been used as reinforcement for asphalt materials for many years in various parts of the world. The use of short random fibers into asphalt concrete is practical in a sense that it does not require much further effort in installation of asphaltic pavement, and additionally fiber reinforcement can be used in combination with other chemical modifiers for further efficiency in mechanical performance of asphalt concrete as needed (Park 2012). In general, Fibers are into asphalt for one of three reasons: (1) to prevent draindown or raveling of porous asphalt (PA) and stone matrix asphalt (SMA) (McDaniel 2015), (2) to improve resistance to mechanical performance, i.e. cracking and rutting resistance (Abtahi *et al.* 2010, Slebi-Acevedo, Lastra-González, *et al.* 2019), and (3) to

enable multifunctional applications (Park 2012). More than half of state agencies in the United States use fibers in AC mixtures, mostly for the purpose of stabilizing agents in PA and SMA (McDaniel 2015). The first documented evidence of fiber reinforcement in asphalt concrete (AC) occurred in the early 1950s as a strategy to prevent reflective cracking in an asphalt concrete overlay (Zube 1956). Later in 1980's, several field studies tried to the use fibers to improve mechanical performance of asphalt concrete pavement (Toney 1987, Maurer and Malasheskie 1989, Huang and White 1996, Serfass and Samanos 1996). These experimentally filed applications indicated some improvement in the rutting and fatigue resistances of asphalt concrete using fibers; however, the benefits of fiber reinforced asphalt concrete (FRAC) was not adequate according to these studies to overcome its initial construction costs (Maurer and Malasheskie 1989). Nevertheless, the use of fibers for the purpose of mechanical reinforcement in asphalt concrete pavements, particularly dense-graded mixtures, has received more attention recently with advancing knowledge of fiber reinforcement technology in the pavement industry (Park 2012). The potential use of fiber as a reinforcement material in asphalt concrete (AC) has been in fact documented in many studies.

2.4 Types of Reinforcing Fibers Used in Asphalt Mixtures

A wide variety of fiber types has been used in asphalt mixtures, including natural fibers (cellulose, lignin, date-palm, oil-palm), mineral (asbestos, rock wool), synthetic polymer (polyester, polypropylene, polyacrylonitrile, Aramid), and glass fibers. Recycled fiber materials such as newsprint, carpet fibers, and recycled tire fibers have also been used. These different types of fibers have benefits and disadvantages that make them better suited

for some applications than others. McDaniel also documents the use of synthetic polymeric fibers (i.e. polypropylene, aramid, polyester, polyacrylonitrile, nylon), glass fibers, and waste or recycled fibers (i.e. recycled carpet) for the purposes of providing mechanical reinforcement and improving rutting and cracking in asphalt concrete (McDaniel 2015).

Cellulose and lignite natural fibers are used in the production of paper and textiles. These fibers are not strong in tension, but it is absorbent and holds asphalt, therefore it is well-suited to reducing draindown in open-graded mixes but not for reinforcing dense-graded concrete. Metallic fibers (steel and carbon fibers) have been used, not only as reinforcing materials but also, to develop electrically and thermally conductive asphalt concrete materials. The conductive asphalt concrete can be used for asphalt-self healing purpose and multiple other applications such as snow melting/deicing thereon, sensing and actuation, electromagnetic interference (EMI) shielding, and energy harvesting/storage (Park 2012, Pan *et al.* 2015).

Synthetic polymeric fibers (i.e., polypropylene, polyester, aramid, and nylon), glass fibers, and recycled fibers are also used for the purposes of providing mechanical reinforcement and improving rutting and cracking in AC, referred to generically as mechanically fiber reinforced asphalt concrete (M-FRAC) (McDaniel 2015). Previous studies investigated the potential benefits of different synthetic fibers using a variety of AC mixtures, and laboratory tests such as indirect tensile tests, pull out tests, repeated load permanent deformation tests, triaxial shear strength tests, and uniaxial fatigue tests (Huang and White 1996, Lee *et al.* 2005, Tapkın 2008, Kaloush *et al.* 2010). Basic physical properties of the listed fibers are summarized in Table 2-1.

Slebi-Acevedo *et al.* (2019) used multi-criteria decision-making analysis methods to select the best fiber candidates for the purpose of mechanical reinforcement in asphalt Concrete. Their study indicated that the synthetic fibers with high tensile strength and elastic modulus were the most suitable option for the reinforcement of asphalt concrete mixtures. One of the ideal candidates is synthetic aramid fibers due to their very high tensile strength and modulus, which is also used in this study. Therefore, its characteristics are explained further in following section.

Table 2-1. Physical Properties of Some Fibers (Löfgren 2005).

Type of Fibre	Diameter [μm]	Specific gravity [g/cm^3]	Tensile strength [MPa]	Elastic modulus [GPa]	Ultimate elongation [%]
Metallic					
Steel	5-1 000	7.85	200-2 600	195-210	0.5-5
Glass					
E glass	8-15	2.54	2 000-4 000	72	3.0-4.8
AR glass	8-20	2.70	1 500-3 700	80	2.5-3.6
Synthetic					
Acrylic (PAN)	5-17	1.18	200-1 000	14.6-19.6	7.5-50.0
Aramid (e.g. Kevlar)	10-12	1.4-1.5	2 000-3 500	62-130	2.0-4.6
Carbon (low modulus)	7-18	1.6-1.7	800-1 100	38-43	2.1-2.5
Carbon (high modulus)	7-18	1.7-1.9	1 500-4 000	200-800	1.3-1.8
Nylon (polyamide)	20-25	1.16	965	5.17	20.0
Polyester (e.g. PET)	10-8	1.34-1.39	280-1 200	10-18	10-50
Polyethylene (PE)	25-1 000	0.96	80-600	5.0	12-100
Polyethylene (HPPE)	-	0.97	4 100-3 000	80-150	2.9-4.1
Polypropylene (PP)	10-200	0.90-0.91	310-760	3.5-4.9	6-15.0
Polyvinyl acetate (PVA)	3-8	1.2-2.5	800-3 600	20-80	4-12
Natural - organic					
Cellulose (wood)	15-125	1.50	300-2 000	10-50	20
Coconut	100-400	1.12-1.15	120-200	19-25	10-25
Bamboo	50-400	1.50	350-50	33-40	-
Jute	100-200	1.02-1.04	250-350	25-32	1.5-1.9
Natural - inorganic					
Asbestos	0.02-25	2.55	200-1 800	164	2-3
Wollastonite	25-40	2.87-3.09	2 700-4 100	303-530	-

2.4.1 Characteristics of Aramid Fiber

Aramid is primarily classified into two classes: meta-aramid and para-aramid and their production are known under trademark names Nomex and Kevlar, respectively. Kevlar (Para-aramid) is further discussed as this is class type used in this study. Kevlar® Para-Aramid is an aromatic polyamide characterized by long rigid crystalline polymer chains. “Para” refers to the specific linkage position of the aromatic rings (Yang 1993). Para-aramid fibers have relatively tensile strength and modulus while low elongation at break. It also has a high strength to weight ratio which is five times as strong as steel, ten times as strong as aluminum and up to three times as strong as E-glass. Aramid fibers, which is golden brown in color, are resistant to chemicals and heat; they are hard to melt and can retain their mechanical properties at temperatures of up to 300-350°C (Mera, H. & Takata 1989, World Health Organization 1993, Yang 1993). Para-Aramid fibers are used predominantly in advanced composite materials to enhance stiffness, strength, stiffness, durability, and heat resistance. Since these improvements are achieved by fibers without adding much weight, it is used commonly in the aerospace industry, sports equipment, and for military purposes (World Health Organization 1993). Other common applications as the reinforcing materials in ceramic composites (i.e. portland cement concrete), thermoplastics, tires and mechanical rubber goods (Mobasher 2011).

2.5 Laboratory Study of Mechanically Fiber Reinforced Asphalt Concrete

There are the plenty of available literature based on using different types of fibers for reinforcing asphalt concrete properties; however, many of these studies are basically repetitions of what has been found in previous studies with very little insight to further help

understand the reinforcement mechanism of fibers. To provide a meaningful review on the current state of knowledge with respect to fiber-reinforcement in AC materials, the literature work on laboratory studies of M-FRAC is discussed in two different sections. The first section reviews the general laboratory findings on mechanical performance of M-FRAC using various types of fibers, and section two specifically focuses on the mechanical test results associated with the use of synthetic fibers in asphalt mixtures.

2.5.1 Mechanical Performance of Asphalt Concrete with Fibers

Previous studies have shown that addition of fiber in dense graded and open graded asphalt concrete mixtures could change the viscoelasticity of the mixture (Huang and White 1996), and improve different properties of asphalt mixtures including increasing dynamic modulus (Shaopeng *et al.* 2007), relaxation ability and rutting resistance (Peltonen 1991, McDaniel and Shah 2003, Mahrez *et al.* 2005, Behbahani *et al.* 2009), resistance to the low-temperature anti-cracking properties, fatigue cracking and reflective cracking (Maurer and Malasheskie 1989, Tapkın 2008, Wu *et al.* 2008, Ye *et al.* 2009, Qian *et al.* 2014, Park *et al.* 2015), and tensile strength and therefore improve moisture susceptibility (Serfass and Samanos 1996, Putman and Amirkhanian 2004).

Jahromi and Khodaii (2008) used Marshall Stability, creep, indirect tension, and repeated load indirect tensile tests to examine the characteristics of carbon fiber-reinforced asphalt mixtures. Improvement in the fatigue life and permanent deformation of the asphalt mixtures was observed with presence of carbon fibers. Park *et al.* (2015) used pull out and indirect tension tests performed at -20 °C to investigate the reinforcement mechanism of steel fibers in the asphalt mixtures in comparison with non-reinforced specimens. The

results suggested improvement of the indirect tensile strength, fracture energy and toughness up to 62.5%, 370% and 895%, respectively.

Mahrez *et al.* (2005) examined the creep and rutting resistance of glass fiber-reinforced asphalt mixtures using wheel tracking test and observed higher resilient modulus, and higher resistance to permanent strain and rutting for asphalt mixtures with glass fibers. Mohammed *et al.* (2020) studied fatigue cracking resistance, moisture damage resistance and fracture toughness of asphalt mixture modified with different contents of glass, cellulose, and steel based on different tests. The test results showed that fibers had a significant impact on the fracture toughness and stiffness modulus of asphalt mixtures at 20°C test temperature. However, the tensile strength or the moisture damage resistance of asphalt mixtures did not change with presence of fibers.

Lee *et al.* (2005) performed indirect tension strength test to study the fatigue cracking resistance of asphalt concrete reinforced with nylon fibers using fracture energy. The results showed 85% higher fracture energy for asphalt mixtures fabricated with fibers of 1% volume and the length of 12 mm compared with non-reinforced asphalt mixtures, indicating increased resistance to fatigue cracking. Both Tapkin (2008) and Huang and White (1996) found asphalt mixtures reinforced with polypropylene fibers improved fatigue life and increased resistance to rutting. Tapkin (2008) reported enhanced resistance to rutting and reduced reflection cracking in asphalt mixture modified with polypropylenes.

Shaopeng *et al.* (2007) investigated the effect of polyester, cellulose, and mineral fibers at dosages of 0.3 %, 0.3 %, and 0.4 %, respectively on dynamic properties of asphalt mixtures and found higher dynamic modulus for fiber-modified asphalt mixtures compared with the control mixture. It is worth mentioning that such high content of fiber use in

asphalt mixture requires modification in the mix design by increasing binder content, which might limit their use as reinforcing agent. In a different study by Serfass and Samanos (1996), they utilized asbestos, rock wool, glass wool and cellulose in asphalt mixtures and examined the low-temperature direct tension, resilient modulus, rutting resistance and fatigue resistance of the mixtures. They reported improvement in the fatigue life and rutting resistance and reduction in the temperature susceptibility of asphalt mixtures modified with the fibers.

Xu *et al.* (2010) examined the effect of polyester, polyacrylonitrile, lignin, and asbestos on rutting, flexural strength and strain, tensile strength, fatigue, and resistance to freeze-thaw cycles of asphalt mixtures. It was observed that resistance to rutting, toughness, flexural strength and ultimate strain, fatigue life of asphalt mixtures improved with incorporation of all four types of fibers. While the improvement in rutting resistance, fatigue life and split indirect tensile strength was greatest for polymer fibers (polyester, polyacrylonitrile) compared with asbestos and lignin, the flexural strength of asphalt mixtures reinforced with asbestos and lignin fibers was higher. Nevertheless, the freeze-thaw study did not show any improvement for asphalt mixtures modified with fiber.

2.5.2 Mechanical Performance of Asphalt Concrete with Synthetic Fibers

The literature in general reports benefit of synthetic fibers in improving the mechanical performance of asphalt concrete mixtures. However, this has not be always the case. There are studies that did not find any notable benefit from using fibers in asphalt mixtures which are discussed as follows. Note that since aramid fibers has gained popularity in recent years including this work, the following review is mainly focused on

reporting the studies related to mechanical performance of synthetic aramid FRAC, while the conclusion of following studies can be applicable to any types of synthetic fibers.

Kaloush *et al.* (2010) investigated the fracture properties of asphalt mixture reinforced with synthetic polypropylene and aramid fibers at -10 °C, 0 °C, and 10 °C using IDT test. They reported improvement in the tensile strength and fracture energy of fiber-reinforced mix in the range of 25–50 % and 50–75 %, respectively compared with their no fiber mix (Kaloush *et al.* 2010). On the contrary, using similar fiber blend type, length and content to Kaloush's study, Muftah *et al.* (2017) showed no significant improvement to the tensile strength of dense-graded asphalt mixtures with and without fibers using IDT test at -10 °C. However, they used Semi Circular Bending (SCB) test to examine the fracture properties of their asphalt mixtures by incorporating higher dosage level of aramid fibers at 5°C, 20 °C, and 37 °C. Their results showed that while fibers did not have improve the performance of the mix before the peak load where the crack initiates, fibers were found to reduce crack propagation significantly during the post peak region. The improvement seemed became more significant along with increasing testing temperature.

Klinsky *et al.* (2018) examined the effect of 19 mm and 0.05% aramid-polypropylene fiber blend on the fracture resistance of a conventional dense-graded hot mix asphalt at 21°C using the semicircular bending (SCB) test. They found 20% and 30% increase in the tensile strength and fracture energy of the fiber-reinforced mixture, respectively relative to no fiber mixtures. In contrast, Apostolidis *et al.* (2019) studied the tensile strength of asphalt mortars reinforced with same fiber blend and the same length and content using a direct tension (DT) test set-up at 20°C. Their results did not show any difference in the tensile strength of fiber and no fiber specimens. Whether this inconsistency in the test

results is due to the different mix types (asphalt concrete vs asphalt mortar) or test type (SCB vs DT) need to be addressed. Moreover, they showed increasing fiber dosage increased the tensile strength at -5, 5, and 20°C, while increasing the length of fibers did not further increase the strength values.

Additionally, some studies report improvement, however, their results appear to be either statistically insignificant. For example, Jaskuła *et al.* (2017) evaluated the low temperature cracking susceptibility of aramid-polyolefin fiber reinforced asphalt concrete at -20°C. They reported fibers improved the low temperature pavement performance; however, a closer look at their results revealed that it is very likely that their test results between fiber and no fiber specimens were statistically insignificant. Qian *et al.* (2014) compared aramid fibers with polyester fiber using multiple-fiber pullout test and found that aramid fibers require much longer embedment length to fully activate its bond with asphalt than the polyester fiber does. However, without a mechanical test result, their conclusion must be taken with great caution. Slebi-Acevedo *et al.* (2020) studied the tensile properties of porous asphalt mixtures reinforced with 0.05% of 19 mm aramid-polyolefin fiber blend and 12mm and 4 mm homopolymer polyacrylonitrile fibers using IDT test at room temperature. Although they concluded that fibers improved the toughness of asphalt mixtures, their results appear to be insignificant regardless of the fiber type and length. In a recent study by (Motamedi *et al.* 2020), the fracture toughness of asphalt concrete reinforced with aramid-polyolefin fiber blends was examined using the Edge Notch Disc Bend (ENDB) specimen. They investigated the effect of several variables including different fiber contents, low temperatures and loading rates on fracture toughness of asphalt mixtures. Their results showed that increasing fiber content consistently increased the

toughness values at all the three temperature and loading rate. The effect of loading rate was not found significant in their studies; however, at testing temperature of -5, -15, and -25°C, the average toughness of asphalt mixtures increased by approximately 30, 15, and 10%, respectively. This indicates that the effect of fiber reinforcement efficacy start diminishing by reducing temperate which might be attributed to fiber breakage point due to exceeding the aramid fiber critical length. Unfortunately, their study did not report any standard deviations and statistical analysis for their toughness results in order to draw conclusion with complete confidence.

2.6 Fiber Mixing Methods

It is known that a good dispersion and distribution of fibers is a key in maximizing the reinforcing benefits in any composite materials. While pre-established procedures for the preparation of asphalt mixtures with conventional bitumen exist, there is a lack of a generally applicable laboratory method to introduce the fibers into asphalt concrete mixtures (Slebi-Acevedo, Lastra-González, *et al.* 2019). Two methods are commonly known. Dispersion and distribution particularly become more important when the introduction mechanism include bundles that may hold thousands of individual fibers. The first method is called wet procedure. In this method, the fibers are previously mixed with the binder before aggregates and filler are incorporated. In this technique a good dispersion between fibers and bitumen should be achieved in order to avoid the formation of clusters; the combination of sonication and high shear mixing procedures helps to achieve a high degree of dispersion (Khattak *et al.* 2012). The second method is known as dry procedure and consists of mixing fibers and aggregates before bitumen is incorporated to the blend

(Abtahi *et al.* 2010). In general, the dry procedure is the most used as it enables a good dispersion of the fibers and reduces the variability in the experimental tests of the asphalt mixtures (Abtahi *et al.* 2010, Slebi-Acevedo, Lastra-González, *et al.* 2019).

Researchers at Arizona State University have already developed a theory of fiber mixing strategy (unpublished work) to determine the optimum laboratory mixing process to create fiber reinforced asphalt concrete (FRAC) and also to understand the impact of various changes to these processes. The study focused on mixing aramid and polyethylene fiber blends, and multiple cases were evaluated based different mixing parameters (time, mixer type, fiber blend, and mixing processes). The summary of the findings are as follows:

- When the fibers are first introduced to the aggregate, the polyethylene fibers will initially shrink, crinkle, and start melting at temperature greater than 130-135°C.
- As the aramid fibers begin to separate, either by being pulled away in individual and clumped form by the polyethylene or by friction during agitation, the exposed surface area of the fibers will increase resulting in an increase in the overall static charge of the system and an increase in the attraction between the fibers (e.g., clumping).
- In the case of the aramid fibers, there may also be additional thermal degradation or loss of a surfactant coating that helps to reduce static charge. This was supported by TGA analysis, which showed an approximate 2% loss in mass in the aramid fibers at 160°C.
- If at the same time that these processes occur the asphalt cement is introduced, then the static charges are apparently reduced, and the individual aramid fibers carried

by the melting polyolefins and dislodged through aggregate friction effects remain separated.

- The adhesive properties of the asphalt may begin pulling the initially agitated bundles of aramid fibers apart even more. In the case of the aramid fibers, the impacts from this third mechanism is theorized to result from differential viscosity at coated and uncoated particles and is therefore believed to become very small once the mixture is fully coated.

2.7 Effect of Fiber State on Mechanical Performance of FRAC

Fundamentally, fibers are used as the reinforcement for enhancing the tensile strength properties of composites. Such mechanism may result in increasing the amount of strain energy which can be absorbed during the fatigue and fracture process of the mix (Abtahi *et al.* 2010). However, one essential key to fully take advantage of fiber reinforcement is the distribution of fibers within the mixture as well as the state of fibers which are distributed. Partl *et al.* (1994) studied the effect of various contents of cellulose fibers in a study of stone matrix asphalt (SMA) using indirect tensile test and thermal stress restrained specimen test (Partl *et al.* 1994). No noticeable improvement in SMA with cellulose fiber was observed considering the two tests performed. The authors however noticed the clumping of fiber during the mixing process and concluded that the poor distribution of cellulose fibers in SMA was the reason for poor performance (Partl *et al.* 1994). Although the importance of fiber dispersion on the performance of asphalt mixtures have been addressed in previous studies, there is very little systematic study to the best knowledge of authors that have quantitatively assessed the distribution of fibers and

attempted to link that distribution to the mechanical performance of asphalt mixtures. Noorvand et al. (2018) recognized that the importance of fiber state on the mechanical performance of AC. Their results indicated that a higher level of dispersion and microfibrillation of aramid fibers enhanced the rutting resistance of asphalt mixtures.

Knowledge of fibers states with respect to their orientation within the matrix is another key factor in the characterization of the fiber reinforced composites (Fu *et al.* 2009). The subject of orientation preference of distributed short fibers in different parts of a structural element is a controversial issue and has been under debate in the scientific community for so long (Suuronen *et al.* 2013). Various empirical and theoretical techniques exist in the literature to directly determine the orientation of fibers (Bentur and Mindess 2006). Some common methods are X-ray tomography, a magnetic technique, AC-impedance spectrometry, and slicing photometry, (Suuronen *et al.* 2013). Stereological concepts have also been predominantly used to infer the fiber orientation in the composites such as cement concrete (Bentur and Mindess 2006). Stereology is based on geometry and probability theory, and it is the three-dimensional interpretation of two-dimensional cross sections of materials. It provides practical methods for obtaining measurable data about a three-dimensional material from measurements carried out on two-dimensional planar sections of the material. A good review of the concept and methods of application can be found in (Stroeve and Hu 2006). The orientation of fibers effect on composites have been experimentally and theoretically measured by i.e. fiber pull-out tests under different fiber inclination angles (Li *et al.* 1990a).

In fiber reinforced asphalt concrete, the study of fiber orientations is very limited. One main reason is due to the complexities and difficulties associated with common

experimental technique such as X-ray approach, due to similarity between the density of natural and synthetic fibers and asphalt. Nevertheless, Mohammed *et al.* (2020) examined the orientation and distribution of short steel fibers in the asphalt mix, which has a higher density than asphalt, by using X-ray CT and image analysis. They found that steel fibers exist in a variety of angles, forming a three-dimensional network throughout the asphalt concrete specimens.

2.8 Understanding the Reinforcement Mechanism of Fibers in Composites

From the perspective of this author, there are two main mechanisms that need to be understood when dealing with the cracking and fracture behavior of fiber reinforced composites. Those include 1) fiber bridging mechanism and 2) the shear stress transfer between fiber and matrix. These two factors have general applicability to the reinforcement roles of fibers in composites regardless of the type of matrix one deals with. However, when the matrix is time/temperature dependent such as asphalt concrete, additional mechanisms takes place that also need to be understood. These will be discussed partly here with refence to shear stress transfer mechanism and some in the body of this work, particularly in Chapter 5.

2.8.1 Fiber Bridging Mechanism

2.8.1.1 Mechanics of Crack Formation and Propagation

It is commonly accepted that the primary effect of fibers is that they improve the cracking resistance of composite materials by simply additional bridging mechanism across cracks which exist in different characteristic sizes and natures. These cracks are

formed and through the composite materials under repeated loading (Anderson 2017). To understand how and to what extent fibers can act as reinforcing elements in composite materials, fracture process of a quasi-brittle concrete material (i.e. portland cement concrete, asphalt concrete at 10-20°C) subjected to a uniaxial load is schematically presented in Figure 2-3 (Löfgren 2005). During a loading process, microcracks will start to grow, initially at the interface between the FAM and the coarse aggregates (A) and at a higher loading level, the microcracks at the interface start to branch inside the FAM phase (B). At the peak stress (C), structure is populated with a certain distribution of microcracks with varying lengths. Most of these micro-cracks are stable, with perhaps one, maybe two, cracks that are about to become unstable. It is the unstable crack in the micro-crack population at peak-load that triggers macro-crack propagation and localization. The stress-drop (D) is the consequence of the macrocracks propagation through the specimen. Crack bridging and crack branching is the primary mechanism responsible for the long softening curve (D-E) observed in experiments (Van Mier and Man 2009).

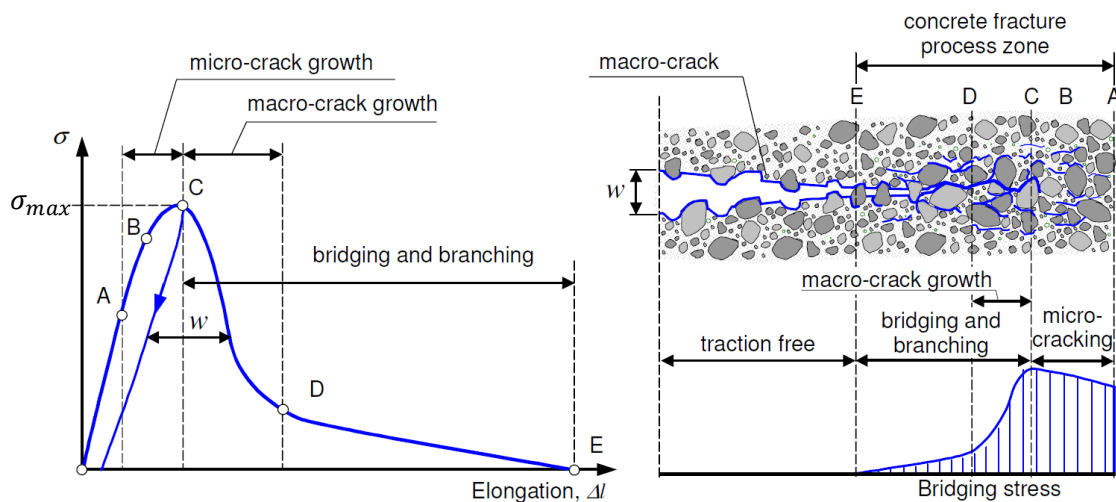


Figure 2-3. Schematic Description of the Fracture Process in Uniaxial Tension and the Resulting Stress-Crack Opening Relationship (Löfgren 2005).

2.8.1.2 Bridging Mechanism of Microfiber Reinforced Asphalt Concrete in Tension

Mechanically, the tensile stress versus displacement curves with a softening response (the case in this study) for AC and M-FRAC can mainly be divided into two different regimes: (1) the pre-peak regime and (2) post-peak regime (softening curve after the peak load). These regions, while related, each represents distinct phenomenon. Microscopically, while pre-peak region is characterized by the formation, coalescence, and propagation of micro-cracks, post-peak region is identified by macrocrack growth and localization along a single crack (Anderson 2017).

The conventional notion of the fiber reinforcement in composites with softening behavior is that they are commonly used to improve the performance of post-peak region rather than the tensile strength (Löfgren 2005). The fibers used for such purpose in these composites are typically 500 μm in diameter and 25–50 mm in length. The effect of these macrofibers is pronounced after macrocrack initiation where stresses after matrix cracking are effectively transferred leading to toughness improvement (Li and Maalej 1996). In order to improve the tensile strength, microcracks need to be arrested and their coalescence into a dominant macrocrack delayed to higher stress levels. Macrofibers have the ability to bridge and interact with macrocracks due to their large dimensions. Besides, these fibers are spaced too far apart to arrest and interact with small cracks because of the small number of fibers per square meter even at relatively high-volume content which is typically 2 vol% (Yi and Ostertag 2001). On the other hand, it has been shown that the use of microfibers (10–20 μm in diameter) in composites such as asphalt concrete (Kaloush *et al.* 2010, Takaikaew *et al.* 2018, Apostolidis *et al.* 2019) or portland cement concrete (Betterman *et al.* 1995, Banthia and Sheng 1996, Lawler *et al.* 2003) increased the tensile strength

through delaying the widening of microcracks (see 2-4). Therefore, the distinction in reinforcement mechanism between microfibers and macrofibers should explain some of the inconsistency in the experimental test results between different types of fibers which have been used for the reinforcement of asphalt concrete.

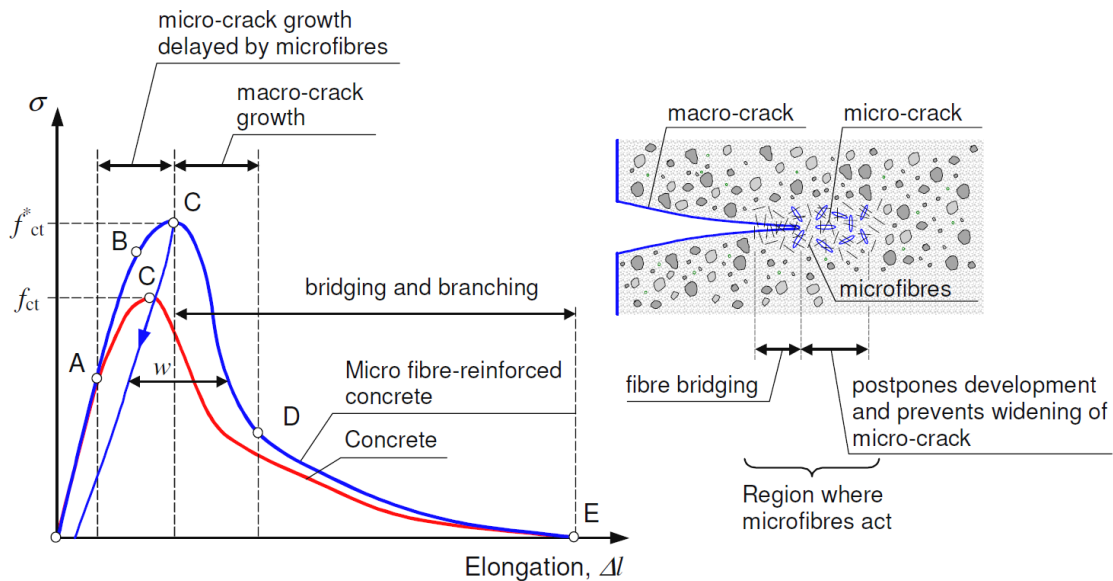


Figure 2-4. Schematic Representation of the Microfibers Effect on the Fracture Process in Uniaxial Tension (Löfgren 2005).

2.8.2 Shear Stress Transfer Mechanism

The fiber-matrix interface controls the quality of the bond and load transfer between the fiber and matrix within a composite material (Zhandarov and Mäder 2005). When composites are exposed to different loading environments, the effectiveness of the load transfer across the interface plays an imperative role in the general performance of the composite (Mobasher 2011, Teklal *et al.* 2018, Clyne and Hull 2019). It is this load transfer that allows the composite to satisfy its mechanical function. So, understanding the mechanisms that govern stress transfer provides the foundation for predicting the stress–

strain curve of the fiber reinforced composite. Such understanding along with measurable prediction may also serve as a basis for developing composites of better-quality performance through modification of the fiber–matrix interaction. This might be accomplished, for instance, through modifications in the geometry of fiber, or fiber surface treatment. A common way to characterize the quality of bond between fiber and matrix is by evaluating the interfacial shear strength which has been found the key to composite toughening and fracture properties (Bentur and Mindess 2006, Gibson 2011, Park *et al.* 2017, Clyne and Hull 2019). Several experimental and theoretical methods exist for characterizing the effect of fiber-matrix interface on the load bearing capacity of composites. These will be discussed in the following sections.

2.8.2.1 Experimental Characterization of Fiber-Matrix Interface

Experimental characterization of the interface property is a challenging task and there is no specific test standard available. These have been explored on various levels: either by indirect approaches such as macroscopic mechanical tests on bulk composite specimens, or by more direct approaches such as micro-droplet/pull-out, push-out (or indentation), compression test (Slice test), micro-bond or fragmentation tests (Teklal *et al.* 2018). These tests consider various scales and specimen geometries to measure the bond quality at the fiber-matrix interface by different parameters. For example, those include the interface shear (bond) strength (IFSS), τ_i , for the bonded interface; and the interface frictional strength (IFS), τ_{fr} , for the debonded interface.

Fiber pull-out test (or debonding test) is a very common micromechanical test used to characterize the interfacial bonding between fiber and matrix. In a pull-out test, developed

in a variety of test configurations, a single fiber is embedded in a block of matrix (usually a resin) and the fiber is pulled out from the cured resin by applying a tensile force on the fiber (Banhozler 2004, Mobasher 2011, Teklal *et al.* 2018). Several modes of fiber pull out stages have been observed; fiber debonding, post debonding friction of fiber against debonded surfaces, and finally, either the fiber breaking or matrix being pulled out by the fiber (Naaman *et al.* 1991a, Mobasher 2011, Teklal *et al.* 2018). It should be noted that the chemical and physical bonds are not distinguishable from the test results of a single fiber pullout, and their interaction is only realized in the context of the initial debonding and frictional sliding.

2.8.2.2 Experimental Characterization of Fiber-Asphalt Matrix Interface

Very few studies have characterized the interfacial properties between fibers and asphalt matrix. Yoo and Kim (2014) performed mechanical test to indirectly evaluate the average interfacial bond strength of thermo-plastic fiber in asphalt concrete through direct tension test. However, these indirect methods take several parameters into account, among which the one linked to the interface is not essentially the most significant. They can only help qualitatively assess materials of the same type, in which the process of rupture involves the interface in the similar way. Others have addressed the bond between fibers and matrix and the effect of fiber length on the properties of FRAC using direct approach (Lee *et al.* 2005, Qian *et al.* 2014, Park *et al.* 2017, Apostolidis *et al.* 2019). The studies used different fiber types, test configurations, test conditions, and methods of analysis.

Qian *et al.* (2014) conducted multiple fiber pull-out test from asphalt mastic using a modified ASTM D6723 test procedure used for direct tension test. Polyester (20 mm

diameter) and aramid (14 mm diameter) fibers were used. Using the multiple fiber pull-out test at -18°C , the authors concluded that the critical embedment lengths required to fully develop interface bond for the polyester and aramid fibers were about 8 and 19 mm, respectively. Therefore, they recommended total fiber lengths of 15 and 38 mm for both fiber types, respectively, however, they did not elaborate whether the critical fiber length was defined by the maximum force from the fiber pull out test or the force at which fiber fractures. Moreover, they reported the value of shear bond strength in order of thousands, which is unrealistic. Upon revision of the paper and recalculating their average shear bond strength by the author of this work, it turned out that the shear bond strength of aramid and polyester fibers are in the range of 0.5-1 MPa and 0.1-0.5 MPa, respectively.

Park *et al.* (2017) investigated the interaction between a straight steel fiber and the surrounding asphalt matrix using single fiber pull-out tests and numerical simulations. Based on their experimental observations, the pull-out process is governed by one of three modes of failure: 1) interface failure mode, 2) matrix failure mode, or 3) mixed-mode failure. The numerical simulations showed that the stress distribution along the fiber surface varies substantially with temperature and fiber dimensions. The simulation results showed that the shear bond strength between steel fibers and asphalt binder is 6.9 MPa, and it is independent of temperature, pulling rate, and fiber dimensions within the ranges used in the study. However, its independence from temperature would be really questionable and the value of 6.9 MPa seems excessively high given the fact that the shear strength value cannot be higher than tensile strength. In the context of a Mohr-Coulomb failure criterion, in the presence of shear and tension, the strength under shear is

significantly lower than the tensile strength. So, if critical shear strength is 6.9 MPa, tensile strength should be around 10 -12 MPa which is questionable.

Lee *et al.* (2005) conducted single fiber pull-out tests from asphalt binder at a constant pulling rate of 5 mm/s at 20°C. They concluded that the critical embedded length was 9.2 mm, which was obtained by the fiber fracture. In another study by (Mohammed *et al.* 2018), they used the adhesion tensile test (ASTM D4541) to measure the cohesive and adhesive properties of an asphalt-fines mastic by measuring pull-off strength. In this test, a steel piston is allowed to adhere to the mastic and pulled at a certain rate. The stress at which the piston is pulled is recorded as the adhesive strength between the two materials or cohesive strength within the mastic, whichever is smaller. The results showed that the cohesive or the cohesive-adhesive strength ranged between 1.5 – 2.5 MPa.

2.8.2.3 Theoretical Calculation of Shear Stress Transfer in Fiber Reinforced

Composites

Theoretical analyses dealing with the stress state (shear and normal stress) at the interface region are critical to understanding how and to what degree the properties of interface effect the mechanical behavior and fracture response of the composites. In many simplified treatments of the shear stress-transfer problem, an average interfacial shear stress value is calculated assuming a uniform distribution of interfacial shear stress along the entire length of fiber length. However, the magnitude of shear bond stress is known to vary along the length of fiber, and the measurement of the shear stress distribution is often done with the help of analytical or numerical approach (Naaman *et al.* 1991b). A variety of analytical and numerical models has been developed to study the shear bond strength

and stress transfer behavior of a fiber embedded in a matrix block to characterize fiber/matrix interfacial adhesion. In general, three different modeling approach exist in the literature: (I) The perfect interface model, (II) the cohesive interface model, and (III) the fracture mechanical model (Banhozler 2004). The first two approaches are based on so called “shear-lag” method in which force equilibrium is established within the fiber/ pull out system and also known as maximum stress criterion; whereas the last model is based on energy balance principles. All three models have one thing in common: that is, they are based on a so-called direct boundary value problem. They use given shear bond properties to simulate the relationship between load and displacement of a fiber pull-out test. Then, optimization algorithm is used to fit the simulated pull-out curve to the experimental data to drive the material parameters, which then unknown shear bond properties can be obtained for a material combination. Detailed description of each approach and the analytical derivations can be found in Banholzer Bjorn’s dissertation (Banhozler 2004). The state of stress along the fiber length in an elastic matrix and a viscoelastic matrix is not treated similarly and each explained separately as follows.

2.8.2.3.1 Theory of Stress Transfer Mechanism Between Fiber and an Elastic Matrix

One of the pioneering models that simulated the behavior of the interface between fiber and elastic matrix is the Cox model (Cox 1952). In his model, he assumed a perfect interface to describe the load transfer between the fiber and elastic matrix, which implies that the displacements are continuous at the interface. In other words, the interface is assumed to be infinitesimally thin, and hence the matrix properties in the neighborhood of the fiber are equal to those of the bulk matrix. The tensile strain in the matrix at a distance

R from the fiber is the same as to the tensile strain of the composite. There is no impact of the stress field around one fiber on adjacent fibers. Cox model is conceptually sketched in Figure 2-5. It can be seen that interfacial shear stresses developed due to load transfer have the maximum amplitude at the fiber ends (Figure 2-5(a)). The model only considers the axial components of the stresses produced in the fiber and the matrix, so any radial displacements is disregarded. Figure 2-5(b) shows that axial stress approaches to zero near the fiber end region, implying that there is no stress transfer over the both end face of the fiber (Teklal *et al.* 2018). In Figure 2-5, the Cox model was actually presented for the case when the length of fiber (L) is larger than critical fiber length (l_c).

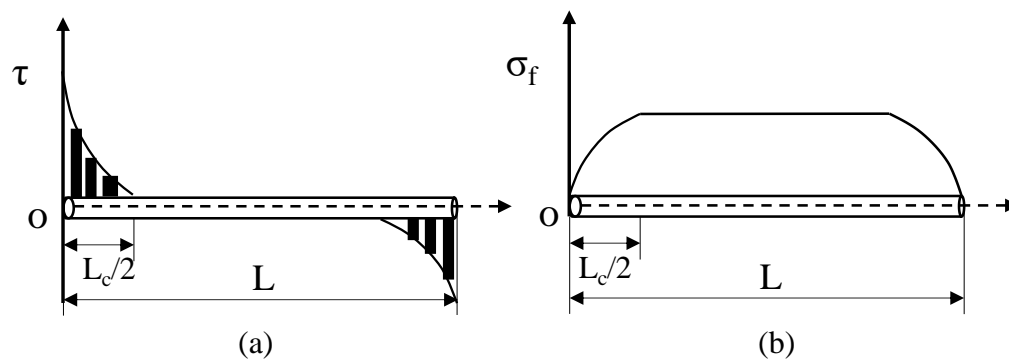


Figure 2-5. Profile of the (a) Tensile Stress in the Fiber and (b) Shear at the Interface from Cox Model.

2.8.2.3.2 Theory of Stress Transfer Mechanism Between Fiber and a Viscoelastic Matrix

The theory of stress transfer mechanism has been considered in numerous studies of viscoelastic composites. These studies are either based on materials or tissues with viscoelastic and hierarchical structure (i.e. tendons, muscles) which are treated as if they are fiber reinforced viscoelastic composites (Ahmadzadeh *et al.* 2013); or polymeric materials that contains randomly distributed short fibers (Obaid 2018). These studies use

theoretical approach to often elucidate the relaxation behavior in viscoelastic materials with fibers. While the addition of short elastic fibers has proven to slow the relaxation process in viscoelastic composites, the particular interest of this review was to explore how the load transfers through the length of fibers in viscoelastic material at different temperature and loading rates. Although there are many studies on development of fibers in asphalt mixtures, there is very limited work on this very important subject in the FRAC, which by itself explains the inconsistency of experimental findings in the published data. To the best knowledge of this author, there is only one published research work by Park *et al.* (2017) who shed light to further understanding shear stress transfer mechanism between fibers and asphalt matrix. Park *et al.* (2017) simulated the stress distribution pattern for different temperature and loading rate as a function of steel fiber embedded length in asphalt binder using a finite element model. The conclusion of their study with respect to temperature/loading rate effect is summarized as follows.

At lower temperature or higher loading rate, the simulation results showed that the stress concentrations are the highest at both ends of fiber as the contribution of viscosity becomes lower and matrix acts like an elastic material. This is a similar observation to the Cox model. At higher temperature, it was observed that the stress concentration at the both ends of fiber disappears and the stress through the entire fiber length becomes more like the average shear stress due to local viscous flow of asphalt binder. When the stress reaches a specific concentration point corresponding to the applied strain rate, it becomes constant because the deformation at that point will be accommodated by viscous flow without additional increase in stress, shifting stress demands to adjacent regions, much like elastoplastic behavior. Interestingly, this very same conclusion was observed in the work of Wu

et al. (2018) who developed a Kelvin-Voigt viscoelastic shear lag model to study stress transfer between fibrils and interfibrillar matrix while tendon is dynamically stretched.

Figure 2-6 illustrates the shear stress distribution along fibril direction at different loading rates of inter-fibrillar matrix. It can be seen that while at very fast loading rate shear stress will be concentrated at both ends of the fibril length, the slower loading rate (lower viscosity of interfibrillar matrix) is more conducive to stress transfer along the fibril length. Note that the stress distribution for the highest loading rate ($K=1000$) in Figure 2-6 is essentially the same as the stress distribution in Figure 5b. The outcome of these two studies suggest two main points; first, the mechanism of stress distribution in the fiber reinforced viscoelastic matrix is a fundamental knowledge and independent of material properties, and second there is a more efficient load transfer between fiber and asphalt at reduced temperature or high loading rate.

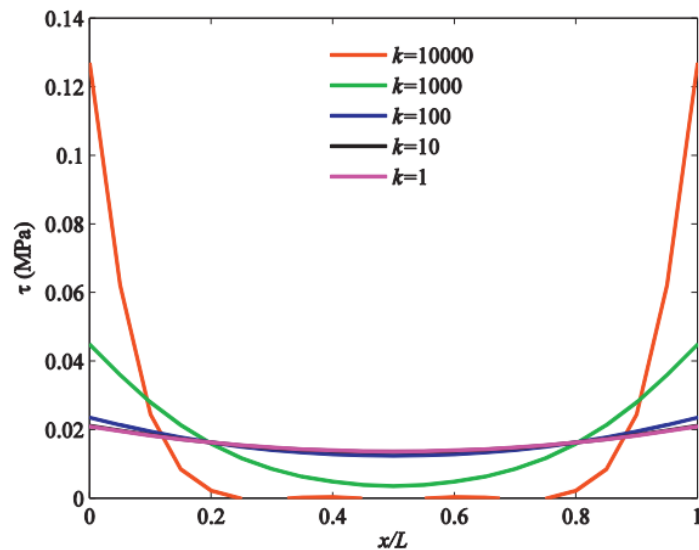


Figure 2-6. Distribution of Shear Stress Along Fibril Direction at Different Loading Rates (Wu *et al.* 2018).

2.9 Micromechanical Models for Fiber Reinforced Composites

There is a large body of analytical derivations and micromechanical methods developed conceptually for elastic composites (i.e. laminates, long fibers and short fiber) in the literature (Kelly and Tyson 1964, Halpin and Kardos 1976, Piggott *et al.* 1986, Kelly and Macmillan 1987, Piggott 1987, Naaman *et al.* 1991b, Shah and Ouyang 1991, Bentur *et al.* 2006, Sueki *et al.* 2007, Mobasher 2011). The main objective of micromechanics is to evaluate the effective properties of the constituents and their microstructure in the composite materials. While a comprehensive review of the basis of these models can be found in (Malekmohammadi 2014), a summary of the well-known theories developed for elastic based composite materials is shown in Table 2-2. Additionally, the micromechanical models for prediction of effective properties of fiber reinforced composites vary in terms of complexity, as shown in Figure 2-7. While the models on the far left represent the simplest closed-form equations, the complexity and computational time increases along with inclusion of more morphological features in the models.

With respect to the scope of this study using low volume fraction of circular fibers in a transversely isotropic composite material, Generalized Self-Consistent (GSC) model, Composite Cylinders Assemblage (CCA) model, and Halpin and Tsai equations appear to be the most ideal candidates to predict the effective properties of FRAC. However, the first two models (GSC and CCA) are widely used for continuous long fiber composites, while the Halpin-Tsai equations have been commonly used for prediction of effective moduli of circular short fiber composites with low fiber volume fraction the with reasonable accuracy (Malekmohammadi 2014). In GSC method, the fiber is surrounded by a matrix shell which is embedded in an effective medium of unknown properties. Using this approach, Hermans

(1967) proposed exact solutions for effective properties of cylindrical and spherical fiber composites. Halpin and Tsai rearranged the GSC equations in terms of engineering constants and presented analytical expressions for the moduli of transversely isotropic short fiber composites (Halpin 1969, Halpin and Kardos 1976).

Table 2-2. Summary of Well-known Micromechanical Models Which Have Been the Basis for Other Developed Models in the Literature (Malekmohammadi 2014).

Model	Inclusion Geometry	Material Properties	Basis	Year
Voigt	arbitrary	isotropic	isostrain	1889
Reuss	arbitrary	isotropic	isostress	1929
Eshelby	ellipsoidal	isotropic	elasticity/ energy	1957
Composite Sphere Assemblage (CSA)	spherical	isotropic	elasticity	1962
Hashin & Shtrikaman	arbitrary	isotropic	variational principles	1963
Composite Cylinder Assemblage (CCA)	continuous long fibres	transversely Isotropic	elasticity	1964
Self-Consistent Scheme (SC)	spherical/ ellipsoidal (long & short fibre)	transversely isotropic	Eshelby equivalent inclusion method	1965
Halpin-Tsai	spherical, cylindrical, rectangular	transversely isotropic	Self-Consistent	1969
Mori-Tanaka Scheme	ellipsoidal	anisotropic	Eshelby equivalent inclusion method	1973
Generalized Self-Consistent Scheme (GSC)	spherical, cylindrical	transversely isotropic	Eshelby equivalent inclusion method	1979
Method of Cells	square short fibres	transversely isotropic	equilibrium conditions at the interface	1983

Micromechanics Models

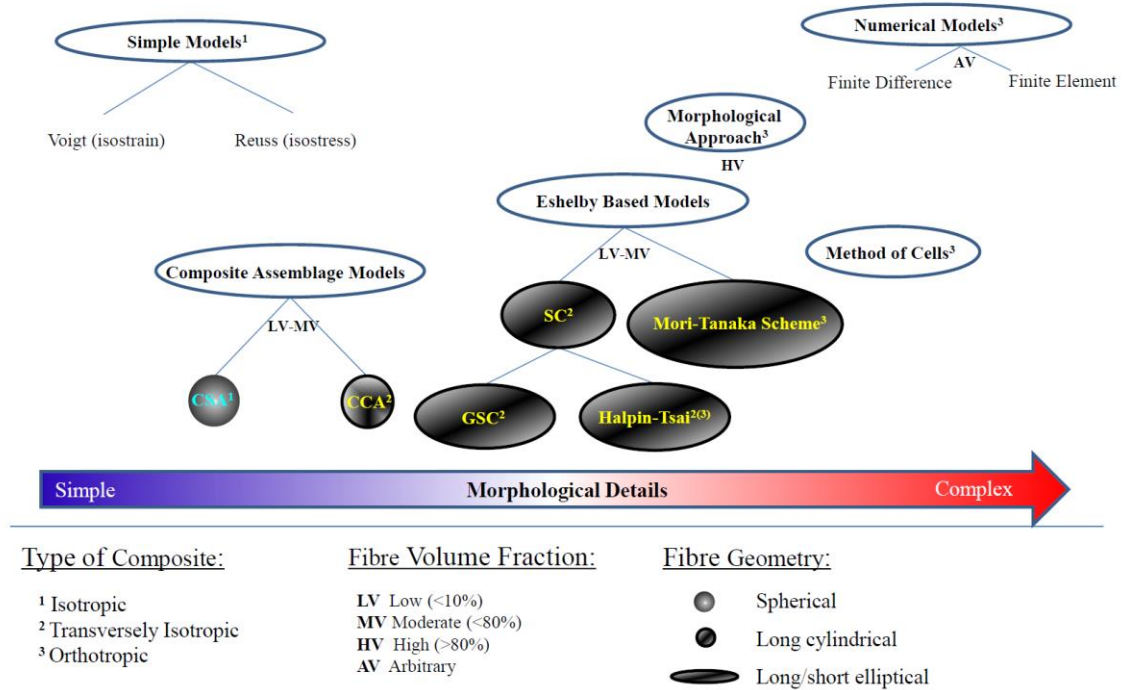


Figure 2-7. Schematic Overview of Various Well-known Micromechanics in Terms of Complexity and Computational Effort (Malekmohammadi 2014).

Another classical micromechanical model that has been used to predict the properties of short fiber reinforced composites is the so called “shear” lag theory, which is based on the work of (Cox 1952) introduced earlier. The work of Cox is commonly referred to in the literature as shear-lag theory. A complete derivation of the shear-lag equation with a method of determining Cox’s parameter is given by Piggott (2002), and will be discussed in more details in Chapter 7. In short, Cox’s shear lag theory examines a unit cell of a cylindrical matrix containing a cylindrical fiber at the middle. At the surface of the cylinder, the matrix experiences a strain that is the same as the strain applied to the composite (Obaid 2018). However, the strain in the matrix is not uniform due to the existence of the fiber. At the fiber-matrix interface, the matrix is confined by the fiber and

experiences a strain much lower than the global strain. Similar to other analytical models, the shear-lag theory is based on several assumptions. Firstly, it is assumed that the interfacial bonding between the fiber and matrix is continuous and perfect, and that stress is transferred between the two constituents without yielding or slip. Second, it is assumed that both the fiber and matrix perfectly elastic and isotropic (Piggott 2002, Bentur and Mindess 2006, Clyne and Hull 2019).

2.10 Summary

This chapter provided a review of topics related to fiber reinforced asphalt concrete (FRAC) technology, critical assessment of experimental work on the mechanical behavior of FRAC, reinforcement mechanism of fibers in the composites as well as asphalt, and an overview of existing micromechanical models used for prediction of fiber reinforced composites. While published studies generally demonstrate positive benefits from using mechanically fiber reinforced asphalt concrete (M-FRAC), the degree of improvement has varied with respect to types of fibers and the particular study. There are also studies that did not find any notable benefit from using fibers. Numerous research studies have used a variety of fiber types including natural, mineral, synthetic polymeric, steel, recycled and glass fibers for reinforcement of asphalt mixtures. Many of these studies are basically repetitions of what has been typically found in previous studies with very little insight to further help understand the reinforcement mechanism of fibers. For example, there are little studies that systematically link the fiber reinforcement efficiency to the compositions of asphalt mixtures and to the state of fiber in the mix which could possibly govern their mechanical response.

In this review, primary fiber reinforcement mechanisms are introduced including fiber bridging and the shear stress transfer mechanisms between fiber and matrix. These two factors have general applicability to the reinforcement roles of fibers in composites regardless of the type of matrix one deals with. However, when the matrix is time/temperature dependent such as asphalt concrete, additional mechanisms possibly takes place that need to be understood. There is very limited work devoted to understanding the mechanism of shear stress transfer between fiber and asphalt in FRAC. Also, the basis of micromechanical models which have been used to predict the mechanical properties of fiber reinforced composites was introduced. In spite of its popularity in any fiber reinforced composites field which shed light to further understanding fibers reinforcement, its use in FRAC is surprisingly non-existent to the best knowledge of this author.

CHAPTER 3

EFFECT OF THE FIBER STATE ON THE MECHANICAL PERFORMANCE OF FIBER REINFORCED ASPHALT CONCRETE

3.1 Introduction

The effect of fiber state as the basic, fundamental mechanisms that govern the mechanical response of FRAC is an undeniable issue. Stated differently, the reinforcement efficiency of fibers in composite are strongly dependent on the fiber state, inclusive of how the fibers are dispersed (dispersion), where the fibers are located (distribution), how they are arranged (orientation) and surface morphology (Noorvand *et al.* 2018). The dispersion particularly becomes important when bundled fibers (yarn) are used as the reinforcement, which is the case in this study. Although these effects have been recognized in previous studies, little to no systematic study has been done to attempt to quantify and correlate the effect of fiber state to the mechanical properties and performance improvements. The specific objectives of this study are:

- to measure the mechanical properties of two M-FRAC specimens with synthetic aramid fibers in different states, and
- to quantify the state of aramid fiber including their distribution, dispersion, morphology, and orientation in mix, and then to examine the impacts of fiber state on laboratory modulus, rutting, and fatigue performance of asphalt mixtures.

3.2 Methodology

The experimental plan approach of this study involved first conducting mechanical tests to evaluate the response and laboratory performance of M-FRAC mixtures. Then,

state of fibers was evaluated with respect to the dispersion, distribution, morphology, and orientation of fibers.

3.2.1 Materials

3.2.1.1 Asphalt Mixture

A 12.5 mm Nominal Maximum Size Aggregate gradation Marshall mixture from an active construction project near Tucson, Arizona was used for this study. The mixture used a PG 70-10 asphalt binder with a total binder content of 5.2%. A total of three variations to this plant-produced mixture were used in this study; a non-reinforced mixture (Control), a M-FRAC mixture with overall good dispersion of synthetic fiber (FA), and a M-FRAC mixture with overall poor dispersion of synthetic fiber (FB).

For each mixture, samples were obtained from the construction site in 19 L (5-gallon) metal pails and transported to the test laboratory. To separate the mixtures for testing, the buckets were heated at 135°C for two hours until the mixture softened enough to remove it from the pail, spread evenly onto a clean table, and then randomly sample into cloth bags. Each cloth bag contained enough material to fabricate one sample and contained an equal amount of mixture from each pail. The combined mixture approach has been adopted in-lieu of separately sampling each bucket so that a homogeneous set of materials could be obtained, and test variability reduced. The same process of sampling was followed for all the mixtures. It should be noted that the blending process was carried out carefully so as not to overagitate the mixtures and cause additional blending beyond what existed at the mixing plant. Nevertheless, some differences between the mixtures tested in the study and the mixtures that were produced at the plant may exist. This potential is acknowledged

but should not affect the interpretation or results since all specimens were subjected to the same handling.

The gradation of all mixes was checked to ensure equivalence in terms of gradation and asphalt content and so that any differences in the performance of the mixes could be attributed to differences in the fiber state. Therefore, representative samples from each mix were selected, the binder was extracted, and sieve analysis was performed. Figure 3-1 shows the gradation for the average of two replicates of each mixture. On average, the difference in percent passing on sieve sizes greater than 4.75 mm and less than 4.75 mm between the mixes was less than 2% and 0.5%, respectively. The binder content and the theoretical maximum specific gravities (G_{mm}) from the extraction were consistent across all three mixtures. Also, the G_{mm} of the mixtures was within the difference of two samples limit stated in AASHTO T209. Based on the results, the three mixtures appear to be consistent, with the exception that FA and FB mixtures contain fibers.

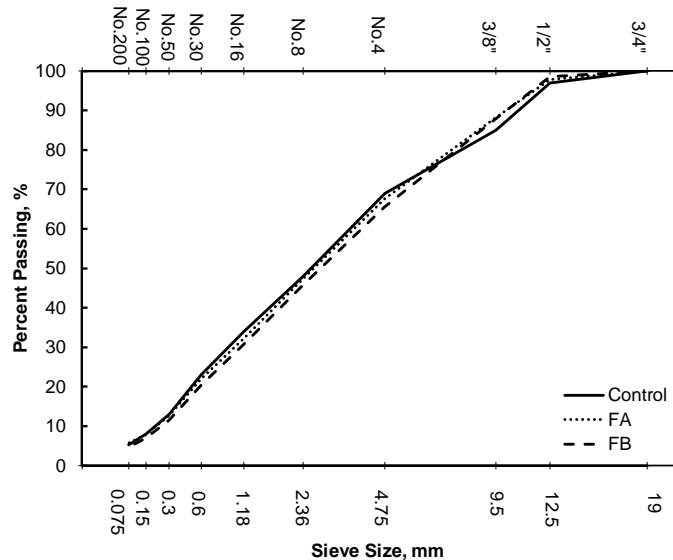


Figure 3-1. Comparison of Gradations for the Mixtures.

3.2.1.2 Fibers

Both M-FRAC mixtures contained synthetic aramid fibers at a dosage of 65.5 g per tonne of mix. The aramid fibers were 19 mm long and were introduced in bundles of approximately 3000 individual fibers each. The fibers have a reported tensile strength between 2700 and 3000 MPa and are not affected by temperatures up to 426°C. The physical properties of synthetic fiber have been measured and summarized in Table 3-1 and Figure 3-2.

Table 3-1. Measured Physical Properties of Fiber.

Material	Aramid	Polyolefin
Form	Multifilament Fiber	Twisted Fibrillated Fiber
Specific Gravity	1.45	0.91
Tensile Strength (MPa)	3000	NA
Length (mm)	19	19
Decomposition Temperature (°C)	> 450	<130

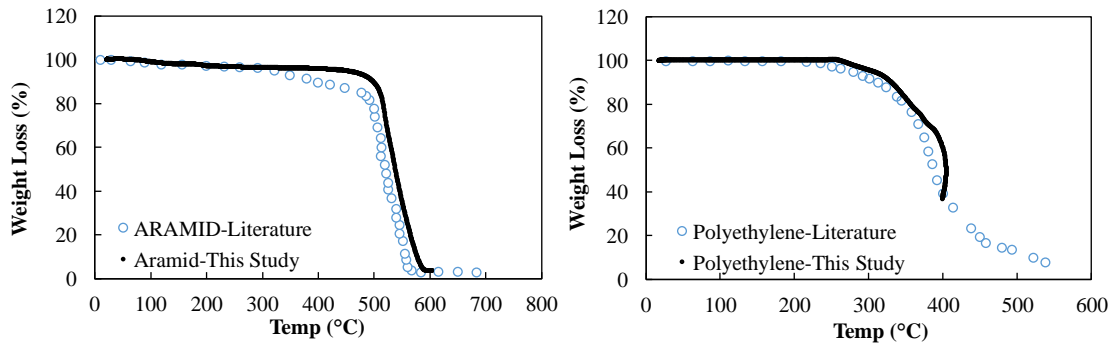


Figure 3-2. Thermogravimetric analysis (TGA) of Aramid and Polyethylene Fibers Compared with the Measurement in the Literature.

3.2.2 *Fiber Mixing Method*

In the field, both fiber mixtures were added directly into the hot aggregates in the drum just before the application of hot binder at the dust port. Both manufacturers products

were added with the addition of forced air. Also, the fibers were mixed with hot aggregates for few seconds before adding the hot binder. Differences in dispersion and distribution are achieved due to the use of different technologies in FA and FB. In FA, the aramid fibers are introduced along with polyolefin fibers while in FB the aramid fibers are coated in a thin membrane of wax, which melts as the fibers are mixed in.

Theoretically, both FA and FB try to deliver fibers into the mixing process with high aspect ratios (ratio of diameter to length) so that early in the mixing process they distribute better and do not interfere with the process. Both technologies then rely on the fibers separating and dispersing throughout the mixture in a low aspect ratio state so that more volume of the mixture can be reinforced. In FA, the polyolefin fibers facilitate this transition by first carrying aramid bundles throughout the mixture. Then as the polyolefin fibers melt, they change shape to help pull aramids away from the bundles and also act to neutralize static charges that can cause aramids agglomerate into cotton-ball like structures. Aramids may also be dispersed by frictional forces between the aramid fibers and the aggregate. In FB, the wax keeps the aramids bundled until it melts at which point the aramids are dispersed through frictional forces between the fibers and the aggregate. It is not known if the wax completely melts into the asphalt mixture or if as it melts it seeps deeper into the bundle so that dispersing the fibers requires continual agitation.

3.2.3 Mechanical Characterization

In total, three different mechanical experiments were conducted: dynamic modulus test, repeated load permanent deformation test, and uniaxial fatigue test. The target air void level for all tests was $5.5 \pm 0.5\%$, which was the target air void content of the overlay

surface course for the project. All specimens were compacted with the gyratory compactor, 150 mm in diameter and 170 mm in height. Specimens were then cut and cored to their final geometry.

3.2.3.1 Repeated Load Permanent Deformation Test

The repeated load permanent deformation, also known as Flow Number, test was conducted to determine the permanent deformation characteristics of the asphalt mixtures. The test procedure followed in general accordance with AASHTO T 378. The test was performed under atmospheric conditions, an axial stress level of 160 kPa, and at 50°C. Prior to testing, a thin and lubricated membrane was placed between the sample ends and the loading platens to create frictionless surface conditions and prevent end effects. Tests were performed using cylindrical specimens 100 mm in diameter and 150 mm in height. The deformations were measured using the average of three linear variable displacement transducers (LVDTs) spaced at 120° intervals on the specimen surface (More details on APPENDIX A).

3.2.3.1.1 Dynamic Modulus Test

Temperature and frequency sweep tests were carried out per AASHTO T 342 protocol. The protocol followed evaluated dynamic modulus, $|E^*|$, at temperatures of 4.4, 21.1, and 37.8°C and frequencies of 25, 10, 5, 1, 0.5, and 0.1 Hz. The -10°C temperature was omitted because previous research suggested that the benefits of fibers with respect to dynamic modulus were largest at intermediate temperature and less at extreme high and low temperature meaning that not having -10°C would not affect the conclusions for this

study. Tests were performed using cylindrical specimens 100 mm in diameter and 150 mm in height and prior to testing they were instrumented with three linear variable displacement transducers (LVDTs) spaced at 120° intervals on the specimen surface. Lubricated membranes were also placed between the sample and the loading platens prior to testing to reduce any end effects.

3.2.3.1.2 Uniaxial Fatigue Test

The uniaxial fatigue test was performed following the general procedure in AASHTO TP 107 with the exception that the test specimens were 75 mm in diameter and 100 mm in height. The test was carried out by applying a repeating sinusoidal deformation long the axis of a cylindrical test specimen until it failed. Axial fatigue tests were performed in controlled actuator displacement mode at a temperature of 18°C and at a 10 Hz frequency. As per AASHTO TP 107, the result of the tests is a damage characteristic function that can then be used to predict the fatigue life of asphalt concrete (Underwood *et al.* 2012).

The dynamic modulus and phase angle are tracked throughout the entire fatigue life. The traditional fatigue analysis method determines failure as the point where the material's modulus drops to 50% of its initial value. However, this method is purely experimental, and a different approach based on the change in the energy dissipation, indicated by the cycle at which the phase angle shows a sharp decrease is defined as the failure cycle (N_f). Figure 3-3 shows this failure definition from a typical test. It is believed that the drop of the phase angle is caused by macrocrack localization, which is normally caused by the coalescence of microcracks under repeated cycles of loading. When a

macrocrack develops, all the work input is concentrated at the crack tip and the remaining body relaxes, thus causing the time dependence of the global stress-strain behavior to reduce. This reduction in the time dependence is physically measured as a reduction in the phase angle. Additional information regarding the uniaxial fatigue test procedure and applied data analysis method is presented in APPENDIX A.

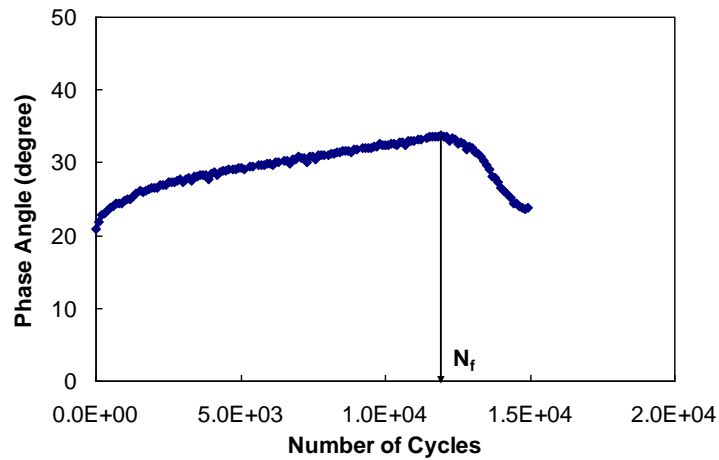


Figure 3-3. Fatigue Life Definition of a Typical Axial Fatigue Test.





3.2.4 Fiber State

The state of the fibers is described based on three parameters: dispersion, distribution, surface morphology, and orientation. Dispersion refers to the process whereby the fiber bundles added to the mixture are dispersed in the mixture. Distribution represents how the dispersed fibers are spatially located through the mixture. Surface morphology characterizes the form and shape of fibers present in the mix. Orientation refers to the alignment of the fibers in them mixtures.

3.2.4.1 Evaluation of Fiber Dispersion

To evaluate dispersion, aramid fibers were extracted using a procedure developed at Arizona State University (ASU) (Zeida *et al.* 2017), which is essentially the same as ASTM D2172 except that attention is given to observing, separating, and cleaning the fibers in the mixture after soaking the mixture and centrifuging off the solvent (for more details refer to APPENDIX B). The centrifugal extraction process has two limitations: 1) it can alter the state of the fibers, but studies at ASU (not shown here) reveal that the effect is generally negligible and does not alter the characteristics to a quantifiable amount and 2) separating and cleaning all individual fibers is tedious and time consuming and in practice a grouping of 3-10 individual fibers (defined as a very small cluster) may be counted as individuals instead of clusters. The ASU test method describes the state of dispersed aramid fibers in AC as one of four conditions; bundles, agitated bundles, clusters, and individuals as described in Table 3-2.

Table 3-2. Aramid Fiber Dispersion States.

State	Definition	Example
Bundle <i>(Least Desired)</i>	A group of many aramid fibers that shows no clear indication of disturbance. This is the original condition of aramid fibers.	
Agitated Bundle <i>(Least Desired)</i>	A grouping of aramid fibers similar to the bundled condition, but that has been visually agitated and has lost some of the individual aramids.	
Cluster <i>(Less Desired)</i>	A grouping of individual aramid fibers that are more dispersed than the agitated bundle.	
Individual <i>(Most Desired)</i>	Single fibers completely separated from other aramids with no resemblance of previous fiber states*.	

**Note: Individual aramid fibers can appear in bunches at the end of the extraction test as shown in the image (resembles cotton candy).*

After the asphalt binder is extracted, the fibers are separated into aforementioned categories and the total aramid dosage rate is determined along with the relative proportions of fibers in each category. Of principle interest is the proportion of fibers in the individual state and Equations (1-1) defines the ratio that quantifies this proportion, known as Fiber Dispersion Percentage (*FDP*). A larger *FDP* signifies the existence of more fibers in the individual state. Supplemental calculations for fibers in the cluster and agitated bundle states are also performed. A test result is reported based on the average of two individual centrifugal extractions.

$$FDP = F_I = \frac{M_I}{M_a} \times 100 \quad (1-1)$$

where;

- FDP* = fiber dispersion percentage,
- F_I* = fibers in the individual state (%),
- M_I* = fibers in the individual state (g), and
- M_a* = total extracted mass prior to separation (g).

3.2.4.2 Evaluation Failure Distribution

Castings of the failure surface of tested specimens were made to observe the distribution of the aramid fibers throughout the asphalt mixture. The process is performed on mechanically tested specimens shown in Figure 3-4(a). First, mechanical test samples are heated to 60°C for 30 minutes and split along a diagonal line extending from the lower edge of the specimen to the upper opposite edge so that fiber orientations could be viewed with respect to both the horizontal and vertical directions, Figure 3-4(b). Although, the different dispersion states are evident on the surface of the split samples, Figure 3-4(c and

d), detailed comparisons are not possible because the fibers are coated with asphalt and hard to see. So, a thin layer of fluid plaster is poured on the fracture surface of samples and embed the surface fibers. Once the casting cures, Figure 3-4(e), the samples are heated to 80°C to carefully separate as much mixture from the cast as possible, Figure 3-4(f). Then the remaining samples are soaked in solvent to dissolve the asphalt and completely remove all remnants of the test specimen from the casting. Finally, photos are taken of the surface and evaluated, Figure 3-4(g).

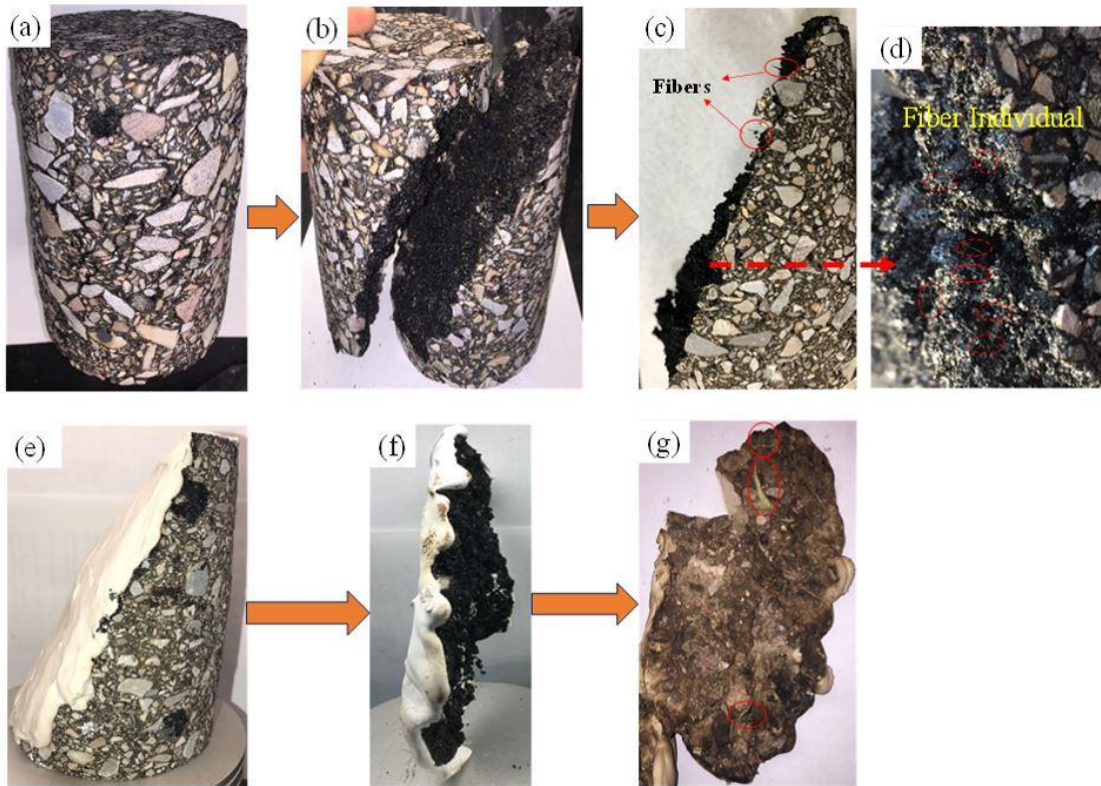


Figure 3-4. Summary of Casting Method to Evaluate In-situ Fiber Distribution; (a) Tested Specimen, (b) Splitting Specimen Along the Diagonal, (c) Half Splitting Specimen, (d) Zoomed in Photo of Region Identified in (c), (e) Casting on Split Specimen, (f) Separated Asphalt Mixtures from Cast Specimen, and (g) Complete Separation of Asphalt Mixture from Cast Specimen.

3.2.4.3 Evaluation of Surface Morphology

Original and extracted fibers were imaged using a Philips SEM-XL30 Environmental FEG scanning electron microscope (SEM) under the following conditions: environmental mode, secondary electron signal, and accelerating voltage of 15 kV. Fibers were also sputter coated with gold for 2 minutes to improve the electrical conductivity and resolution of the images.

3.2.4.4 Evaluation of Orientation

In fiber reinforced asphalt concrete composites, the orientation of fibers could be possibly affected by the compaction of specimens. The fibers may tend to orient themselves horizontally in the cylindrical gyratory plug perpendicular the compactor. This could largely impact the performance of fibers in testing and the lack of understanding in the orientation of fibers could lead to underestimate their true mechanical performance benefit.

To investigate the orientation of fibers and the mentioned hypothesis, initially three methods were considered. First, the use of X-ray image analysis which is common in cement concrete composite. However, this system does not really work on aramid fiber reinforced asphalt concrete specimens mainly because the density of asphalt is similar to aramid fibers, hence such techniques are not really able to capture any useful information. Second, asphalt samples with a mono-filament type of fiber that have larger diameters were made, then the cored specimens were sliced with very thin cuts (<1 mm). After each thin cut, high resolution photos were taken from the surface of the samples. After that, image processing technique was used to capture the location of fibers (Image J could also work), which was possible. Finally, the fibers could have been connected by stacking all the

images (taken from the surface of each thin cut) and using a right matrix algorithm. However, because of the time restraint and complexity of the system this method was not followed. The third method that was used to study the fiber orientation was a more simple and straightforward method. In this method, a laboratory prepared specimen was prepared and were compacted at 150 mm diameter and 180 mm height. The mix design information, fiber blend type, and fiber mixing procedure can be found in Chapter 4; which is the same as mix type A. Also, the fiber blend is similar to the FA field mix used in this Chapter. The compacted specimens were cored in horizontal and vertical angles, although the process of coring samples horizontally is not common. 3-5 illustrates the preparation of horizontal coring direction from a gyratory specimen. Flow number test was performed on two replicates for each directionally cored specimens of 75 mm in diameter and 100 mm in height. These geometries were selected because the initial study showed the at such geometry consistent air void level can be obtained for both horizontally and vertically cored specimens so that any comparison can be made based on the orientation of fibers. The air void level for the test specimens was $5.5 \pm 0.5\%$.

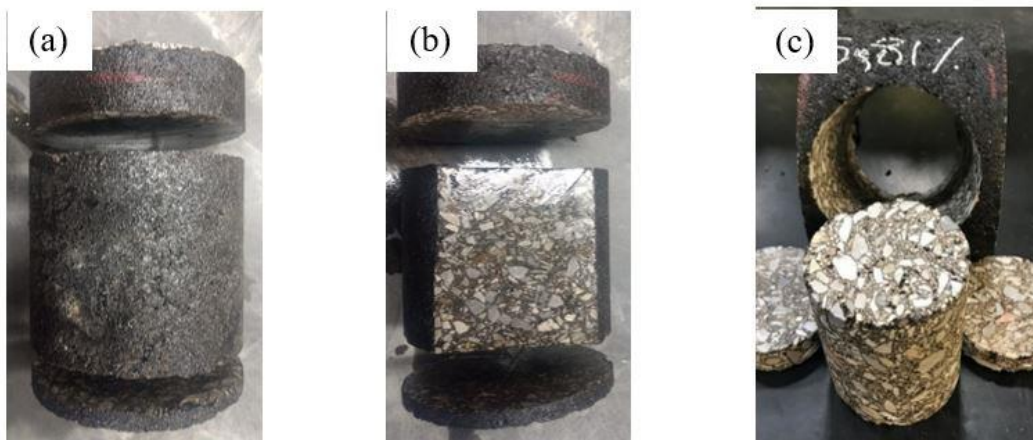


Figure 3-5. Photo of Sample Preparation for Horizontal Core.

3.3 Results

3.3.1 Mechanical Characterization

3.3.1.1 Dynamic Modulus Test

The most common method to report dynamic modulus data is the mastercurve function, which is so named because it shows the joint effects of temperature and frequency on the modulus of asphalt concrete. A mastercurve is created by plotting the data at each temperature as a function of frequency in log-log space and then horizontally shifting the data for each temperature to produce a single, continuous and smoothly varying function. The amount of horizontal shift required to create such a curve is referred to as the time-temperature shift factor (t-T shift factor) and varies according to temperature. Upon shifting, the x-axis is relabeled as reduced frequency to denote that the curve was not actually developed with measurements at a single temperature (Ferry 1980, AASHTO R 62-13). The reduced frequencies in this study are within the measurement range. The mathematical representation of reduced frequency is not shown for the interest of brevity. Additional information regarding the dynamic modulus test procedure and applied data analysis method is presented in APPENDIX A.

Data from the $|E^*|$ experiment is presented in the form of dynamic modulus mastercurves in Figure 3-6. The dynamic modulus data is shown in both log-log and semi-log scales so that any differences in the moduli at high and low temperatures respectively can be observed. It is seen that the moduli values for all three mixtures are very similar at the intermediate temperature. However, at lower temperatures (higher reduced frequencies) the mixes with aramid fibers yield lower moduli values and at higher

temperature (lower reduced frequencies) they yield higher moduli. At these higher temperatures, the FA mix exhibits slightly higher average values than the FB mix.

An ANOVA and statistical t-test analysis were performed at a 95% confidence level. The ANOVA analysis was used to compare the difference between all means and evaluate the significance of the total differences and the t-test was performed to compare individual cases to the control mixture and individually between the fiber mixes. In all cases, the results indicated a lack of statistical significance in the moduli. Thus, while on-average differences are evident these effects are not significant. The results are consistent with laboratory prepared specimens from previous section.

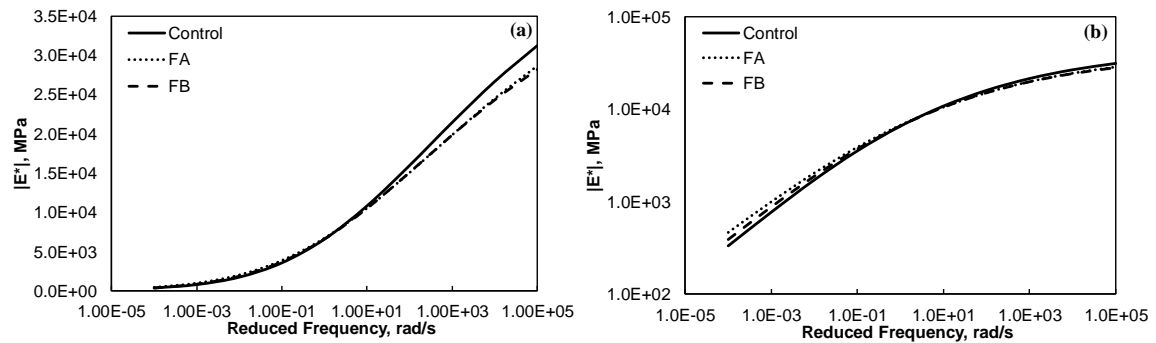


Figure 3-6. Comparison of $|E^*|$ Mastercurves in; (a) Semi-log and (b) Log-log Scale.

3.3.1.2 Repeated Load Permanent Deformation Test

Figure 3-7 shows the accumulated permanent strain during the repeated load permanent deformation test for each of the mixtures. The resulting flow number values from this analysis are also shown as a tabular inset into this figure. Figure 3-7 shows that the FB and Control mixture exhibit similar permanent strain response under the repeated loading, but that FA mixture accumulates strain at a slower rate and undergoes more

repetitions before reaching the onset of flow. In fact, the FA mixture exhibits an increase in average flow number of 139% compared to the control and FB aramid mixtures.

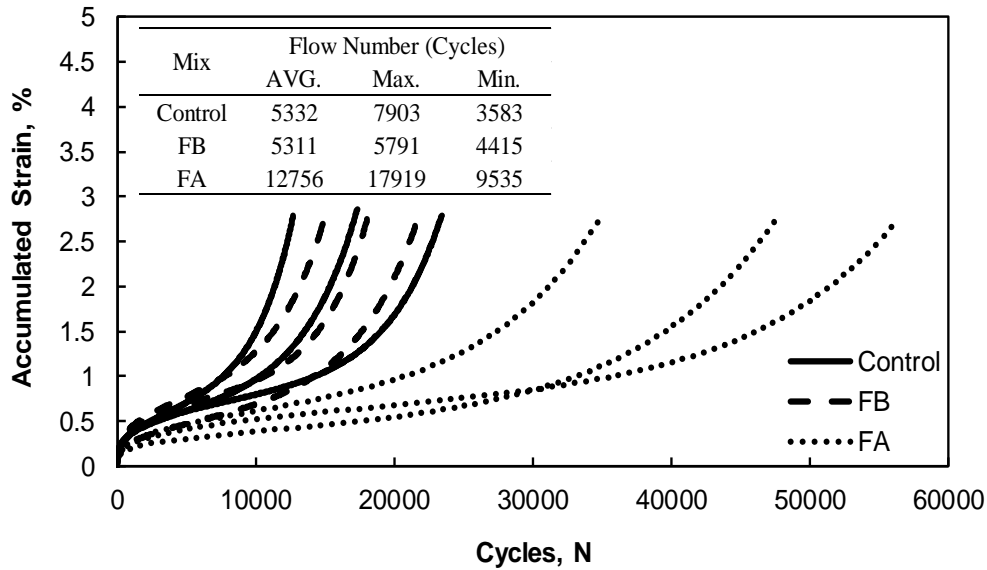


Figure 3-7. Accumulated Strain and Flow Number Results for Control (No Fiber), FA and FB Mixes.

3.3.1.3 Axial Fatigue Test

The uniaxial fatigue test results are analyzed using the simplified viscoelastic continuum damage (S-VECD) approach to characterizing fatigue behavior. This analysis approach as applied to asphalt concrete has been described in great detail elsewhere (Underwood *et al.* 2010, Wang *et al.* 2018) and interested readers are directed here and the citations therein to learn more. In short, the method is based on characterization of a damage characteristic ($C-S$) curve, which describes the relationship between the material integrity or pseudo-stiffness, C , and internal micro-damage, S . This function is typically described using the power-law function shown in Equation (1-3). Through the VECD

theory, this function can be used along with the dynamic modulus and a failure criterion to calculate the number of cycles to failure in a pure controlled strain case (Equation (1-2)).

$$C = 1 - C_1 S^{C_2} \quad (1-3)$$

$$N_f = \frac{(f_{red})(2^\alpha) \left[\frac{(1-C_f)}{C_1} \right]^{\frac{(\alpha-\alpha C_2+1)}{C_2}}}{(\alpha-\alpha C_2+1)(C_1 C_2)^\alpha [(\varepsilon_{0,pp})(|E^*|) \left(\frac{\beta+1}{2} \right)]^{2\alpha} K_1} \quad (1-4)$$

where;

C = pseudostiffness (also referred to as the material integrity, which is calculated for each cycle during the fatigue test),

S = internal state variable to quantify damage (calculated according to the procedure given in AASHTO TP107),

C_1, C_2 = fitting coefficients,

N_f = predicted cycle number of cycles to failure,

f_{red} = reduced frequency for the condition being simulated, and

α = damage accumulation rate (calculated from the linear viscoelastic properties of the mixture),

C_f = stiffness ratio at failure,

$\varepsilon_{0,pp}$ = peak-to-peak strain amplitude,

$|E^*|$ = dynamic modulus at the temperature and frequency being simulated,

β = wave shape factor (taken as 0 for this study in order to simulate tension-compression loading), and

K_1 = loading shape factor (Underwood *et al.* 2012).

The damage characteristic curve for the samples tested in this task is shown in Figure 3-8(a) for Control, FA, and FB. These curves show that mixes with fibers have damage curves that are very similar to those of the control mixtures. These damage curves are fit to the analytical expression to predict the fatigue life of the mixtures. Details on the

analytical process to characterize the damage functions and to predict the number of cycles to failure can be found in APPENDIX A. Figure 3-8(b) shows the failure envelopes for each mix type for constant strain-based analysis, which shows that the fiber reinforced samples have slightly better performance at a fixed strain level compared with control sample.

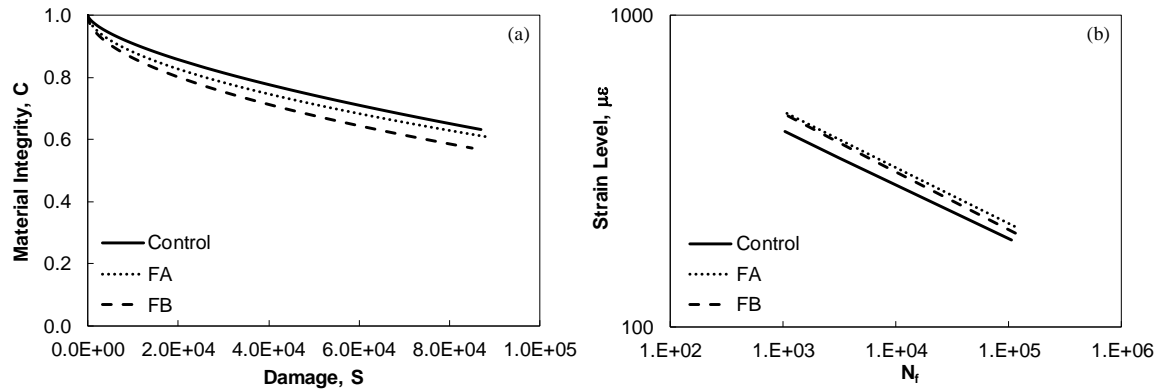


Figure 3-8. Results of Fatigue Evaluation; (a) Damage Characteristic Curve and (b) Predicted Fatigue Life Relationships.

3.3.1.4 Repeated Load Permanent Deformation Test (Orientation Study)

Figure 3-9 shows the accumulated permanent strain during the repeated load permanent deformation test for horizontally and vertically cored no fiber specimens. Also, the resulting flow number values from this analysis are also shown as a tabular inset into this figure. The flow number test results for no fiber sample suggest the vertical core specimens have higher FN values than horizontal specimens, implying that mix A is not a perfect isotropic specimen probably attributed to the gradation.

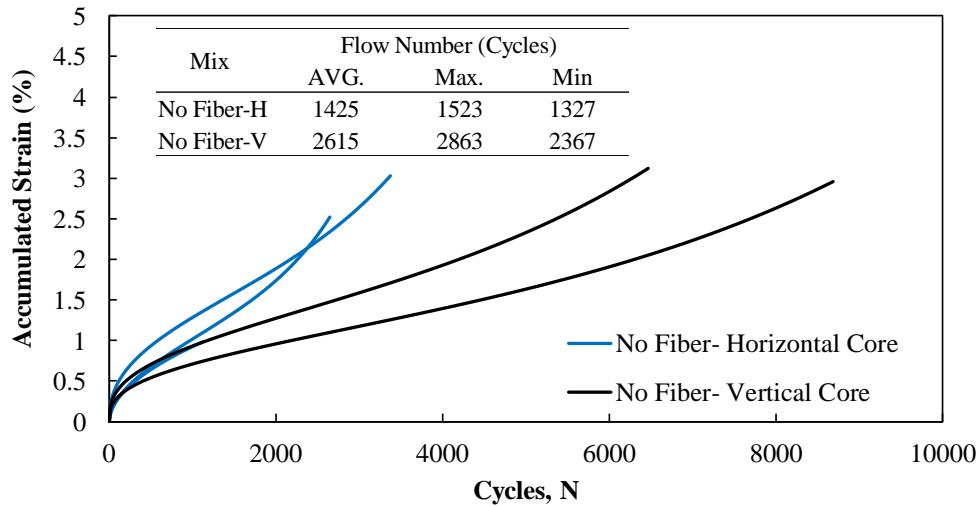
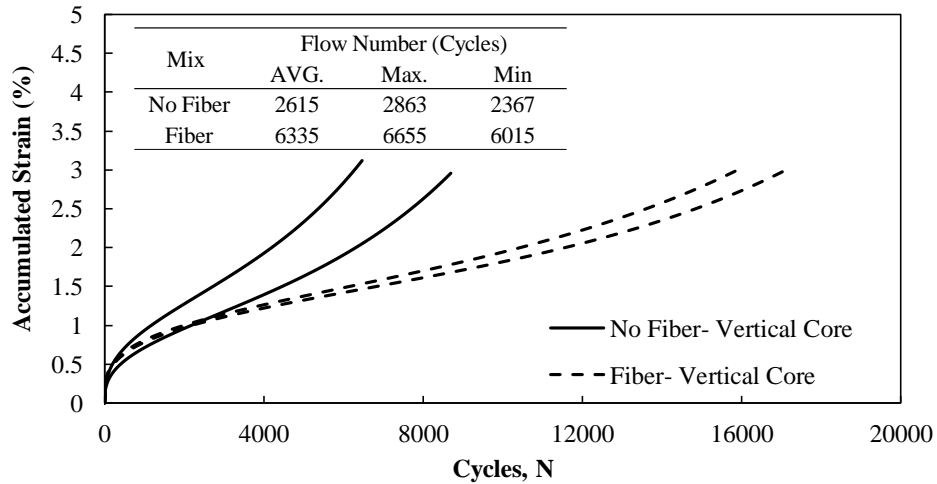
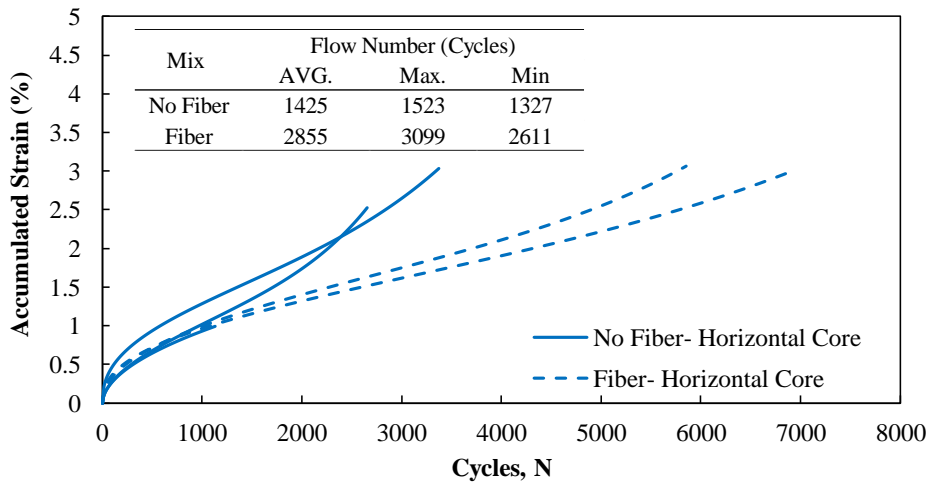


Figure 3-9. Accumulated Strain During Flow Number Test for No Fiber Specimens Cored Horizontally and Vertically.

To analyze the effect of fiber orientation from the test results, the vertically and horizontally cored fiber and no fiber specimens were compared separately as shown in Figure 3-10. The results indicated that the fibers accumulated strain at a slower rate and undergoes more repetitions before reaching the onset of flow compared with no fiber specimens. The improvement was consistent across both horizontal and vertical cored specimens. The analysis of FN values for both horizontal and vertical fiber and no fiber specimens are shown as tabular inset into Figure 3-10. It is evident that while the use of fiber increased the FN of vertically cored asphalt mixtures by 140%, the increase for horizontally cored was about 100%. This suggests that there could be possibility an orientation tendency of fibers in the asphalt concrete specimens. This might be attributed to the compaction of asphalt concrete specimens under gyratory which pushes the fibers to lay towards horizontal direction perpendicular to the gyratory loading.



(a)



(b)

Figure 3-10. Accumulated Strain During Flow Number Test for (a) Vertically and (b) Horizontally Cored Fiber and No Fiber Specimens.

3.3.2 Fiber State

3.3.2.1 Quantity and Condition of Dispersed Aramid Fiber After Mechanical

Testing

Table 3-3 summarizes the extraction results first in terms of the aramid dosage rate, which is simply the mass of the aramid fiber with respect to the total weight of the mixture.

Both FA and FB contained similar dosage levels (within approximately 8% of one another) and were within 1-5% of the target rates (recall that the target fiber dosage rate was 65.5 g/tonne). The difference between replicates was higher in the FB mixture than the FA mixture. Also, the percentages of each of fiber states (*FDP*, agitated bundles and clusters) were determined. The FA mixtures had an average *FDP* value of 88.5% while FB mixtures had an average *FDP* of 16%. In the FB case, most of the fibers are dispersed in the agitated bundle condition (73.5% on average). These findings provide some support for the variation observed in the dosage rates of FB replicates because agitated bundles can lead to larger differences in sample-to-sample aramid mass since one or two additional or fewer bundles can alter the mass substantially.

Table 3-3. Summary of Extracted Aramid Dosage and Fiber State.

Specimen ID	Aramid Dosage Rate (g/tonne)/(oz/ton)	State of Aramid (%)		
		<i>Agitated Bundle</i>	<i>Cluster</i>	<i>FDP (Individual)</i>
FA-1	68.7/2.2	2.0	8.0	90.0
FA-2	65.6/2.1	0.0	13.0	87.0
AVG FA	67.1/2.15	1.0	10.5	88.5
FB-1	50/1.6	69.0	12.0	19.0
FB-2	96.8/3.1	78.0	9.0	13.0
AVG FB	71.8/2.3	73.5	10.5	16.0

Figure 3-11 also shows the clear difference between state of the fibers in the FA and FB mixtures after extraction. Figure 3-11(a) shows that only individuals and clusters exist in FA, and Figure 3-11(b) shows the presence of agitated bundles in FB and a much lower proportion of individuals than FA. It is important to mention that for the individual fibers, the extraction and cleaning process result in the *cotton ball* like agglomeration as

seen in these figures. This structure in no way represents how the individual fibers exist in the mixture.

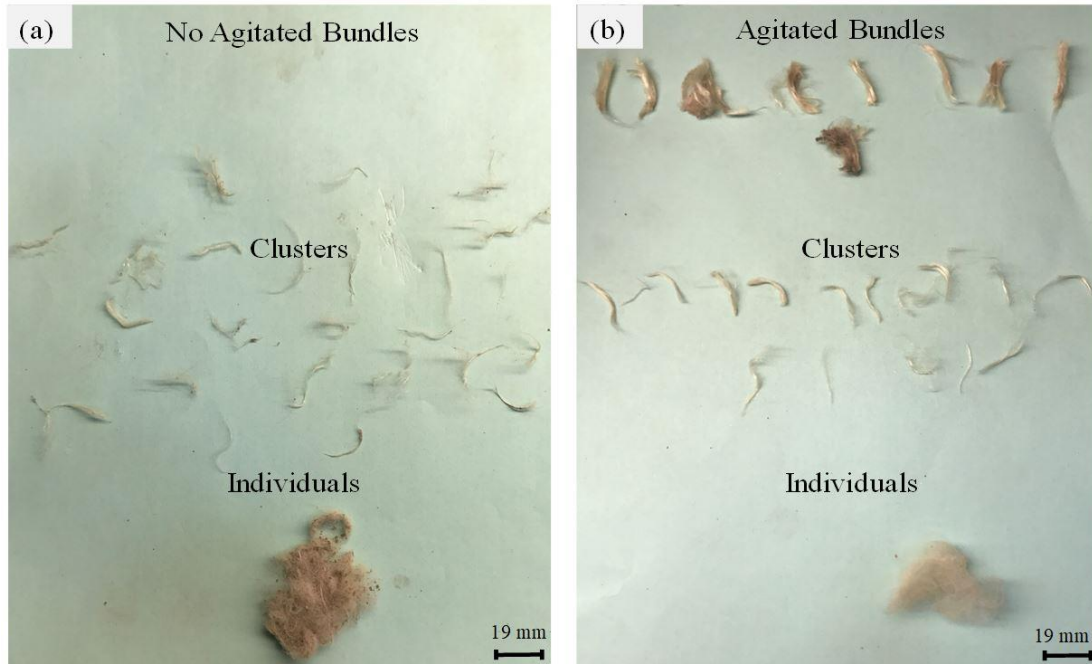


Figure 3-11. State of Extracted Aramid Fibers from a Single Sample of (a) FA and (b) FB.

3.3.2.2 Qualification of Distribution of Aramid Fibers

Images of the castings from the internal diagonal planes of both FA and FB mixtures are shown in Figure 3-12 and Figure 3-13. A best effort was made to clearly capture fibers in each photo; and for further clarity of the fibers state and location, the images were modified with stars, circles, and squares to show locations of fibers in the form of individuals, clusters, and bundles, respectively. Part of the photos in Figure 3-12(a) and Figure 3-13(a) was enlarged to more clearly show the existence of individual fibers as seen in Figure 3-12(b) and Figure 3-13(b).

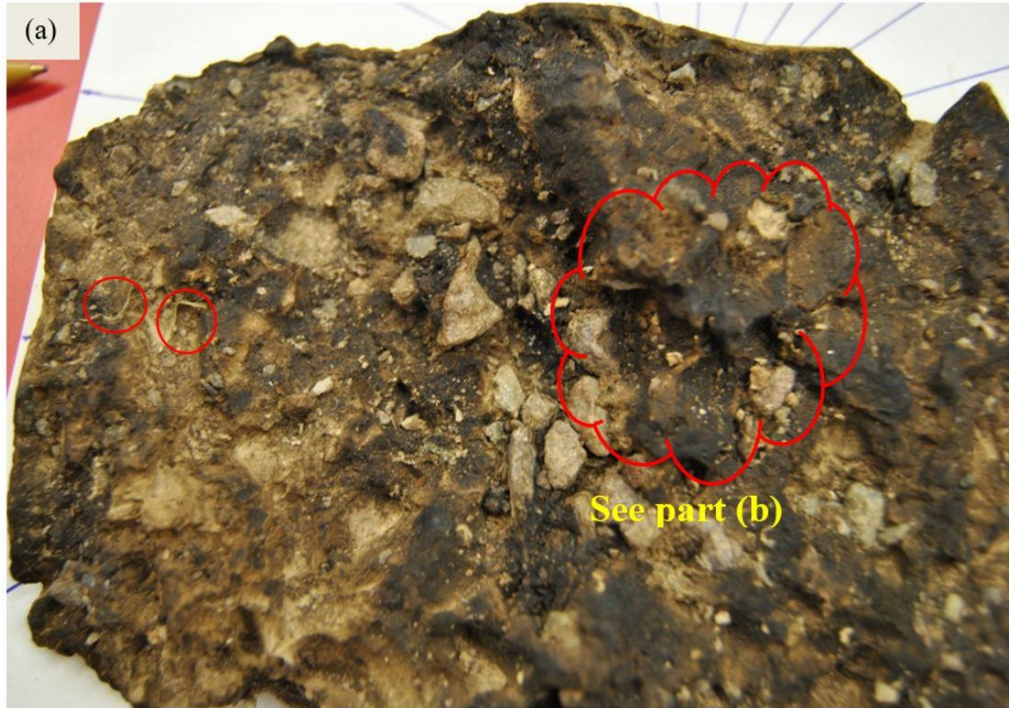


Figure 3-12. Photos Taken from the Aramid Fibers Distributed on the Surface Fracture of Each FB Mix; (a) Overall View of Casting Surface and (b) Enlarged Photo of Central Section.

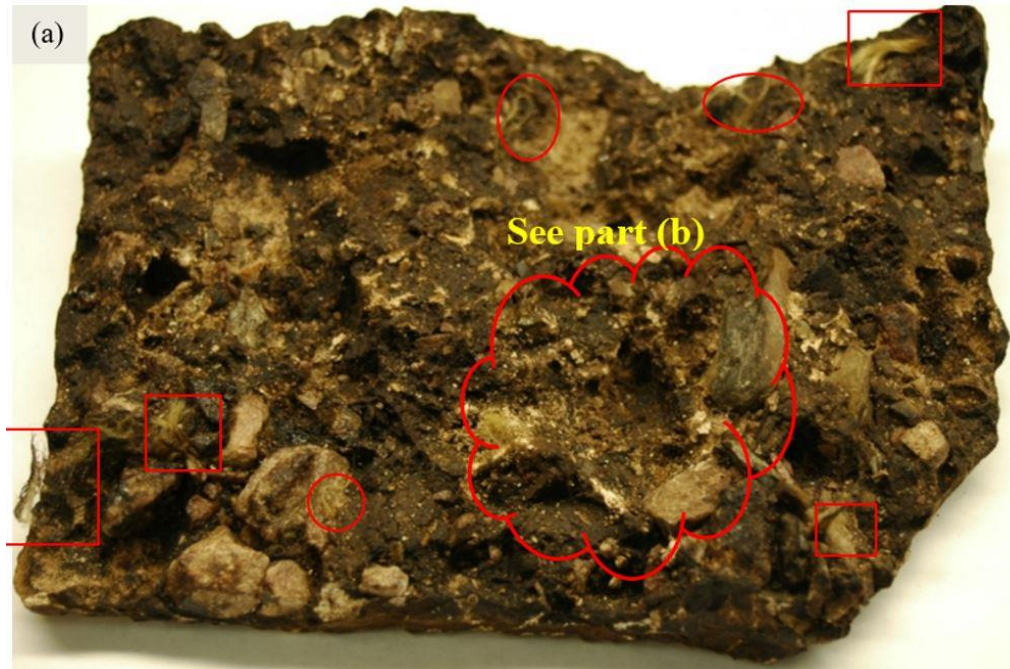


Figure 3-13. Photos Taken from the Aramid Fibers Distributed on the Surface Fracture of Each FB mix; (a) Overall View of Casting Surface and (b) Enlarged Photo of Central Section.

Overall, as the *FDP* values suggest, a substantially greater number of individual fibers were observed in the casting of the FA mixture (Figure 3-12). Conversely, the casting of FB yielded a considerably greater number of agitated bundles (Figure 3-13). Additionally, it was recognized that individual fibers were evenly distributed throughout both FA and FB and they were oriented in all directions (horizontal, diagonal, and vertical). In this study, no attempt was made to quantify the relative proportion of individual fibers oriented in each direction, but it was observed that a larger proportion of the individual fibers were oriented with their long axis perpendicular to the compaction and testing direction.

With respect to distribution and orientation of bundles and clusters, it was observed that clusters and bundles were mostly distributed and located toward edges of samples and they are oriented either horizontally or vertically unlike individual fibers that tend to be oriented mostly horizontally. It should be noted that the location of clusters and bundles toward edges of the samples observed in this study might not necessarily be interpreted as the distribution behavior of clusters or bundles. Rather it could have been a random distribution of such fibers that happen to be located at the edges.

3.3.2.3 Fiber Surface Morphology

Representative results from the multiple images taken of aramid fibers before and after mixing are shown in Figure 3-14 and Figure 3-15. Aramid are highly oriented aromatic polyamides, which presents challenges in creating fibers. The process of wet-spinning is typically adopted and yields a fiber with very high strength along the axis of the fiber held together by covalent bonds, but made up of many layers bonded together by

hydrogen bonds with relatively low strength (Hahn 2000). During mixing and agitation of aramid fiber in the mix, since the strength of the hydrogen bonds along the radial direction is substantially weaker than the covalent bonds along the axis of the fiber, fibrillation can occur. The very tiny strands of fibrils can effectively increase the bonding area of the fiber which increase pull-out resistance.

Figure 3-14(c) and Figure 3-15(b) show the surfaces of the clustered fibers and again they appear much the same with only slightly greater surface fibrillation. However, the images from individual condition showed a different morphology, Figure 3-14(d) and Figure 3-15(c). In these fibers, micro-fibrillation is apparent. Although it is not quantified, it also appears that the individual fibers from FA are more fibrillated than FB. This effect may occur because the fibers disperse more quickly in FA and are therefore agitated in the individual condition for longer time compared with the wax coating on FB. The significance of this effect is that not all individual fibers have the same state even though they may be dispersed and distributed in the same way.

Figure 3-14(a) shows the fibers in their original condition and it is seen that each fiber is cylindrical and 10-14 μm long in diameter. Most of the fibers are smooth, with a few occasional micro-fibrillations (circled in red). These fibrillations are approximately 0.5-2 μm wide and 35-150 nm thick. In Figure 3-14(b-d) and Figure 3-15(a-c), small dots appear on the surface of the fibers, which are left-over dust from the extraction and cleaning process. Figure 3-14(b) and Figure 3-15(a) show the surface of the agitated bundles, and it is seen that the fibers retain much of the same morphology as the unagitated bundles.

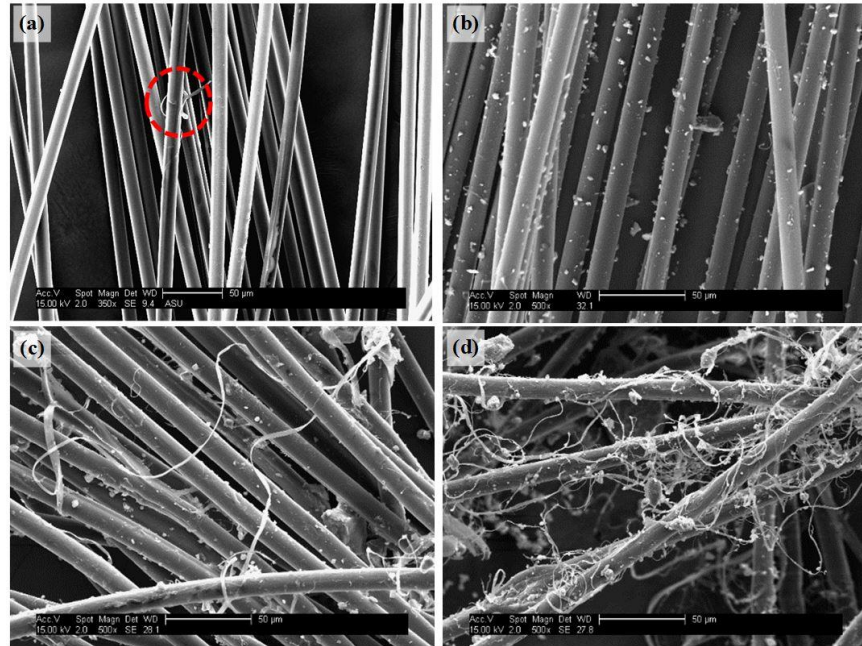


Figure 3-14. SEM Images of Aramid Fibers of FA mix at Different Conditions; (a) Original Bundles (Unagitated); (b) Extracted Agitated Bundles; (c) Extracted Clusters; and (d) Extracted Individual Fibers (all images at 500x magnification).

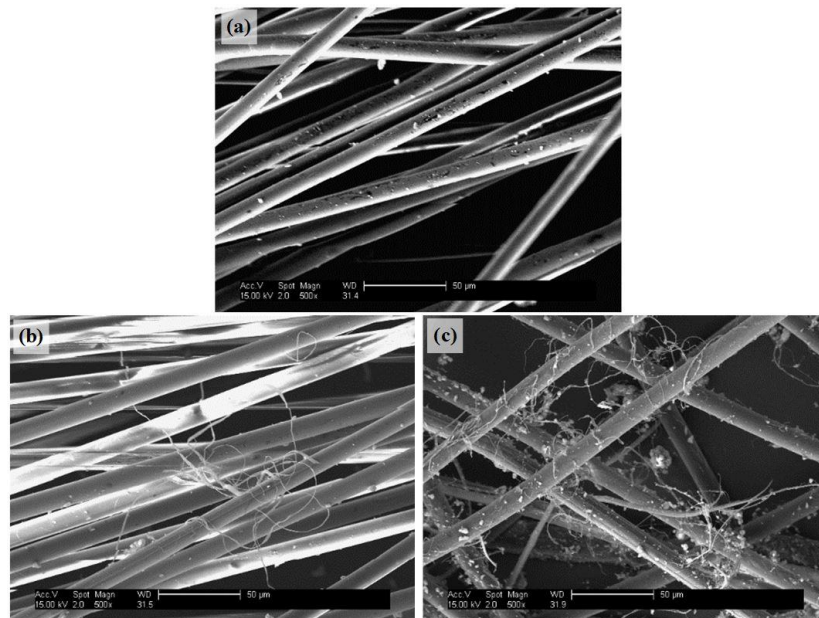


Figure 3-15. SEM Images of Extracted Aramid Fibers of FB Mix at Different Conditions; (a) Agitated Bundles; (b) Clusters; and (c) Individual Fibers (all images at 500x magnification).

3.4 Summary and Discussion

In this study, the repeated load permanent deformation test showed improved performance in FA mixture over FB and control mixtures. Since both FA and FB mixtures contained aramid fibers at the same volumetric content but yielded different behaviors, it can be inferred that volumetric content alone is not a sufficiently descriptive metric to quantify fibers in M-FRAC. The fact that FA exhibits substantially less permanent strain accumulation and has a larger flow number along with the fact that the fibers in FA were more dispersed, distributed, and fibrillated, may suggest that additional fiber metrics play a role in the effectiveness of fibers.

From the improved permanent deformation test results and in light of the orientation findings, it is theorized that the fibers function, as they do in other composites, by bridging or reinforcing cracks. In this case horizontal cracks are developed during the flow number test. In this theory, it is postulated that a more dispersed and distributed fiber system acts to reinforce more flaws and thus more greatly improve the performance. In the case of FB mix, since the agitated bundles are not well distributed, their effectiveness is reduced. The existence of fiber bundles decreases the number of fibers (individual fibers) directly interacting with the matrix and they could also introduce weak spots in the matrix. Stated differently, a well distributed network of fiber reinforcement in the proper directions is necessary since failure can occur on any plane. A large volume of the material left unreinforced can dictate the overall performance of the material. It is also possible that the effectiveness of the fibers in bridging cracks is aided by micro-fibrillation of the fiber surfaces although this is not verified in anyway here. A higher level of this

micro-fibrillation would mean a higher surface area of fibers in the matrix and a stronger overall bond.

The combined behavior of fatigue on the field mixtures and permanent deformation test results on horizontally and vertically cored specimens provided additional fundamental insights with respect to the reinforcement mechanism of fibers in asphalt mixtures. Fatigue test results showed that both FA and FB showed slight improvement over the control, but there was no discernable difference between the two M-FRAC mixtures. The orientation effect of fibers could be another key reason justifying the poor performance of fibers in fatigue. It was found that there is tendency of the individual aramid fibers in these mixtures to be oriented perpendicular to compaction. In the uniaxial fatigue test configuration, the fibers are not ideally oriented for reinforcing cracks that develop perpendicular to the loading direction (tension) because the samples are cored vertically. While in flow number test are ideally oriented to reinforce cracks that form parallel to the loading direction (compression loading).

This study does not identify a critical threshold of individual fibers needed to achieve an effective network. It can only be stated that this threshold is somewhere between an *FDP* of 16% (that from FB) and an *FDP* of 88.5% (that from FA). Whether this network formation follows a simple linear, nonlinear, or percolation type relationship cannot be determined from the current data. Finally, it should be stated that the orientations of the fibers with respect to the testing configuration in this study is a direct result of the laboratory fabrication procedure. The evaluation of field cores was beyond the scope of this study but would provide additional insights. Here the gyratory compactor is used to create specimens by compacting them along the same direction that the major principal

stress is applied during tests. In the case of compression, these orientations generally align with pavement construction and vehicular loading. However, in tension these orientations differ since tension in a pavement is induced in a direction perpendicular to the compaction direction. Failure to consider these differences may lead to laboratory results that underestimate the true fatigue benefits from M-FRAC mixtures. Also, the study findings are isolated to the single mixture studied, and additional testing incorporating more careful documentation of fiber state is warranted in order to refine the theory further. What this study does demonstrate is that understanding M-FRAC benefits can be improved by considering the state of the fiber within the mixture.

CHAPTER 4

EVALUATING INTERACTION OF FIBER REINFORCEMENT MECHANISM WITH MESOSTRUCTURE OF ASPHALT CONCRETE

4.1 Introduction

Published studies generally demonstrate beneficial effects of fibers in asphalt mixtures. However, some studies found that it is not always the case, and when improvements are found they vary with respect to the types of fibers and the particular asphalt mixture used in the study. In previous chapter, it was shown that the fiber state, inclusive of how the fibers exist in the mixture, singular or bundled in some quantity, where the fibers are located (if well distributed), and their surface morphology could directly dictate the effectiveness of their reinforcement in asphalt mixtures. However, the study was limited to one mixture type and the generalizability of their findings was not demonstrated. To the best knowledge of the authors, little to no systematic study has been done to attempt to quantify and correlate the effect of interaction between fiber reinforcement mechanisms and asphalt mixtures composition, inclusive of gradation and binder content, has been systematically undertaken in the literature. Additionally, there exists a lack of a generally applicable laboratory method to introduce the fibers into asphalt concrete mixtures. In the laboratory, agencies often encounter unexpected difficulties in preparing FRAC samples. From practical point of view, without careful attention to the mixing process fibers will not distribute in a homogeneous manner leading the agency to have reduced confidence in the ability of the product to distribute in a full-scale mixing plant. In this chapter, in an effort to determine an optimum laboratory mixing process to create representative FRAC, the

interaction of multiple mixing parameters including time, mixer type, fiber blend, temperature, and mixing processes were considered. Therefore, the specific objectives of this study are to:

- develop an optimal laboratory mixing process of fibers in an effort to improve the dispersion of fibers in asphalt mix;
- evaluate the mechanical properties of various asphalt mix designs reinforced with and without aramid fibers;
- identify and quantify the key factors in the composition of asphalt mixtures attributed to the reinforcement mechanism of fibers; and
- link the performance indicators developed from asphalt mixture constituents to the laboratory modulus, rutting and fatigue performance of M-FRAC.

4.2 Experimental Program

4.2.1 Asphalt Mixture Selection

In the first part of this study, binder/mix types and pavement performance within the United States were evaluated using the Asphalt Institute (AI) and Long-Term Pavement Performance (LTPP) database. The results from such analysis are summarized in Figure 1. The main goal was to identify representative mixtures and test methods for the laboratory evaluation phase of the research that are commonly used by State Departments of Transportation across the United States.

To evaluate the most common binder/mixture type around the United States, The AI database was used to extract all binder grades specified by each State, and LTPP database was used to extract information regarding nominal maximum aggregate size

(NMAAS) and asphalt binder grade. Among all asphalt experiments in the LTPP database, the asphalt specific including General Purpose Sections (GPS) and Special Purpose (SPS) were used to extract asphalt binder and aggregate gradation information. This initial extraction yielded several thousand lines of data and included both new construction and rehabilitation projects. However, many necessary data elements were not present in each line of the database and these were eliminated from the dataset. The dataset was further refined to only include sections with Performance Graded (PG) binder. The next step in the analysis was extraction of pavement distress data from the LTPP database and interpretation of the performance trends with respect to location. The same project sites used in identifying material characteristics was used to extract information regarding distresses for each climate region including Dry, freeze (DF), Dry, non-freeze (DNF), Wet, freeze (WF), and Wet, non-freeze (WNF). The LTPP database was used because it is the most comprehensive database with historical pavement distress information in the United States.

The results from analysis of the common binder/mix type and performance trends for each climatic region are summarized in Figure 4-1. It can be seen that the dry climatic regions (i.e. Arizona, California, ...) tend to use (19 mm) 3/4" NMAAS mix compared to the wet regions (i.e. Pennsylvania, Georgia) that tend to use gradations with NMAAS of 9.5 mm (3/8") and 12.5 mm (1/2"). Also, from these data PG 64-22 was found the most common binder type being used throughout the United States based on both the LTPP experiments and AI database. Additionally, while different types of distresses were identified in LTPP, rutting depth (RD) and fatigue cracking (FC) were found as the two key distresses. It can be seen that fatigue cracking is the most concerning distress in DNF and WF region while

rutting is the main concern WNF region. The analysis also suggested that both rutting and fatigue cracking are equally considered as concerning issue in the DF region. Yet, it should be noted that states within a climatic region have different critical distresses. For example, while fatigue cracking was the most prevalent distress in the wet, freeze region, rutting depth was the most dominant distress in Maine and Wisconsin based on LTPP data. Therefore, evaluation of RD and FC were considered for experimental testing program in this study.

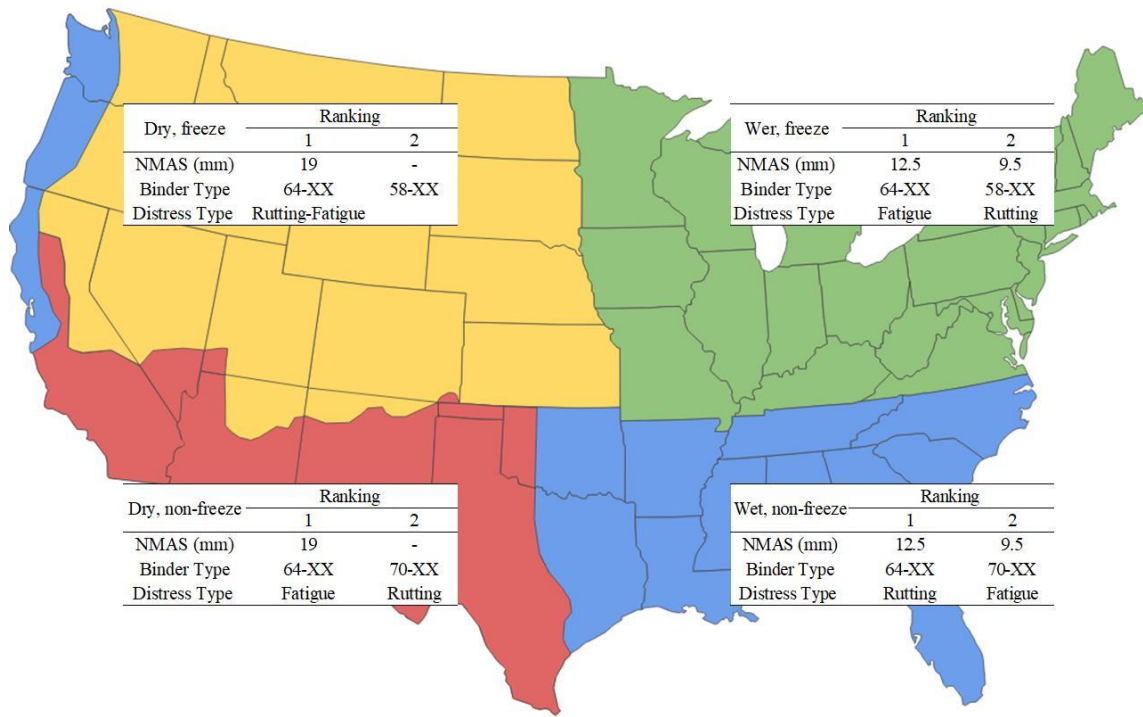


Figure 4-1. Summary of Trends with Respect to The Binder/Mix Type and Performance Based on LTPP Climatic Regions.

4.2.2 Materials

4.2.2.1 Asphalt Mixtures

Based on findings of asphalt mixture selection study in previous section, a total of

seven different mix designs were used in this study; four from the state of Arizona (AZ) and then one each from Pennsylvania (PA), Georgia (GA), and Ohio (OH). It should be noted that each of these mixtures are designed according to the standards of the respective states. The mix design and relevant mix information are summarized in Table 4-1 and Table 4-2. While mixes A-F are laboratory prepared asphalt mixtures, mix G is a plant-produced mixture (both the fiber reinforced and non-fiber reinforced counterpart which are the same mixes labelled as FA and Control in Chapter 3). The binder content (from solvent extraction) and the maximum theoretical specific gravities (G_{mm}) for both plant-produced mixtures were examined and used to determine whether an equitable comparison of the two plant produced mixtures was feasible. Based on the results, the two mixtures appear to be consistent with the exception that one mixture contained fibers.

The OH mixture was also subjected to a special study involving asphalt binder content. In this case, testing was carried out on mixtures at the volumetric optimum asphalt content (6.2%) and $\pm 0.4\%$ from this optimum. The selection of the OH mix among all the mixes is explained later. The PG binder type and content (P_b), *NMAS*, the Reclaimed Asphalt Pavement (RAP) content, and the location of each mix are shown in Table 4-1. Also, the gradation, specific gravity of the binder (G_b), and bulk specific gravity of aggregates (G_{sb}) are illustrated in Table 4-2. In addition, G_{mm} for each mix was determined in the laboratory which were within the difference of two samples limit stated in accordance with AASHTO T209.

Table 4-1. Mix Design Information.

Represented Climatic Region	RAP Content (%)	P _b (%)	Binder Grade	NMAS (mm)	States	Sample ID
DF	0	5.3	PG 64-22	19.0	AZ	A
DNF	18	4.9	PG 70-22	19.0	AZ	B
DF	0	5.5	PG 64-22	12.5	AZ	C
WF	0	5.5	PG 64-22	9.5	PA	D
WNF	30	5.0	PG 64-22	12.5	GA	E
WF	20	5.8	PG 64-22	9.5	OH	F-1
WF	20	6.2	PG 64-22	9.5	OH	F-2
WF	20	6.6	PG 64-22	9.5	OH	F-3
DNF	0	5.2	PG 70-10	12.5	AZ	G

Table 4-2. Gradation and Basic Volumetric Properties of All the Mixes.

Sieve Size		Passing (%)						
Standard	Metric	A	B	C	D	E	F-2	G
1"	25.0 mm	100	100	100	100	100	100	100
3/4"	19.0 mm	98	96	100	100	100	100	100
1/2"	12.5 mm	80	80	87	100	96	100	97
3/8"	9.5 mm	72	69	78	96	84	92	85
No. 4	4.75 mm	51	52	61	61	59	53	62
No. 8	2.36 mm	30	37	45	44	42	33	48
No. 16	1.18 mm	19	25	34	30	32	22	34
No. 30	0.60 mm	14	17	24	21	24	14	23
No. 50	0.30 mm	8.1	7.2	13	13	16	9.0	13
No. 100	0.15 mm	2.6	3.7	7.0	7.0	9.5	6.0	8.0
No. 200	0.075 mm	3.3	2.5	4.3	4.1	5.2	4.4	5.3
	G _{mm}	2.416	2.438	2.399	2.473	2.458	2.427*	2.448
	G _b	1.025	1.029	1.029	1.030	1.035	1.030	1.025
	G _{sb}	2.580	2.578	2.599	2.667	2.649	2.628	2.588

*The Values for F-1 and F-3 were 2.428 and 2.423, respectively.

4.2.2.2 Poly-Aramid Fiber Blend

This bend of aramid-polyolefin fiber has been among one of the most promising types of synthetic fiber used for the purpose of mechanical reinforcement of asphalt

concrete. The popularity of aramid fibers is not just because of its high tensile strength and modulus but also it is used in the low dosage level for reinforcement purpose in asphalt concrete. The low dosage of aramid fibers makes them ideal reinforcing candidates because of first cost competitiveness and second un-disturbance to adjustment of asphalt mix design. Polyethylene and aramid (Poly-Aramid) fiber blend was used for all the mixes at 0.05% dosage level by weight of asphalt mixtures, and the proportion of polyethylene to aramid fiber was 87% to 13% throughout the entire dissertation. The synthetic aramid fibers were dosed at 65 g per tonne of mix which is similar to the mix FA in Chapter 3. The aramid fibers were 19 mm long and were introduced in bundles of approximately 1500-2000 individual fibers each. The dosage level and length were selected for this study because these were the recommended dosage levels from the manufacturer. The physical properties of synthetic fiber were measured and summarized in previous chapter. It should be noted that the volumetric properties of mixtures (i.e. G_{mm} , void content, ...) were not notably affected by the presence of fibers.

4.2.3 Fiber Mixing Methods

A good dispersion and distribution of fibers is a key in maximizing the reinforcing benefits of fibers in composite materials. There is no laboratory standard test method to introduce the fibers into asphalt concrete mixtures. As shown in Chapter 3, poly-aramid fibers can be dispersed and distributed very well in the field with over 95% of fiber being dispersed in the mix (Noorvand et al., 2018). Duplicating the same fiber mixing mechanism in the laboratory has presented a challenge; however, mainly due to inadequate access to the similar resources existing in the field. This issue is important though because many

agencies first assess the efficacy of different M-FRAC technologies by using laboratory tests. Thus, without careful attention to the mixing process in the laboratory, fibers may not distribute in a manner consistent with full scale deployment and ultimately undermine the agency's confidence in using the product.

Given the need for an optimal fiber mixing procedure to create representative FRAC, a preliminary study was conducted to examine several controlling parameters (mixing time, mixer type, mixing process, ...). For the interest of brevity only the three laboratory dry mixing procedures that yielded to the best possible dispersion of aramid fibers will be presented and discussed below. A full description of all the mixing methods can be found in APPENDIX C. Note that in all three methods the aggregate and asphalt are first preheated to the appropriate mixing temperature.

- *Method A (traditional method)*: the appropriate amount of asphalt binder is first added to a crater formed in the middle of the aggregate heated to the target mixing temperature. Then, aramid fibers are sprinkled onto aggregate around the crater and the mix is blended for 90 seconds. Finally, the proportioned amount of polyethylene fiber is added directly to the hot asphalt binder and the mix is blended for 90 seconds. Evidence from preliminary laboratory mixing studies at Arizona State University (ASU) showed that when PE is added directly to hot aggregate in a laboratory mixer it may melt to the aggregate. This effect is not observed in plant mixed materials where the fibers disperse through tumbling aggregates and, it is hypothesized, are not in as direct and intimate contact with the aggregates.
- *Method B (two-layer system)*: One full batch of aggregate is approximately divided to half (by mass). Next, the first half of the aggregates is poured into the mixing

bucket and then the aramid fibers are evenly spread on the top of the first layer of aggregate. After pouring the second and final layer of aggregates into the mixing bucket, the same process of method A was followed (Addition of binder, polyethylene, and mixing for 90 seconds).

- *Method C (three-layer system)*: One full batch of aggregate is roughly divided to thirds. The first third of the aggregates is poured into the mixing bucket and then half of the aramid fibers are evenly spread on the top of the first layer of aggregate. This process is repeated for the second layer of aggregate and second half of the fibers. After pouring the third and final layer of aggregates into the mixing bucket, the same process of method A was followed (Addition of binder, polyethylene, and mixing for 90 seconds).
- *Method D (pre-dispersed)*: This method is similar to method C except that consideration was given to devising a laboratory fiber pre-dispersion technique. Under this method, air pressure technique was used to disperse aramid fibers prior to the use. There were also several other variables that needed to be controlled in order to effectively pre-disperse these fibers. After pre-dispersion of these fibers they were added into the mix the procedure described under method C. The details of the experiment can be found in APPENDIX C.

It should be noted that the fiber mixing procedure in the layering system (C-D) takes longer than usual which causes aggregates to lose heat prior to mixing. Therefore, aggregates are initially preheated 10 C higher (which was determined in a separate study) than mixing temperature to account for the heat lost.

4.2.4 Laboratory Test Methods

Three different mechanical test protocols were carried out to study the laboratory performance of asphalt mixtures with and without fibers; these protocols targeted characterization of the overall response to cracking (uniaxial fatigue), loading (modulus), and permanent deformation (flow number). In all cases, the tests were performed using an IPC UTM-25 machine and for all specimens the target air void content was between 6 and 7%. This air void content was chosen because it is commonly encountered in practice immediately after construction and is therefore the most critical air void content. All specimens were compacted with the gyratory compactor, 150 mm in diameter and 180 mm in height. Specimens were then cut and cored to their final geometry. Note that all the mechanical tests were similarly used in Chapter 3 except that for Flow Number test, the stress level varied by the mixture in order that all testing would fail between approximately 5000 and 10000 cycles. Although the stress level varied from state-to-state, within a given state the same stress level was used for the fibers and non-fibers mixture of each mix (More details in APPENDIX A). In addition, fiber extraction was used to evaluate the best optimum mixing procedure and to study the state of fibers in all the mixes (See APPENDIX B for the complete test procedure).

4.3 Results

4.3.1 Optimum Fiber Mixing Method

To select an optimum fiber mixing method throughout this study, fiber extraction was performed to compare the dispersion level of individual fiber states (*FDP*) for the mixes produced through different mixing methods (A-D). For each extraction, samples

were obtained from the laboratory prepared mixtures right after the fibers were mixed with the binder and aggregate. After mixing, mixtures were spread evenly onto a clean table, and then 1500 g were randomly sampled for each extraction replicate. Table 4-3 presents the extracted aramid dosage rate and aramid fiber states (*FDP*, agitated bundles and clusters) for each mixing method. The dosage rate simply represents the mass of the aramid fiber with respect to the total weight of the mixture. All the recovered aramid fibers from extraction contained similar dosage levels (within approximately 5% of one another) and were within 1-5% of the target rates, except mix method D which was 10% less than the target. It should be noted the polyolefin is melted during the mixing and only aramid fibers are recovered. Also, fiber extraction was performed on two separate samples of each fiber mixing method.

The results indicated that highest average *FDP* value of 88% for mixes produced by mixing method D followed by methods C, B and A with average *FDP* value of 72%, 59% and 44%, respectively. Two observations were made from different fiber mixing methods.

- Aramid puffing process yields more individual fibers. So, an internal study was undertaken to compare the mechanical performance of fiber specimens produced through mixing methods C and D (not shown for brevity), and the mechanical results were found to be insignificant between the two methods. Therefore, method D was dropped due to the challenges existed in the method such as visual fiber loss puffing, handling, and mixing (airborne) and variability of Puffing process (single operator), Puffed fibers adhered to the mixing tools and bucket. This also explains the lower equivalent aramid dosage rate (0.96%) than other mixing methods.

- The use of layering system to introduce fibers into the mixture can allow the aramid fibers to disperse more efficiently. The reason for this result could be related to first a better initial spread of fibers with appropriate distance from each other within the aggregate to be effectively agitated upon mixing. Second, the layering method give the fibers enough time for the agitation prior to them exposing to hot binder which could otherwise lead to agglomerations that further interfere with the dispersion of aramid bundles in the mix. Therefore, Method C was selected as the optimal fiber mixing method throughout this study.

Table 4-3. Summary of Extracted Aramid Dosage and Fiber State for Various Fiber Mixing Methods.

Specimen ID	Aramid Dosage Rate (g/tonne)	State of Aramid (%)		
		<i>Agitated Bundle</i>	<i>Cluster</i>	<i>FDP (Individual)</i>
Method-A-1	68.0	42	13	45
Method-A-2	69.2	48	9	43
<i>AVG Method A</i>	68.6	45	11	44
Method-B-1	69.3	12	21	57
Method-B-2	69.0	22	21	61
<i>AVG Method B</i>	69.1	17	21	59
Method-C-1	67.3	12	17	70
Method-C-2	68.5	9	18	73
<i>AVG Method C</i>	67.9	11	18	72
Method-D-1	59.9	0	15	85
Method-D-2	57.1	0	10	90
<i>AVG Method D</i>	58.5	0	13	88

4.3.2 State of Aramid Fibers in the Asphalt Mixes

Extraction was performed to compare the dispersion level of individual fiber states (*FDP*) for each mixture using the ASU procedure after flow number testing. Table 4-4 presents the extraction results both in terms of the aramid dosage rate and the percentages

of each of fiber states (*FDP*, agitated bundles and clusters). The Coefficient of Variation (*CV*) of dosage rate and *FDP* state of recovered aramids from extraction were within approximately 5-15% of one another. Also, the recovered dosage rate of aramid fibers was within 5-20% of the target rates for all the mixes. The higher variation observed in the dosage rates might have resulted from the fact that extraction was carried out on the tested flow number specimens each having a mass of roughly 2000 grams, which is more than the amount required for normal extraction and recovery. Moreover, due to randomly distributed fibers, it is likely that the test specimens may contain slightly different aramid dosage rates from one specimen to the other. Therefore, the extraction was performed on three to four separate samples of each mix. Additionally, an ANOVA and statistical t-test analysis were performed at a 95% confidence level. The ANOVA analysis was used to compare the difference between all means for *FDP* and evaluate the significance of the total differences and the t-test was performed to compare individual cases of *FDP* values between each fiber mix.

The extraction results indicated that most of the fibers are dispersed in the individual condition with an average of *FDP* in the range of about 50-70% for all the laboratory prepared mixes and 88.5% for the Plant-produced mix G. As discussed earlier, plant produced mixtures are able to disperse more effectively due to larger mix volumes and effective mixing method practiced in the field. Extraction results of laboratory prepared specimens also revealed an interesting observation. Statistical analysis of extraction results of *FDP* values did not show any significant difference between mixes A, B, C and E as well as between mixes D and F. However, comparing mixes A, B, C, and E with D and F by ANOVA and t-test, a statistical significance was observed. This suggests that mixes

with a higher nominal maximum aggregate size yielded to an overall more effective dispersion of aramid fibers. For example, mixes A, C, and D with *NMAS* of 19, 12.5, and 9.5 mm indicated *FDP* of 71%, 61%, and 52%, respectively. This could be due a higher degree of defibrillation and separation of bundles of aramid fibers and effective mechanical agitation of fibers upon exposure to large aggregate particle size during mixing time. It also appears that the existence of RAP in the mixes B and E and the different binder content (F1-F3) caused slight impact on dispersion of aramid fibers. Nevertheless, based on the extraction results of this study a conclusive statement cannot be drawn.

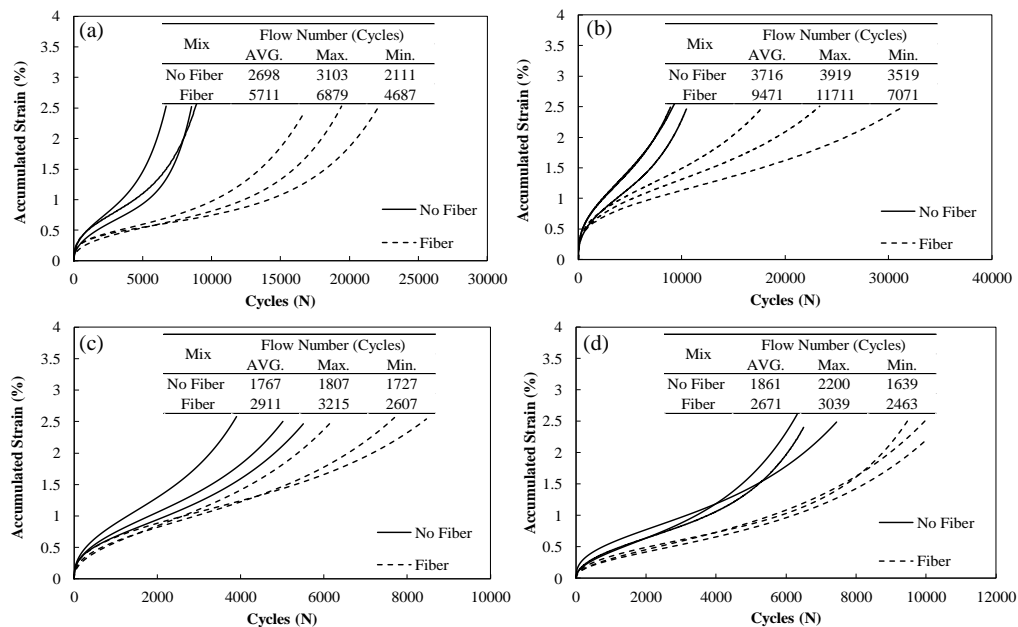
Table 4-4. Summary of Extracted Aramid Dosage and Fiber State for Various Mix Designs.

Specimen ID	Aramid Dosage Rate (g/tonne) (%CV)	State of Aramid (%)		
		<i>Agitated Bundle</i>	<i>Cluster</i>	<i>FDP</i> (%CV)
A	80.8 (15)	11	18	71 (5)
B	77.4 (5)	16	23	61 (14)
C	65.8 (13)	10	24	66 (12)
D	69.7 (7)	30	18	52 (7)
E	69.1 (10)	16	24	60 (16)
F1	85.3 (20)	33	19	48 (9)
F2	77.1 (19)	26	24	50 (6)
F3	79.5 (9)	18	28	54 (10)

4.3.3 Repeated Load Permanent Deformation Test

Figure 4-2 illustrates the accumulated permanent strain using the flow number test for each of the mixtures. The resulting flow number values from this analysis are also shown as a tabular insert into the figures. It can be seen that in some mixes (i.e. A and B) the M-FRAC variant accumulates strain at a slower rate and undergoes more repetitions before reaching the onset of flow compared with no fiber variants. The results also show

that this pattern is not universal since the fiber variants in mixes D and F exhibit similar permanent strain response as their non-fiber variants under the repeated loading. Incorporation of fibers in mixes B, E, G and A exhibited the highest increase in average flow number values with 155%, 141%, 139%, and 112%, respectively, Figure 4-2(a, b, e, and i). In comparison, the use of fibers in mixes C, F-1, and D indicated less degree of improvement in average flow number values recorded at 65%, 58%, 44%, respectively, Figure 4-2(c, d, and f). Additionally, F-2 and F-3 mixes with and without fiber showed almost similar permanent strain response under the repeated loading with no notable changes in flow number values as shown in Figure 4-2(f). Therefore, while fibers enhanced the flow number values of asphalt mixtures in general, the degree of improvement for each mix was different. While these differences could result from different states of aramid fibers, particularly *FDP* values, the constituents of asphalt mix (i.e. binder content, gradation) play a more pronounced effect on the fibers reinforcement efficiency in rutting. This will be discussed later.



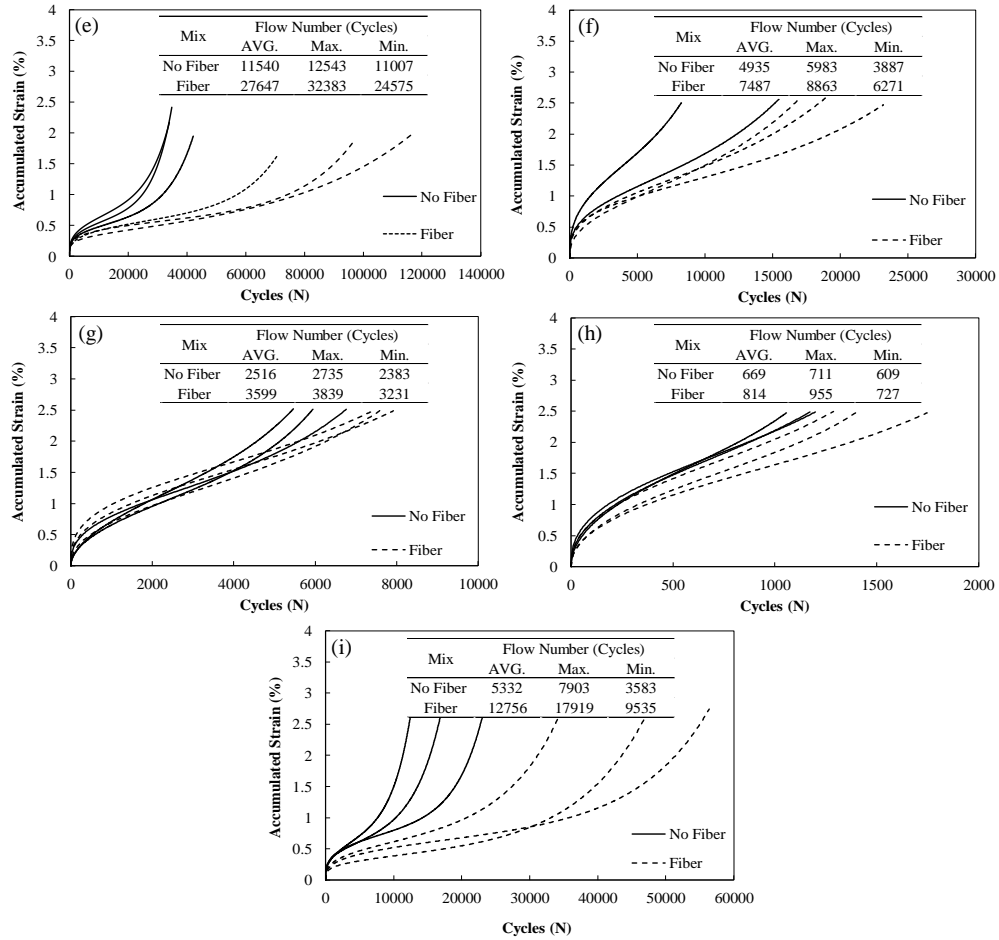
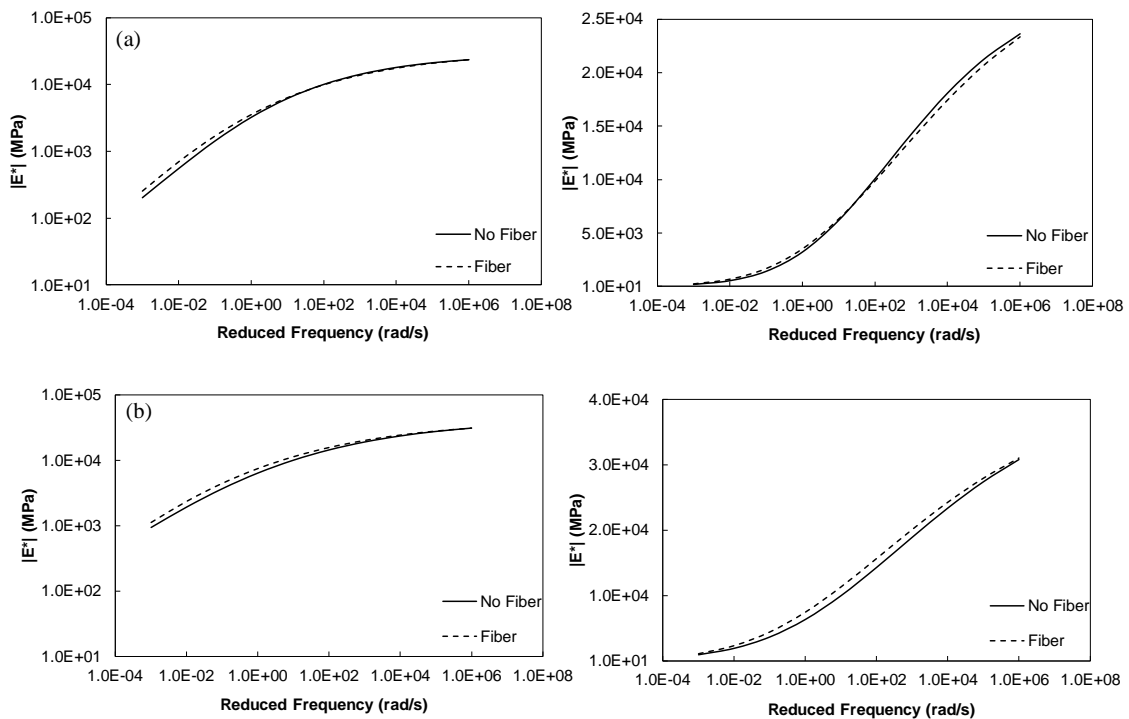


Figure 4-2. Average Accumulated Strain During Flow Number Test for Mixes (a) A, (b) B, (c) C, (d) D, (e) E, (f) F-1, (g) F-2, (h) F-3, and (i) G.

4.3.4 Dynamic Modulus Test

The results of $|E^*|$ experiment are shown in the form of dynamic modulus master curves in Figure 4-3. The dynamic modulus data is shown in both log-log and semi-log scales to better detect differences in the moduli at high and low temperatures. It is seen that the moduli values for all the mixtures are relatively similar, yet there appears to be some deviations in the average mastercurves of mixes C and D with and without fibers. An ANOVA and statistical t-test analysis were performed at a 95% confidence level for all

measured temperatures and frequency combinations. The ANOVA analysis was used to compare the difference between all means and evaluate the significance of the total differences and the t-test was performed to compare individual cases to the control mixture and individually between the fiber mixes. In all cases, the results (not shown for interest of brevity) indicated that the differences in moduli are not statistically significant. Thus, while on-average differences are evident these effects are not significant. This finding is not consistent with some previous studies that report changes in moduli values as a result of incorporating fibers in the asphalt mix (Shaopeng *et al.* 2007, Kaloush *et al.* 2010). It is noted that in the Kaloush et al. study, the type of polyolefin fibers used were different, and the asphalt mixture used was for local municipality application. In other word, the fibers used in that study may have had larger impacts on improving lower quality mixtures compared to higher quality mixtures used by State DOTs, such as those used in this study.



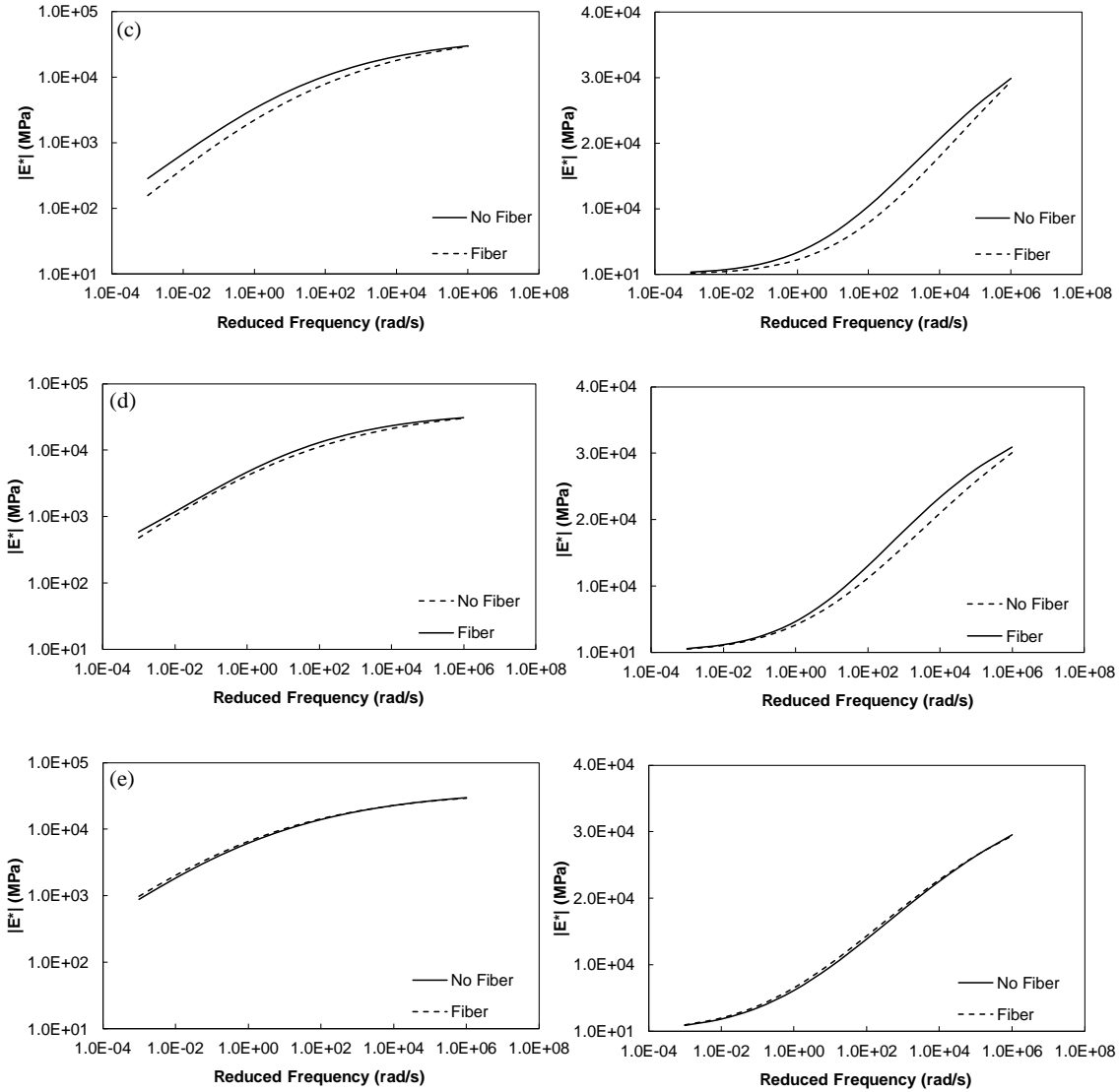


Figure 4-3. Comparison of $|E^*|$ Mastercurves for Mixes (a) A, (b) B, (c) C, (d) D, and (e) E in; Log-log Scale (Left Figures) and Semi-log Scale (Right Figures).

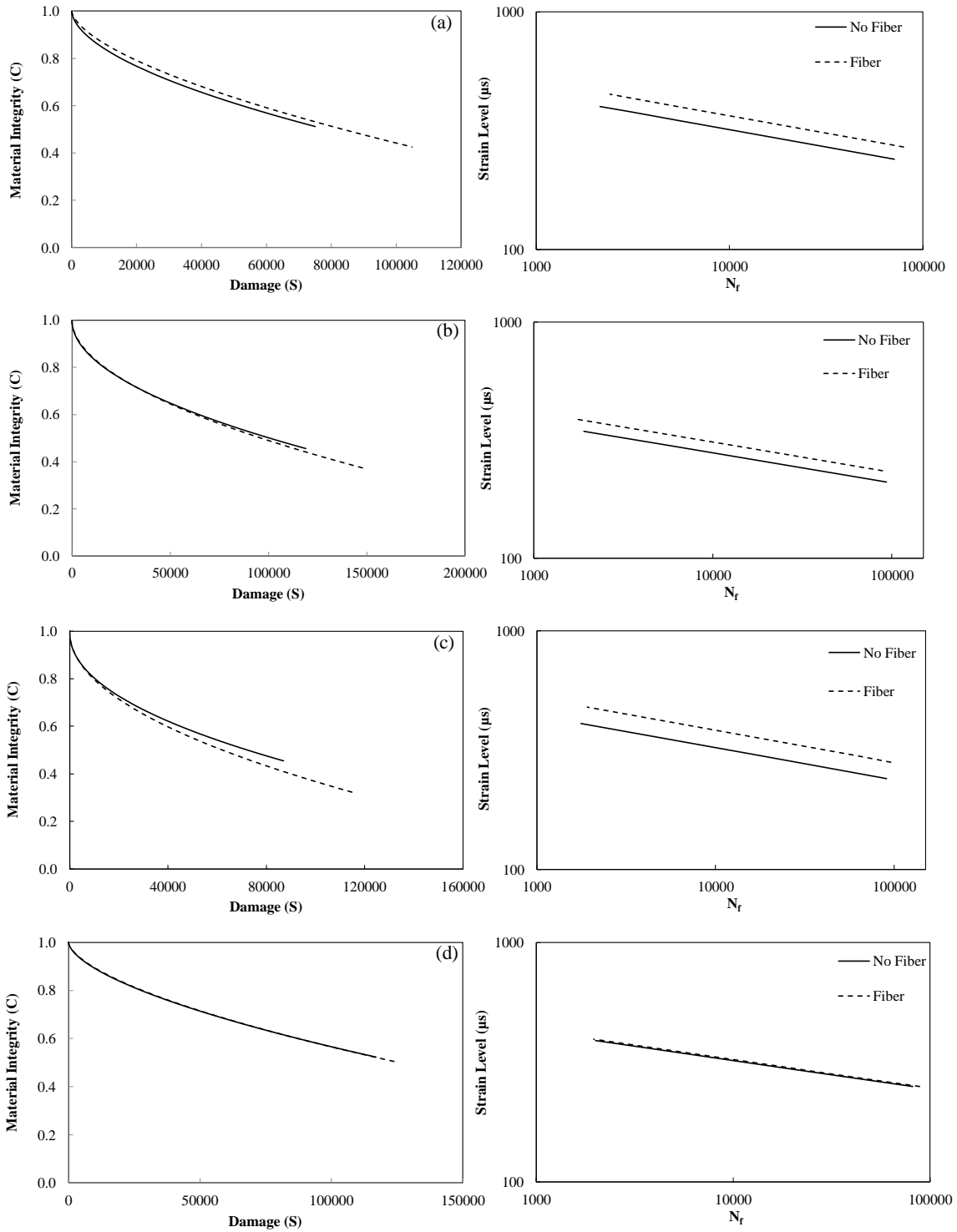
On the other hand, this author feels that the results in this part of the study are accurate since; 1) the actual volume fraction of fibers in the mixture is low and 2) the dynamic modulus test is a non-destructive test (inherent micro-defects in the asphalt mixture do not grow). Effective medium theories suggest that fiber reinforcement can increase the composite modulus if the individual fibers have substantially higher moduli

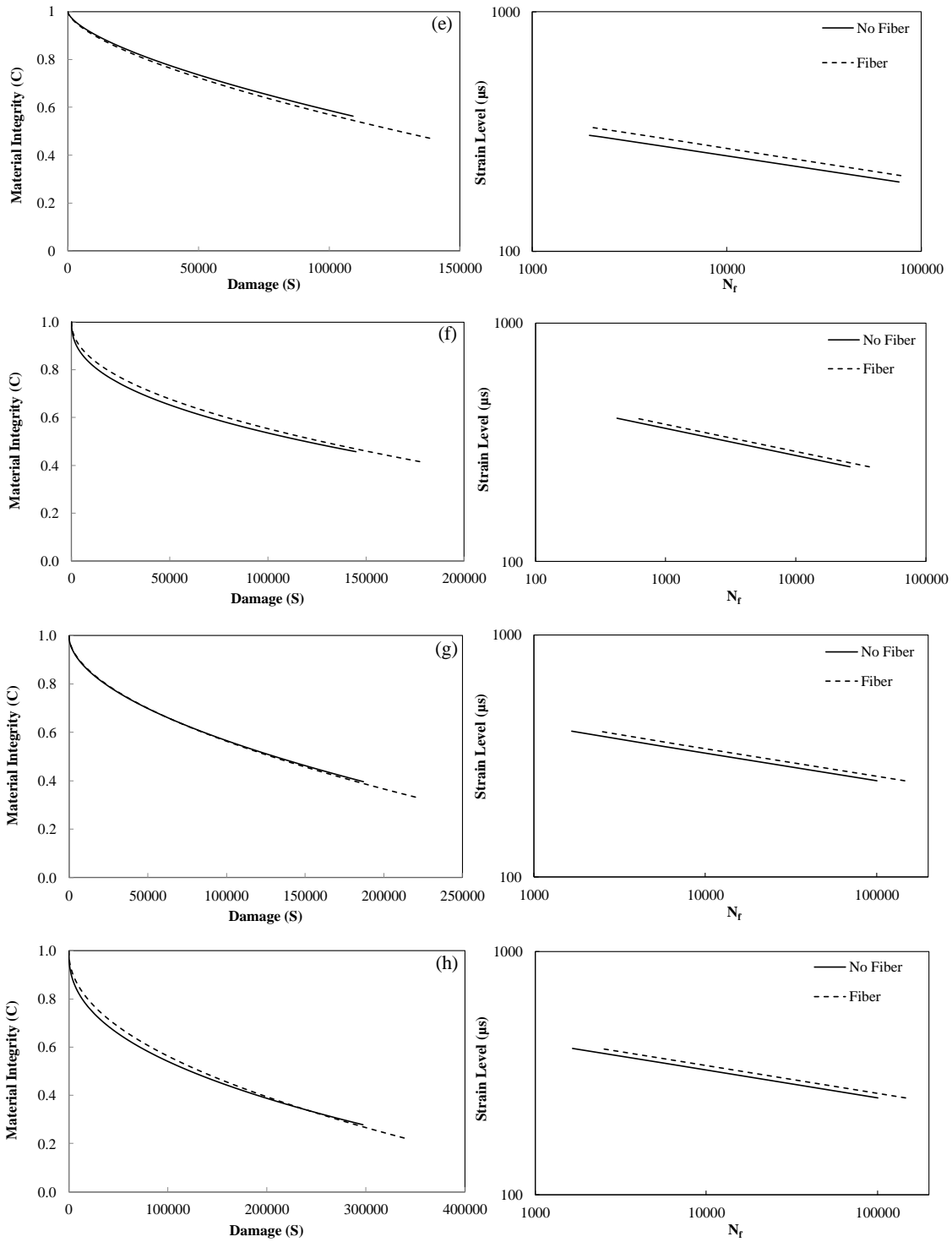
than the other components of the composite and if the volume of fibers is large enough (Choy 2015), but aramid fibers only constitute a small part of the total volume of the asphalt mixture. The other mechanism whereby fibers can increase the modulus is through reinforcement of growing defects because mechanically reinforced fibers alter the mechanical properties by of transferring stresses and loads across cracks. Since the specimen strain is low (typically around 60 micro-strains) the growth of micro-defects is generally considered to be non-existent. Based on these findings the authors elected not to perform dynamic modulus testing on the M-FRAC variant for F1-F3 and instead treated the modulus as equivalent to the non-fiber variant values. The dynamic modulus test data was required as part of analysis and simulation of the fatigue life.

4.3.5 Uniaxial fatigue test

The damage characteristic curve for all the mixes with/without fibers are shown in (left figures). To have a better understanding of fatigue life of asphalt mixtures it is necessary to evaluate damage curves along with $|E^*|$ of mixtures tested earlier. Since it was found there was no significant difference between fiber and no fiber specimens in $|E^*|$ data, the average modulus data of only no fiber specimens for each mix were used for the analysis of their corresponded fatigue life. This was done to avoid using potential bias in interpreting fatigue life of mixes with and without fibers. These curves show that the effect of fibers on the damage characteristic varies from one mix to another. For example, fiber reinforced samples of mixes A and C outperformed their no fiber samples in sustaining damage before failure, while fiber samples of mixes D and G have damage curves that are very similar to those of the no fiber samples. Similar to the damage characteristics, the

effect of fibers on the fatigue life of asphalt mixtures differ depending on the mix design types ((right figures)).





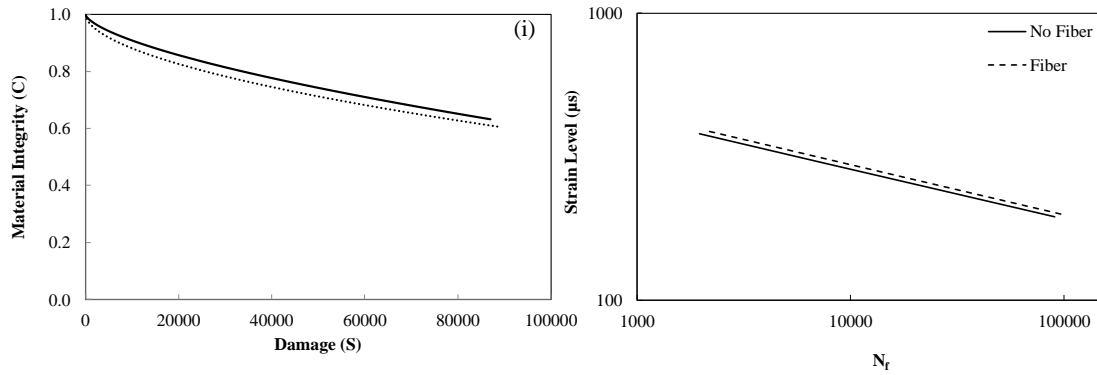


Figure 4-4. Comparison of Damage Characteristic Curves (Left Figures) and Predicted Fatigue Life Relationship Based on Constant Strain (Right Figures) for Mixes (a) A, (b) B, (c) C, (d) D, (e) E, (f) F-1, (g) F-2, (h) F-3, and (i) G.

4.3.6 Interaction of Fiber Reinforcement Mechanism with Composition of Asphalt Concrete

The AC meso-structure can be considered as the coarse aggregates enclosed by the Fine Aggregate Mixture/Matrix (FAM) that consist of fine fillers, fine aggregates, asphalt binder, and the air voids. The overall mechanical response of an AC is governed by the properties of its constituents. For instance, the viscoelastic response of AC in cracking is primarily controlled by the viscoelastic properties of the asphalt binder (or more accurately by the viscoelastic properties of FAM). The positions or orientation of aggregate, aggregate interlocking, and friction between the aggregates mostly control the viscoplastic response of AC, particularly in compression. Therefore, the viscoelastic and viscoplastic properties of AC are strongly related to their microstructure (Darabi *et al.* 2012).

In this study, to further examine the rutting resistance and fatigue life of asphalt mixes with and without fiber, FN values and N_f simulated at 300 μs were plotted, respectively for all the specimens in Figure 4-5. While fibers generally enhanced the FN values and

fatigue life of asphalt mixtures, the degree of improvement varied from one mix to another. For example, while the use of fiber in the mix E increased the FN values by 140%, this increase in mix C was only 65% (Figure 4-5(a)). A similar trend was found in the fatigue test results (Figure 4-5(b)). The largest increase in the fatigue life of asphalt mixtures reinforced with fibers was recorded for mix C with 245%, followed by mixes A, B, and E with 140%, 130%, and 70%, respectively. Fiber in mixes D, F1-3, and G increased the fatigue life in the range of 10-50%. It is recalled that mix G was the field mix highly dispersed ($ASDR=88.5\%$). Nevertheless, the high individual state of fibers in the mix did not result in significant improvement in fatigue.

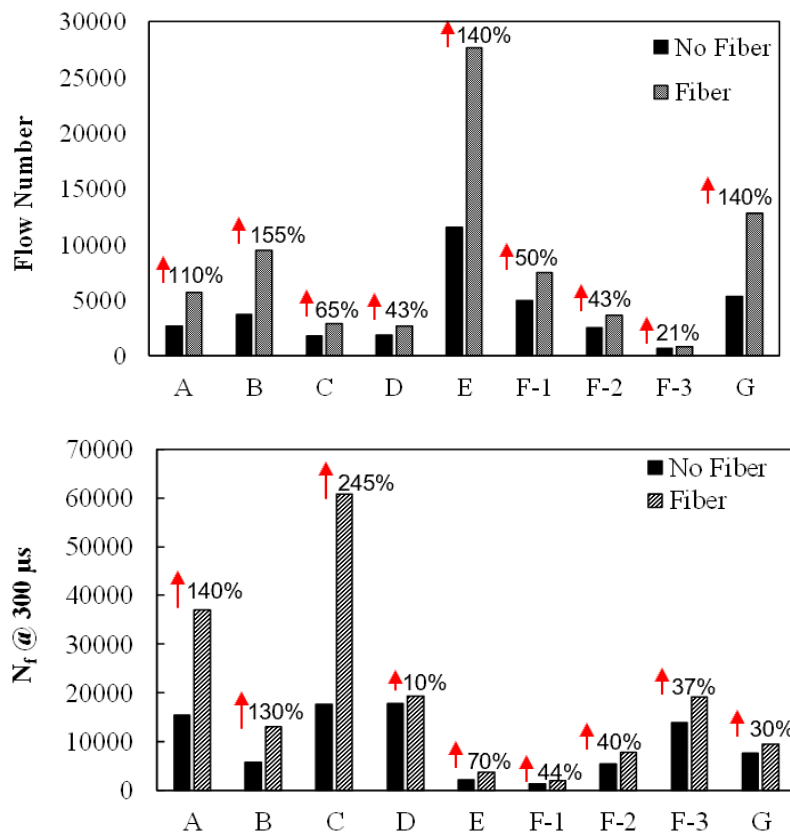


Figure 4-5. (a) FN and (b) N_f Simulated at 300 μs Level of All the Mixes with and without Fibers.

It was postulated that the efficiency of fiber reinforcement in improving the mechanical performance of asphalt mixtures was linked to the microstructure of asphalt mixtures. In particular, it appears that depending on the different gradation, binder content, binder types, and volumetric properties of asphalt mixtures, fibers reinforcing mechanism in fatigue cracking and rutting resistance is significantly affected. On the composition of asphalt mixtures, the volume of binder content and gradation were found as two key factors that determine the fiber reinforcing efficiency in rutting resistance and fatigue cracking, respectively. The relationship of these parameters with the laboratory findings of the mechanical performance of MFRAC was carefully examined and will be discussed in the following sections.

4.3.6.1 Binder Content Effect on Rutting Resistance of M-FRAC

The effect of several external and internal factors on rutting resistance of AC mixtures have been previously recognized. Internal factors consist of pavement thickness, asphalt binder, aggregate and mixture properties (Golalipour *et al.* 2012). Several studies have argued that the properties of aggregates are usually considered as the primary factors leading to rutting of AC (Button *et al.* 1990, Ahlrich 1996). Stakston and Bahia (2003) found that aggregate gradation rutting resistance is very dependent on gradation of aggregate. In this study, the effect of aggregates properties, particularly the gradation on the rutting performance of M-FRAC for different mixes was carefully examined, nevertheless, no direct link was observed between the gradations of the mixes and performance of M-FRAC in flow number test. Asphalt binder content is another critical parameter which affects the shear resistance of asphalt mixtures. There should be adequate

film thickness to coat the aggregate which provides cohesion, but presence of too much binder (high film thickness) can essentially have a lubricating impact, thus reducing the efficiency of the aggregate skeleton and generating an unstable mix that is susceptible to premature rutting (BRossEAUD *et al.* 1993). Further analysis of other mix constituents revealed a connection between the asphalt binder content in the mixes and the enhanced flow number of the mixes with fiber. For example, when comparing F1 to F3 mixes having the same gradation but different binder contents, it is evident that effectiveness of fibers in improving flow number diminishes with increasing binder content.

The volume of effective binder volume (V_{be}) was selected to represent the index parameter in examining the performance improvement of M-FRAC in flow number test. Besides, V_{be} is a percentage of total volume, just like air voids content; each individual mix type has an exceptional volume of effective binder, giving a spectrum of values for this independent variable. Therefore, V_{be} was determined for the compacted test specimens of each mix type using basic volumetric properties from Table 4-1 and Table 4-2 to navigate any possible correlation between the rutting resistance of M-FRAC and the effective asphalt binder content, as shown in Equation (4-1).

$$V_{be} = V_b - V_{ba} \quad (4-1)$$

$$V_{be} = \frac{P_b \times (G_{mm} - AV \times G_{mm})}{G_b} - \left((G_{mm} - AV \times G_{mm}) - \frac{P_b}{G_{mm} - AV \times G_{mm}} \right) \times \left(\frac{1}{G_{sb}} - \frac{1}{G_{se}} \right) \quad (4-2)$$

$$G_{se} = \frac{100 - P_b}{\frac{100}{G_{mm}} - \frac{P_b}{G_b}} \quad (4-3)$$

Where;

- V_{be} = volume of effective asphalt binder;
 V_b = volume of asphalt binder;
 V_{ba} = volume of absorbed asphalt binder;
 P_b = total asphalt binder content, %;
 G_{mm} = theoretical maximum specific gravity;
 G_b = specific gravity of Binder;
 AV = target Air void of the compacted specimens for the test which is 6.5%;
 G_{sb} = bulk specific gravity of aggregate; and
 G_{se} = effective specific gravity of aggregate, which is sometimes given or can be experimentally obtained.

The calculated V_{be} values and the improved FN values of asphalt mixtures due to fiber for all the mixes A-G were generated in Figure 4-6. The error bar indicates the standard deviation between the maximum and minimum improvement in FN values of AC due to fibers. It can be seen that there is a very strong correlation between the V_{be} of each mix and the degree of improvement in average FN values in the specimens reinforced with fibers which is defined according to Equation (4-4). It should be noted that since the effect of air void variations in the compacted specimens was not investigated in this study, the proposed effective volume of binder should only be representative of mixes compacted at the same AV level. Nevertheless, the changes of AV values as inputs in Equation (4-1) did not notably affect the correlation between the V_{be} and the degree of improvement in FN values.

$$\text{Improved FN due to Fiber (\%)} = \frac{FN_{Fiber} - FN_{No Fiber}}{FN_{No Fiber}} \times 100 \quad (4-4)$$

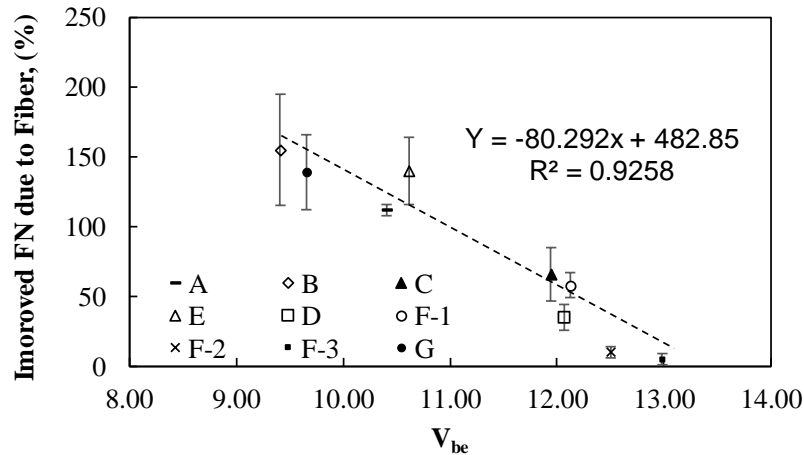


Figure 4-6. Comparison of V_{be} Values with Enhanced Flow Number of Asphalt Mixtures Due to Fiber for All the Mixes.

Although, no further experimental works and/or numerical modelling were done to explore the mechanism of such pattern, the findings of this study may be postulated as follows. Asphalt concrete experiences permanent deformation due to its exposure to repeated traffic loading during its service lifetime at high temperatures. There are three different mechanisms which lead to permanent deformations of asphalt mixtures during traffic loading. These include reduction in the friction between aggregates coated with bitumen, overcoming the interlock between aggregates that it pushes the aggregates away from each other, and the loss of adhesion between aggregate and bitumen in asphalt mixture (Golalipour *et al.* 2012). Darabi *et al.* (2012) provided an interesting argument on the microstructural changes for hardening-relaxation mechanism of asphalt concrete.

They argue that during the compressive loading stage, the aggregates become slightly reoriented, and their interlock system is defeated by the asphalt binder confined amongst them, which starts to push the aggregates away and/or together. During the rest period, the viscoelastic response of confined asphalt binder is such that a time-dependent

residual stress occurs to push the aggregates back and as a result the induced residual stresses are released. This creates a time-dependent rearrangement in the aggregate skeleton which allows partial recovery of viscoplastic hardening of asphalt composites. Though Darabi *et al.* (2012) do not explicitly evaluate the role of binder, it is surmised that in the presence of higher binder content, a relatively thicker film is formed on the aggregate particles, which provides more mobility for the aggregates especially during the loading stage. The researches also argue that this increased mobility causes a faster relaxation of residual stress and rearrangement of the microstructure during the rest period, which leads to more hardening recovery (Darabi *et al.* 2012). Therefore, asphalt concrete with higher effective binder content can endure more viscoplastic deformation through the next loading cycles as well as faster microdamage growth rate.

In the case of fiber reinforcement efficiency, it is theorized that fibers may not get mobilized when the rate of the initiation and growth of microdamage is relatively fast. The lack of fiber reinforcement efficiency can be further accompanied by the fact that higher binder content in the asphalt concrete can reduce the effect of interparticle friction and the degree of interlock between aggregates. In other words, the failure mechanism of performant deformation of AC under repeated loading is more dominantly driven by deformation of binders where they push the aggregates away from each other more easily to defeat the interlock between them. Given the physical characteristics of fibers, one should expect that a randomly distributed fibers in asphalt concrete matrix acts to bridge across aggerate particles, particularly fine particles, rather than the binder itself. Therefore, fibers are more effective in a system where interlock and stone-on-stone friction between aggregates are the dominant failure mechanism under compression loading condition.

4.3.6.2 Mix Gradation Effect on Fatigue Life of M-FRAC

Additional insights on the interaction of reinforcement effect of fibers with compositions of asphalt mixtures are gained by considering the fatigue tests for various mixes. It was observed that FAM phase based on different gradation of mixtures play a very pronounced impact on the uniaxial fatigue performance of M-FRAC. FAM is a term initially used by Kim (2003) to define the material used in his studies with sand asphalt and is created by combination of asphalt binder, air, filler, and fine aggregate particles with a specific gradation (Kim 2003). Also, Kim (2003) created FAM samples using aggregate particles smaller than 1.18 mm. This size was chosen based on the availability of the standard sand required by ASTM C778, which is mostly uniform and of sizes from 0.6 mm to 0.3 mm. Zollinger (2005) followed the work of Kim and created a FAM from actual asphalt concrete mixture gradations by taking only material finer than 1.18 mm (Zollinger 2005). Other researchers have defined the scale below asphalt concrete using aggregate sizes smaller than 2.36 mm (Dai and You 2007, Kim, Wagoner, *et al.* 2008), 2.26 mm (Valenta *et al.* 2010), or 2 mm (Lackner *et al.* 2005).

The Bailey Method, which is rooted in packing theory, has been used for examining and developing aggregate gradations in asphalt concrete. This method proposes a phenomenologically vindicated concept using the definition of a primary control sieve (Vavrik *et al.* 2001). This sieve size is calculated based on the ideal aggregate diameter which would just fit inside the void space formed by three of the nominally largest coarse particle sizes touching in the most ideal arrangement. For mixtures with a *NMAS* of 25.0 mm and 19.0 mm this dimension corresponds to roughly 2.36 mm sieve, and for 12.5 mm and 9.5 mm *NMAS* mixtures this dimension is approximately the 4.75 mm sieve. These

classifications would suggest that for 25.0 mm and 19.0 mm mixtures the FAM should be fabricated with aggregates that are smaller than 4.75 mm while for 12.5 mm and 9.5 mm mixtures the FAM material the FAM should contain all of the aggregates smaller than 2.36 mm (Underwood 2011). Therefore, the concept of The Baily method was used in this study to distinguish coarse aggregates from fine aggregates based on the sieve size and the nominal maximum aggregate size. In this study, FAM was determined in a form of a thickness index ($FAM_{T(Index)}$) as follows.

$$FAM_{T(Index)} = \frac{V_{FAM}}{SA_{CA}} \quad (4-5)$$

$$SA_{CA} = \sum_{i=No.4}^{i=25\text{ mm}} \frac{1}{4/3\pi r_i^3} \times \left(1 - \frac{VMA}{100}\right) \times 4\pi r_i^2 R_i \quad \text{For } NMA\text{S}(mm) = 25 \& 19 \quad (4-6)$$

$$SA_{CA} = \sum_{i=No.8}^{i=25\text{ mm}} \frac{1}{4/3\pi r_i^3} \times \left(1 - \frac{VMA}{100}\right) \times 4\pi r_i^2 R_i \quad \text{For } NMA\text{S}(mm) = 12.5 \& 9.5 \quad (4-7)$$

$$V_{FAM} = V_{sb}V_{FA} + V_{be} \quad (4-8)$$

$$V_{FA} = 100 - \text{Passing No.4 (\%)} \quad \text{For } NMA\text{S}(mm) = 25 \& 19 \quad (4-9)$$

$$V_{FA} = 100 - \text{Passing No.8 (\%)} \quad \text{For } NMA\text{S}(mm) = 12.5 \& 9.5 \quad (4-10)$$

$$V_{sb} = \frac{(G_{mm} - AV \times G_{mm}) - \frac{P_b}{G_{mm} - AV \times G_{mm}}}{G_{sb}} \quad (4-11)$$

Where;

SA_{CA} = the total surface area of coarse aggregate (cm^2) (Panda 2016);

r_i = radius of the sieve size;

R_i = percentage of retained aggregates size;

V_{FAM} = the volume of fine aggregates material (cm^3);

V_{sb} = volume of aggregate; and

V_{FA} = total volume fraction of fine aggregates;

In the calculation process the effect of effective asphalt binder content (V_{be}) on the overall value of volume of fine aggregate matrix (V_{FAM}) is very negligible; and therefore it can be eliminated from the equation for further simplification. The gradation and basic volumetric properties for these mixtures from Table 4-1 and Table 4-2 were simply used to calculate the $FAM_{T(Index)}$ for all the mixes. Figure 4-7 was plotted for $FAM_{T(Index)}$ versus the improved fatigue life (N_f) due to fibers defined by Equation (4-12).

$$\text{Improved } N_f \text{ due to Fiber (\%)} = \frac{N_{f(Fiber)} - N_{f(No Fiber)}}{N_{f(No Fiber)}} \times 100 \quad (4-12)$$

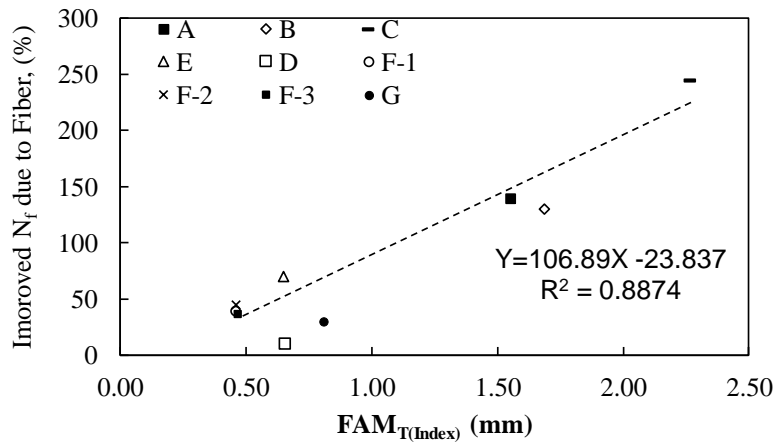


Figure 4-7. Comparison of $FAM_{T(Index)}$ with Enhanced N_f of Asphalt Mixtures Due to Fiber.

The results evidently suggest that there is a good correlation between the FAM thickness level and the degree of improvement due to fibers. This is an interesting discovery providing a powerful screening tool of fiber reinforcement efficiency in improving the fatigue life of asphalt mixtures. The concept of FAM and its role in performance improvement of fatigue life of asphalt mixture by fibers may be schematically explained from Figure 4-8 as follows.

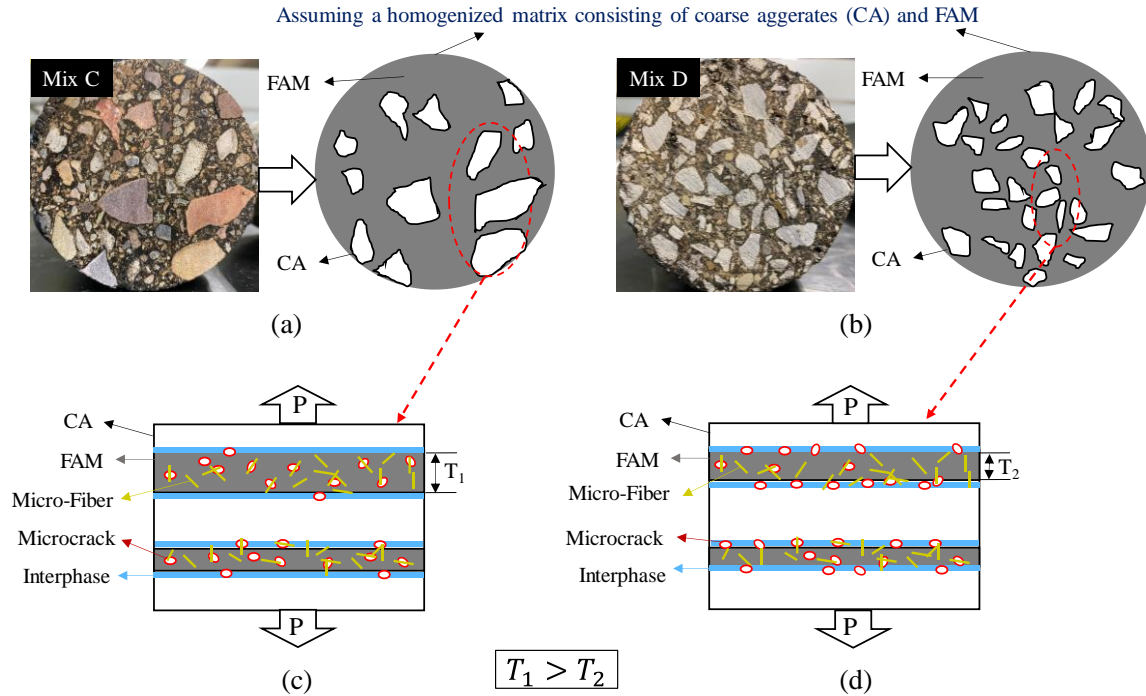


Figure 4-8. Schematic Representation of FAM Phase in M-FRAC.

First, asphalt concrete was assumed as a homogenized material consisting of FAM and coarse aggregates as well as the interface between FAM and coated coarse aggregate, as shown in Figure 4-8(a and b). As these three components of asphalt concrete subject to loading under tension, cracks should initiate and propagate through the weakest component which are either interface (hereby they are assumed as adhesion failure) and/or FAM phase (hereby they are assumed as cohesion failure). In the case of mix C representing a high FAM thickness asphalt concrete (Figure 4-8(a)), it was hypothesized that more larger number of microcracks are distributed within the FAM materials (Figure 4-8(c)). In contrast, for mix D with a low FAM thickness (Figure 4-8(b)), the distribution of microcracks might have happened to frequently occur within the interface as shown in Figure 4-8(d). This hypothesis was also observed on the surface failure of the fatigue

specimens in this study. As an example, the two cases of mixes C and D with high and low values of FAM thickness, respectively were selected and examined as shown in Figure 4-9.

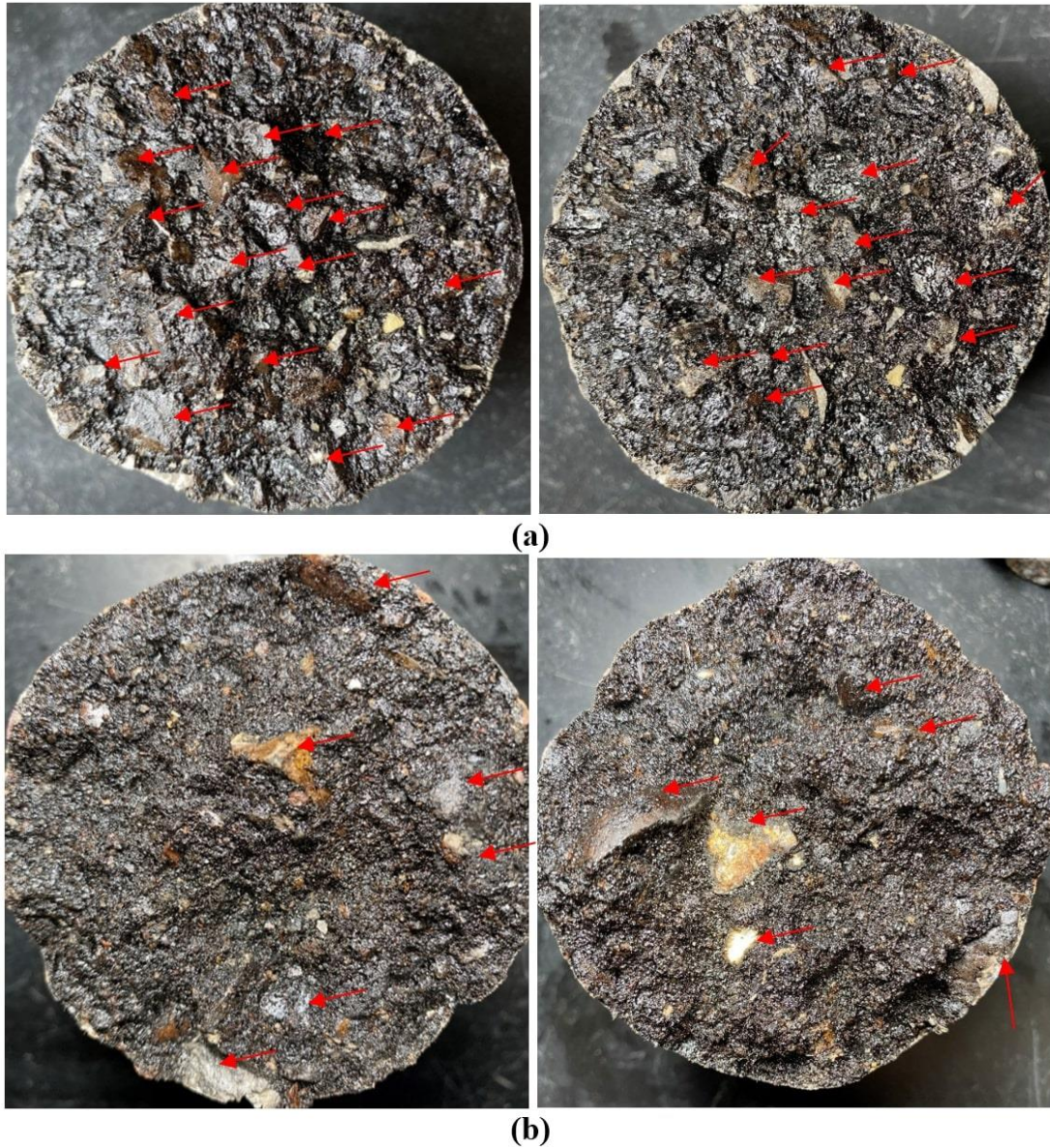


Figure 4-9. Surface Failure of Specimens After Fatigue Test for (a) Mix D and (b) Mix C.

It is evident that there are a greater number of exposed coarse aggregates (\geq No. 4) for mix D in the Figure 4-9(a) compared mix C in the Figure 4-9(b). The higher number of exposed coarse aggregate for mix D may suggest a greater number of adhesion failures

which exists in the interface between FAM and Coarse aggregates (Figure 4-9(a)). Whereas for Mix C in Figure 4-9(b), the failure seems to be a cohesion type of failure which here is defined failure within FAM. Given the diameter of aramid fibers ($=12 \mu\text{m}$), it is anticipated for aramid fibers to aid in bridging the cracks more effectively through the FAM phase rather than the interface between FAM and coarse aggregates. Therefore, with increasing the FAM thickness from one mix to another, it is likely that a greater number of random microcracks can be distributed through the FAM at which point fibers can get engaged and mobilized to transfer the load more efficiently. It is also important to note that the findings of this study and the effect of FAM thickness on the fiber efficiency in enhancing the fatigue life of asphalt mixtures can only be interpreted with respect to microcrack size effect because the failure in uniaxial fatigue test in this study is defined by localization which occurs when unstable microcracks are coalesced to form a macrocrack. Stated differently, this test does not characterize the propagation of macrocracks in asphalt mixtures.

4.4 Summary

One goal of this paper was to investigate the interaction of aramid fibers with the microstructure properties of asphalt mixtures. The following conclusions were reached in this study.

- Fiber mixing procedure in the laboratory poses a challenge in terms of obtaining highly dispersed aramid fibers compared with the mixing procedure in the field. In this study, a 3-layer system of fiber mixing procedure was used to improve the dispersion of fibers.

- A fiber extraction method was investigated and developed in this study to identify the state of aramid fibers in the asphalt mix.
- The dispersion of aramid fibers was affected by the *NMAS* of the asphalt mixture. Mixes with a higher *NMAS* overall yielded more effective dispersion of aramid fibers.
- The mechanical tests indicated that the poly-aramid fibers used in this study did not affect the dynamic modulus of asphalt mixtures. However, fibers improved the overall mechanical performance in fatigue and flow number of asphalt mixtures; and the degree of improvement were found to be different from one mix to another.
- A strong link was found between the compositions of asphalt mixtures and fiber reinforcement efficiency in mechanical performance.
- It was found that effective binder content and gradation play significant roles in reinforcement effectiveness of fiber in rutting and fatigue cracking, respectively. One of the most important findings of this study were that indices of V_{be} and FAM thickness were established as indicators of M-FRAC performance in rutting and fatigue cracking, respectively.

Finally, it is noted that this study findings were limited to the single fiber type, dosage and length; additional testing incorporating more performance evaluation of fibers interaction at different dosage and length with microstructure of asphalt concrete in cracking and rutting is warranted. What this study demonstrated is that understanding the interaction of M-FRAC with composition of asphalt mixtures can explain some of the driven factors and inconsistencies in the literature.

CHAPTER 5

MECHANISM OF MECHANICALLY-FIBER REINFORCED ASPHALT

CONCRETE IN TENSION

5.1 Introduction

One of the most common distresses in asphalt pavements is the cracking due to the low tensile strength. The nature and causes of several types of cracking can be attributed to thermal, fatigue, reflective, and block cracking. In each case, the asphalt concrete is subjected mostly to tension developed for different reasons. For example, thermal cracking occurs due to tensile stresses developed by non-uniform contraction of the asphalt layer at low temperatures, while block cracking occurs due to the tension developed due to aging and loss of volatiles in the asphalt binder (Kennedy 1983). Tensile strength of the mixture is one of the critical pavement design indicators for construction of durable and sustainable asphalt pavement. For example, Roque *et al.* (1999) investigated the use of the tensile strength to determine the fracture properties of asphalt mixtures. The cracking behavior of asphalt mixtures can also be characterized by their fracture response (i.e. toughness, fracture energy parameters). The use of reinforcing fibers is primarily known to its benefits in improved tensile strength of composite materials through bridging across micro-cracks to carry the tensile forces. Such mechanism may result in increasing the amount of strain energy that can be absorbed during the fatigue and fracture process of the mix (Abtahi *et al.* 2010).

Previous work generally reported reassuring benefits of various fiber types in enhancing the cracking resistance and tensile properties of asphalt concrete. However, laboratory findings about the performance benefits of fibers in cracking for AC have been

inconsistent. While in some studies fibers enhanced cracking resistance of AC but to different degrees, there have been cases that fibers did not indicate any improvement in the fracture or tensile properties. These studies were reviewed in Chapter 2. The inconsistency in the results are based on using various parameters including fiber type, fiber dimension (length and diameter), test type and test temperature/ loading rate, and mix type. The Objectives of this chapter is to:

- study the effect of temperature and loading rate on the tensile property of M-FRAC
- evaluate the mechanical behavior of M-FRAC in tension using different tests.
- evaluate the cracking resistance of M-FRAC with respect to different mix design types, fiber dosage, and fiber length.

5.2 Materials

Earlier in Chapter 5 of this study, a strong link was found between the compositions of asphalt mixtures and fiber reinforcement efficiency in mechanical performance. It was found that the gradation plays a substantial role in reinforcement effectiveness of fiber in fatigue cracking. In particular, an index of Fine Aggregate Matrix/Mixture thickness ($FAM_{T(Index)}$) was established as an indicator of M-FRAC efficiency performance in fatigue cracking. Therefore, to study the interaction of fibers reinforcement with the tensile and fracture properties of AC, mixes C, D and F-2 were selected for this study; each representing a mixture with high, low, and low FAM thickness, respectively (refer to Chapter 4 for more details).

5.3 Test Methods

In total, three different mechanical experiments were conducted to study the cracking resistance of M-FRAC including uniaxial cyclic fatigue test, monotonic direct tension (DT) test and Semi-Circular Bending (SCB) test. The test procedure and test parameters for uniaxial fatigue test is similar to the one described in CHAPTER 3 and more details can be found in APPENDIX A. All testing specimens were obtained from Superpave gyratory compactor (SGC) cylindrical samples compacted to a geometry of 150 mm in diameter and 180 mm in height. The target air void level for all test specimens was $6.5 \pm 0.5\%$ and all the specimens were kept in the chamber for four hours prior to the test. A three later system of fiber mixing procedure was selected explained in detail in CHAPTER 4.

5.3.1 Direct Tension Test

Tensile behavior of asphalt concrete mixtures is typically examined using the indirect test methods such as splitting tensile test and flexural test. Tension stresses are created at the center part of the cylindrical specimen by the compression load causing the specimen to fracture. Perhaps the most popular standardized test method is the indirect tensile test (IDT) used to study the cracking behavior of asphalt concrete specifically at low temp (AASHTO T322) due to its relatively easy procedure such as sample preparation and set up. However, such tests may not accurately capture the tensile response of asphalt mixes because the specimen is subjected to a complex stress state including tension, compression, shear, and significant stress gradients (Li 1998). In IDT test, the disturbance of the tensile stress field in indirect test methods (i.e. IDT) is more of a concern for testing

temperature above 0°C since the effect of compressive load on specimens during testing is even more significant (Qian *et al.* 2014).

To study tensile strength, toughness and energy absorption capability of FRAC, direct uniaxial tensile test method has been recommended as an ideal test with the most authentic results (Li 1998). Direct tension test has been previously used in some studies to evaluate the tensile properties of asphalt concrete. These studies used different geometries such as dog-bone geometry (Erkens 2004), cylindrical shape similar to uniaxial fatigue test (SHRP-A-641), and rectangular shape (Yoo and Al-Qadi 2014). However, such test configurations still present challenges such as eccentricity as a result of test misalignment in the case of cylindrical specimens leading to end failure, formation of bending stresses and high variability in the results (SHRP-A-641), the lack of realistic specimen dimension (i.e. dog-bone geometry) not large enough to represent 3-dimensional random fiber orientation (Erkens 2004, Apostolidis *et al.* 2016, 2019), complexity of sample preparation and set up as well as absence of a controlled environment chamber (Yoo and Al-Qadi 2014).

In this study, a direct monotonic uniaxial tensile test was performed on a circumferentially notched cylindrical specimens to study the tensile and fracture properties of asphalt concrete with and without fibers. The experimental test configuration developed in this study is similar to the one documented in SHRP-A-641 with the exception that there is a circular notch in the center of cylindrical specimens in this work. The most prominent advantage of cylindrical specimens with circular cracks is their ability to assure the plane strain state under tensile load because the circumferential crack has no end in the plane stress region (Stark and Ibrahim 1986). However, the state of stress would not be

necessarily uniform in a notched specimen, especially at the tip of notch. The sample preparation and system set up are explained in the following section.

5.3.1.1 Sample Preparation

Two different test specimen geometries were used in this test. For mix C, a core of 75 mm× 140 mm (d × h) specimen was obtained from a gyratory compacted plug. For mixes D and F-2 with the NMAS of 9.5 mm, since the ratio of maximum particle size to the diameter of testing specimens was just above 5, smaller sized specimens at the geometry of 50 × 100 mm (d × h) were used as shown in Figure 5-1. When the testing specimen geometry was reduced to 50 × 100 mm (d × h), it was possible to extract three vertically cored specimens from one gyratory compacted plug. This would significantly increase the productivity of the work. A preliminary study of the effect of samples geometry on the stress strain response also indicated that there is no significant difference between samples of mix D and F-2 tested at 75 mm× 140 mm (d × h) and 50 × 100 mm (d × h).

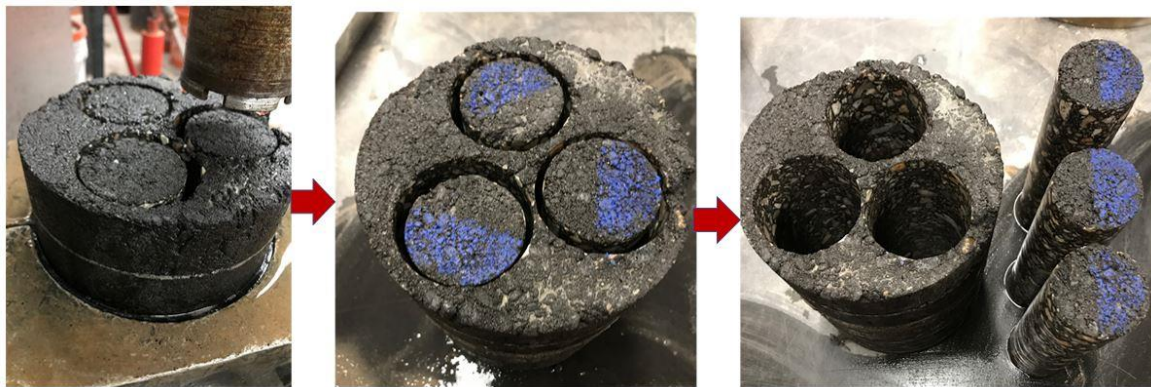


Figure 5-1. Close-up Image of the Vertically Cored Specimens (the Part of Specimens Near the Edge Was Painted with Blue Color for Air Void Distribution Study).

Additionally, since the vertically cored specimens shown in Figure 5-1 were taken from near the edge of gyratory compacted plugs which normally has a higher air void content than the core, a separate study was devised to evaluate the variability of air void distribution in the small sized specimens. As expected, a higher air void distribution at the edge of small sized specimen was observed compared with core, however, the difference was less than 10%. After the samples were cored and cut to the target geometry, a circular notch was placed in the middle of the specimens with width of 2 mm. For 75 mm \times 145 mm ($d \times h$) and 50 mm \times 100 mm ($d \times h$) specimens, the smaller diameters (d) of the specimens were 61 and 43 mm. The configuration of the large size specimen is schematically illustrated in Figure 5-2.

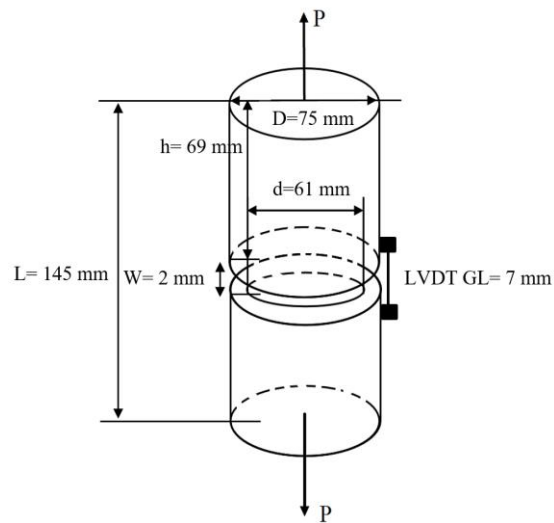


Figure 5-2. Cylindrical Asphalt Concrete Specimen with a Symmetric External Annular Crack Subjected to Applied Tensile Load.

5.3.1.2 Experimental Set-up

The samples in this study were subjected to static tension loading and so all specimens were glued to end platens before testing. The instrumentation and testing

machine were similar to uniaxial fatigue test. Specialized gluing jigs that ensured proper vertical alignment were built and gluing was performed using Devcon 5-min epoxy. Brass buttons were glued onto the sample surface 90° apart. The specimens were then instrumented with four axial linear variable displacement transducers (LVDTs) to monitor the on-specimen deformation. The gauge length (GL) of LVDTs was 7 mm placed right next to the circular notch. The experiment was carried out under a monotonic load system using servo hydraulic testing machine (UTM-25) in a temperature-controlled environment as shown in Figure 5-3. Direct tension test was performed on average of 2-3 replicates and 3-4 replicates for 75 mm × 145 mm (d × h) and 50 mm × 100 mm (d × h) specimens, respectively per mix condition and depending on the data variability.

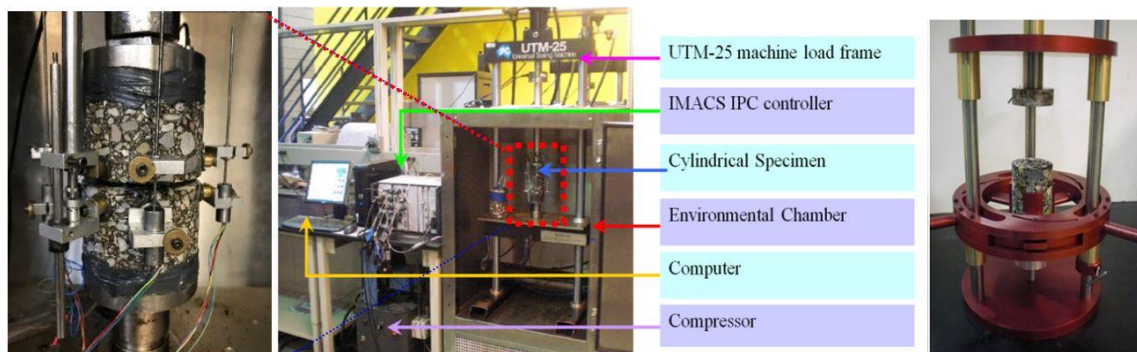


Figure 5-3. Direct Tension Test Setup and Gluing Jig.

5.3.1.3 Data Quality of Monotonic Uniaxial Direct Tensile Test

Direct tensile testing for asphalt concrete is not specified in standards or recommended practices and is typically conducted only in research. This is because the validity of test results is challenged for essentially two practical reasons. First, the sample preparation for direct tension test requires a careful alignment which otherwise lead to end failure or high variability of test results due to eccentricity. No end failure was found in

this study because of the presence of notch in the middle of the specimens, which practically help reduce the variability of displacement data. Another advantage of having a notch was acquiring displacement measurements from LVDTs right across the failure plane around the crack opening which further lowered the data variability. The second challenge with data validity was to perform the test under constant loading rate to obtain a reliable stress strain curve, which requires a closed-loop controlled testing arrangement for the tensile test. These two underlined issues were further analyzed from LVDT measured data and are discussed in the following sections.

5.3.1.3.1 Displacement Behavior

In presenting displacement data, average of four LVDTs are reported. Figure 5-4 shows the typical deformations measured by the four LVDTs as functions of time for the two replicates of mix D at the same testing condition. All of the measured displacement curves from individual LVDTs for each replicate developed upward orientation (more or less). The slope of all the LVDTs for both replicates are consistent until the peak load at around 30 seconds and after that they start to deviate from each other in the post-peak region. The variability of deformation behavior from individual LVDTs in the post-peak region was more pronounced for replicate 2 (Figure 5-4(b)) compared with replicate 1 (Figure 5-4(a)). The change of slope for replicate 2 implies that the portion of the specimen covered by the corresponding LVDT experienced compression instead of tension due to crack propagation (Figure 5-4(b)). In contrast, the typical steady development of deformations for cases like replicate 1 (Figure 5-4(a)) infers that strain localization is suppressed, and more transverse cracks occurred.

Figure 5-5 further represents the optical observation of the typical failure pattern of specimen after that test completion. A non-uniform failure pattern around the notched area is evident which is possibly resulted from amplification of unevenly stress concentration around the notched region especially in the post-peak region. This was expected given that misalignment (minor in this study) during the sample preparation was inevitable. Nevertheless, averaging the four LVDTs appeared to effectively minimize the variability of individual LVDTs. Comparison between the average of four LVDTs from replicates 1 and 2 demonstrated a very good consistency in the deformation behavior as shown in Figure 5-6.

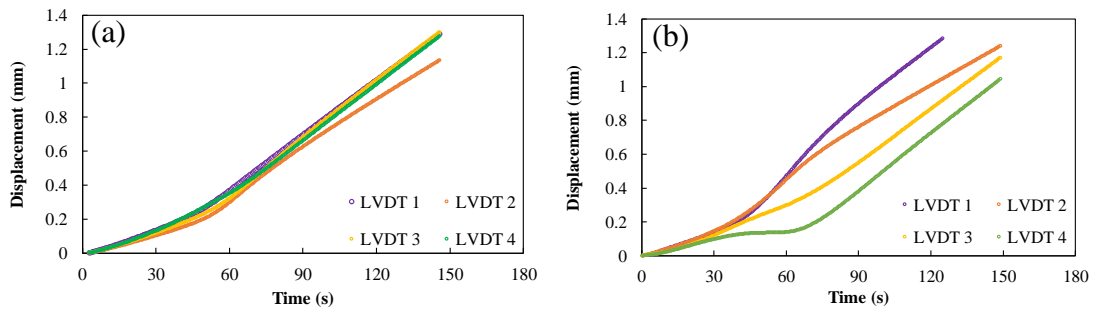


Figure 5-4. Typical Deformation Behavior under Tensile Load for (a) Replicate 1 and (b) Replicate 2 of Mix D at 20°C and 0.6 mm/min.



Figure 5-5. Photo of Sample Failure and Crack Plane Under Direct Tension Test.

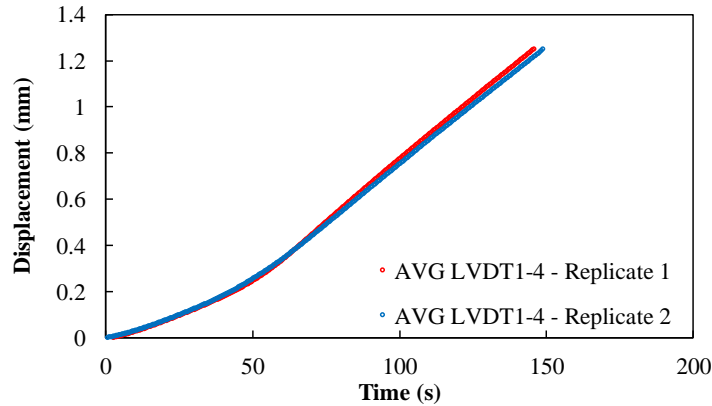


Figure 5-6. Comparison of Average of Four LVDTs for Each Replicate.

5.3.1.3.2 Analysis of Displacement Rate on Specimen

Figure 5-7 shows typical stress displacement curves of no fiber and fiber specimens for the cases of mix C at 10°C and 0.6 mm/min and at 20°C and 11 mm/min, respectively. The fiber length and dosage level were 19 m and 0.15%, respectively. While an improvement in the maximum tensile stress of fiber specimens over no fiber sample is evident for the cases of mix C, the post-peak response overall indicated the an increased in the slope of the descending curve, implying the reduced performance of specimens with fiber. To further elaborate this, the actual displacement rate on fiber and no fiber specimens were analyzed using measured data from the average of four LVDTs on specimens shown in Figure 5-7.

Two key patterns were observed from the analysis of displacement rate on specimens. First, it can be seen that the displacement rate on specimens continuously increases along with increasing the displacement. For all tests, it was observed that the on-specimen LVDT displacement rate followed a power law in time (up to the peak load/stress point). For example, Figure 5-7(a) represents the case of mix C at 10°C and 0.6 mm/min

but the displacement rate on specimens until the peak load/stress was 0.35 mm/min fitting a power law function for both fiber and no fiber samples. Second, it was observed that the displacement rate on fiber and no fiber specimens for the cases of mix C started to deviate after the peak load/stress point (Figure 5-7(a, b)). While the displacement rate for no fiber specimens increased by a factor of 2 after the peak stress, the sharp increase in the rate for fiber specimens of mix C was in the range of 8-10 times using a power law function. This pattern was always observed for the mixes C with fiber regardless of the testing temperature and loading rate; however, the effect was more pronounced at high loading rates and lower temperatures.

These findings were attributed to nonconstant loading rate on direct tensile test specimens. As mentioned earlier, monotonic uniaxial direct tension test was performed using servo a hydraulic testing machine (UTM-25), however, the monotonic test is not programmed to operate in closed-loop controlled testing arrangement whose function is to minimize or remove the release of strain energy from the testing system, so that a stable descending portion can be obtained from test specimens in tension. In a closed-loop controlled system, an input function such as the on-specimen displacement measured by LVDT(s) is fed back to the controller and compared with the reference input signal. The difference between two signals are minimized by an adjusting amplifier. The feedback signal is a key to maintain stability of the system. Since the displacement rate can well match the predetermined actuator loading rate, any tendency of sudden specimen failure or energy release during the softening regime will be avoided (Li 1998).

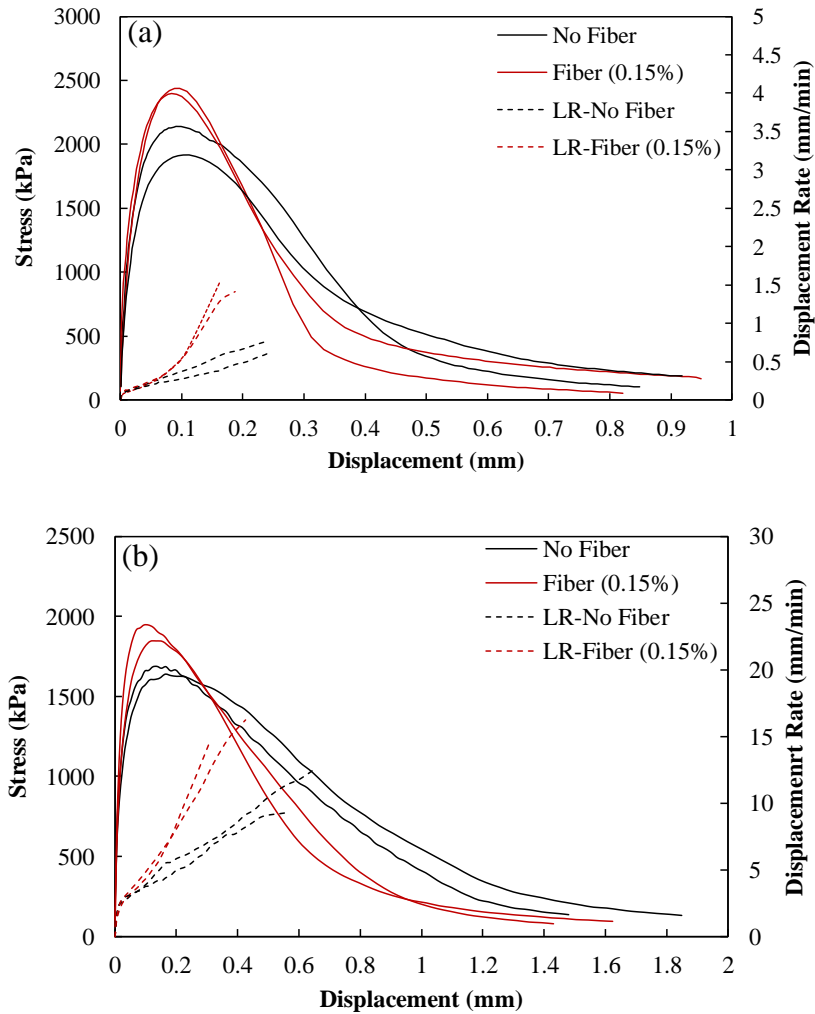


Figure 5-7. Analysis of Loading Rate in Mix C Specimens (a) at 10°C and 0.6 mm/min and (b) 20°C and 11 mm/min.

5.3.2 Semi-circular Bending Test

Semi-circular bending (SCB) test was selected to further study the fracture properties of M-FRAC based on advantages that it offers over conventional cracking test methods such as IDT and even the direct tension test developed in this study. The SCB test protocol developed at the University of Illinois (IL-SCB) was performed in this study in a

closed-loop computer-controlled fracture test setting, which allows a constant strain rate on specimens.

5.3.2.1 Sample Preparation

Two 50-mm thick slices were obtained from the center part of SGC cylindrical samples and the top and bottom plates were discarded as they are known to exhibit different mix distributions (Doll *et al.* 2017). Each of the two middle slices were cut perpendicular to the thickness into two equal semicircular halves, and a vertical edge notch was made with a saw in the middle of the semi-circle specimen. Therefore, a total of four SCB specimens were obtained from one SGC cylindrical sample as shown in Figure 5-8. The final geometry of a SCB specimen tested had a diameter of 150 mm, thickness of 50 mm, notch length of 15 mm and notch width about 2 mm (the width of the saw).

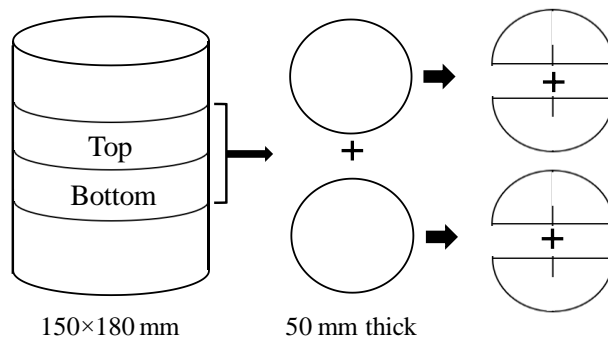


Figure 5-8. Schematic of SCB Sample Preparation.

5.3.2.2 Experimental Set-up

The SCB test set is schematically illustrated in Figure 5-9. As can be seen the specimen is supported symmetrically at the bottom and loaded at the top. SCB specimen is supported by two rollers used to minimize the friction in the contact area at the bottom of

specimen. For all experiments, the spacing between the two supports was 120 mm. The asphalt mixtures were tested 10°C using an ITS Interlaken load frame system, equipped with an environmental chamber to carry out experiments at the target temperature. The experiment was conducted based on a displacement controlled using a crack mouth opening displacement (CMOD) signal to provide a constant displacement rate on specimens. An extensometer mounted on the bottom of SCB specimen by means of two metal buttons glued on the specimen is used to measure CMOD. The range of the two extensometers is from -1 mm to 1 mm.

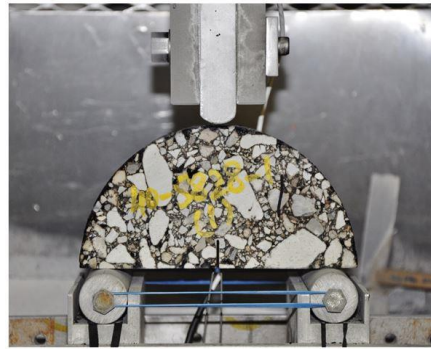


Figure 5-9. SCB Test Fixture.

5.3.3 Design of Experiment

To understand the mechanism of synthetic fiber reinforcement efficacy in enhancing the AC cracking resistance, the synergic effect of multiple parameters on the mechanical response of laboratory tests were considered. These included the mix type (C, D, F-2), fiber length (10, 19, 38 mm), fiber content (0.05, 0.15, 0.25), test temp (10 and 20°C), loading rate (0.1, 0.6, 0.9, 1.5, 11), and test type (Uniaxial Fatigue, DT, and SCB). Conducting a full factorial test was not really possible due to time and resources limits; therefore, a partial factorial design of experiment was conducted to study the mentioned tasks (objectives) of this study. Table 5-1 exhibits the experimental design of mechanical

testing in this study. It should be noted that for DT experiment, initially 3 temperatures (0, 10 and 20°C) were considered. However, the AC specimens showed brittle behavior by failing at the peak load at 0°C. Therefore, DT test was performed only at 10 and 20°C. Note that the interpretation of M-FRAC response at 0°C could be still projected using the time-temperature superposition principle provided that it holds true for M-FRAC.

Table 5-1. Design of Engineering Experiment for the Effect of Multiple Variables on the Mechanical Response of M-FRAC Mixtures.

Mix Type	Fiber Properties		Sample ID	Temperature (°C)								Frequency (HZ)
				10				25			18	
	Length, mm	Content, %		Actuator Loading Rate (mm/min)							10	
				0.1	0.6	0.9	1.5	0.6	1.5	11		
C	0	0	C-0	DT	DT, SCB	DT	DT	DT	DT	DT	DT	Uniaxial Fatigue
	10	0.05	C-10-0.05								DT	
		0.15	C-10-0.15		DT, SCB							
	19	0.05	C-19-0.05	DT	DT, SCB	DT					DT	Uniaxial Fatigue
		0.15	C-19-0.15	DT	DT, SCB	DT			DT	DT	DT	
		0.25	C-19-0.25	DT	DT	DT	DT	DT	DT	DT	DT	
	38	0.05	C-38-0.05								DT	
		0.15	C-38-0.15		DT							
D	0	0	D-0		DT, SCB				DT			Uniaxial Fatigue
	10	0.15	D-10-0.15		DT, SCB							
	19	0.05	D-19-0.05		DT				DT			Uniaxial Fatigue
		0.15	D-19-0.15		DT, SCB				DT			
F-2	0	0	F2-0		DT					DT		Uniaxial Fatigue
	10	0.05	F2-10-0.05							DT		Uniaxial Fatigue
		0.15	F2-10-0.15		DT							
	19	0.05	F2-19-0.05							DT		Uniaxial Fatigue
		0.15	F2-19-0.15		DT					DT		
	38	0.05	F2-38-0.05									Uniaxial Fatigue

5.4 Results

5.4.1 State of Dispersed Aramid Fibers with Different Lengths and Dosages

Fiber extraction was performed to compare the dispersion level of individual fiber states (*FDP*) for the mixes C and D specimens with different fiber length and dosage level. Extraction was carried out on the tested specimens each having a mass of roughly 1500 grams. Table 5-2 presents the extraction results in terms of fiber states (*FDP*, agitated bundles and clusters). The Coefficient of Variation (*CV*) of dosage rate and *FDP* state of recovered aramids from extraction were within approximately 5-10% of one another. Also, the recovered dosage rate of aramid fibers was within 5-20% of the target rates for all the mixes. The results show that increasing dosage of fiber does not change the *FDP* level, but it appears that increasing fiber length reduced the fiber dispersion level. For mix F2, the *FDP* values for 10, 19, and 38 mm fiber is 59%, 50%, and 33%, respectively. This is expected given the difficulty in agitating the fiber in the mix as the length increase.

Table 5-2. Relative Percentages of the Different Fiber Dispersion Categories by Weight After Extraction for Mixes C and F2 with Various Fiber Length and Dosage.

Specimen ID	State of Aramid (%)		
	<i>Agitated Bundle</i>	<i>Cluster</i>	<i>FDP (%CV)</i>
C-19-0.05	10	24	66 (12)
C-19-0.15	13	19	68 (11)
C-19-0.25	9	21	70 (7)
C-10-0.15	10	12	78 (7)
C-38-0.15	22	12	56 (16)
F2-10-0.05	22	19	59 (12)
F2-19-0.05	26	24	50 (6)
F2-38-0.05	47	20	33 (15)

5.4.2 Fatigue Life of M-FRAC

The uniaxial fatigue test results are analyzed using the simplified viscoelastic continuum damage (S-VECD) approach to characterizing the fatigue behavior (For analysis approach refer to APPENDIX A). Figure 5-10 shows fatigue life (N_f) of no fiber and fiber specimens of mixes C, D, and F-2 simulated at 300 μ s. The content and length of fibers were 0.05% and 19 mm, respectively for all the mixes. The effectiveness of fiber is evident in mix C compared with mixes D and F-1, which was attributed to the FAM thickness parameter articulated in CHAPTER 4. Moreover, the effect of different fiber length on the fatigue performance of mix F2 was further studied as shown in Figure 5-10. The results suggest that longer fibers (19 and 38 mm) equally performed better in sustaining damage before failure compared with shorter fibers (10 mm) and no fiber cases. It should also be noted that although the target fiber dosage remained to be the same, their dispersion level was different as shown in Table 2. If the number of individual fibers between 19- and 38-mm fiber specimens were similar in the mix, it is speculated that 38 mm fiber would even show higher fatigue life compared with 19 mm fibers.

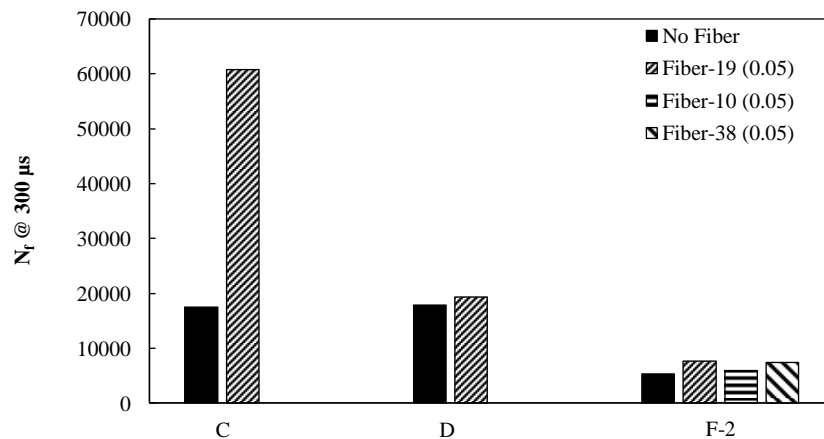


Figure 5-10 . N_f of Mixes C, D, and F-2 for No Fiber and Fiber Specimens at 300 μ s.

5.4.3 Tensile capacity of M-FRAC

In this study, the maximum tensile stress values from DT tests were used as indicative measures of approximated AC and M-FRAC tensile strengths. A relatively good repeatability and reproducibility of maximum tensile stress values were obtained from both DT tests with STDV ranging between 5-10% in the peak stress. The tensile stress of the notched DT (σ_{DT}) specimens was calculated according to Equation (4-12).

$$\sigma_{DT} = \frac{P}{\pi r^2} \times 10^6 \quad (4-12)$$

Where; P is the axial peak load (kN) and r is smaller radius of the DT specimen (mm). In the following sections, the tensile stresses of M-FRAC and AC with respect to temperature/loading rate and properties of fiber (length and dosage) are discussed.

5.4.3.1 Effect of Loading Rate and Temperature

In this section the effect of various loading rates and two temperatures on the tensile stress of asphalt concrete with and without fibers are studied through the application of time-temperature superposition principle. This was done through development of a mastercurve of strength as a function of reduced strain rate at a desired reference temperature (20°C) using the maximum stress values from the direct tension experiment.

5.4.3.1.1 Development of Strength Mastercurves for M-FRAC Using Superposition

Previous research has shown that asphalt concrete is a thermorheologically simple material in linear viscoelastic (LVE) state (Goodrich 1991). This means that by applying a time-temperature superposition to the undamaged states of asphalt concrete, a single

parameter, reduced time/frequency, is produced to combine the effects of time and temperature to create material mastercurves for fundamental material properties. These mastercurves can then be used along with the time-temperature shift factor to determine the material response under any combination of temperature and time/frequency. Chehab et al. (2002) proved that this same concept can be used under tension test setting beyond the LVE limits to highly damaged levels. It was shown that material performance at a certain temperature and input history can be matched at a different temperature by selecting an input history such that the reduced history is equal. One of the most significant implications of such technique is reduction of the required laboratory testing program and test condition for comprehensive material characterization of asphalt mixtures (Chehab *et al.* 2002). In this study, σ_{DT} mastercurves as function of log reduced strain rate were constructed using the time-temperature superposition principle. While the details of this approach can be found in (Chehab *et al.* 2002), a summary of procedure is described as follows.

First, the actual displacement rate on-specimen for each temperature loading rate combination was determined using a power law in time function. The function was fit to the displacement-time (average of four LVDTs) curve up to the peak load. Next, reduced strain rate was calculated according to Equation (4-13) and summarized in Table 5-3. Note that the shift factor and the fitting coefficient were obtained from the dynamic modulus test data for mix C discussed earlier in CHAPTER 4.

$$k' = k a_T \quad (4-13)$$

$$a_T = 10^{\alpha_1(T^2 - T_{ref}^2) + \alpha_2(T - T_{ref})} \quad (4-14)$$

Where;

- k' = the reduced strain rate;
- k = the strain rate on-specimen;
- a_T = the time-temperature shift factor at a given temperature;
- T = the temperature (°C or °F);
- T_{ref} = the reference temperature (°C or °F); and
- α_1, α_2 = the fitting coefficients.

Table 5-3. Data Summary of Stress-Log Reduced Strain Rate Mastercurves for No Fiber Case.

Test Temp (°C)	Actuator Loading Rate (mm/min)	Displacement Rate on Specimen (mm/min)	Strain Rate on Specimen per second	k'	$\sigma_{DT(No\ Fiber)}$ (kPa)
10	0.1	0.03	0.00009	0.010	1232
	0.60	0.35	0.001	0.142	2045
	0.9	0.65	0.002	0.259	2465
	1.5	1.04	0.0035	0.418	3045
20	0.6	0.24	0.0008	0.001	719
	1.5	0.60	0.002	0.0020	890
	11	14	0.05	0.047	1648

Figure 5-11 shows how the application of time temperature superposition principle can shift the data of stress strain rate (Figure 5-11(a)) to construct the mastercurve of stress reduced strain rate for no fiber case (Figure 5-11(b)). The combination of temperatures and loading rates were selected to represent a large range of σ_{DT} values of asphalt concrete mixtures. The lowest σ_{DT} value was around 720 kPa which may represent the tensile strength of asphalt concrete at relatively a high temperature condition. While the highest σ_{DT} was recorded at 3000 kPa at which asphalt concrete showed a brittle failure representative of a strength of low temperature asphalt concrete.

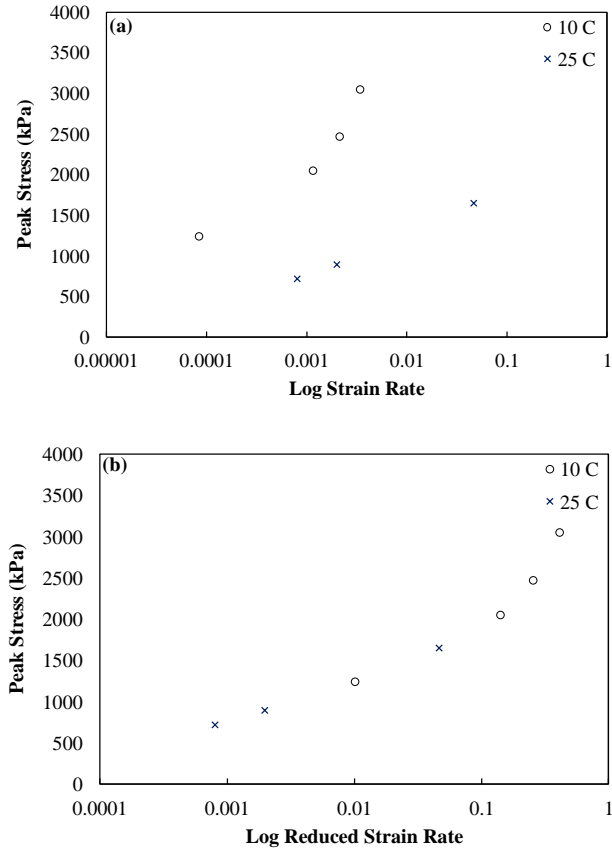


Figure 5-11. Example of Time-Temperature Superposition Application to Shift (a) Maximum Stress-Log Strain Rate Data to (b) Construct Maximum Stress Mastercurves as a Function of Reduced Strain Rate for the No Fiber Case.

The same procedure was used to develop mastercurves for the case of fiber specimens of mix C at two different dosage levels (0.15% and 0.25%) and 19 mm length, as shown in Figure 5-12. Following observations were made from the figure.

- At slowest strain rate and 20°C, fibers showed slight improvement in the tensile stress of asphalt concrete mixtures. At very low loading rate, the viscoelastic effect of asphalt is high and therefore the efficiency of load transfer between fiber and matrix is hampered by the viscos effect of asphalt (Park *et al.* 2017).

- At higher strain rate, the benefit of fibers emerged. At reduced strain rate between 0.002-0.05 (or the maximum stress of no fiber between 1000 and 1600 kPa), fibers improved σ_{DT} of asphalt concrete by about 15-20% for both 0.15% and 0.25% of fibers. Thus, higher fiber content did not necessarily further enhance the σ_{DT} of specimens particularly at 20°C.
- At lower testing temperature (10°C), increasing fiber dosage evidently benefited the performance in the pre-peak region of stress displacement curves of asphalt concrete. For example, at reduced strain rate of 0.14 where the $\sigma_{DT(No\ Fiber)}$ was 2045 kPa, 0.25% of fiber increased σ_{DT} by about 35% while the improvement for the mix with 0.15% fiber was only 15% over no fiber specimens. At highest strain rate, 0.15% and 0.25 fibers did not show notable increase in the maximum tensile stress of asphalt concrete. Perhaps, a higher fiber dosage was needed.

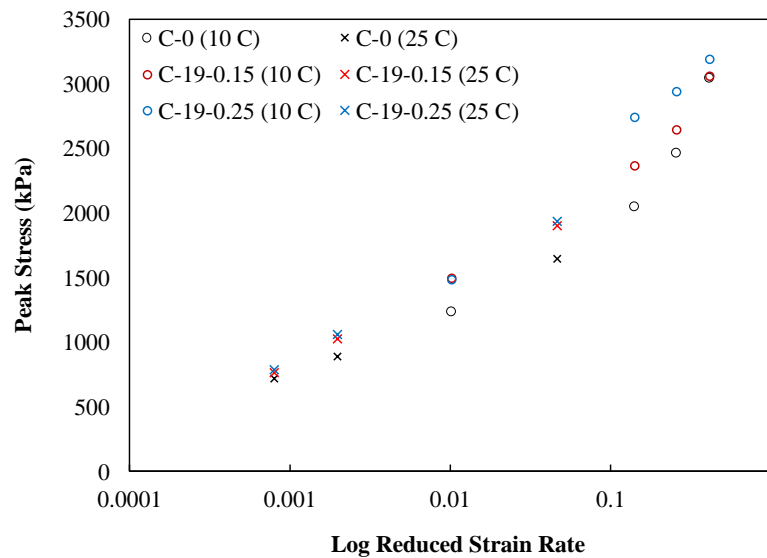


Figure 5-12. Stress-log Reduced Strain Rate Mastercurve for No fiber and Fibers Specimens of mix C and 19 mm fiber.

5.4.4 Evaluation of Fracture Energy and Toughness of M-FRAC

Fracture parameters were calculated using the load-displacement curves of SCB and DT specimens to further characterize the effect of fiber properties, mix type, and test type on the cracking resistance of M-FRAC compared with AC. For DT, specimens tested at 10°C and strain rate of 0.001 per s and 20°C and strain rate of 0.05 per s (Table 5-3) were selected for analysis of fracture parameters.

5.4.4.1 Effect of Fiber Properties and Mix Type

The effects of fiber length, dosage, mix type, and test type were studied using fracture toughness and energy parameters. Given the benefits of fiber found in the previous sections, the DT test were performed at 20°C for mixes C, D, and F-2 at different strain rates of 0.05, 0.0015, 0.006, respectively. These strain rates were selected to achieve $\sigma_{DT(No\ Fiber)}$ in the range of 1000 to 1700 kPa. At 10°C, the test was only performed at equal strain rate of about 0.001 per second for all the mixes (Figure 14b). Also, the effect of fiber length on fracture parameters was considered for mixes C at both 20°C and 10°C and mix D at 10°C using both DT and SCB tests.

5.4.4.1.1 Fracture Toughness

Fracture toughness is an intrinsic property of the material, which helps explain the material's resistance against fracture and is obtained from the measurement of stress intensity factor defined as the state of stress near the crack tip (Saha and Biligiri 2016). The fracture toughness can be correlated to the rate of crack growth, particularly the crack propagation (Anderson 2017). For both DT and SCB geometry, stress intensity factor in

mode I (K_{Ic}) was determined in linear elastic fracture mechanics (LEFM). In this study, it is assumed that there was a small scale yielding where all substantial non-linearity is confined within a linear-elastic field surrounding the crack tip. Also, K_I is a function of geometric factor of the specimen and loading conditions (Anderson 2017). It increases with increasing applied stress and reaches a critical value (K_{Ic}) when failure occurs, which is assumed to be at the peak load in this study (Saha and Biligiri 2016).

The K_{Ic} parameter in the LEFM for SCB specimens was calculated from Equation (4-16) developed by several studies. Equation (4-15) for the Y factor was specifically developed for SCB test specimen by (Lim *et al.* 1993) and verified through finite element analysis in another study (Li and Marasteanu 2004) .

$$K_{Ic} = Y_{I(0.8)}\sigma_{max}\sqrt{\pi a} \quad (4-16)$$

$$Y_{I(0.8)} = 4.782 + 1.219\left(\frac{a}{r}\right) + 0.063\exp\left(7.045\left(\frac{a}{r}\right)\right) \quad (4-17)$$

$$\sigma_{max} = \frac{P_{max}}{2rt} \times 10^{-3} \quad (4-18)$$

Where;

$K_{Ic(SCB)}$ = critical stress intensity factor ($MPa\sqrt{m}$) obtained from SCB test,

P_{max} = maximum applied load (KN),

r = Specimen radius (m),

t = Specimen thickness (m),

a = notch length (m) which was measured as 14 ± 0.5 , and

$Y_{I(0.8)}$ = dimensionless normalized stress intensity factor when span ratio $s/r = 0.8$.

In reviewing literatures, no study was found with regards to evaluating the fracture toughness of cylindrical asphalt concrete specimens having circular notch under tensile load. Additionally, no attempt was done in this study to investigate rigorous solutions involving finite element analyses as it was out of scope of this study. The development required extensive laboratory testing (i.e. different notch dimensions, geometry, ...) for validation. Alternatively, closed form solutions of critical stress intensity factor for a circumferential crack emanating from a notch in a round tensile bar was available in other studies. The approximation method of evaluating K_{Ic} for an external circumferential crack in a thick-walled cylinder presented by (Tada *et al.* 2000) was used in this study given by Equation (4-19).

$$K_{Ic} = X\sigma_{max}\sqrt{\pi r} \quad (4-20)$$

$$X = 0.5 \left(1 - \frac{r}{R}\right)^{1/2} \left(1 + 0.5 \left(\frac{r}{R}\right) + 0.375 \left(\frac{r}{R}\right)^2 - 0.363 \left(\frac{r}{R}\right)^3 + 0.731 \left(\frac{r}{R}\right)^4\right) \quad (4-21)$$

$$\sigma_{max} = \frac{P_{max}}{\pi r^2} \times 10^{-3} \quad (4-22)$$

Where;

$K_{Ic(DT)}$ = critical stress intensity factor ($MPa\sqrt{m}$) obtained from DT test,

p_{max} = maximum applied load (KN),

r = radius of circular net ligament (m),

R = Specimen radius (m), and

X = dimensionless configuration correction factor for stress intensity factor

shows the measured fracture of fiber and no fiber DT specimens 20°C for different mix types and fiber length and dosage. Critical stress intensity factor, $K_{Ic(DT)}$ increased by about 15% with presence of fibers for mix C at 20°C but no difference was found between

the $K_{Ic(DT)}$ of fiber and no fiber specimens of mixes F-2 and D. Comparing mixtures C-19-0.05, C-19-0.05, and C-19-0.05, it is evident that increasing fiber content from 0.05% to 0.25% did not further increase in $K_{Ic(DT)}$. Also, no significant difference in the $K_{Ic(DT)}$ values was observed comparing different length of fibers at 20°C.

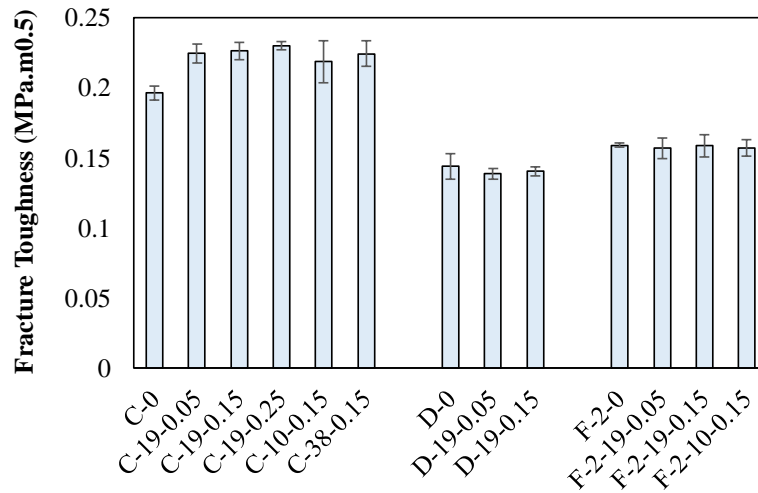


Figure 5-13. Fracture Toughness of DT Asphalt Concrete Specimens with and without Fibers for Different Mix Types and Fiber Length and Dosage at 20°C.

Figure 5-14 presents the calculated critical stress intensity factor from both DT and SCB tests ($K_{Ic(DT)}$ and $K_{Ic(SCB)}$) at testing temperature of 10°C and strain rate of 0.0012 per second for different mix types and fiber length and dosage. The measured K_{Ic} for the no fiber SCB and DT specimens (C-0) are around 0.45 and 0.25 $MPa\sqrt{m}$, respectively. $K_{Ic(SCB)}$ is consistent with values of fracture toughness obtained previously for asphalt concrete in the range of 0.5-1.5 $MPa\sqrt{m}$ (Kim and El Hussein 1997, Marasteanu *et al.* 2002). The lower values obtained in this study is however due to the higher testing temperature (10°C) compared with the mentioned studies.

Figure 5-14(a) shows no significant difference in the fracture toughness between C-0 and C-19-0.05 for DT specimens, while the use of 0.05% fiber increased the fracture toughness of SCB asphalt concrete specimens by 10% (Figure 5-14(b)). At higher dosage level for mix C, the fracture toughness of asphalt concrete further increased. C-19-0.15 specimens from SCB and DT test increased the $K_{Ic(DT)}$ and $K_{Ic(SCB)}$ by 15% and 20%, respectively. Also, 0.25% fiber case (C-19-0.25) improved the $K_{Ic(DT)}$ by almost 35%.

Comparing the different fiber length in the mix C, 10- and 19-mm fibers showed similar $K_{Ic(DT)}$ values with 15% increase in toughness while 38 mm fiber specimen (C-38-0.15) increased $K_{Ic(DT)}$ by 22% (Figure 5-14(a)). The length study result from SCB test showed similar trend for mix C, but the $K_{Ic(SCB)}$ values increased by 10% and 20% for 10 mm and 19 mm fiber, respectively (Figure 15b). The fracture toughness findings for fiber length study from both monotonic axial DT and SCB tests agreed well with cyclic fatigue test results. However, knowing that there exists a smaller number of individual 38 mm fibers ($FDP = 56$) in the mix compared with 19 mm $FDP = 68$), even higher fracture toughness value values for 38 mm fiber could be anticipated at equal number of dispersed individual fibers, particularly at lower temperatures.

Similar to the findings at 20°C, no notable difference was found between the toughness of no fiber and fibers specimens for mixes D and F2 at 10°C for both DT and SCB tests. These results are consistent with the findings of uniaxial fatigue test at 18°C presented earlier, which further verifies the effect of mix type on cracking performance with respect to FAM thickness parameter.

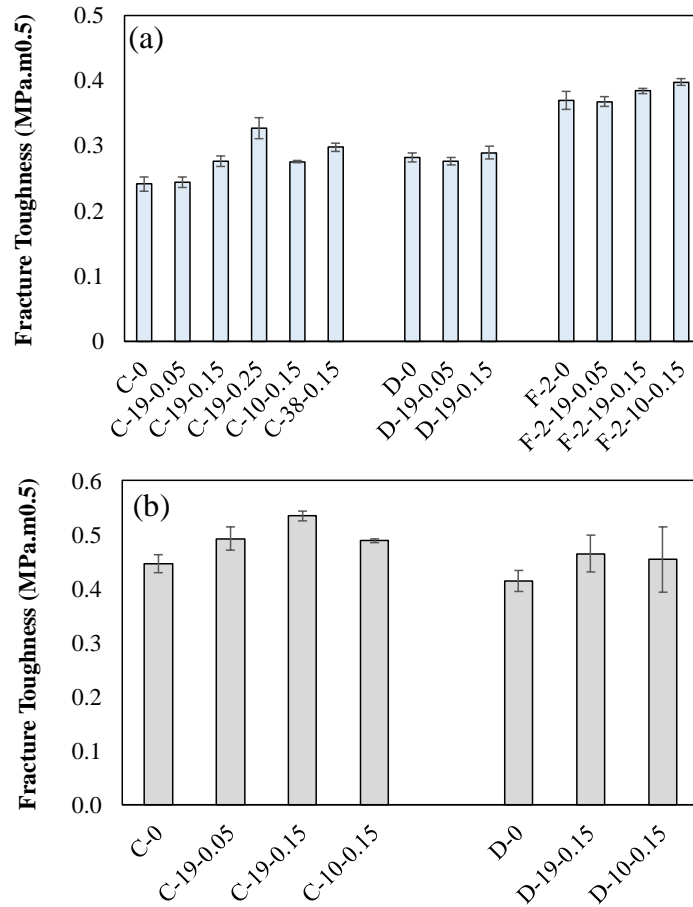


Figure 5-14. Fracture Toughness of Fiber and No Fiber Specimens from (a) DT Test and (b) SCB Test at 10°C and Strain Rate of 0.0012 Per S for Different Mix types, Fiber Length and Dosage.

5.4.4.1.2 Fracture Energy

Fracture energy is expressed as joules per square meter (J/m^2) and determined based on the work-of-fracture method which by definition is the area under the load-displacement curve until the failure of specimen (Hillerborg 1985, Bažant 1996). Fracture energy (G_f) corresponds to all of the work of load P which is dissipated by crack formation and propagation. G_f is determined by dividing the work of fracture over ligament area (the

product of the specimen thickness and ligament length) for SCB specimens and the smaller diameter area for DT specimens expressed in Equations (5-10) and (5-11), respectively.

$$G_{f(SCB)} = \frac{W_f}{A_{lig}} = \frac{\int_0^{u_{final}} P(u) du}{A_{lig}} \quad (5-10)$$

$$G_{f(DT)} = \frac{W_f}{A_d} = \frac{\int_0^{u_{final}} P(u) du}{A_d} \quad (5-11)$$

Where;

W_f = the work of fracture;

A_{lig} = the ligament area of SCB specimen.

A_d = the smaller diameter area of DT specimen.

u_{final} = the displacement at a cut-off load value where the test is considered at an end (usually taken as 0.1 kN).

It should be noted that the method of work-of-fracture in fact measures apparent fracture energy since not all the energy may be dissipated at the crack tip. The fracture energy results for both DT and SCB tests are presented in Figure 5-15. The fracture energy of DT test specimens was determined as a mean to compare the effect of test types on the fracture properties of FRAC. These test parameters were similar to those of SCB specimen except that the strain rate on DT and SCB specimens were not similar given the different geometry of specimens used for each test. No attempt was also made to perform these tests at a similar strain rate on specimen condition because fiber specimens in DT test were underperforming in the post-peak region regardless of test temperature and loading rate. So, a general comparison of test types (SCB vs DT) on fracture properties of FRAC should still be valid. Figure 5-15 exhibits that there is no difference between the fracture energy of no fiber and fiber DT specimens, while the SCB test clearly indicated the benefits of

fiber in enhancing the fracture energy of asphalt concrete. The fracture energy results for DT test was expected due to nonconstant loading rate on specimens found and discussed earlier which resulted in narrower post-peak response for fiber specimens compared with no fibers samples.

The SCB test results showed that the use of 0.05% and 0.15% fiber increased the average fracture energy of asphalt concrete specimens for mix C by 5% and 25%, respectively. The results suggest first the importance of a fracture test type with controlled loading rate and second the benefit of increasing fiber dosage lower temperature in enhancing the total fracture energy. However, the 10 mm fiber did not show any benefit in the fracture energy of asphalt concrete specimens. The results for mix D showed increase of fracture energy for 19- and 10-mm fiber by 15% and 19%, respectively. The fracture energy test results for Mix D with low FAM thickness did not agree with the fracture toughness and uniaxial fatigue findings. This is an interesting observation which will be discussed later.

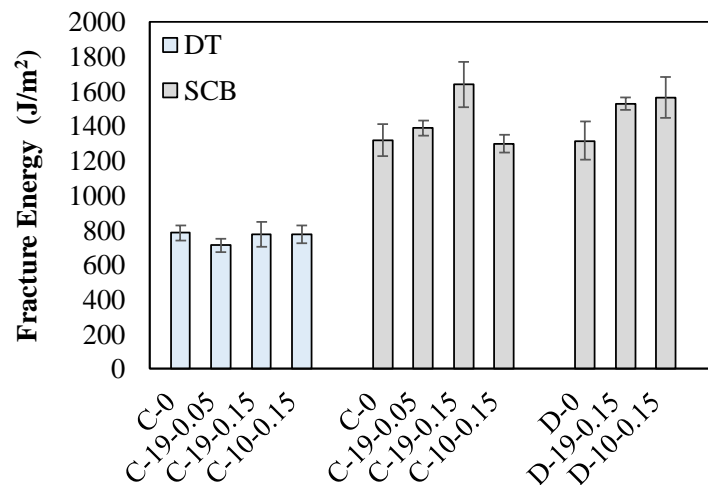


Figure 5-15. Total Fracture Energy of Asphalt Concrete with/without Fibers at 10°C Based on DT and SCB tests for Different Fiber Dosage, Length and Mix Types.

5.5 Summary and Discussion

The experimental findings have shown that fibers do serve as reinforcement element in asphalt concrete; however, their reinforcing efficiency is dependent on the temperature, rate of loading, properties of fiber (i.e. dosage, length), and properties of mix type (gradation). Moreover, the specific type of mechanical testing adopted to study M-FRAC is imperative in understating the interaction of fibers with the mentioned properties and how fibers can affect the crack growth in the asphalt matrix. In this section, laboratory findings of mechanical performance test are further discussed.

5.5.1 *Effect of Test Type*

To understand the effect of test type on evaluation of fiber reinforced asphalt concrete in cracking, the mechanism of crack growth under tensile load is schematically shown in Figure 5-16 which can be simply explained as follows. During a loading process, microcracks will start to grow at point (B), at the peak stress (C), structure is populated with a certain distribution of microcracks with varying lengths (Figure 5-16(a)). Most of these micro-cracks are stable, with perhaps one, maybe two, cracks that are about to become unstable. It is the unstable crack in the micro-crack population at peak-load that triggers macro-crack propagation and localization. The stress-drop (D) is the consequence of the macrocracks propagation through the specimen. In a monotonic direct or indirect type of tension tests (i.e. DT, SCB, IDT), complete stress strain curve response that includes crack propagation stage can be captured as shown in Figure 5-16(b). On the other hand, the failure in uniaxial cyclic fatigue test is defined by the cycle at which the phase angle shows a sharp decrease which is caused by macrocrack localization due to

coalescence of microcracks under repeated cycles of loading. This point of failure is corresponded with the peak load as shown in Figure 5-16(c). Therefore, while the cyclic uniaxial fatigue test is useful in characterizing the pre-peak response of M-FRAC under tension, it fails to evaluate the contribution of fibers to the post-peak regime where fibers may potentially show some additional benefits. This incapability of the test method to differentiate between crack initiation and crack propagation has also been previously noted (Roque *et al.* 1999). The use of such test becomes particularly more questionable when characterizing cracking behavior of asphalt concrete reinforced with macrofibers.

Recognizing the importance of monotonic crack propagation test in tension in evaluating the full stress strain response of FRAC, various studies have widely used IDT, SCB, and DT tests. However, these tests technically lack to operate in a constant loading rate due to the use of loading head displacements. Therefore, when loading head displacements are used to control testing, the speed of crack propagation cannot be maintained equal. This may result in slower or faster propagation of cracks depending on the stiffness of the specimens as shown in Figure 5-7 with the distinctively different actual displacement rates measured on the specimen. Since asphalt is a viscoelastic material with its response changing with rate, this becomes an issue of concern when evaluating the microfiber fracture response in the post-peak regime of stress strain curve which is the case for DT analysis approach. For example, the analysis of fracture energy using area under curve for the fiber specimens can significantly misinterpret the reinforcement efficiency of fibers in asphalt concrete due to the lack of stable and controlled strain rate on specimens. In this study, SCB test was used along with CMOD as the monitoring signal to sustain the stability of test in the post-peak region of the test to evaluate the fracture properties of M-

FRAC. While DT specimens did not show any benefit of fiber in the fracture energy of asphalt concrete, the SCB results indicated improvement in the fracture energy of asphalt concrete specimens by aramid fibers, as shown in this study for DT test results. Nevertheless, the analysis of pre-peak response of stress strain curves from these are still valid since the strain rates on specimens until the peak load are similar for AC and M-FRAC specimens.

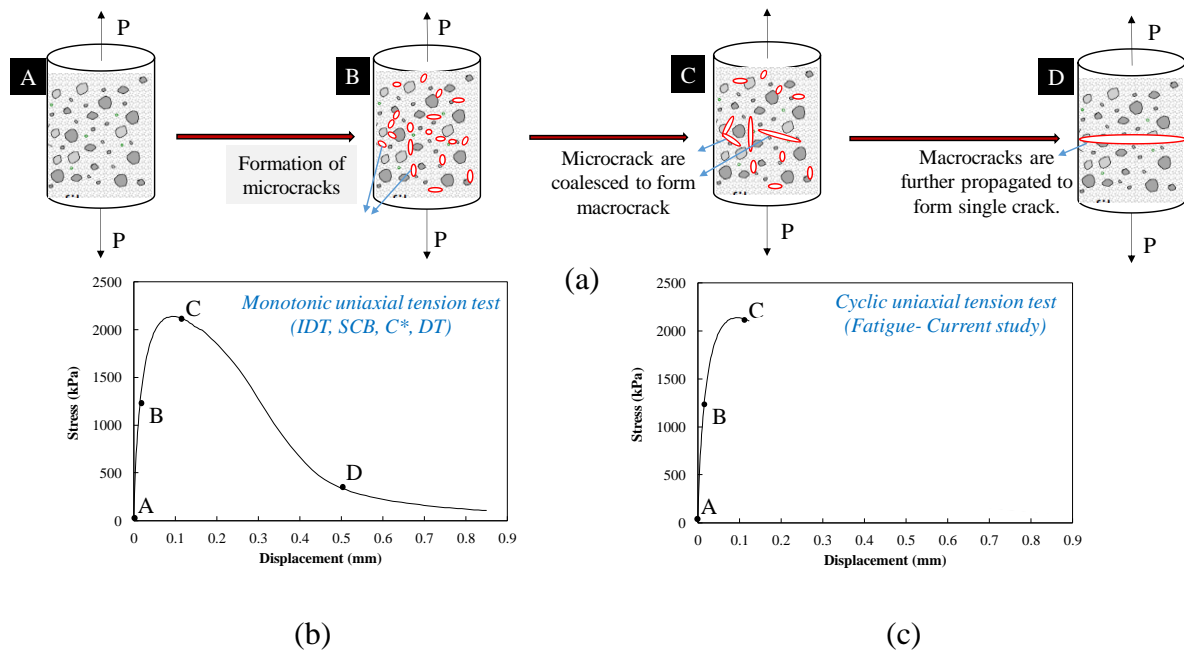


Figure 5-16. Schematic Representation of (a) Crack Growth Mechanism, (b) Typical Monotonic Tension Test, and (c) Uniaxial Cyclic Fatigue Test.

5.5.2 Effect of Temperature/Loading Rate

The effect of loading rate and temperature on the mechanical response of FRAC can be explained by the viscoelasticity behavior of asphalt mixtures on the basis of two mechanisms; one is the crack path in the mix and the other the stress transfer mechanism in the interface between fiber and asphalt matrix. These are elaborated as follows.

5.5.2.1 Crack Path Mechanism

It has been shown that the propagation of crack through asphalt concrete is influenced by temperature and loading rate. Doll *et al.* (2017) studied the fracture process zone and crack path in a pre-notched asphalt concrete SCB specimen using digital image correlation (DIC) at temperatures of -12°C and 25°C and several loading rates. They found that the embrittlement of the matrix at lower temperature/ higher loading rate minimized crack branching/kinking. It was shown that a relatively straight crack at low testing temperature while the crack path was tortuous for higher temperature as exhibited in Figure 5-17.

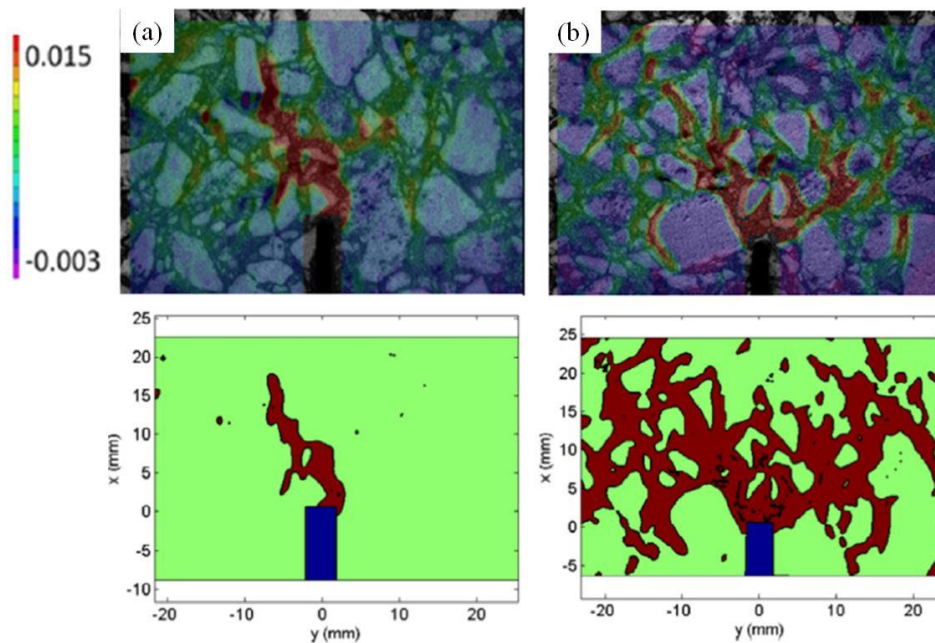


Figure 5-17. Strain Field Superimposed on the Aggregate Structure at (a) -12°C and 0.7 mm/min and (b) 25°C and 50 mm/min at Peak Load in Each Case. The Bottom Figures are the Corresponded Fracture Process Zone Estimation Using Thresholding the DIC-Measured Strain Fields. Also, the Strain Contour Color Scale is Shown Next to the Top Figures (Doll *et al.* 2017).

In this study, the surface failure of specimens suggested propagation of cracks along a tortuous path for the testing temperature 20°C as well as 10°C but relatively to a less degree. This might imply that the cracks branched through mostly FAM (consisting of binder, fine aggregate, and filler) rather than at the coarse aggregates/FAM interface in this study. Since the aramid fibers in this study had a diameter of roughly 10-12 μm , they can act as bridging sites in wake of distributed microcracks within FAM component under tension loading.

5.5.2.2 Stress Transfer Mechanism

When a low-modulus matrix such as asphalt concrete reinforced with and high-modulus and high-strength fibers such as aramid fibers subject to a tensile load, the matrix will transfer a portion of the load to the fiber. Thus, some of the loads will be carried by the aramid fibers and the rest by the asphalt matrix prior to formation of any macrocracks in the matrix. However, the load transfer from fiber to matrix can be dominated by presence of a viscoelastic material. At lower temperature or faster loading rate, the modulus of asphalt concrete is high and acts like an elastic material while at higher temperature or slow loading rate asphalt concrete is more viscous. Park *et al.* (2017) observed that the stress concentration at the both ends of fiber disappears at higher temperature or slow loading rate, and the stress through the entire fiber length becomes more like the average shear stress due to local viscous flow of asphalt binder. When the stress reaches a specific concentration point corresponding to the applied strain rate, it becomes constant because the deformation at that point will be accommodated by viscous flow without additional increase in stress, shifting stress demands to adjacent regions, much like elasto-plastic

behavior. Therefore, in the absence of asphalt viscosity the load can be more effectively transferred within the interface from fiber to matrix, which causes improved reinforcement role of fibers in the system. Comparing the fracture toughness of M-FRAC with AC at 10°C and 20°C, fibers showed more benefit in improving the toughness at 10°C implying a relatively more effective load transfer occurring at reduced temperature even though the asphalt concrete is not perfectly elastic at 10°C. Whether this theory will hold true at further lower testing temperature (i.e. 0 to -20°C) is a question for future work. Moreover, the load transfer is also reliant on the properties of fiber length and dosage which will be discussed in the following sections.

5.5.3 Effect of Fiber Dosage and Length

The effect of fiber properties (length and dosage) is discussed on the basis of previous discussions of crack path in the mix and stress transfer mechanism in the interface, which played a profound role in reinforcing capacity of fibers.

5.5.3.1 Crack Path Mechanism

The experimental results from direct tension test at 20°C showed that 0.05% fiber content increased the fracture toughness of asphalt concrete by 15% and higher fiber content (0.15% and 0.25%) did not further improve the maximum tensile stress. Moreover, no significant difference in the toughness values of M-FRAC was observed comparing different length of fibers at 20°C. Considering tortuosity of propagated cracks at 20°C, it is postulated that there is a critical volume of a saturated homogenously distributed fibers (0.05% fiber dosage) and critical fiber length (10 mm) within FAM which can effectively

delay the widening of microcracks and beyond that there is no further improvement in the fracture toughness.

In contrast, higher fiber dosage was needed to increase the fracture toughness at testing temperature of 10°C. While 0.05% fiber content in asphalt concrete did not show any benefit, incorporation of 0.15% and 0.25% fiber dosage level increased the fracture toughness by 15% and 35%, respectively. In addition, longer fibers were more effective at reduced temperature (10°C) in increasing the fracture toughness of asphalt mixtures. This is possibly attributed to the relatively less tortuosity of microcracks and straighter crack path emanating from the crack tip at 10°C which requires a greater number of fibers (>0.05%) to arrest the growth of microcracks. Longer fibers also ensure that the microcracks are in close vicinity of fiber bridging sites and therefore there is more likelihood of existence of fibers bridging sites upon propagation of microcrack through matrix.

5.5.3.2 Stress transfer mechanism

At 20°C, it was shown that the fracture toughness of M-FRAC is almost independent of fiber properties, specifically length and dosage due to the fact that the load transfer is driven by the viscous flow of asphalt binder as explained earlier. However, at 10°C when asphalt concrete shows more elastic behavior, the underlying effect of fiber length and dosage on the stress transfer start to emerge. The effect of fiber length on the load transfer can be elucidated by comparing the relationship between fiber length (L) and fiber critical length (L_c). A critical fiber length is defined as the minimum fiber length required to build up stress (or load) in the fiber which is equal to its strength (or failure

load) (Kelly and Macmillan 1987, Bentur and Mindess 2006). The effect of different fiber lengths (L) relative to L_c can be similarly analyzed in terms of the stress transfer mechanisms using Cox theory (Cox 1952), as shown in Figure 5-18. For $L < L_c$ (Figure 5-18(a)) there is inadequate embedded length to create a stress equal to the strength of fiber and the fiber is not reached to its full efficiency. However, as the length of the fiber increases and exceeds L_c , the stress along most of the fiber reach its yield or tensile strength (Figure 5-18(c)), hence mobilizing most of the potential of the fiber reinforcement (Bentur and Mindess 2006). Moreover, A higher number of fibers in the matrix reduces the spaces between fibers and can effectively facilitate the efficiency of stress transfer mechanism by the transmission of load from one fiber to another.

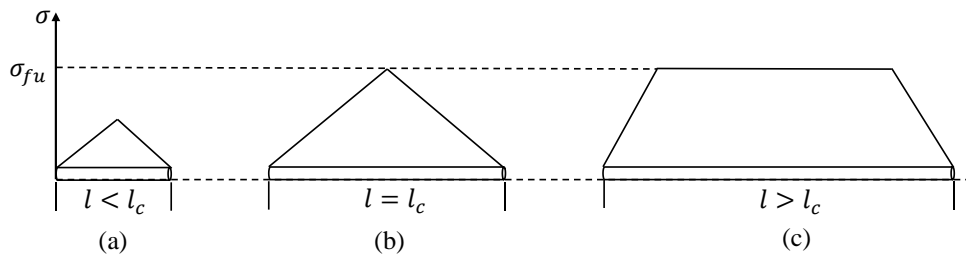


Figure 5-18. Stress Profile Along an Embedded Fiber in a Matrix as a Function of Fiber Length.

5.5.4 Effect of Mix Type

The results from various mix types showed that the fiber reinforcement efficiency is affected by gradation of asphalt mixtures. FAM thickness index was introduced as an indicator for fiber efficiency in cracking. The concept was verified by measured fatigue life using uniaxial cyclic fatigue test as well as fracture toughness using monotonic SCB and DT tests. Improvement from mixtures with higher FAM thickness could be explained

by the mechanism of crack path discussed earlier. With reference to propagation of cracks along a tortuous path under tension loading, at larger FAM thickness there is a better chance for fibers to function as bridging sites to delay the microcrack propagation. The fracture energy test result, however, shed further light into understanding the reinforcement mechanism of fibers. It was found that the fracture energy of SCB specimens increased by presence of fibers regardless of the mix types and the FAM thickness concept. This is a very important observation in a sense that after the peak load, fibers start actually debonding from matrix, which at that point they can function to bridge across the crack to delay the macrocrack propagation regardless of the mix type and the corresponded FAM thickness. This also accentuates the use of a crack-controlled test in evaluating the full response of M-FRAC.

CHAPTER 6

EVALUATION OF INTERFACIAL SHEAR BOND STRENGTH AND CRITICAL FIBER LENGTH IN FIBER REINFORCED ASPHALT CONCRETE

6.1 Introduction

The interface between fiber and matrix plays a significant role in understanding the mechanical behavior of fiber reinforced composites which were discussed in CHAPTER 2. In short, the interface governs the load bearing capacity and the efficiency of load transfer between the fiber and the matrix. Quality of interface between fiber and matrix is commonly characterized by the shear bond strength from which a critical fiber length can be determined. The interface can be examined by a number of micromechanical techniques, such as pull-out, push-out, microbond, and fragmentation tests, have been extensively used in recent decades. A bond between two surfaces can be formed through different mechanisms including molecular entanglement, electrostatic attraction; interdiffusion of elements; chemical reaction, and mechanical interlocking. All these mechanisms occur at the interface region most likely in combination to form the final bond. A detailed review of these mechanisms can be found in (Teklal *et al.* 2018). While the importance of all different bonds in evaluating the interfacial properties of fiber reinforced composites is recognized, and they are definitely worth being investigated, the particular focus of this research is to study the bond characteristic in the interface with respect to solely mechanical interlocking at the fiber surface.

The present study investigates the interfacial shear strengths of fiber-reinforced asphalt matrix using the single-fiber pull-out test at different displacement rates. Because

of the viscoelastic nature of FRAC, the shear bond strength between the fibers and the asphalt matrix are affected by the displacement rate. At slow displacement rates, the shear bond strength is low. Inversely, at high displacement rates, the shear bond strength is high. Very few studies have addressed the bond between fibers and matrix and the effect of fiber length on the properties of FRAC (Lee *et al.* 2005, Qian *et al.* 2014, Park *et al.* 2017, Apostolidis *et al.* 2019). The studies used different fiber types, test configurations, test conditions, and methods of analysis. The recommended critical embedded length varied from one study to another depending on fiber types and the test conditions used. More research is still needed to evaluate the interaction between fibers and asphalt concrete matrix and to determine the critical fiber embedded length under different shear bond strengths. To this date, there is no single study to relate the shear bond strength between fibers and asphalt matrix from pull-out test to the stiffness of asphalt binder, mastic or concrete in the mix. This is this relationship that allows one to suggest a practical fiber length in the asphalt concrete mix and can provide fundamental understanding on the mechanisms of shear bond strength and its roles into fiber reinforcement in asphalt concrete.

6.2 Objective

The main objectives of this study are summarized as follows:

- Analyze the nature of shear bond strength between fibers and asphalt mastic from pull-out test under different displacement rates and fiber dimensions.
- Develop an analytical framework to establish a relationship between the shear bond strength and asphalt concrete modulus.

- Recommend a practical fiber length as a function of temperature for use in asphalt concrete.

6.3 Experimental Program

6.3.1 Materials

A PG 70-22 binder grade was used in this study. Three types of fibers were also used including a multi-filament aramid fiber and two different nylon fibers, a multi-filament (named here Nylon 1), and a monofilament (named here Nylon 2) with properties subjected to tension. Table 6-1 and Figure 6-1 show the measured physical properties of the three fiber types. It can be seen that the aramid fibers have the smallest diameter and the largest tensile strength and modulus of elasticity than the nylon fibers.

Table 6-1. Measured Physical Properties of Fibers Types.

Fiber Type	Diameter (mm)	Tensile strength (MPa)	Percent Elongation*	Melting Temp (°C)
Aramid	0.012	3,000	10	>450
Nylon 1	0.025	966	45	210
Nylon 2	0.260	350	65	210

*Percent elongation is the elongation at failure as a percentage of the original length.

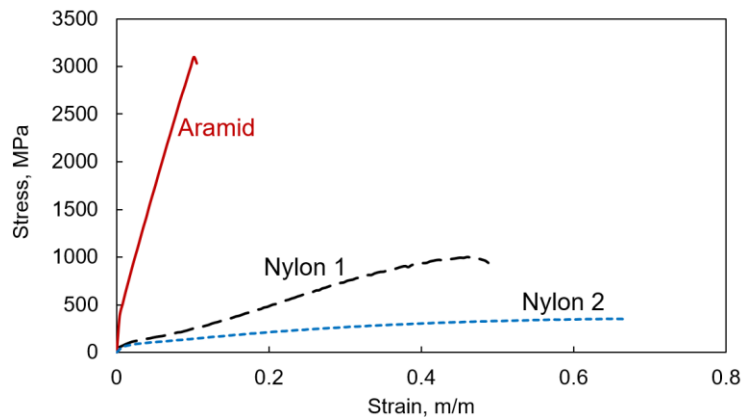


Figure 6-1. Measured Stress-Strain Relationship of Fibers.

6.3.2 *Sample Preparation*

Sample preparation included three steps: 1) alignment of the fibers in the container; 2) preparation of the mastic; and 3) pouring the binder/mastic into the container.

6.3.2.1 **Fiber Alignment**

Multiple parameters were considered in fiber alignment procedure to ensure minimum eccentricity. 3D-print cup containers and alignment gadgets were designed, and fibers were aligned using the laser beam device. The assembly is shown in Figure 6-2. PLA Filament 1.75mm was used in fabrication of all the needed testing parts which had a temperature tolerance of 180-220°C so the cups were not degraded upon pouring hot binder/mastic in them. The cups however were not reused and for each test new cups were printed. Note that the diameter of the circular hole at the bottom of the cups was 1 mm, which was large enough to allow fibers to pass through and small enough not to allow hot liquid binder/mastic to pass through upon pouring into the cups. The cups were designed at 50 mm diameter and different heights depending on the fiber embedded length. Different geometries of cups were considered in the initial study to make sure that pull-out test is independent of the geometry of containers. Another important parameter in the fiber alignment process was to have a good gripping system to make sure the embedded fibers (L_e) are perfectly straight and in tension during pouring the hot liquids into the cups. The embedded length was also verified by the measurement of L_e after the test, which was almost similar to the target L_{em} .

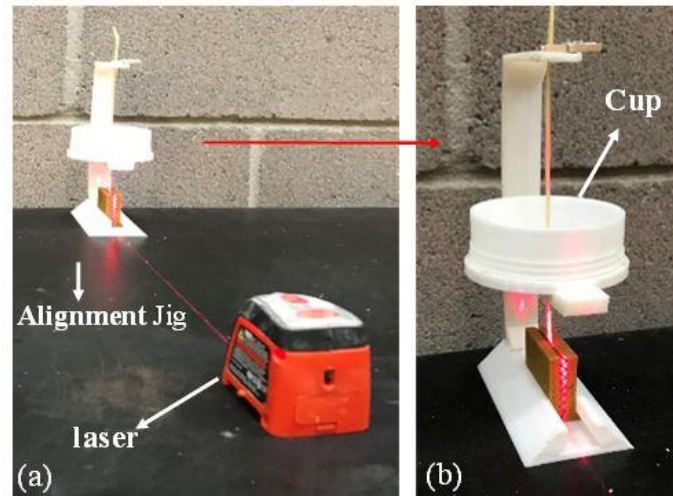


Figure 6-2. Photos of (a) Laser Beam, Cup, and Alignment Gadget for Fiber Pull-out Test Set up and (b) the Close-up of the Alignment Gadget and the Cup.

6.3.2.2 Mastic Preparation

Asphalt mastic was prepared mixing binders and fillers (passing sieve No. 200) proportionally based on the basis of volumetric calculations documented in (Gundla 2014). In preparation of mastic samples, the volumetric properties of Mix B (For the mix design details refer to CHAPTER 4) were used. To determine the mass percentage ratio between filler and binder, the effective specific gravity of filler was assumed to be similar to that of aggregate. The mass percentages of filler to binder in mastic specimen was calculated as 48.4% to 51.6%.

For preparation of the mastic the mixing temperature was 160°C. Accordingly, the filler was heated at 160°C for a minimum of 6 hours and binder was heated until it attained the mixing temperature of 160°C. The binder was then added to the filler in appropriate proportions in metal and mixed thoroughly using a mechanical blender. To be consistent with the process, a mixing time of 60 seconds was adopted across all the mastics. The

prepared mastic was then put back in the oven, so it reaches the target temperature for pouring into the fiber cups.

6.3.2.3 Casting samples

The prepared asphalt mastics were poued into the cups prepared eariler in the alignment step at 135°C, which was fluid enough, at the specified depth depending on the target embedded fiber length, L_e . To make sure the target L_e is consistently achieved, mass volume relationship was used to put known mass of hot mastic into the cups using a scale. After casting the samples, they were left to cool down to ambient temperature. Once the temperature of mastic was equilibrated at the specified level, the extra pieces of fibers were carefully cut from the bottom and top of the cup. The cups were then moved to the environmental chamber for pull out testing.

6.3.3 Test Methods

6.3.3.1 Pull-out Test

Figure 6-3 shows the assembly of embedded fiber in the asphalt mastic container fixed in a 3D designed cup holder which was connected to the loading machine at the bottom inside a controlled-temperature chamber. The fiber pull out tet was performed using an Instron tensile testing machine with a 25 lbs. (5.6 N) load cell capability by pulling out the other end of the fiber. The test specimens were conditioned in the environmental chamber for three hours and the temperature was monitored using a dummy specimen next to the test sample by a thermocouple. The machine had a designed external LVDT to measure the displacement during pull out test. Also, A 3D designed cup holder was used

to connect the fiber cup to the and a 3D designed base to attach the load cell to the lower part of machine as shown in Figure 6-3.

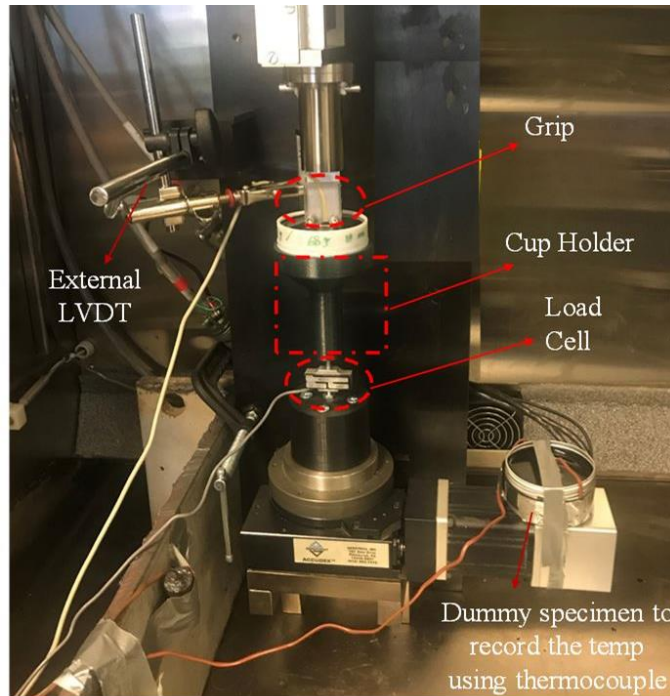


Figure 6-3. Fiber Pull-out Test Set up.

Attention was also given to make sure that there is no inclination between fiber and grip and the fiber is perpendicular to the test specimen, as shown in Figure 6-4. The free length (FL) was reduced as much as possible to 1.5 mm in this study.

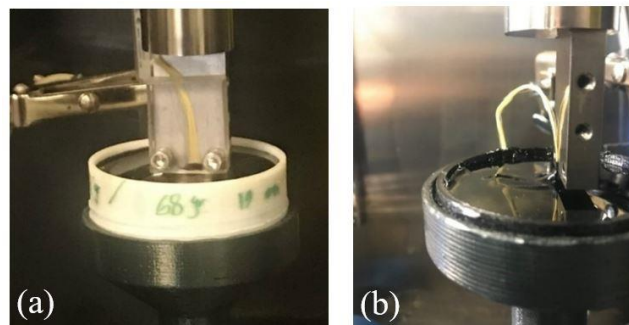


Figure 6-4. The Alignment of (a) Front and (b) Sideview of Fiber vs. Grip in the Pull-out Test.

Once the temperature of mastic specimens was equilibrated at the specified level, the fiber pullout test was conducted at a specified displacement rate. Table 6-2 shows the experimental design parameters for single fiber pull-out test, which was considered for this study.

Table 6-2. Experimental Design Factors of Single Fiber Pull-out Test.

Parameter	Description
Loading Modes	Constant Elongation Rate
Binder Type	PG 70-22
Fiber Types	Nylon, Aramid
Embedded Fiber Length (mm)	5, 10
Temp (°C)	20±0.5
Displacement Rates, mm/s	0.1, 0.5, 1
Loading Device	Instron

6.3.3.2 Optical Microscopy Imaging

The diameter of individual aramid fibers before and after pull-out test was measured by optical microscopy imaging. Initially, Atomic Force Microscopy (AFM) indentation technique on a Bruker MultiMode 8 operating in AC mode with RTESPA-150 tips (150 kHz nominal frequency, 5–10 N/m nominal spring constant) was used to measure the diameter. However, the test specimens were quite moving under AFM tip even though the fiber specimens were taped on glass plates. Nevertheless, the optical microscopy method was simply good enough to obtain clear images of fibers coated with and without asphalt binder for the purpose of diameter measurement.

6.3.3.3 Dynamic Shear Rheometer (DSR)

Dynamic shear rheometer (DSR) was conducted on both the prepared mastic and binder for determining the intermediate viscoelastic properties of the asphalts. The AASHTO T315 standard test protocol was performed based on oscillatory, parallel plate testing to determine $|G^*|$ and δ of the asphalt binder and mastic. DSR was carried out using an 8 mm parallel plate geometry for temperatures and frequencies in the range of 10 - 40°C and 1-100 rad/s using a sinusoidal waveform as described in the AASHTO T315 test protocol. Also, two replicates were tested for each binder and mastic specimen.

6.4 Results

6.4.1 Pilot Study for Improvement of Data Quality

In preliminary study of fiber pull out test, virgin binders were initially used. However, asphalt binders were found to be too soft at 20°C (a weak matrix) in order to activate the interface failure. In almost all of the cases studied using binder, a matrix mode failure was observed as described by Park *et al.* (2017). Figure 6-5 shows the matrix mode failure for both aramid and nylon fibers with different L_e in this study at testing condition of 20°C and 0.1 mm/s using PG 70-22 binder as the matrix. Such cohesive failure is not really indication of a fiber interface property and therefore cannot characterize the shear bond strength. This problem can be tackled by reducing temperature, increasing displacement rate and mixing filler with binder (mastic). In this study, asphalt mastic was used as the matrix for pull out test because testing at very low temperature was not possible at the time of experiment. Therefore, mastic was used to increase the stiffness of asphalt matrix to further activate the interface failure.

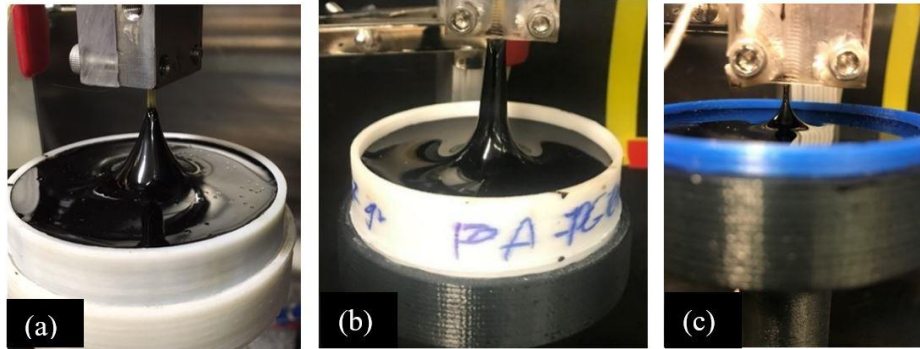


Figure 6-5. Matrix Failure Mode of Fiber Pull-out Test at 20°C and 0.1 mm/s Using PG 70-22 Binder for (a) Aramid fiber with $L_e=10$ mm, (b) Aramid Fiber with $L_e=20$ mm, and (c) Nylon Fiber with $L_e=10$ mm.

In the second attempt of pull-out pilot study, attention was given to variability and repeatability of load displacement data. To the best knowledge of this author, there is no established standard test protocol defining a specific standard deviation (STDV) or sample size for the pull-out data at least in asphalt matrix. The studies typically indicate high variability in their pull-out test data. Park et al. (2017) observed a large scatter in the test results of fiber pull out test in asphalt binder particularly at lower testing temperature with over 100% STDV. They stated that the high variability was attributed to the increase in brittleness that occurs in asphalt behavior as temperature decreases. One way to minimize the data variability is to test a larger number of replicates. Initially, a total number of 10 replicates were tested for pull out test based on nylon fibers in mastic at $20^{\circ}\text{C}\pm 0.5$ and displacement rate of 0.5 mm/s. Figure 6-6 shows the load displacement results for the pull-out test.

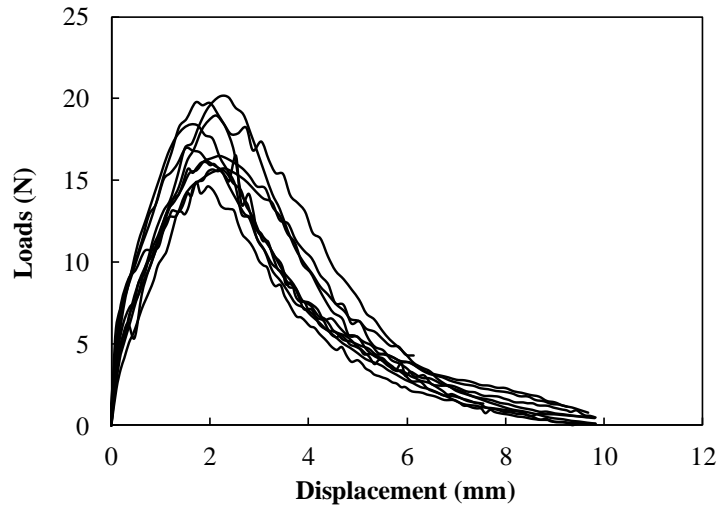


Figure 6-6. Load Displacement Curves of Pull-out Test Performed at 20°C and 0.5 mm/s for Different Replicates of Nylon 1 in the Asphalt Mastic.

The results suggested comparatively good variability in the experimental measurement with STDV of about 40%, which might be justified by carefully controlling the sample preparation as explained earlier. However, testing 10 replicates for each test condition might be unnecessary and even impractical because of several different variables this study considered for pull-out test. Therefore, a minimum number of replicates, n , for pull out test which can statistically satisfy STDV of 30% and a confidence interval of 90% was calculated according to the following formula.

$$n = \left(\frac{Z^* \sigma}{\sigma'}\right)^2 = \left(\frac{1.644 \times 0.4}{0.3}\right)^2 = 4.64 \cong 5 \quad (6-1)$$

Where; Z^* is the confidence interval which is 1.644 for 90% interval; and σ and σ' are the STDV of experimental test results and the target margin of error set for this study. Therefore, 4-5 replicates were performed for fiber pull-out test in this study.

6.4.2 General Observation of Load-Displacement Data

The force used to pull the fibers and the corresponding displacement are continuously recorded during the test. Figure 6-7 shows an example of the load-displacement relationships of fiber during pulling from the asphalt mastic at different displacement rates. As expected, as the displacement rate increases, the force increases because of the viscoelastic response of the mastic. At high displacement rates, the asphalt mastic gets stiffer and the shear resistance opposing the fiber gripping force that is holding the fiber increases.

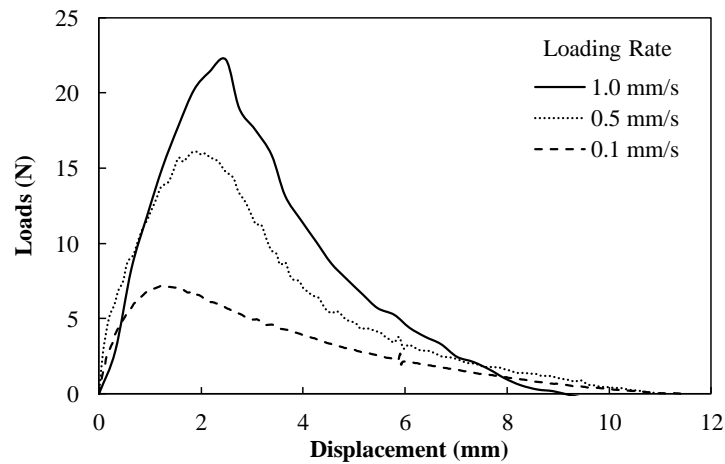


Figure 6-7. Example of Force Displacement Relationship of Fiber During Pulling from Asphalt Mastic at Different Displacement Rates.

After the test, the fiber pull-out failure mode was observed. It was observed that the behavior of matrix failure mode is dominated by the viscoelastic nature of the asphalt binder at low strain rate (0.1 mm/s) with matrix failure while at a faster displacement rate (1 mm/s) the behavior is more dominated by the interface failure. Figure 6-8 shows the four fiber pull-out modes of failure in this study: a) matrix failure mode (cohesion failure of the asphalt mastic), b) mixed mode failure, c) interface failure mode (shear bond failure

between the two materials), and (d) fiber rupture. The mode of failure varied depending on both fiber type and displacement rate. In this study, the matrix failure mode occurred using the aramid and Nylon 1 at the slow displacement rate of 0.1 mm/s while the mixed and interface modes occurred at the high displacement rates of 0.5 and 1 mm/s. Nylon 2 showed the mixed mode at the slow displacement rate of 0.1 mm/s and interface mode at 0.5 and 0.1 mm/s. The fiber failure mode occurred in the cases of higher embedded length in the matrix as they were exceeding their critical length value.

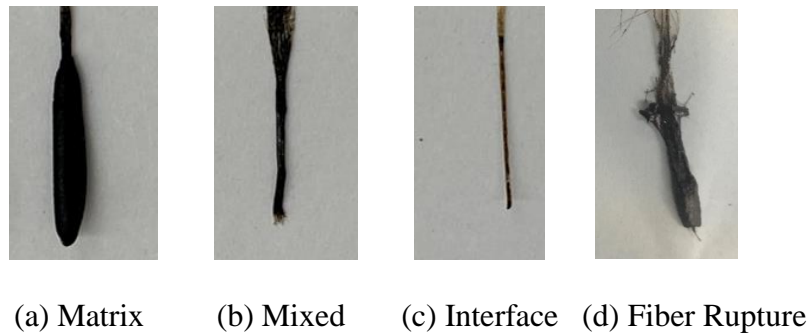


Figure 6-8. Fiber Pull-out Failure Modes.

Fiber aspect ratio, defined as the ratio of fiber length and diameter ($AR = L/D$), is an important parameter that influences the mixing quality and reinforcing effect. For the pull-out test, an embedded aspect ratio is defined as a ratio of embedded fiber length to the diameter of fiber. Assuming that a crack lies over a fiber in asphalt concrete, probabilistically, the pull-out will occur at the shorter part of the fiber, and hence, L_e will be less than a half of the fiber length, L . Figure 6-9 shows the effect of different L_e for aramid fibers at 20°C and 0.5 mm/s. Clearly, increasing the embedded length yields to a higher peak load response as well as a larger deformation.

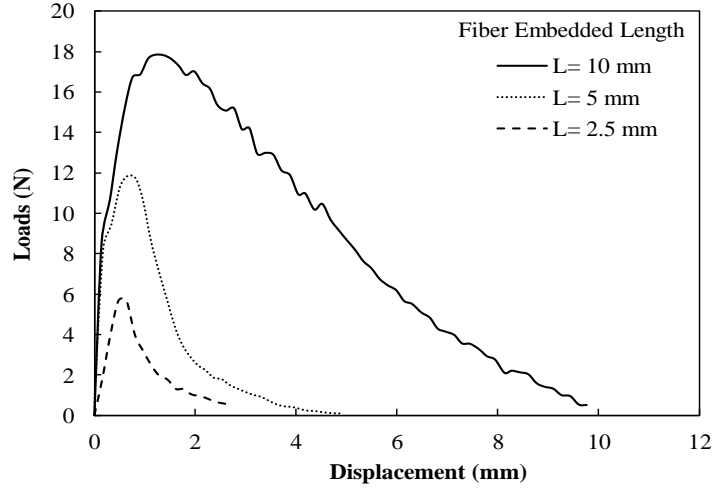


Figure 6-9. Example of Fiber Pull-out Load Displacement Curve for Different L_e based on Aramid Fibers at 20°C and 0.5 mm/s.

6.4.3 Evaluation of Effective Fiber Diameter

The force F required to pull the fiber bundle from the asphalt mastic was measured. Although the stress distribution varies along the fiber surface (Park *et al.* 2017), the average shear bond strength was used. Knowing the embedded length and the effective diameter of the embedded fiber bundle (d_{eff}), the average nominal shear bond strength ($\bar{\tau}$) were determined using the following equation of equilibrium (Kelly and Tyson 1965).

$$\bar{\tau} = \frac{F}{\pi d_{eff} L_e} \quad (6-2)$$

The experimental approach developed in this work provide direct measurement for values of L_e and the debonding force, F , which can used in the Equation (6-2). However, assigning a certain value with high reliability for the fiber diameter in form of bundles is quite challenging. To estimate the effective diameter, d_{eff} , different methodologies exist

each have their own advantages and disadvantages. Two methods were selected considered for further evaluation as follows.

- Method 1: The perimeter of the hole left in the asphalt mastic by the pulled-out fibers could be estimated by a caliper if the hole is large enough or more accurately by optical imaging technique (Viel *et al.* 2018). The pulled-out fibers actually leave a volume of conical shape on the surface of mastic container, as shown in Figure 6-10. This diameter is close to the diameter of pull-put fiber coated with asphalt mastic which can be measured either by caliper or more accurately by an optical microscopy.

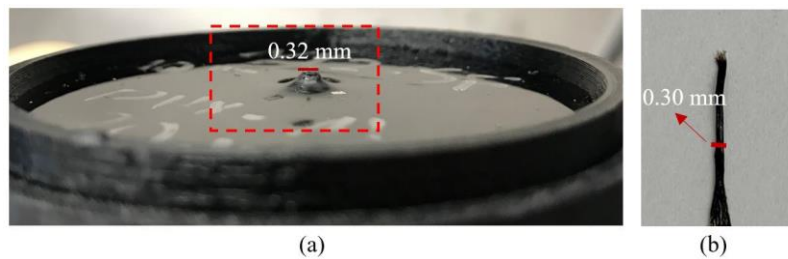


Figure 6-10. Example of Fiber Diameter Measurement from (a) the Conical Shape of Hole Left After Pulled-out Fiber and (b) the Diameter of Fiber Coated with Asphalt Mastic.

- Method 2: Another approach to estimate the diameter of fibers is to assume fiber bundles are hexagonally packed (Li *et al.* 1990b). This is a theoretical consideration unlike method 1 which is a direct approach. This method was not used because the number of fibers that can engage in the pull-out activity is really unknown, so it is not rational to count all the number of individual fibers in a bundle for calculation of the effective diameter. The actual number of contacted fibers in a bundle with

asphalt mastic can vary from one fiber bundle to another depending on the degree of penetrated asphalt mastic into the bundles of fibers, the arrangement of fiber bundles, and the sample preparation procedure. In addition, the contribution of fibers located on the perimeter vs the core in the bundle to the overall pull-out force might not be the same so the weighted average may be used to overcome this. Nevertheless, the theoretical approach requires consideration of arbitrary numbers of individual fibers in the bundle which might underestimate or overestimate the average shear strength. Therefore, method 1 was used in this study to estimate d_{eff} .

6.4.4 The Effect of Fiber Dimension on the $\bar{\tau}$

The effect of fiber length was studied by Nylon 1 while the effect of diameter was studied using aramid fibers. Aramid fiber was selected because they have large bundle size compared with Nylon 1, so it was more convenient to divide the large bundles into smaller pieces of aramid bundles. A methodology was devised to carefully separate off the bundles of aramid fibers without disturbing or causing any damage to the fibers as much as possible. The different diameters of aramid fiber are represented by different size of bundles as shown in Figure 6-11.

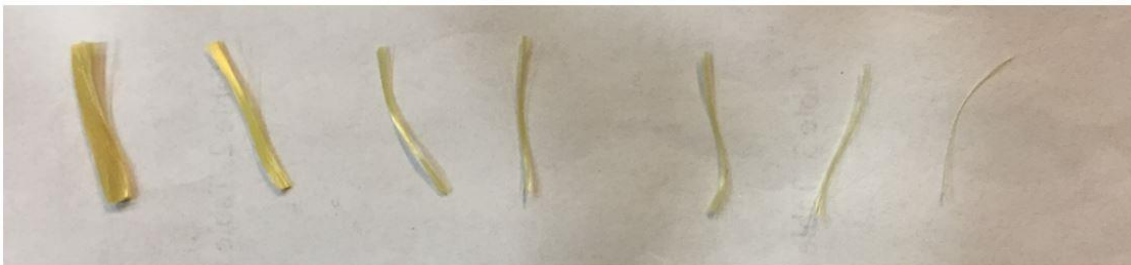


Figure 6-11. Bundles of Aramid Fibers Each Representing a Distinct Diameter.

The effect of fiber diameter and embedded length on the average shear bond strength, $\bar{\tau}$, and maximum pull-out force were studied as shown in Figure 6-12. The results show that the maximum pull-out force increased with increasing the fiber diameter and embedded length, while the $\bar{\tau}$ actually reduced (Figure 6-12). The reduction of the $\bar{\tau}$ with increasing diameter and embedded length was therefore attributed to the increment of the effective pull-out volume represented in the form of conical shape.

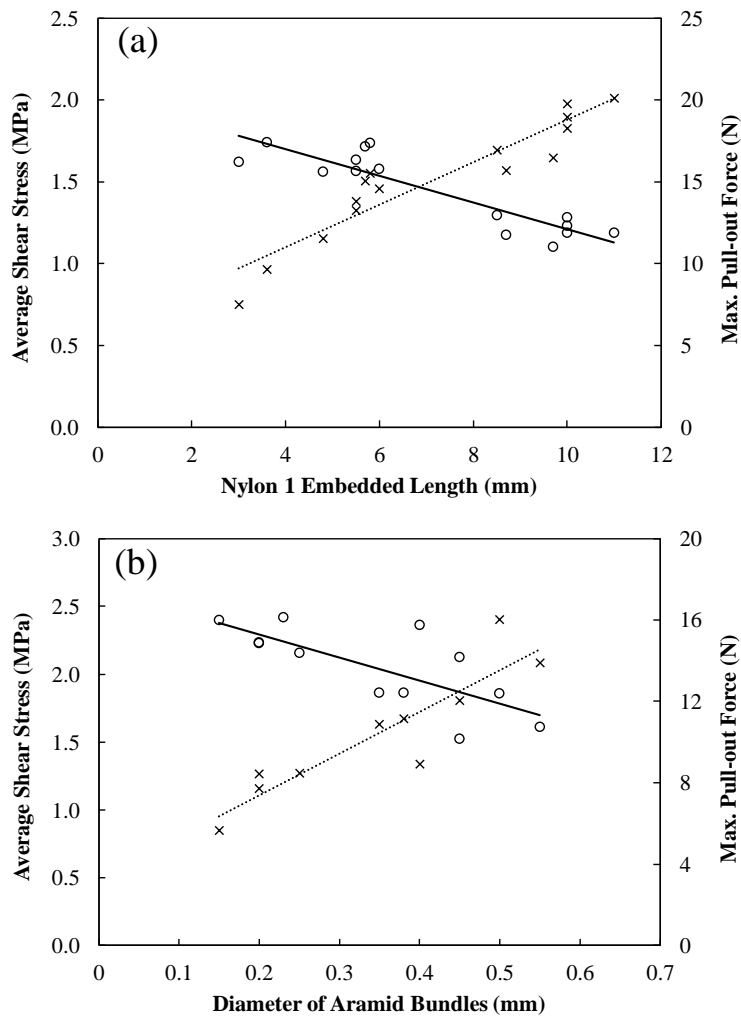


Figure 6-12. Effect of Different (a) Embedded Length of Nylon 1 and (b) Diameter of Aramid Fiber on the $\bar{\tau}$ and F at 20°C and Displacement Rate of 0.5 mm/s.

Figure 6-13 illustrates the surface of asphalt mastic container after pull-out test indicating a distinct difference in the disproportionality of the effective pull out volume with respect to different fibers length and diameter. These results suggest that thinner and shorter fibers are able to carry more stress at high service temperature and are hence more beneficial for enhancing rutting resistance (Park *et al.* 2017).

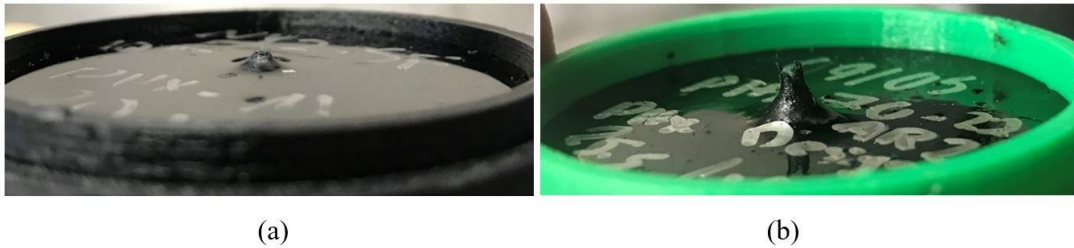


Figure 6-13. Example of the Effective Pull-out Volume for (a) Thin and Short Fibers (b) Thick and Long Fibers.

Another significant interpretation with respect to the effect of diameters of aramid fibers on the shear bond strength, $\bar{\tau}$, can be linked to the importance of fiber dispersion in enhancing the mechanical performance of asphalt mixtures, particularly flow number test which was identified and studied in the CHAPTER 2. The larger $\bar{\tau}$ for smaller diameter fibers implies that individual fibers can be more effectively mobilized in the asphalt matrix system, particularly at higher temperature and smaller displacement rates. This essentially accentuates the benefits of a larger *FDP* value (higher number of individual aramid fibers) in the asphalt mix to improve the rutting resistance of asphalt mixtures.

6.4.5 The effect of Fiber Types on $\bar{\tau}$ at Different Displacement Rates

The average shear bond strengths for the different fiber types at different displacement rates of 0.1, 0.5, and 1.0 mm/s, and different embedded length of 5 and 10

mm were analyzed. Since the earlier results indicated that the values of $\bar{\tau}$ is not independent of fibers diameter at the testing temperature of 20°C, comparison between fiber types would not be really possible without testing the fibers at the same or at least similar effective diameter, d_{eff} . For Nylon 1 and Nylon 2, their comparison was not possible at 20°C because the d_{eff} was 0.26 mm and 0.49 mm, respectively which was constant throughout the study. However, it was possible to compare aramid with nylon fibers separately since the $\bar{\tau}$ results were available for multiple different diameters of aramid (See Figure 6-11).

Figure 6-14 was plotted to compare the $\bar{\tau}$ of aramid fibers with that of Nylon 1 and Nylon 2 in asphalt mastic at 20°C and different displacement rates and fiber embedded lengths. The results show that the measured shear bond strength values vary between 0.4 and 2.2 MPa for the different fiber types and displacement rates. At 0.5 mm/s, the aramid fibers showed larger shear bond strength than both nylon fibers. The $\bar{\tau}$ of aramid fibers was about 25% and 60% higher than that of Nylon 1 and Nylon 2, respectively, regardless of fiber embedded length. At 0.1 mm/s, while the $\bar{\tau}$ of aramid fiber was higher than Nylon 1, the difference was found to be statistically insignificant using ANOVA analysis at 95% confidence interval. The different behavior in the comparison of the $\bar{\tau}$ between aramid and Nylon 1 at 0.1 vs 0.5 mm/s are attributed to different mechanisms of failure in the pull-out test discussed earlier. At lower displacement rate (0.1 mm/s), fiber pull-out mechanism is impeded by the viscoelastic nature of the asphalt binder; and therefore, the experimentally measured shear strength is in reality measurement of both asphalt viscosity and shear bond strength.

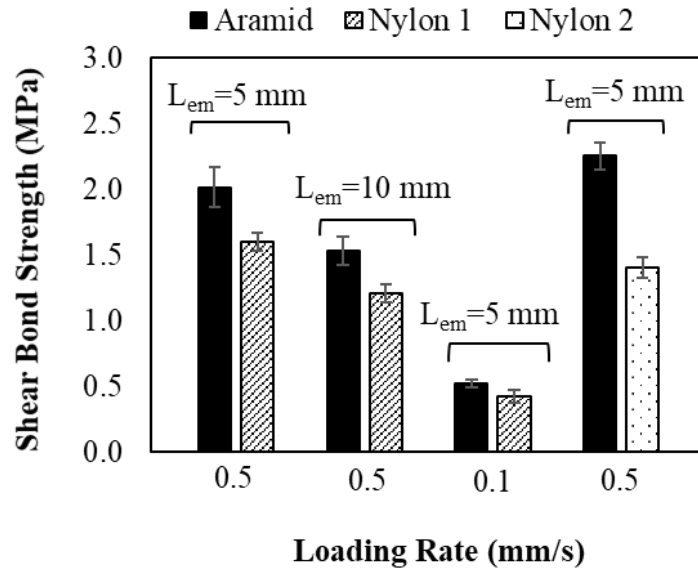


Figure 6-14. Average Shear Bond Strength for Different Fiber Types at Different Displacement Rates.

6.4.6 Relationship Between Asphalt Mastic Stiffness and Shear Bond Strength

In this study, the average shear bond strength, $\bar{\tau}$, was found to be a function of fiber types and fiber dimensions and its value changes with respect to the different displacement rates at 20°C. This indicates that the shear strength between fibers and matrix is a time-dependent property similar to the asphalt stiffness, which has been too found in previous work (Park *et al.* 2017). However, the $\bar{\tau}$ values would be not entirely meaningful if its property cannot be linked to the viscoelastic stiffness parameter of asphalt matrix. For example, the pull-out test results showed an $\bar{\tau}$ value of 2 MPa for aramid fibers with specific dimension at the testing temperature of 20°C and 0.5 mm/s. However, this specific value of shear strength from pull-out test is not necessarily the same as the shear bond strength between fiber and asphalt matrix in the mix. This is because the $\bar{\tau}$ value is not linked to the modulus of asphalt mastic. There is not any straightforward experimental method to be

able to measure the moduli of the asphalt mastic as a time dependent parameter. While DSR test is commonly used to measure the moduli of asphalt binder and mastic, which was also done in this study; it is a frequency-based test, and it cannot be directly linked to the results of a constant displacement-rate pull-out experiment. Accordingly, a method was devised based on elastic-viscoelastic correspondence principle to determine a relationship between shear bond strength and the modulus of asphalt mastic. This is explained as follows.

Introducing the uniaxial pseudo strain, ε^R , in form of a convolutional integral in the Hooke's Law, the stress, σ , can be obtained as follows:

$$\sigma = E_R \varepsilon^R = \int_0^t G(t - \tau) \frac{d\varepsilon}{d\tau} d\tau \quad (6-3)$$

Where; t is the time of interest; τ is an integration constant; and $G(t - \tau)$ is the relaxation modulus of the mastic and its response function is analytically represented by the common Prony series formulations expressed in Equation (6-4).

$$G(t - \tau) = G_\infty + \sum_{i=1}^m G_i e^{-(t-\tau)/\rho_i} \quad (6-4)$$

The method given by Underwood et al. (2006) was adopted to obtain the values of Prony coefficients in Equation (6-4). In summary, the solution involves first pre-smoothing the storage modulus, $G'(\omega)$ experimental data obtained from DSR test using the function presented in Equation (6-5) for a range of reduced angular frequencies roughly two decades bigger and smaller than the measured range. Then, the storage modulus is fit to a Prony representation via the collocation methods as shown in Equation (6-6).

$$G' = \frac{10^g}{\left(1 + \left(\frac{\omega_c}{\omega_R}\right)^k\right)^{\frac{m_e}{k}}} \quad (6-5)$$

$$G' = \sum_{i=1}^m \frac{G_i \omega_R^2 p_i^2}{\omega_R^2 p_i^2 + 1} \quad (6-6)$$

Where;

G' = dynamic shear modulus (Pa);

10^g = binder glassy modulus, determined through optimization (Pa);

ω_c = crossover frequency (rad/s), a fitting coefficient;

m_e, k = fitting coefficients;

ω_R = angular frequency;

G_i = modulus of i^{th} Maxwell element (fitting coefficient); and

p_i = relaxation time (fitting coefficient).

The Prony representation approach is the preferably used to analytically represent LVE materials (i.e. asphalt concrete) because of its computational effectiveness and because it can be simply used to determine exact solutions for converting between time and frequency domain functions. Additional details on this particular analytical method are presented in the literature (Park and Schapery 1999).

The strain from pull out test is simply represented by Equation (6-7).

$$\varepsilon = Ct \quad (6-7)$$

Where C is a constant obtained from displacement rate of pull out test. Since 0.5 mm/s of displacement rate was used the constant is the 0.5 over the embedded length of fiber in the experiment.

Substituting Equations (6-7) and (6-4) into (6-3), stress can be rewritten as:

$$\sigma = \int_0^t G_\infty C d\tau + \int_0^t \sum_{i=1}^m G_i e^{-(t-\tau)/\rho_i} C d\tau \quad (6-8)$$

Solving the integral gives the following form Equation (6-9).

$$\sigma(t) = C(G_\infty + \sum_{i=1}^m G_i \rho_i (1 - e^{-t/\rho_i})) \quad (6-9)$$

It should be noted that for binders the lower asymptote does not exist; therefore, the term G_∞ is zero. This further simplifies the Equation (6-9) as follows:

$$\sigma(t) = C(\sum_{i=1}^m G_i \rho_i (1 - e^{-t/\rho_i})) \quad (6-10)$$

Now, the apparent modulus, E_a , is defined as follows:

$$E_a = \frac{\sigma(t=t_n)}{\varepsilon(t=t_n)} \quad (6-11)$$

Where t_n is the time of maximum load, F, from the pull-out experiment. Apparent modulus, E_a , was calculated and generated for various replicates of aramid fibers pull-out test with different embedded length and diameter at 20°C and 0.5 mm/s and compared with the experimentally measured average shear bond strength, $\bar{\tau}$, as shown in Figure 6-15.

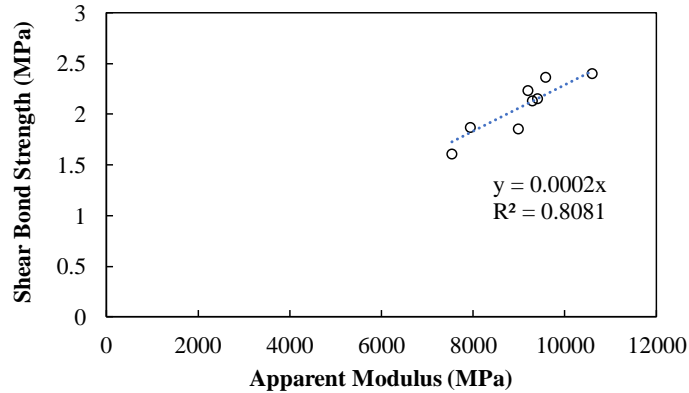


Figure 6-15. Relationship Between E_a of Binders with the Measured $\bar{\tau}$ from the Pull-out Experiment.

It was found that the E_a values are in the range of 7500 to 10500 MPa for the pull-out testing condition of asphalt mastics at 0.5 mm/s and 20°C. As expected, an almost linear

relationship was found between shear strength and apparent modulus values. The experimentally fitting function can now be used to establish a relationship between the asphalt concrete stiffness and shear strength of fibers in the mix.

For the asphalt mixtures, the same procedure applied in development of E_a for the mastics used to evaluate the apparent modulus, E_a , for asphalt concrete mixtures. Note that in developing apparent modulus for the asphalt mixtures the dynamic modulus data was used to determine the Prony coefficients. Recall that direct tension test was conducted on asphalt concrete specimens with and without fibers at different displacement rates and temperatures. The experimental data of tensile strain at peak load was then used to determine the E_a for the asphalt mixtures at different displacement rates and temperatures. Finally, the experimentally fitting equation obtained from Figure 6-15 was used to estimate the shear bond strength for the asphalt concrete samples. Figure 6-16 is plotted to compare the estimated $\bar{\tau}$ for the asphalt mix and measured $\bar{\tau}$ for the asphalt mastic against the corresponded E_a calculated for both asphalt concrete and asphalt mastic specimens. The results indicated that the shear bond strength of fibers in the DT asphalt concrete specimens at all testing conditions are lower than those obtained from pull-out test at 20°C and 0.5 mm/s. The range of shear bond strength were 0.5-1 MPa for the testing temperature of 10°C except the lowest displacement rate while at 25°C testing condition the shear bond strength of aramid in the mix was less than 0.5 MPa. These $\bar{\tau}$ values can now allow one to establish a relationship between asphalt matrix stiffness and the critical fiber length which is elaborated in the next section.

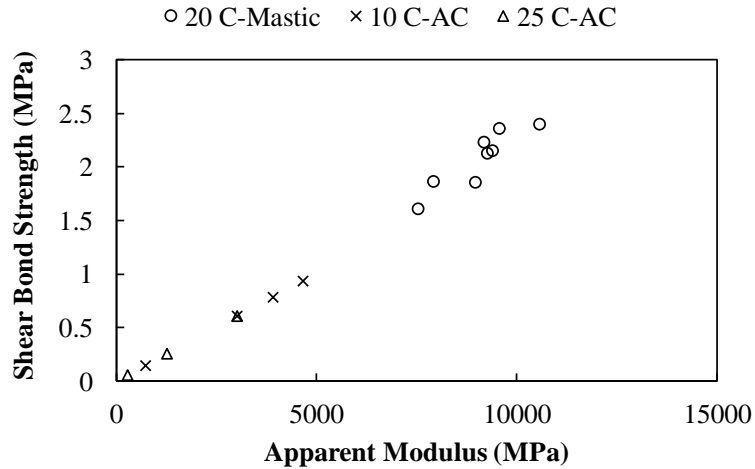


Figure 6-16. Relationship Between E_a and $\bar{\tau}$ for both Asphalt Concrete and Mastic Specimens.

6.4.7 Relationship Between Matrix Stiffness and Theoretical Critical Fiber Embedded Length

When fibers are subjected to a tensile load, they are either pulled out of the matrix or broken. Understanding the critical fiber length can help identify which mechanism is a dominating factor, which by itself allows engineers to develop a certain minimum critical embedded length (L_{ce}) design guidelines to maximize the fiber efficiency in the asphalt concrete composites. The embedded length corresponding to the fiber breaking force is the critical embedded length, L_{ce} .

Figure 6-17(a) shows the tensile force F on a single fiber and the reaction bond force between the fiber and the matrix. The reaction force is the surface area of the embedded length of the fiber multiplied by the shear bond stress between the fiber and the matrix. If the embedded length on either side of the crack is small, the fiber will be pulled from the smaller side before breaking. A certain minimum L_{ce} on each side of the crack is

required to prevent debonding the fiber. If the embedded length is further increased, the fiber will resist pulling until the stress in the fiber reaches its strength, above which the fiber will break. Figure 6-17(b) shows the critical equilibrium case when the tensile strength of the fiber is reached, and the maximum shear bond force is achieved. In such a case, the equilibrium forces can be represented by Equation (6-12) (Teklal *et al.* 2018).

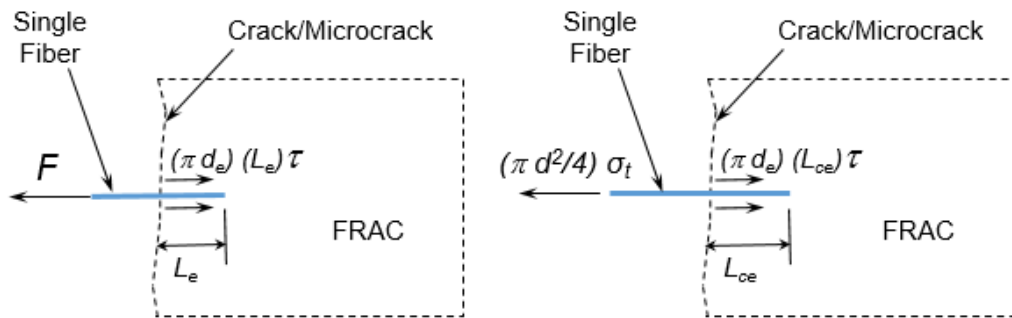
$$\left(\frac{\pi d^2}{4}\right) \sigma_t = \tau d_e L_{ce} \tau \quad (6-12)$$

Rearranging Equation (6-12), L_{ce} can be calculated as follows:

$$L_{ce} = \frac{d^2 \sigma_t}{4 d_e \tau} \quad (6-13)$$

where,

- d = diameter of a single clear fiber,
- d_e = diameter of a single fiber embedded in the FRAC,
- σ_t = tensile strength of a single fiber,
- L_{ce} = critical embedded length of a single fiber, which is the minimum embedded length required to reach its full efficiency, and
- τ = shear bond strength between asphalt matrix and fiber.



(a) Forces Applied on Fiber (b) Critical Case Before Breaking

Figure 6-17. Forces Applied on a Single Fiber at the Crack/Microcrack.

The critical length of fiber can be experimentally obtained by testing fibers at multiple different embedded length and measurement of the force required to pull-out the fiber from the matrix. As the pulling force increases, the embedded length increases up to a critical embedded length, at which the tensile strength of the fiber is reached and the fiber breaks. This was practiced by (Lee *et al.* 2005) and they concluded a critical embedded length of 9.2 mm for nylon fibers tested at 20°C. However, their conclusion does not represent the critical length of a single nylon fiber, which exist upon their dispersion, in the mix knowing that the shear bond strength of fibers varies with different fiber dimensions at 20°C (See Figure 6-12(b)). Their study, however, would be conclusive if the effect of asphalt viscoelasticity was eliminated from the pull-out test by reducing temperature similar to Park et al (2017). Therefore, recognizing the same limitation in this study, a theoretical critical embedded length for single aramid fiber was developed from Equation (6-13).

From Equation (6-13), the embedded diameter d_e is not necessarily equal to the clear fiber diameter d . In cases when the fiber is pulled at the interface without mastic coating, the two diameters are the same. In cases when the fiber is pulled with mastic coating, which was the case in this study, the effective embedded diameter is larger than the clear fiber diameter. In this study, the optical microscopy test was used to compare between the clear diameter and the embedded diameter after the pull-out test, shown in Figure 6-18. It can be seen that the diameter of the single fiber before and after pull-out test is 14.2 and 18.1 μm , respectively. The images showed that the average diameter of fibers coated with asphalt mastic after pull-out test is about 25% larger than the clear

diameter of the fiber. This procedure was selected to be consistent with previous measurement of effective fiber diameter, d_{eff} , obtained from the direct measurement.

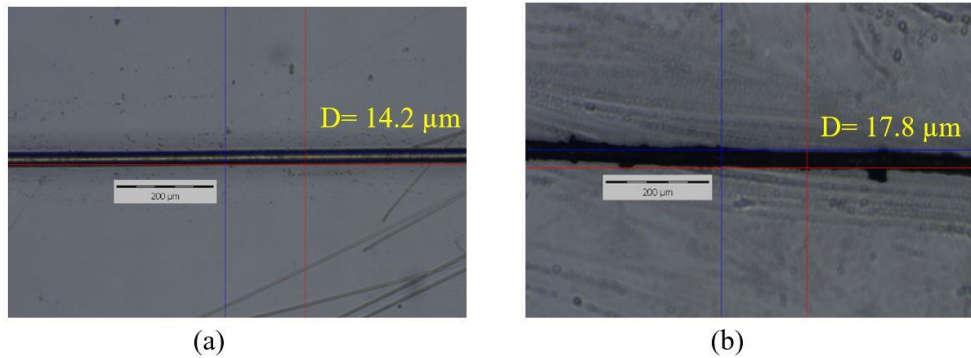


Figure 6-18. Optical Microscopy Images of Aramid Fiber (a) Before and (a) After Pull-out Test.

The critical embedded length, L_{ce} , of a single aramid fiber was therefore calculated using Equation (6-13) based on shear bond strength values obtained from the experimental data of pull-out test and theoretical data of asphalt concrete specimens. Table 6-3 shows the calculated L_{ce} for DT asphalt concrete specimens tested in CHAPTER 5 at different combinations of temperatures/ displacement rates and asphalt mastic samples, as well as the corresponded apparent modulus, E_a , and shear bond strength values. The results indicate that increasing displacement rate on asphalt concrete specimens at both 10 and 25°C increased the critical fiber embedded length. This shows that the fiber is most likely to pull out rather than break at the higher temperature condition. But at lower testing temperature or more intermediate temperature, the selected embedment length of aramid fibers is crucial for their optimal performance. For example, the critical length of fibers in the asphalt concrete tested at 10°C and 0.0059 mm/s is 24 mm (twice the embedded length of fiber =12 mm). So, when comparing the different fiber length studied in CHAPTER 5,

it can be inferred that 10 mm fibers were pulled at smaller forces and therefore they could have lost some of their efficiency under the tensile load because 10 mm fiber is embedded at a length less than its critical embedded length. In contrast, 38 mm fiber appears to be beyond the critical embedded length and the fibers might have therefore reached their breaking force, which is when the fiber tensile strength is reached.

Table 6-3. Theoretical Critical Embedded Length of a Single Aramid Fibers for Mastic and AC Specimens Tested at Different Temperatures and Displacement Rates.

Specimen Type	Test Temp (°C)	Displacement Rate (mm/s)	Apparent Modulus, E_a (MPa)	Shear Bond Strength (MPa)	L_{ce} (mm)
Mastic	20	0.5000	9500	2	4
Asphalt Concrete	10	0.0004	723	0.14	50
		0.0059	3019	0.60	12
		0.0108	3922	0.78	9
		0.0173	4659	0.93	8
	25	0.0040	276	0.06	131
		0.0099	1259	0.25	29
		0.2333	3018	0.60	12

Figure 6-19 shows the theoretical data for critical fiber length (L_c), which is simply double of the approximate embedded length obtained from Equation (6-13) vs arbitrary shear strength values between fiber and matrix in the range of 0-4 MPa. The critical fiber length ranges between 5-10 mm for a shear bond strength of above 1.5 MPa, which was the case for pull-out test at 0.5 mm/s. This large shear bond strength occurs if a binder harder than what should be used for that climate, low temperatures, and/or fast fiber displacement rates. When the shear bond strength is reduced below 1.5 MPa, the critical length exponentially increases. This small shear bond strength occurs if a binder softer than what should be used for that climate, high temperatures and/or slow displacement rates. Given that the relationship developed between shear bond strength and apparent modulus

of asphalt concrete, zones A, B, and C are recommended a range of critical aramid fiber length which can be used for high, intermediate and low temperature application of fiber reinforced asphalt concrete, respectively.

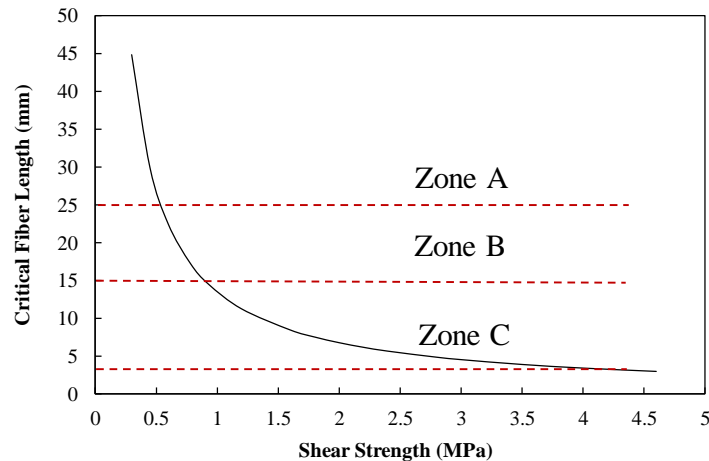


Figure 6-19. Theoretical Critical Length of Aramid Fiber vs. Shear Bond Strength.

6.5 Fiber Length Recommendations

Based on the results obtained in Figure 6-19, the approximate values of the recommended total length, which is simply equal to the theoretical critical fiber length, for different pavement distresses are shown in Table 6-4 to ensure high fiber efficiency. Table 6-4 is arranged based on the distresses commonly associated with asphalt concrete pavements in a certain region. Since different distresses apply tension or shear to fibers at different binder stiffness conditions, temperatures and/or displacement rates, the recommended fiber lengths are selected to match these conditions. Long fibers ($L > 25$ mm) are recommended if rutting is common; while short fibers ($L < 15$ mm) are more acceptable if thermal cracking is a common distress. A fiber length in the range of 15-25

mm is also recommended for fatigue cracking which is more prevalent at intermediate temperature.

Table 6-4. Recommended Fiber Lengths for Different Pavement Distresses and Fiber Types to Ensure High Efficiency.

Common Pavement Distresses	Applicable Conditions	Typical Shear Bond Strength (MPa)	Recommended Critical Fiber Length (mm)
Rutting	High Temperatures / Slow displacement Rate	$\tau < 0.5$	$L > 25$
Fatigue Cracking	Intermediate Temperatures	$0.5 < \tau < 1$	$15 < L < 25$
Thermal Cracking	Low Temperatures / Fast displacement Rate	$\tau > 1$	$L < 15$

It is important to recognize that fibers are not expected to eliminate pavement distresses but may delay their occurrences and reduce their severities. For example, fatigue cracking occurs because of the excessive repeated bending of the asphalt layer due to traffic loading applied on a weak structure. Fibers will stiffen the asphalt layer to some extent and reduce bending but may not totally compensate for the weak pavement condition.

Note that the total critical length of the fiber should be larger than twice the critical embedded length on either side of the crack in order for the fiber to reach its full effectiveness. Under ideal conditions, the crack would be in the middle of the fiber and the fiber is oriented perpendicular to the crack. Obviously, the chance of this condition to happen is limited. Since short fibers are typically randomly distributed and are not necessarily perpendicular to the cracks or equally embedded on the two sides of the cracks, these recommended fiber lengths may not ensure 100 percent fiber efficiency but are practical values with reasonable efficiency. Fiber efficiency factors are discussed in the next chapter.

CHAPTER 7

DEVELOPMENT OF MICROMECHANICAL MODEL FOR PREDICTING THE TENSILE STRENGTH OF FIBER REINFORCED ASPHALT CONCRETE

7.1 Introduction

This study attempted to experimentally investigate the interaction of these properties to some extent; however, a full factorial experiment to study all these parameters, while needed, are time-consuming and costly. Alternatively, mathematical models can be used to similarly examine the relationships between the mentioned parameters which can support further understanding into the fundamental mechanisms of reinforcement. Along this line, numerous studies have proposed via analytical and numerical models to predict the static properties of polymer and ceramic matrix composites based on the size, shape, and orientation of the reinforcing phase (Bentur and Mindess 2006, Gibson 2011, Mobasher 2011, Clyne and Hull 2019).

Micromechanical models select a common set of assumptions including perfect alignment fibers, and homogeneous, isotropic, elastic, and are free of voids system for both fibers and matrix (Das *et al.* 2017). Furthermore, in this theory, a representative volume element concept is used to extrapolate the interactions between the phases in the element to predict the interactions occurring within the entire composite, and therefore, they can be employed to predict the behavior of the bulk composite. The models are also based on the mechanical interactions between the elements and specific molecular interactions are typically disregarded (Das *et al.* 2017). Micromechanical models are mainly suitable since they can predict the properties of a composite material on the basis of simply quantifiable

properties of the individual phases including the material, such as the individual stiffness, Poisson's ratio, fiber aspect ratio, and volume fraction of the phases. Various micromechanical models have considered these properties to predict the mechanical properties of fiber reinforced composites. Micromechanical analyses for fiber reinforced composites are based on three categories including mechanics of composite materials, the elasticity theory, and empirical solutions. This objective of this study is to attempt to present a variety of micromechanical techniques that could be potentially instructive in predicting the tensile strength of mechanically-fiber reinforced asphalt concrete. The presented models have simple and practical closed-form solutions that may be used to provides further insight in better understanding the mechanism of fiber reinforced asphalt concrete.

7.2 Formulation of Micromechanical Model for Fiber Reinforced Asphalt Concrete

Among several well-established micromechanical models to predict the mechanical behavior of composites. However, some have been adopted and commonly used in predicting mechanical properties of short fiber reinforced composites. These models are expressed in terms of tensile strength and the relevant parameters to this study are further discussed as follows.

7.2.1 Voigt's and Reuss's Models

The Voigt's or parallel model refers to the assumption that fiber and matrix experience the same strain condition simply expressed by rule of mixtures in Equation (7-1). In contrast, the Reuss's or series model assumes an isostress condition where the applied

transverse stress is equal in both the fiber and the matrix and presented by the inverse rule of mixture in Equation (7-2) (Gibson 1994).

$$\sigma_c = \sigma_F V_F + \sigma_M V_M \quad (7-1)$$

$$\sigma_c = \frac{\sigma_F V_M}{V_M \sigma_F + V_F \sigma_M} \quad (7-2)$$

Where; σ_c , σ_F , and σ_M are the strength of composite, fiber, and matrix, respectively. V_F and V_M are the volume fraction of fibers and matrix, respectively. It should be noted that the parallel and series models are used to predict the mechanical properties of aligned continuous fiber composites; however, they are still used for the sake of comparison with other micromechanical models.

7.2.2 Modified Rule of Mixture

The ultimate tensile strength of short fiber composites can be also modeled by the modified rule of mixtures according to Equation (7-3) (Clyne and Hull 2019):

$$\sigma_c = \mu \sigma_F V_F + \sigma_M V_M \quad (7-3)$$

Where μ is the fiber efficiency factor which can be defined as the product of the fiber orientation factor (χ_θ) and the fiber length and interface factor (χ_L) (Fu and Lauke 1996). The efficiency factors are dependent on the adhesion degree at fiber–matrix interface and characterizes the effect of fiber reinforcement in the composite. When the value of μ approaches to the unity, this corresponds to the maximum reinforcing capacity of the fibers. However, typical values of μ (the product of χ_θ and χ_L) are in the range of

0.17–0.20 for good quality of interfaces (Fu and Lauke 1996). The determination of orientation and length factors will be discussed later.

7.2.3 Hirsch Model

Hirsch's model is a combination of parallel and series models which is obtained from Equation (7-4) (Hirsch 1962). Parameter β is the interfacial adhesion parameter which determines the stress transfer between fiber and matrix (Kalaprasad *et al.* 1997). It is to be noted that Hirsch's model reduces to series model when the parameter β is 1 and to parallel model when the parameter is 0.

$$\sigma_c = \beta (\sigma_F V_F + \sigma_M V_M) + (1 - \beta) \frac{\sigma_F V_M}{V_M \sigma_F + V_F \sigma_M} \quad (7-4)$$

7.2.4 Cox Shear-Lag Model

Cox's shear lag theory is one of the most widely used analytical models for prediction of the tensile strength of short-fiber composites presented in Equation (7-5) (Cox 1952). This equation is similar to the rule of mixture described earlier except that the stresses in the fiber are scaled down by an efficiency factor known as shear lag parameter (λ) which varies between 0 and 1 and can be obtained from Equation (7-6). This shear lag parameter accounts for the difference in the strain along the fiber length. If the entire fiber length is fully strained, the efficiency factor approaches 1 and the equation becomes the parallel model (Obaid 2018).

$$\sigma_c = \sigma_F \left[\frac{1 - \tanh\left(\frac{\lambda L}{2}\right)}{\left(\frac{\lambda L}{2}\right)} \right] V_F + \sigma_M V_M \quad (7-5)$$

$$\lambda = \sqrt{\frac{2 G_M}{E_F r^2 \ln\left(\frac{P_F}{V_F}\right)}} \quad (7-6)$$

$$G_M = \frac{E_M}{(1+\nu_M)} \quad (7-7)$$

Where;

G_M = shear modulus of the matrix obtained from Equation (7-7);

E_F = the moduli of fiber determined experimentally;

E_M = modulus of the matrix determined experimentally;

ν_M = Poisson's ratio of the matrix assumed to be 0.35;

P_F = packing factor which is indicative of the geometrical arrangement of the fibers with π as square packing and $2\pi/\sqrt{3}$ as hexagonal packing (Rao *et al.* 2012);

r = the fiber radius; and

L = the fiber length

7.2.5 Nairn's Modified Shear-Lag Model

While the micromechanical shear lag model has been used in many studies of fiber reinforced composites, it is often criticized by their theoretical flaws. The original shear lag theory disregards radial displacements in its calculation of the shear strain. In fact, it only assumes the axial displacements as a result of shear stress within the matrix whereas it is argued that the shear stress should correspond to the summation of the derivatives of both the radial and axial displacements according to an exact elasticity analysis (Nayfeh 1977, Nairn 1997). Therefore, a modified shear lag model proposed by (Nairn 2004), which enabled the original shear-lag model to be described in a generalized case by including shear stresses as shape functions and addition of the interfacial adhesion parameter. The generalized shear lag parameter is expressed in Equation (7-8).

$$\lambda = \sqrt{\frac{2}{E_F E_M r^2} \left[\frac{E_F V_F + E_M V_M}{\frac{V_M + 1}{4G_F + 2G_M} \left[\frac{1}{V_M} \ln \left(\frac{1}{V_F + \kappa} \right) - 1 - \frac{V_M}{2} \right] + \frac{1}{r D_s}} \right]} \quad (7-8)$$

Where;

κ = a constant equal to 0.009 added to correct for a problem in the use of shape functions without which Equation (7-8) would become infinity with V_f of 0 (Nairn 2004);

G_F = shear modulus of the fiber equal to 16 GPa which was experimentally measured by (Tsai and Daniel 1999); and

D_s = imperfect interface parameter which has dimension of stress divided by length (Hashin 1991).

7.2.6 Halpin-Tsai Model

The theory of Halpin-Tsai solution is based on the early micromechanical works of Hill (Hill 1965) and Hermans (Hermans 1967). Hermans generalized the form of Hill's self-consistent solution by considering a single fiber enclosed in a cylindrical shell of the matrix, that is embedded in an infinite medium assumed to have the average properties of the composite. Halpin and Tsai then reduced Herman's solutions into a simpler analytical model modified for various reinforcement geometries, including discontinuous filler reinforcement. Halpin-Tsai model has long been popular for predicting the properties of short fiber reinforced composites over a wide range of elastic properties and fiber volume fractions, which is developed by curve fitting to results that are based on elasticity (Gibson 1994). The Halpin-Tsai equations are semi-empirical in nature due to the fact that the involved parameters in the curve fitting carry physical meaning (Halpin 1969, Halpin and Kardos 1976). Although other micromechanical models exist, some of which are

recognized to have a more rigorous theoretical foundation discussed earlier, the Halpin-Tsai equations are the most commonly used because of their relative simplicity of form and their capability to describe experimental results with a rational degree of precision for a variety of reinforcement geometries (Mouritz and Gibson 2007). A detailed review and derivations of this model can be found in (Halpin and Kardos 1976). The following form of the Halpin and Tsai equation is used to predict the tensile strength of M-FRAC.

$$\sigma_C = \sigma_M \left(\frac{1 + \xi \eta V_F}{1 - \eta V_F} \right) \quad (7-9)$$

$$\eta = \frac{(\sigma_F/\sigma_M) - 1}{(\sigma_F/\sigma_M) + \xi} \quad (7-10)$$

where ξ is a shape fitting parameter in the range of 0 and ∞ which is determined by $2(L/D)$ for the circular fiber and $2(L/T)$ for rectangular fiber according to (Halpin and Kardos 1976). L , T , and D refer to the length, diameter, and thickness of fiber. Also, Halpin-Tsai equation reduces to the inverse rule of mixture with $\xi \rightarrow 0$ and to the rule of mixture with $\xi \rightarrow \infty$ (Halpin and Kardos 1976).

7.2.7 Incorporation of Viscoelasticity

The existing micromechanical models for short fiber reinforced composites are fundamentally developed based on elastic type of matrix composites. There have been several efforts to model the time-dependent response of viscoelastic short-fiber composites, particularly focusing on the stress relaxation of fiber reinforced polymer composites. Viscoelastic polymers have been modeled by tensor analysis using an exact elasticity analysis to understand the stress transfer in viscoelastic composites,

phenomenological models using for example Maxwell elements in various forms, and finite-element models (Obaid *et al.* 2017). Modeling approaches often encounter complexities when dealing with viscoelastic materials. In this study, the effect of viscoelasticity was initially considered using a viscoelastic continuum damage theory model and experimental stress-strain data from uniaxial direct tension test. The approach undertaken in this study is explained in the following section.

7.2.7.1 Viscoelastic Continuum Damage Theory

Viscoelastic continuum damage (VECD) theory was used to account for both the inherent linear viscoelasticity of the composite as well as the damage resistance. VECD theory is particularly used to detect the unique relationship between the amount of damage, S , and material integrity, measured as pseudo-stiffness, C . Schapery's work of potential theory based on thermodynamic principles was used to develop this relationship denoted as the damage characteristic curve. (Underwood *et al.* 2010). The VECD model includes three primary components (Underwood *et al.* 2006):

Pseudo strain energy density function:
$$W^R = \frac{1}{2}(\varepsilon^R)^2 C ; \quad (7-11)$$

Stress-pseudo strain relationship:
$$\sigma = \frac{dW^R}{d\varepsilon^R} = C \times \varepsilon^R ; \quad \text{and} \quad (7-12)$$

Damage evolution law:
$$\frac{dS}{dt} = \left(-\frac{\partial W^R}{\partial S} \right)^\alpha = \left(-\frac{1}{2}(\varepsilon^R)^2 \frac{dC}{dS} \right)^\alpha \quad (7-13)$$

Where, in Equations (7-11) - (7-13), σ is stress, ε^R is pseudo strain and α is the damage evolution rate. Pseudo strains is the response from linear viscoelastic stress to a certain strain input. According to elastic-viscoelastic correspondence principle, elastic

solutions can be used to solve viscoelastic problems when physical strains are replaced by pseudo strains (ε^R) (Schapery 1984). Using pseudo strain in place of physical strain, Hooke's Law for linear elastic material can be rewritten as follow:

$$\sigma = E_R \varepsilon^R \quad (7-14)$$

Supplementary theoretical details of this concept can be found in the literature (Schapery 1984, Chehab 2002). The most important effect of ε^R is that they eliminate any time effects when plotted with stress, which allows measurement of damage through the use of simplified continuum damage models (Kim, Baek, *et al.* 2008). The uniaxial pseudo strain (ε^R) is defined in form of a convolutional integral according to Equation (7-15).

$$\varepsilon^R = \frac{1}{E_R} \int_0^t E(t - \tau) \frac{d\varepsilon}{d\tau} d\tau \quad (7-15)$$

Where; E_R is a reference modulus included for dimensional compatibility and is typically taken as one (Underwood 2011); $E(t)$ is the relaxation modulus; t is the time of interest; and τ is an integration constant. Also, a primary assumption of the constitutive relationship in Equation (7-15) is that the $E(t - \tau)$ is representative of the time dependence component in the material (i.e., there is no time dependence in Poisson's ratio). This assumption is typically used when working with LVE materials, which should be fairly a valid assumption in this study given the experimental test condition considered for modeling of asphalt concrete. The convolutional model in Equation (7-15) is solved by transforming into an algebraic operation using the so-called state variable formulation. Theoretical derivations of state variable methods can be found elsewhere (Simo and Hughes 2006). In short, the state variable approach allocates a variable to each Maxwell component in the Prony representation of the relaxation modulus (Equation (7-16)). This variable then tracks

the behavior, or state, of the given element throughout loading. The formulation applied in this research is represented in Equation (7-17):

$$(\varepsilon^R)^{n+1} = \frac{1}{E_R} (\eta_0^{n+1} + \sum_{i=1}^m \eta_i^{n+1}) \quad (7-17)$$

Where η_0 and η_i are internal state variables for the elastic response and for the specific Maxwell element, i , at time step, $n+1$, respectively. These variables are defined per Equations (7-18) and (7-19), respectively:

$$\eta_0^{n+1} = E_\infty (\varepsilon^{n+1}) \quad (7-18)$$

$$\eta_i^{n+1} = e^{-(\Delta t)/\rho_i} \eta_i^n + E_i \left(\frac{\varepsilon^{n+1} - \varepsilon^n}{\Delta t} \right) \rho_i (1 - e^{-(\Delta t)/\rho_i}) \quad (7-19)$$

Equation (7-13) can be recast using the chain rule and an approximation of finite differences to determine the damage at each time step, i as shown in Equation (7-20) (Lee and Kim 1998).

$$S_i = S_{i-1} + \left(-\frac{1}{2} (\varepsilon^R)_i^2 (C_i - C_{i-1}) \right)^{\alpha/1+\alpha} (\xi_i - \xi_{i-1})^{1/\alpha+1} \quad (7-20)$$

When identified, the damage characteristic curve (C-S) can be produced by plotting the damage along with the pseudo stiffness from Equation (7-12). To fit the damage characteristic curve, Equation (7-21), the power law equation (One of the most common functional forms), was used.

$$C = 1 - aS^b \quad (7-21)$$

Where; coefficients a and b are fitting parameters which are evaluated by minimizing the error between the model equation and experimental data using the solver

function in Microsoft EXCEL. In predicting the tensile stress behavior of a viscoelastic material, damage and pseudo stiffness for the full loading history are the first quantities required. In this case, the damage function would be known and Equation (7-13) can be solved either analytically or numerically using the coefficients a and b to represent the damage function. Once the damage history is known the pseudo stiffness at each time increment can also be calculated and used with Equation (7-22) to predict the stress response to a specified strain.

$$\sigma_M = C \times \int_0^t E(t - \tau) \frac{d\varepsilon}{d\tau} d\tau \quad (7-22)$$

7.2.8 Incorporation of Efficiency Factors

In fiber reinforced composites containing randomly distributed short fibers, not all the fibers are aligned in the direction of the applied load which is the case for continuous fiber, instead, the majority of fibers are likely to lie at angles to the load direction (Li *et al.* 1990b). This inherently reduces the efficiency of fibers reinforcement in transferring shear stress transfer within matrix, and consequently in enhancing the properties of composites (Bentur and Mindess 2006, Fu *et al.* 2009). This is particularly an important issue to be addressed in using micromechanics to predict the properties of composites since most of the developed micromechanical models discussed previously are mainly based on assumption of unidirectional discontinuous fiber reinforced composites. The effect of fiber efficiency has been stated in terms of an efficiency factor, which is a value between 0 and 1, described by the ratio of the reinforcing effect of the short, inclined fibers over the reinforcement anticipated from continuous fibers aligned parallel to the load. In this study, the efficiency factors which are accounted for include fiber orientation (χ_θ), fiber length

(χ_L), fiber dispersion factor (χ_D), and matrix factor (χ_M). While the first two factors have been recognized and quantified in many previous studies on the basis of analytical treatment as well as empirical calculations (Bentur and Mindess 2006, Fu *et al.* 2009), the latter two factors are particularly introduced in this study which are determined based on experimental measurements. These factors will be used in modification of micromechanical models for fiber reinforced asphalt concrete described earlier and the quantification methods are separately elaborated as follows.

7.2.8.1 Fiber Orientation Factor

Fiber orientation has a significant effect on the mechanical behavior of short fiber reinforced composites. For a composite containing randomly distributed short fibers, a higher strength is achieved when fibers are oriented predominantly in the direction of the applied load compared with fibers oriented transversely to the force. Various experimental procedures such as X-ray tomography, a magnetic method, and slicing photometry, and AC-impedance (Suuronen *et al.* 2013) and theoretical derivations have been used to quantify the orientation of short fibers in the composites (Li *et al.* 1990b, 1991, Fu and Lauke 1996). The fiber orientation factor was theoretically determined using a probabilistic approach based on the work of (Jayaraman and Kortschot 1996) who corrected the Fukuda-Kawata model for the strength theory (Fukuda and Kawata 1974). The theoretical derivations to determine orientation factor are explained as follows.

The model considers a circular fiber of length L with cross-sectional area $A_F = \pi r_F^2$ embedded inside a matrix and misoriented at an angle θ to the direction of loading illustrated in Figure 1. An arbitrary scan line (cross-section), perpendicular to the loading

direction, is used to evaluate the total fiber contribution to the stress in the composite normal to the scan line.

According to Fukuda and Kawata (1974), the fibers orientation distribution satisfies the two-dimensional condition of probability density function per Equation (7-23).

$$\int_0^{\pi} g(\theta) d\theta = 1 \quad (7-23)$$

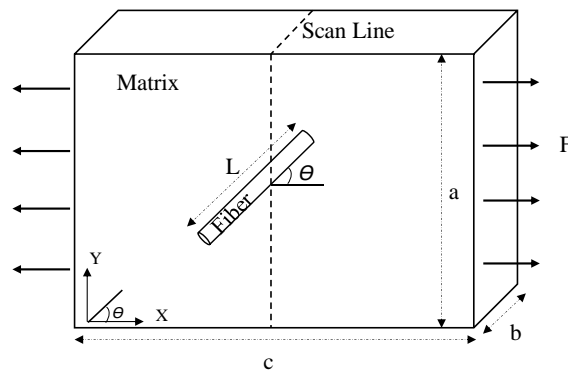


Figure 7-1. Schematic Drawing of a Fiber at an Angle Across an Arbitrary Crack Plane.

The projected length of fiber on X-axis orientated with angle θ from the loading direction can be represented by:

$$L_x = L \cos\theta \quad (7-24)$$

The volume fraction of the fibers is obtained by the total volume of fibers over total volume of the specimen:

$$V_F = \frac{N A_F L}{abc} \quad (7-25)$$

Total number of fibers with an orientation between $(\theta + d\theta)$ is expressed by revising Equation (7-25) and the probability density function from Equation (7-23):

$$N_{\theta} = \left(\frac{V_{Fabc}}{A_{FL}} \right) g(\theta) d\theta \quad (7-26)$$

The total projected fiber length, L_T , along the loading direction is calculated by:

$$L_T = N_{\theta} L_x = \left(\frac{V_{Fabc}}{A_{FL}} \right) g(\theta) d\theta (L \cos \theta) \quad (7-27)$$

Now, the total number of fibers of orientation between θ and $(\theta + d\theta)$ crossing the scan line, N_{scan} , can be simply defined by the total projected length of the fibers on the X-axis divided by the length of the specimen in the loading direction, c , as follows:

$$N_{scan} = \frac{L_T}{c} \quad (7-28)$$

The total load carried by all fibers in the scan line is:

$$F_T = \sum_{\theta} N_{scan} F_x \quad (7-29)$$

Fukuda and Kawata (1974) previously defined the average axial force in a fiber of length L and orientation θ in the specimen by:

$$\bar{F}_F = A_F \Phi E_F \varepsilon_0 (\cos^2 \theta - \nu_s \sin^2 \theta) \quad (7-30)$$

Where E_F is the Young's modulus of the fiber, Φ is a dimensionless function of fiber length and other material properties, ε_0 is the strain in the material, and ν_s is the Poisson's ratio of the material. The projected average axial force in a fiber of length L and orientation θ on X-axis direction) is:

$$F_x = \bar{F}_F \cos \theta = \Phi A_F E_F \varepsilon_0 (\cos^3 \theta - \nu_s \sin^2 \theta \cos \theta) \quad (7-31)$$

Substituting Equation (7-31) in (7-29), we have:

$$F_T = \int_0^{\frac{\pi}{2}} \phi A_F E_F \varepsilon_0 (\cos^4 \theta - \nu_s \sin^2 \theta \cos^2 \theta) \left[\left(\frac{V_F ab}{A_F} \right) g(\theta) d\theta \right] \quad (7-32)$$

$$F_T = \phi V_F E_F \varepsilon_0 ab (C_{PP}) \quad (7-33)$$

$$C_{PP} = \int_0^{\frac{\pi}{2}} g(\theta) (\cos^4 \theta - \nu_s \sin^2 \theta \cos^2 \theta) d\theta \quad (7-34)$$

C_{PP} is the fiber orientation factor (χ_θ) and can be solved by applying a boundry condition to the following probability density function:

$$g(\theta) = \frac{1}{\frac{\pi}{2}} \quad \text{if} \quad 0 < \theta < \frac{\pi}{2} \quad (7-35)$$

$$g(\theta) = 0 \quad \text{if} \quad \theta > \frac{\pi}{2} \quad (7-36)$$

The above boundry condition is true assuming a complete random orientation of the fibers in the matrix as there is equal probability that the fiber has a misorientation angle (θ) between 0 and $\pi/2$ (Jayaraman and Kortschot 1996, Obaid 2018). If $g(\theta) = \pi/2$, the integration of the fiber orientation factor, C_{PP} , from Equation (7-34) can be calculated as follows:

$$\chi_\theta = C_{PP} = \frac{2}{\pi} \times \frac{3}{8} \times \frac{\pi}{2} - \frac{2}{\pi} \times \frac{35}{100} \times \frac{\pi}{16} = 0.33 \quad (7-37)$$

Note that the Poisson's ratio was assumed to be 0.35 which is typical for asphalt concrete material. Also, the variation in Poisson's ratio of the asphalt concrete with applied load and relaxation is disregarded for the calculation. The orientation factor of 0.33 obtained in this study is reasonable based on the recommendation of the range given in the previous studies (Bentur *et al.* 2006, Fu *et al.* 2019), and close to the value of 0.375 as presented by the well-known Krenchel factor for a random-planar distribution (Krenchel

1964) and the experimentally measured value of 0.386 using stereolithography approach (Cheah *et al.* 1999).

7.2.8.2 Fiber Length Factor

The effect of fiber length can be examined in terms of the stress transfer mechanisms. As discussed in CHAPTER 6, a critical fiber length, L_c , can be described by the minimum length of fiber required for the stress (load) build-up in the fiber which is equivalent to its strength (or failure load) (Laws 1971, Bentur and Mindess 2006). For a frictional shear stress transfer (or linear stress transfer), The critical fiber length is calculated by:

$$L_c = \frac{\sigma_{Fu} \times r_F}{\tau_{Fu}} \quad (7-38)$$

The fiber length efficiency factor is obtained by following the Equations (7-39) and (7-40) (Kelly and Macmillan 1987, Bentur and Mindess 2006).

$$\eta_L = 1 - \frac{L_c}{2L} \quad \text{For} \quad L > L_c \quad (7-39)$$

$$\eta_L = \frac{\tau_{Fu}}{2r_F \sigma_{Fu}} = \frac{1}{2} \frac{L}{L_c} \quad \text{For} \quad L < L_c \quad (7-40)$$

7.2.8.3 Fiber Dispersion Factor

It has been recognized that a good dispersion and distribution of fibers in the composites is a key in maximizing the reinforcing efficiency of any composite materials. It was reported that the mechanical performance of composites materials are strongly governed by the state of fibers, inclusive of how the fibers are dispersed (dispersion), where

the fibers are located (distribution), how they are arranged (orientation) and their surface morphology (Noorvand *et al.* 2018). The dispersion particularly becomes more important when short fibers are used in composite materials in a form of bundles (multifilament fibers), which is the case in this study. Nevertheless, while the fiber efficiency factors of orientation and length have been widely used in correcting the micromechanical models containing short randomly distributed fiber reinforced composites, there is no or very few studies on using the efficiency of fiber dispersion in the theoretical methods. The main reason should be attributed to the difficulty in measurement of fiber dispersion.

In CHAPTER 3 of this study, a procedure of fiber extraction from an asphalt mix was introduced to determine the percentage of individual fibers in the mix called *FDP*. Here, fiber dispersion factor, χ_D , is equal to the value of *FDP* with 0 representing very poor dispersion (no dispersion of fibers and all are remained in the form of bundles in the mix) and 1 indicating a perfect dispersion (where the state of fibers are all individual in the specimen). The value of 1 is what the micromechanical models in reality present which might not be possible particularly when fabricating specimens in the laboratory (For more details refer to CHAPTER 3). Therefore, in this study the fiber efficiency dispersion factor, χ_D , was applied to modify the volume fraction of fibers for use in the micromechanical models, as shown in Equation (7-41).

$$V_{F'} = \chi_D \times V_F \quad (7-41)$$

Where $V_{F'}$ is adjusted volume fraction of fibers which will be used to replace the V_F in all the presented micromechanical models.

7.2.8.4 Matrix Factor

In the CHAPTERS 4 and 5 of this study, it was found that the reinforcement efficiency of poly-aramid microfibers depends on the composition of asphalt concrete mix. In other words, the experimental test results showed that the degree of fibers reinforcement efficiency on improving the mechanical performance of asphalt concrete varied from one mix to another. Then, an index parameter, $FAM_{T(Index)}$, related to the gradation of the mix was introduced to elucidate the discrepancies in varied mechanical test result due to fibers. It was observed that the experimental calculation of $FAM_{T(Index)}$ falls within the range of 0.5-2.5 mm for a dense-graded asphalt concrete mix. Note that the FAM parameter may not be valid when dealing open graded asphalt mixes and asphalt mortars (they contain only fine aggregates) and they may to be treated differently. The matrix parameter, χ_M , was then introduced by normalizing the parameter $FAM_{T(Index)}$ from Equation (4-23) to fall in the range of 0 to 1, expressed in Equation (7-42).

$$\chi_M = \frac{FAM_{T(Index)}}{2.5} \quad (7-42)$$

The higher value of the matrix parameter, χ_M , implies higher efficiency from the matrix and the mix type (specifically gradation) which maximizes the reinforcement benefits of fibers.

7.2.9 *Model Assumptions*

In formulation and selection of micromechanical models, several assumptions were adopted to predict the tensile strength of fiber reinforced asphalt concrete which are listed as follows:

- In CHAPTER 5, monotonic direct tension test results revealed the efficiency of fiber reinforcement in enhancing the tensile capacity of asphalt concrete mix varied by different loading rates and temperatures. This was attributed to the different mechanisms including crack propagation and shear stress transfer between fibers and matrix, which was particularly noted in pull-out test results in CHAPTER 6. This necessitates the consideration of viscoelasticity effect into modeling approach in predicting the tensile strength of M-FRAC. It was hence attempted to introduce the viscoelastic component of asphalt concrete into micromechanical models using Equation (7-22). However, the viscoelastic component in the model did not provide any information on the interfacial properties of fibers and asphalt matrix and mechanism of crack propagation as function of loading rate and temperature. Therefore, the viscoelasticity theory in the modeling approach was abandoned. the experimental test condition selected to compare with the theoretical models were 10°C and 0.35 mm/min on specimen, and it was assumed that the deformation of asphalt binder matrix is negligible until the peak load for the test condition.
- The existence of notch on the specimens do not notably change the percentage improvement in the maximum tensile stresses of M-FRAC compared with asphalt concrete. So, it was assumed that the values of maxim tensile stresses are indicative of tensile strength of specimens.
- The individual aramid fibers are linearly elastic, either isotropic or transversely isotropic, identical in shape and size, and can be characterized by an aspect ratio; and the matrix is isotropic.

- The fibers were assumed to be randomly distributed in terms of both orientation and location and thus, so a probabilistic approach needed is valid.
- The matrix and the interface between matrix and fibers are free of voids.

7.3 Results and Discussion

Figure 7-2 compares the tensile strengths results from the experiment and the micromechanical models for C-19-0.05, C-19-0.15, and C-19-0.25 specimens. It can be seen that all the models expect Reuss's overpredict the strength of FRAC compared with the experimental data. Among all the models, Hirsch, shear lag, and Halpin-Tsai models showed the closest agreement with experimental data.

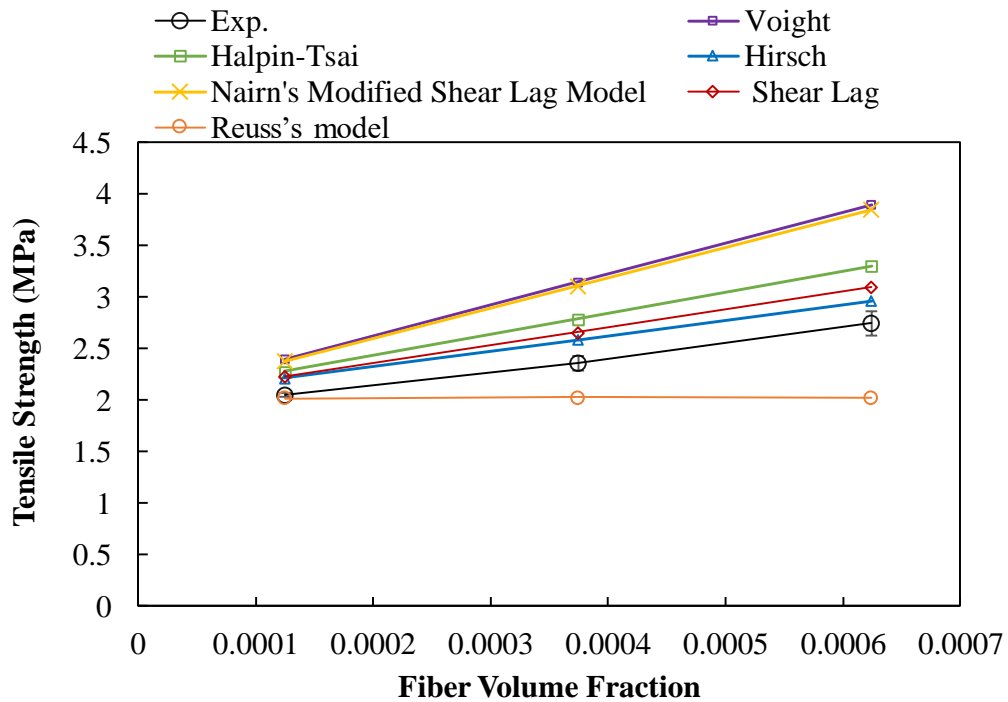


Figure 7-2. Comparison of Empirically and Theoretically Measured Tensile Strength of FRAC at Different Fiber Volume Fractions.

7.3.1 Hirsch Model

As mentioned earlier, Hirsch (1962) applied an adhesion parameter, β , into parallel-series models to account for the imperfect interface existing in short fiber reinforced composites. Previous studies have shown a good agreement between calculated theoretical data and measured experimental results of mechanical properties of short fiber reinforced composites when the value of β is between 0.4-0.6 (Kalaprasad *et al.* 1997, Rao *et al.* 2012). In this study, the value of 0.5 for the parameter β showed the best fit with the experimental data. However, since this parameter in essence is an arbitrary value given to the model to obtain the best experimental fit, therefore, the further use of this theory is abandoned due to the lack of contribution to the overall understanding into the reinforcement mechanism of fibers in the asphalt concrete.

7.3.2 Shear Lag Model

The shear lag model developed by Cox (1952) has been often criticized for two of its fundamental assumptions. One is discounting the effect of stress amplification at the fiber ends, and the other is ignoring that the radial displacement due to matrix tensile stress (Nayfeh 1977, Nairn 1997). Nairn (1997) proposed a modified version of shear lag model in which both the radial and axial displacements were included into the shear lag theory. However, other studies reported that Nairn's 1997 model significantly overpredicted the mechanical properties of fiber reinforced composites compared with experimental data, he further modified his model by incorporating an adhesion parameter, D_s , to account for imperfect interface in the model (Nairn 2004). However, unlike Hirsch' model, the parameter D_s has a physical quantity defined by stress over displacement and introduced

by (Hashin 1991). While in perfect interface assumption all displacements are considered continuous between the fiber and the matrix, Hashin (1991) modeled the concept of imperfect interface in unidirectional fiber composites through use of displacement discontinuities between fiber and matrix on the basis of the generalized self-consistent scheme model. He specifically did this by introducing a physical term and finite dimension for an interface zone commonly known as an interphase. Within the interphase, the mechanical properties vary from both the matrix and fiber. If the interphase has an effect on the properties of a composite, then it must allow displacement of the fiber proportionate to the matrix.

Realizing that the theoretical derivatizations of the thickness or the mechanical properties of the interphase is a very complicated task, Nairn and Liu (1997) and Paipetis et al. (1999) evaluated stress transfer in the fragmentation test using a stress-function method based on a Bessel-Fourier series stress function. The Bessel-Fourier analysis is a full axisymmetric analysis of fiber/matrix stress transfer that includes imperfect interface effects and is nearly exact (Nairn and Liu 1997). It was shown that the Nairn's modified shear lag analysis and the Bessel-Fourier analysis agreed well for both a perfect and an imperfect interface which verifies the modified shear lag method (Nairn and Liu 1997, Paipetis *et al.* 1999). By varying the interface parameter, Nairn (2004) fit his model prediction to the experimental data in order to determine the quality of interface. The higher value of D_s implies a better fiber–matrix interfacial adhesion and $D_s = \infty$ literally means a perfect interface between the fiber and matrix. In this study, by excluding the interface parameter the model prediction significantly overpredicted the strength of the materials which was expected due to the inclusion of the radial displacement in the shear lag

parameter, as shown in Figure 7-2. However, by introducing the interface parameter into the model, a very good fit the experimental data was obtained. For 19 mm fiber specimens as shown in Figure 7-2, the best fit of the Nairn's modified shear lag model was determined by setting the interface parameter to $rD_s = 3 \text{ MPa}$. Nevertheless, the original shear lag model was further used and modified in this study for predicting the tensile properties of M-FRAC since it has a simpler form and requires no experimental parameter fitting.

7.3.3 Generalized Micromechanical Models for Predicting Tensile Strength of FRAC

Both shear lag and Halpin-Tsai models were modified using the fiber efficiency factors, discussed earlier. The fiber dispersion factor, χ_D , and the matrix factor, χ_M , were included in both models to correct the volume fraction of fibers ($V_{F'}$) and to account for the asphalt mix composition, respectively. Because of the empirical nature of Halpin-Tsai equations, the value of shape fitting parameter, ξ , have been adjusted in different studies as appropriate to obtain the best fit to their experimental data (Mouritz and Gibson 2007). The parameter ξ is based on the fiber geometry, fiber distribution, and fiber loading conditions (Tucker III and Liang 1999, Facca *et al.* 2006). In this study, the parameter ξ was modified by the product of χ_θ and χ_M to account for orientation and mix composition of M-FRAC. The parameter χ_θ was included since the model is suitable for predicting the properties of unidirectionally oriented short-fiber-reinforced composites according to Halpin and Kardos (1976). The modified version of Shear lag and Halpin-Tsai models are summarized and presented in Table 7-1. It should be noted that no arbitrary values were used in the models for predicting the tensile strength values. The only assumed values were Poisson's ratio, ν_M , and fiber packing factor which were 0.35 and $2\pi/\sqrt{3}$, respectively

used in shear lag model, which are close approximation to their actual values. Nevertheless, their effects on the final outcome values of tensile strength were insignificant.

The accuracy of these proposed micromechanical models for predicting the tensile strength of M-FRAC relative to experimental measurements are now discussed with respect to fiber volume fraction and aspect ratio. Recall that the experimental measurements are those from monotonic direct tensing testing from CHAPTER 5 of this study at 10°C and 0.35 mm/min on specimens. In addition, general applicability of these models will be further examined and validated by considering experimental work of others in the literature.

Table 7-1. Proposed Modified Micromechanical Models for Predicting the Tensile Strength of FRAC.

Model	Equation	Nomenclature
Modified Shear Lag Model	$\sigma_C = \chi_M \sigma_F \left[\frac{1 - \tanh\left(\frac{\lambda L}{2}\right)}{\left(\frac{\lambda L}{2}\right)} \right] V_{F'} + \sigma_M V_M$ $\lambda = \sqrt{\frac{2 G_M}{E_F r^2 \ln\left(\frac{P_F}{V_{F'}}\right)}} \quad G_M = \frac{E_M}{(1 + \nu_M)}$	σ_C : Strength of composite σ_F : Strength of fiber σ_M : Strength of matrix V_M : Volume fraction of matrix $V_{F'}$: Volume fraction of fiber L : Fiber length r : Fiber radius λ : Shear-lag parameter G_M : Shear modulus of matrix E_M : Elastic Modulus ν_M : Matrix Poisson's ratio P_F : Packing factor ($2\pi/\sqrt{3}$ for hexagonal packing)
Modified Halpin-Tsai Model	$\sigma_C = \sigma_M \left(\frac{1 + \xi \eta V_{F'}}{1 - \eta V_{F'}} \right), \quad \eta = \frac{\left(\frac{\sigma_F}{\sigma_M}\right) - 1}{\left(\frac{\sigma_F}{\sigma_M}\right) + \xi}$ $\xi = 3 \left(\frac{L}{D}\right) \chi_\theta \chi_M$	χ_θ : Fiber orientation factor χ_M : Matrix factor ξ : Shape fitting parameter D : Fiber diameter

7.3.3.1 The Comparison with Different Fiber Volume Fractions

Figure 7-3 shows the comparison between theoretical tensile strength values of M-FRAC using shear lag and Halpin-Tsai equations, presented in Table 7-1, and experimental

measurement at different fiber volume fractions and 19 mm fiber length. A very close agreement is obtained between calculated values of both modified models and experimental data with less than 5% difference, while the original models overpredicted the strength values relative to the experimental measured strength.

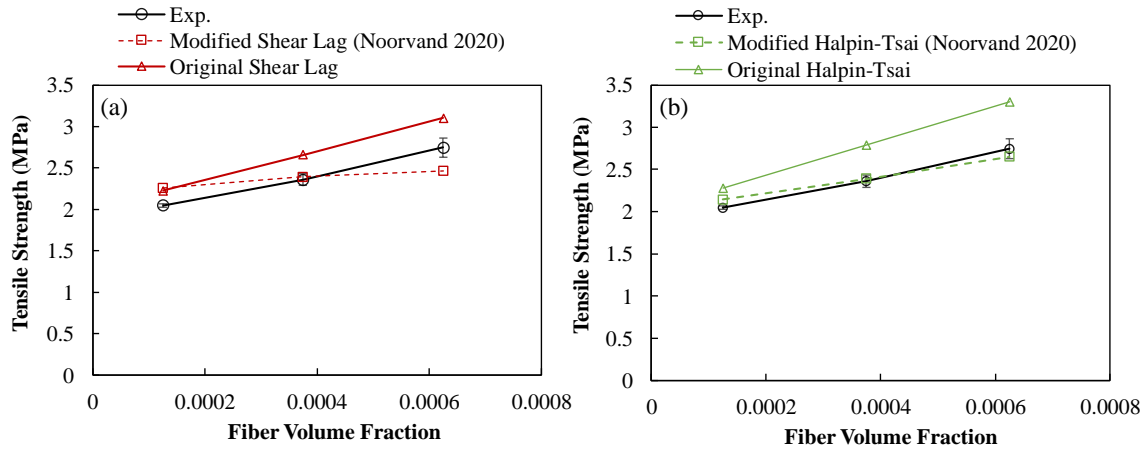


Figure 7-3. Comparison of Predicted Theoretical Tensile Strength Values Using (a) Shear Lag and (b) Halpin-Tsai Models with Experimental Data of M-FRAC at Different Fiber Volume Fractions and 19 mm Fiber Length.

7.3.3.2 The Comparison with Different Fiber Aspect Ratio

Figure 7-4 represents the calculated tensile strength values of M-FRAC from the micromechanical models compared with experimental measurement at different aspect ratios of fiber. A reasonable agreement was obtained between theoretical calculations and empirical data. The different aspect ratios here represent different fiber lengths used in this study including 10, 19, and 38 mm; however, the comparison shown with respect to aspect ratio is a more reasonable parameter for general comparison which is also common in other studies. The results show that the models could provide the reasonable prediction of strength values compared with experimental data. On the other hand, the predicted

strengths by the original models were higher compared with the experimental measured strengths.

It was also noted that the differences between tensile strength values measured experimentally for different fiber length in this study was relatively insignificant, which was already acknowledged and discussed in CHAPTER 5. It was argued that the dispersion of fibers is affected with varying fiber length in the mix; with shorter fiber having a better dispersion and therefore having a higher volume fraction. Even though the same fiber content (0.15%) was dosed for the 10, 19, and 38 mm fiber specimens, the actual volume fraction of individual fibers in the mix, which really account for the fiber reinforcement efficiency, is different for each fiber length. Future study needs to take the effect of fiber aspect ratio (or length) into consideration when comparing the theoretical calculations with experimental data.

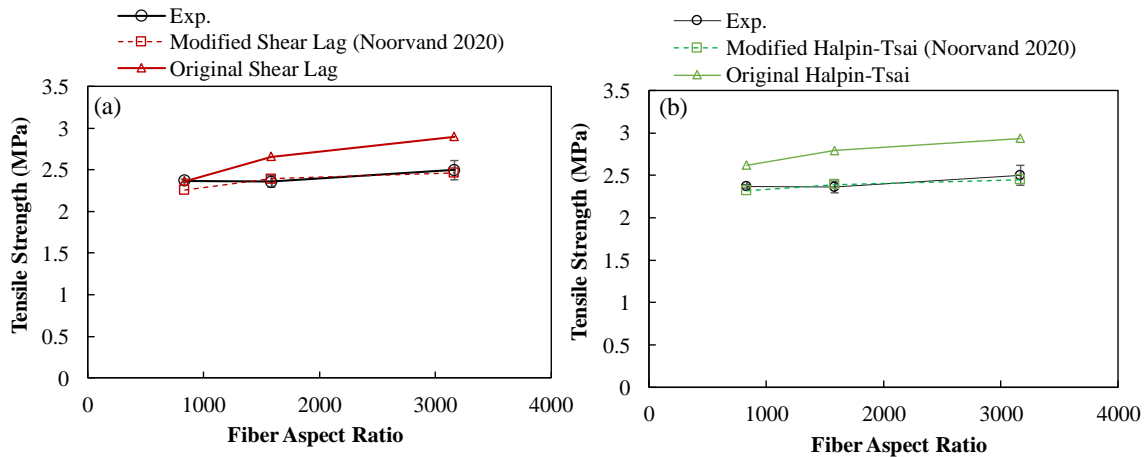


Figure 7-4. Comparison of Predicted Theoretical Tensile Strength Values Using (a) Shear Lag and (b) Halpin-Tsai Models with Experimental Data of M-FRAC at Different Fiber Aspect Ratio and 0.15% Fiber Content.

7.3.3.3 The Comparison with Different Mix Gradations

Figure 7-5 exhibits the comparison of experimental and theoretical data for the mixes C, D, and F-2 for the case of 19 mm fibers and 0.15% fiber content using both original and modified micromechanical models. It can be seen that there is a very good agreement in predicted tensile strength of different M-FRAC mixes relative to experimentally measured data using the modified models. The difference between theoretical calculation and experimental data also show that the better prediction from shear lag compared with the Halpin-Tsai equation.

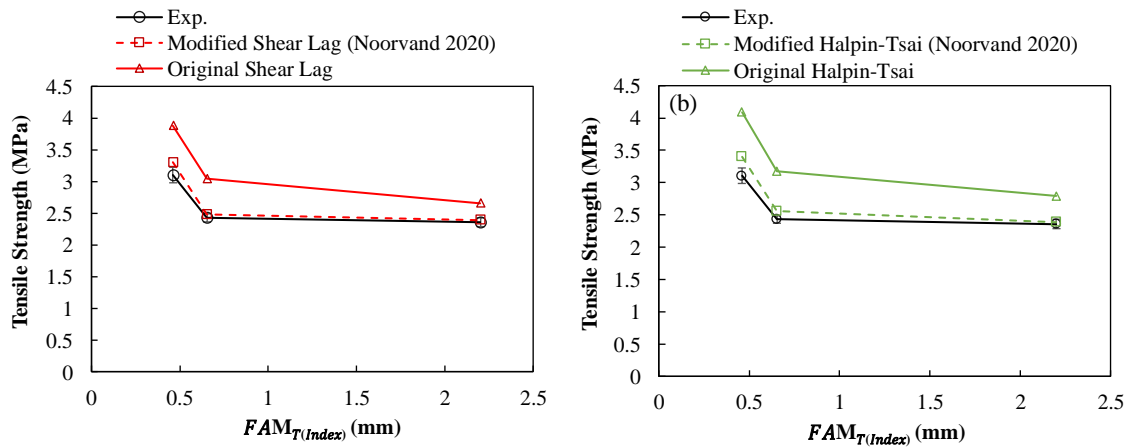


Figure 7-5. Comparison of Predicted Theoretical Tensile Strength Values Using (a) Shear Lag and (b) Halpin-Tsai Models with Experimental Data of M-FRAC for Different Mixes (C, D, and F-2) at 19 mm Length and 0.15% Content.

As discussed in CHAPTERS 4 and 5 of this study, asphalt mix gradation affects the reinforcement efficiency of fibers in the asphalt mix. The matrix parameter, χ_M , was therefore formulated based on the FAM thickness calculations from CHAPTER 4 and incorporated into the micromechanical models to account for the asphalt mix compositions. The $FAM_{T(Index)}$, calculated in CHAPTER 4, were 2.2, 0.65, and 0.46 for mixes C, D, and

F-2, respectively. When the values of $FAM_{T(Index)}$ are normalized by 2.5 assuming this is the maximum FAM thickness which can be obtained from a dense graded mix, χ_M is calculated. The parameter, χ_M , 0.88, 0.26, and 0.18 for mixes C, D, and F-2, respectively.

7.3.3.4 The Comparison with Literature

As part of the validation of the proposed micromechanical models, the work of other studies on fiber reinforced asphalt concrete were considered to examine the accuracy of these models. The literature search was limited to those studies that examined fibers reinforced asphalt concrete using direct tension test for the prediction of tensile strength. Through the search, one such study was found by (Yoo and Al-Qadi 2014), who studied the reinforcement of recycled plastic fibers in asphalt concrete using direct tensile loading tests. Table 7-2 summarizes the input parameters obtained from the work of Yoo and Al-Qadi (2014) and used in shear lag and Halpin-Tsai models to predict the tensile strength of recycled plastic fiber reinforced asphalt concrete. Although, the modulus of matrix was not reported in their study; a typical range of modulus values for uncracked asphalt concrete at 20°C between 2000 – 3500 MPa was selected and given into the shear lag model. The effect of matrix modulus value in the range of 1000-4000 MPa was found to be insignificant on the final outcome of predicted tensile strength results. Also, similar assumption was made for the values of the Poisson's ratio and fiber packing. The thickness of FAM index was calculated from the gradation and other properties given in Yoo and Al-Qadi's paper using procedure developed in CHAPTER 4 of this study. It should be also noted that while plastic fibers were used up to 1%, only 0.2 and 0.4% fiber content were

used for prediction since the benefit of fiber was observed only up to 0.4% in Yoo and Al-Qadi's study.

Table 7-2. Properties of Recycled Plastic Fiber and Asphalt Concrete Matrix Used for This Study (Yoo and Al-Qadi 2014).

Fiber Property		Matrix Property (Asphalt Concrete)	
Fiber Width (mm)	0.7-1	1.73	σ_{Matrix} (MPa)
Fiber Length (mm)	30	1000-4000	E_m (GPa)
E_f (GPa)	13	0.7	FAM_T (index) (mm)
Fiber content (%)	0.2, 0.4	0.35	Poisson Ratio
σ_{Fiber} (MPa)	300-350	3.14	P_f (Square Packing)

Figure 7-6 shows the theoretical measurements of the tensile strength of recycled fiber reinforced asphalt concrete compared with experimental data by (Yoo and Al-Qadi 2014). Excellent agreement was found between the modified shear lag model and empirical data with less than 5% difference in their tensile strength values. However, the modified Halpin-Tsai model was underpredicted the strength of FRAC. It was found that the adjustment of shape fitting parameter, ξ , could improve the fit between the theoretical and experimental data. The original Halpin-Tsai, on the other hand, showed a good agreement with the experimental data. It appears that both of these models could have been used for prediction of fiber reinforced asphalt concrete containing short randomly distributed fibers; however, the modified shear lag model specifically indicated better fit with experimental data for different types of fibers (synthetic microfiber and recycled macrofibers) and different asphalt mix designs compared with the modified Halpin-Tsai model. Further studies on the modification of, the parameter, ξ , in the Halpin-Tsai model may be considered with regards to the use of different fibers in asphalt mixtures.

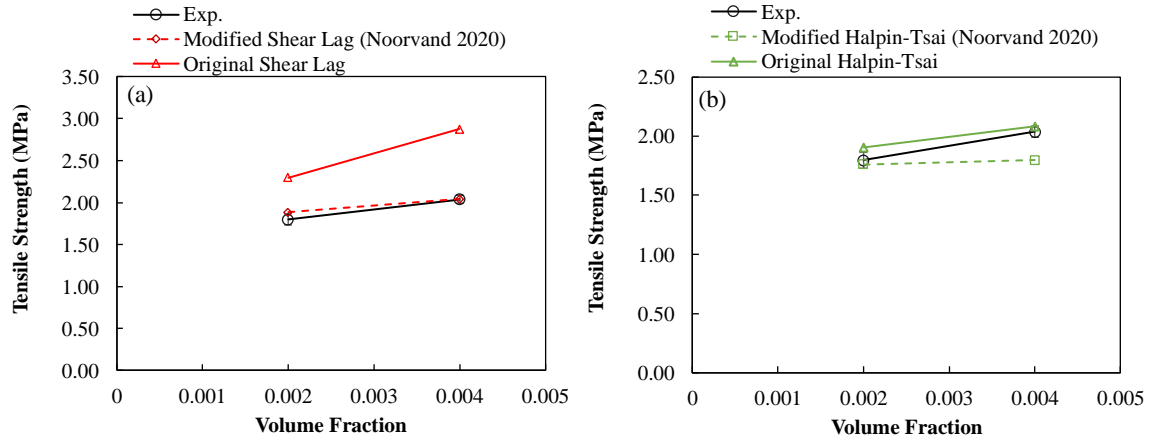


Figure 7-6. Comparison of Predicted Theoretical Tensile Strength Values Using (a) Shear Lag and (b) Halpin-Tsai Models with Experimental Data of M-FRAC at Different Volume Fractions of Recycled Plastic Short Fiber and 30 mm Length.

CHAPTER 8

SUMMARY, CONCLUSIONS AND FUTURE WORK

8.1 Summary and Conclusions

Modification of the asphalt concrete by incorporating new additives either in the bitumen or in the asphalt mixture is one of the common strategies to enhance the service lifetime of asphalt pavements. Fibers have been used as reinforcement for asphalt materials for many years in various parts of the world. Generally, these efforts have made favorable conclusions regarding the use of fiber reinforcement in AC. While published studies generally demonstrate positive benefits from using FRAC, it is not always the case, and when improvements are found they vary with respect to the types of fibers, properties of fiber (length, dosage, state), mix type and the mechanical experiment. In some cases, no statistically significant improvement has been identified from using fibers into asphalt mixtures. Due to this inconsistency, the widespread acceptance of fibers use in asphalt industry is plagued. The current state of knowledge with respect to fiber reinforcement in AC materials has been mainly driven from an experimental basis, with little fundamental investigation. The following sections present a summary and conclusions from this research effort.

8.1.1 Effect of Fiber State on Mechanical Performance of Fiber Reinforced Asphalt Concrete

The following conclusions were reached from the effect of aramid fibers state on the mechanical properties of asphalt mixtures. In the FA mix, the aramid fibers are

introduced along with polyolefin fibers while in FB the aramid fibers are coated in a thin membrane of wax, which melts as the fibers are mixed in.

- Dynamic moduli values showed no statistical differences between the mixtures. The FA mixture exhibited a 139% improvement in flow number compared with the control while the FB mixture had a similar performance to the control mixture. Fatigue simulations showed that both FA and FB mixtures had two times fatigue improvement compared with the control.
- Aramid fibers in FA mix were well dispersed and most of the fibers were in the individual state (*FDP* of 88.5%) while FB fibers were poorly dispersed (*FDP* of 16%). Aramid fibers in FA mix showed a higher degree of micro-fibrillation compared with aramid fibers in FB mix. The orientation study using different coring direction indicated that individual fibers tend to be oriented mostly horizontally.
- The different behavior in fatigue and permanent deformation for each FA and FB was attributed to the orientations of the fibers with respect to the testing configuration. It was postulated that in the flow number test the fibers are ideally oriented to strengthen cracks that form parallel to the loading direction, whereas fibers are not preferably oriented for reinforcing cracks that develop perpendicular to the loading direction in the fatigue test.

8.1.2 Evaluating Interaction of Fiber Reinforcement Mechanism with Mesostructure of Asphalt Concrete

The interaction of fibers with the compositions of asphalt mixtures was studied and following conclusions were reached.

- Fiber mixing procedure in the laboratory is a challenge task in terms of obtaining highly dispersed aramid fibers compared with the mixing procedure in the field. In this study, a 3-layer system of fiber mixing procedure was used to improve the dispersion of fibers.
- The mechanical tests indicated that the fibers improved the overall mechanical performance in fatigue and flow number of asphalt mixtures; however, the degree of improvement varied from one mix to another.
- A strong link was found between the compositions of asphalt mixtures and fiber reinforcement efficiency in mechanical performance. It was found that effective binder content and gradation play significant roles in reinforcement effectiveness of fiber in rutting and fatigue cracking, respectively. Accordingly, indices of V_{be} and FAM thickness were established as indicators of M-FRAC performance in rutting and fatigue cracking, respectively.

8.1.3 Mechanism of Mechanically-Fiber Reinforced Asphalt Concrete in Tension

Mechanical properties of asphalt concrete with and without fibers in tension were evaluated using monotonic fracture tests. The experimental findings have shown that fibers do serve as reinforcement element in asphalt concrete; however, their reinforcing efficiency is dependent on the temperature, rate of loading, properties of fiber (i.e. dosage, length), and properties of mix type (gradation). These parameters were studied using a semi-circular bending (SCB) test with crack mouth opening displacement (CMOD) and a

direct tension (DT) test on circumferentially notched cylindrical specimens. Following conclusion were reached from this study.

- The effect of temperature and loading rate on tensile capacity of asphalt concrete with and without fibers were examined by constructing a mastercurve of strength as a function of reduced strain rate using the DT test. At the lowest reduced strain rate, fibers showed slight improvement in the tensile stress of asphalt concrete mixtures. However, with increasing loading and reducing temperature, the benefit of fibers emerged.
- At 20°C, the fracture toughness values, represented by critical stress intensity factor, increased by about 15% with presence of fibers for mix C. Comparing different fiber dosages and lengths, increasing fiber content from 0.05% to 0.25% and length from 10 to 38 mm did not further increase the toughness of asphalt concrete. At 10°C, fracture toughness of asphalt concrete increased by increasing the fiber length and dosage. While 10- and 19-mm fibers from DT test increased the toughness similarly by 15%, the 38-mm fiber specimen (C-38-0.15) increased toughness by 22%. The trend was quite similar for SCB specimens.
- The effects of mix type on the cracking resistance of M-FRAC compared with AC were evaluated using fracture toughness and energy parameters. At both 10°C and 20°C, while the use of fiber in mix C increased fracture toughness of asphalt concrete, no difference was found between the fracture toughness of fiber and no fiber specimens of mixes F-2 and D using DT and SCB tests.

- The fracture toughness results were consistent with the findings of uniaxial fatigue test which further verifies the parameter FAM thickness as a good indicator on the tensile capacity of M-FRAC.
- However, the analysis of fracture energy analysis using the crack-controlled test (SCB with CMOD) provided further insights into interaction of fiber reinforcement efficiency with compositions of asphalt mixtures. Comparing different mix types, the SCB test results showed that the use of 0.05% and 0.15% fiber increased the average fracture energy of asphalt concrete specimens for mix C by 5% and 25%, respectively. The results for mix D showed increase of fracture energy for 19- and 10-mm fiber by 15% and 19%, respectively. The fracture energy results obviously showed the importance of a crack-controlled test (i.e. SCB with CMOD) to fully characterize the M-FRAC in tension. the SCB with CMOD.

8.1.4 Evaluation of Interfacial Shear Bond Strength and Critical Fiber Length in Fiber Reinforced Asphalt Concrete

Because of the viscoelastic nature of FRAC, the shear bond strength between the fibers and the asphalt matrix are affected by the displacement rate. A pull-out test was developed and used to determine the interfacial shear strength between fibers and the asphalt mastic. The following conclusions were reached from this study.

- A fiber pull-out was developed with relatively good variability in the experimental measurements by carefully controlling the sample preparation and fiber alignment.
- The effect of fiber diameter and embedded length on the average shear bond strength and maximum pull-out force were studied. The results showed that the maximum

pull-out force increased with increasing the fiber diameter and embedded length, while the average shear bond strength actually reduced.

- The effect of diameters of aramid fibers on the shear bond strength can be linked to the importance of fiber dispersion in enhancing the mechanical performance of asphalt mixtures, particularly higher temperature. The larger shear bond strength for smaller diameter fibers implies that individual fibers can be more effectively mobilized in the asphalt matrix system, particularly at higher temperature and smaller displacement rates. This essentially accentuates the benefits of a larger *FDP* value (higher number of individual aramid fibers) in the asphalt mix to improve the rutting resistance of asphalt mixtures.
- Comparing different types of fibers, aramid fiber showed larger shear bond strength than both nylon fibers. At 0.5 mm/s of displacement rate, the shear bond strength of aramid fiber was about 25% and 60% higher than that of Nylon 1 and Nylon 2, respectively, regardless of the fiber embedded length.
- At 0.1 mm/s of displacement rate, the difference in shear bond strength was found to be statistically insignificant for both aramid and Nylon 1. This was because the fiber pull-out mechanism was hampered by the viscoelastic nature of the asphalt binder.
- An analytical framework on the basis of elastic-viscoelastic correspondence principle was developed to determine a relationship between shear bond strength and the apparent modulus of asphalt mastic and asphalt concrete in the mix.
- The results indicated that the shear bond strength of fibers in the DT asphalt concrete specimens at all testing conditions are lower than those obtained from pull-

out test at 20°C and 0.5 mm/s. For asphalt concrete mix, the range of shear bond strength were 0.5-1 MPa for the testing temperature of 10°C except the lowest displacement rate while at 25°C testing condition the shear bond strength of aramid in the mix was less than 0.5 MPa.

- A range of total fiber length was recommended for different pavement distresses to ensure high fiber efficiency based on the relationships developed between critical fiber length, apparent modulus, and shear bond strength for DT asphalt concrete specimens. Long fibers ($L > 25$ mm) are recommended if rutting is common; while short fibers ($L < 15$ mm) are more acceptable if thermal cracking is a common distress. A fiber length in the range of 15-25 mm is also recommended for fatigue cracking which is more prevalent at intermediate temperature.

8.1.5 Development of Micromechanical Models for Predicting the Tensile Strength of FRAC

In this study, modified micromechanical models were proposed to predict the tensile strength of M-FRAC. Following conclusion were reached from this study.

- Shear lag and Halpin-Tsai micromechanical models were selected for predicting the tensile strength of fiber reinforced asphalt concrete composites, and further modified with efficiency factors to improve the accuracy of models. These efficiency factors included a fiber dispersion factor, a matrix factor, and a fiber orientation factor.

- The fiber dispersion factor was obtained from the experimental parameter *FDP* in CHAPTER 3 to correct the volume fraction of fibers in the mix with respect to the state of individual aramid fibers in the mix.
- The matrix factor developed experimentally based on FAM thickness index in CHAPTER 4 to account for the different asphalt mix design gradation.
- For Halpin-Tsai equation, a fiber orientation factor was also incorporated into the model theoretically determined using a probabilistic approach. The calculated fiber orientation factor was 0.33.
- The accuracy of these proposed micromechanical models for predicting the tensile strength of M-FRAC relative to experimental measurements and the original model were discussed with respect to fiber volume fraction and aspect ratio. The experimental measurements were obtained from monotonic direct tensing testing from CHAPTER 5 of this study at 10°C and 0.35 mm/min on specimens. Both modified shear lag and Halpin-Tsai models showed very good fit with the experimental data in this study.
- As part of the validation of the proposed micromechanical models, the work of other studies on fiber reinforced asphalt concrete were considered to examine the accuracy of these models. Excellent agreement was found between shear lag model and empirical data with less than 5% difference in their tensile strength values.

8.2 Industry Use and Implementation

This study identified key aspects attributed to the reinforcement mechanism of fibers. The outcomes of this study provide insight into the underlying mechanisms of fiber

reinforcement required to enhance its efficiency for use in asphalt concrete. This improved insight will translate into better deployment of existing fiber-based technologies; development of new, and more effective fiber-based technologies in asphalt mixtures. The key findings of this study, which will contribute to the use and implementation of M-FRAC technology in industry, are summarized as follows:

- Fiber dispersion: dispersion of fiber is the key in ensuring their mechanical performance benefit. This study developed and proposed a fiber extraction method, particularly *FDP* parameter, which can be used as a quality control of fiber dispersion in asphalt mixtures.
- Fiber mixing procedure: there exists a lack of a generally applicable laboratory method to introduce the fibers into asphalt concrete mixtures. In the laboratory, agencies often encounter unexpected difficulties in preparing FRAC samples. Without careful attention to the mixing process fibers will not distribute in a homogeneous manner leading the agency to have reduced confidence in the ability of the product to distribute in a full-scale mixing plant. In this study, a three-layer system of fiber mixing method was proposed by which fiber dispersion and distribution in the asphalt mix improved. This allows fabricating a more representative FRAC samples in the laboratory.
- Asphalt mixture composition: this study identified indices of V_{be} and FAM thickness which can serve as powerful indicators and screening tools for fiber reinforcement efficiency in enhancing rutting resistance and fatigue life of the asphalt mixtures.

- *Mechanical test type*: this study indicated that the selection of the appropriate testing protocol is critical to understand fiber's contribution to AC mechanical performance, particularly in cracking. This study proposed the use of mechanical tests that are able to provide a controlled constant loading rate on specimen during testing, which allows to capture and present the full benefit of reinforcing fibers in the asphalt mixtures.
- *Engineered fiber*: this study suggested that there is a need to divert from a “one solution fits all” approach, to better engineer fiber blends that can address performance improvement geared toward dominant pavement distress in a specific environmental location. For example, at very low temperature the length and dosage of fiber need to increase to ensure the full capacity of fiber reinforcement in asphalt mixtures. Based on this knowledge, engineered fiber should be a more cost-effective approach to provide agencies with a product designed for the specific climate challenges.

8.3 Future Work

This study provided a framework to critically characterize the reinforcement efficiency of fibers in asphalt concrete. Number of factors were studied including a) fiber state (dispersion, orientation, morphology and distribution); b) interaction of fiber with compositions of asphalt mix; c) viscoelastic properties of asphalt mix (temperature and loading rate); d) fiber properties (i.e. length, dosage); e) test type to characterize fiber reinforcement; f) interfacial properties (the shear bond strength between fiber and asphalt matrix); and g) a micromechanical framework to predict the tensile strength of M-FRAC.

Future and follow up work recommendations are as follows:

- Use of a crack-controlled fracture tests to characterize the effect of fiber length on the low temperature cracking resistance of asphalt mixtures.
- Use of other types of fibers (macrofibers) to validate whether all the concepts developed in this study can be generalized (i.e. FAM thickness parameter).
- Evaluation of the shear bond strength of fiber at lower temperature using pull-out test and the analytical framework developed in this study
- Evaluation of fiber reinforcement mechanism in other asphalt concrete technologies other than dense graded hot mix asphalt concrete used in this study.
- Development of a micromechanical model that takes into account the viscoelastic response of asphalt concrete with reference to shear bond strength property.

REFERENCES

- Abtahi, S.M., Sheikhzadeh, M., and Hejazi, S.M., 2010. Fiber-reinforced asphalt-concrete—a review. *Construction and Building Materials*, 24 (6), 871–877.
- Ahlich, R.C., 1996. *Influence of aggregate gradation and particle shape/texture on permanent deformation of hot mix asphalt pavements*. Army engineer waterways experiment station Vicksburg MS geotechnical lab.
- Ahmadzadeh, H., Connizzo, B.K., Freedman, B.R., Soslowsky, L.J., and Shenoy, V.B., 2013. Determining the contribution of glycosaminoglycans to tendon mechanical properties with a modified shear-lag model. *Journal of biomechanics*, 46 (14), 2497–2503.
- Anderson, T.L., 2017. *Fracture mechanics: fundamentals and applications*. CRC press.
- Apostolidis, P., Liu, X., Daniel, G.C., Erkens, S., and Scarpas, T., 2019. Effect of synthetic fibres on fracture performance of asphalt mortar. *Road Materials and Pavement Design*, 1–14.
- Apostolidis, P., Liu, X., Scarpas, A., Kasbergen, C., and van de Ven, M.F.C., 2016. Advanced evaluation of asphalt mortar for induction healing purposes. *Construction and Building Materials*, 126, 9–25.
- Banhözler, B., 2004. Bond Behaviour of a Multi-Filament Yarn Embedded in a Cementitious Matrix. *Doctoral dissertation, Bibliothek der RWTH Aachen*.
- Banthia, N. and Sheng, J., 1996. Fracture toughness of micro-fiber reinforced cement composites. *Cement and Concrete Composites*, 18 (4), 251–269.
- Bažant, Z.P., 1996. Analysis of work-of-fracture method for measuring fracture energy of concrete. *Journal of Engineering Mechanics*, 122 (2), 138–144.
- Behbahani, H., Nowbakht, S., Fazaeli, H., and Rahmani, J., 2009. Effects of Fiber Type and Content on the Rutting Performance of Stone Matrix Asphalt. *Journal of Applied Sciences*, 9 (10), 1980–1985.
- Bentur, A. and Mindess, S., 2006. *Fibre reinforced cementitious composites*. Crc Press.
- Bentur, A., Mindess, S., and Routledge, 2006. *Fibre Reinforced Cementitious Composites*, 624.
- Betterman, L.R., Ouyang, C., and Shah, S.P., 1995. Fiber-matrix interaction in microfiber-reinforced mortar. *Advanced Cement Based Materials*, 2 (2), 53–61.
- BrossEAUD, Y., Delorme, J.-L., and Hiernaux, R., 1993. Use of IPC wheel-tracking rutting tester to select asphalt pavements resistant to rutting. *Transportation Research Record*, 1384, 59.
- Button, J.W., Perdomo, D., and Lytton, R.L., 1990. Influence of aggregate on rutting in asphalt concrete pavements. *Transportation Research Record*, (1259).
- Cheah, C.M., Fuh, J.Y.H., Nee, A.Y.C., and Lu, L., 1999. Mechanical characteristics of fiber-filled photo-polymer used in stereolithography. *Rapid Prototyping Journal*.
- Chehab, G.R., 2002. Characterization of asphalt concrete in tension using a viscoelastoplastic model. North Carolina State University.

- Chehab, G.R., Kim, Y.R., Schapery, R.A., Witczak, M.W., and Bonaquist, R., 2002. Time-temperature superposition principle for asphalt concrete with growing damage in tension state. *Journal of the Association of Asphalt Paving Technologists*, 71.
- Choy, T.C., 2015. *Effective medium theory: principles and applications*. Oxford University Press.
- Clyne, T.W. and Hull, D., 2019. *An introduction to composite materials*. Cambridge university press.
- Cox, H.L., 1952. The elasticity and strength of paper and other fibrous materials. *British journal of applied physics*, 3 (3), 72.
- Dai, Q. and You, Z., 2007. Prediction of creep stiffness of asphalt mixture with micromechanical finite-element and discrete-element models. *Journal of Engineering Mechanics*, 133 (2), 163–173.
- Darabi, M.K., Al-Rub, R.K.A., Masad, E.A., Huang, C.-W., and Little, D.N., 2012. A modified viscoplastic model to predict the permanent deformation of asphaltic materials under cyclic-compression loading at high temperatures. *International Journal of Plasticity*, 35, 100–134.
- Das, O., Kim, N.K., and Bhattacharyya, D., 2017. The mechanics of biocomposites. *In: Biomedical Composites*. Elsevier, 375–411.
- Doll, B., Ozer, H., Rivera-Perez, J., Al-Qadi, I.L., and Lambros, J., 2017. Damage zone development in heterogeneous asphalt concrete. *Engineering Fracture Mechanics*, 182, 356–371.
- Erkens, S.M.J.G., 2004. Asphalt concrete response (ACRe): Determination, modelling and prediction. Technische Universiteit Delft (The Netherlands).
- Facca, A.G., Kortschot, M.T., and Yan, N., 2006. Predicting the elastic modulus of natural fibre reinforced thermoplastics. *Composites Part A: Applied Science and Manufacturing*, 37 (10), 1660–1671.
- Ferry, J.D., 1980. *Viscoelastic properties of polymers*. John Wiley & Sons.
- Fu, S.-Y. and Lauke, B., 1996. Effects of fiber length and fiber orientation distributions on the tensile strength of short-fiber-reinforced polymers. *Composites Science and Technology*, 56 (10), 1179–1190.
- Fu, S.-Y., Lauke, B., and Mai, Y.-W., 2009. *Science and engineering of short fibre reinforced polymer composites*. Elsevier.
- Fu, S.-Y., Lauke, B., and Mai, Y.-W., 2019. *Science and Engineering of Short Fibre-reinforced Polymer Composites*. Woodhead Publishing.
- Fukuda, H. and Kawata, K., 1974. On Young's modulus of short fibre composites. *Fibre science and technology*, 7 (3), 207–222.
- Gibson, R.F., 1994. Principles of Composite Material Mechanics. *McGraw-Hill Science/Engineering*, (205), xxvii, 579 p.
- Gibson, R.F., 2011. *Principles of composite material mechanics*. CRC press.

- Golalipour, A., Jamshidi, E., Niazi, Y., Afsharikia, Z., and Khadem, M., 2012. Effect of aggregate gradation on rutting of asphalt pavements. *Procedia-Social and Behavioral Sciences*, 53, 440–449.
- Goodrich, J.L., 1991. Asphaltic binder rheology, asphalt concrete rheology and asphalt concrete mix properties (with discussion). *Journal of the Association of Asphalt Paving Technologists*, 60.
- Gundla, A., 2014. *Use of Micro-Mechanical Models to Study the Mastic Level Structure of Asphalt Concretes Containing Reclaimed Asphalt Pavement*. Arizona State University.
- Hahn, C., 2000. Characteristics of P-aramid Fibers in Friction and Sealing Materials. *Journal of industrial textiles*, 30 (2), 146–165.
- Halpin, J.C., 1969. Stiffness and expansion estimates for oriented short fiber composites. *Journal of Composite Materials*, 3 (4), 732–734.
- Halpin, J.C. and Kardos, J.L., 1976. The Halpin-Tsai equations: a review. *Polymer engineering and science*, 16 (5), 344–352.
- Hashin, Z., 1991. Thermoelastic properties of particulate composites with imperfect interface. *Journal of the Mechanics and Physics of Solids*, 39 (6), 745–762.
- Hermans, J.J., 1967. The elastic properties of fiber reinforced materials when the fibers are aligned. *Proc. Roy. Academy Amsterdam*, B70, 1.
- Hill, R., 1965. A self-consistent mechanics of composite materials. *Journal of the Mechanics and Physics of Solids*, 13 (4), 213–222.
- Hillerborg, A., 1985. The theoretical basis of a method to determine the fracture energy G_F of concrete. *Materials and structures*, 18 (4), 291–296.
- Hirsch, T.J., 1962. Modulus of elasticity of concrete affected by elastic moduli of cement paste matrix and aggregate. *In: Journal Proceedings*. 427–452.
- Huang, H. and White, T., 1996. Dynamic properties of fiber-modified overlay mixture. *Transportation Research Record: Journal of the Transportation Research Board*, (1545), 98–104.
- Jahromi, S.G. and Khodaii, A., 2008. Carbon fiber reinforced asphalt concrete. *Arabian Journal for Science & Engineering (Springer Science & Business Media BV)*, 33.
- Jaskuła, P., Stienss, M., and Szydłowski, C., 2017. Effect of polymer fibres reinforcement on selected properties of asphalt mixtures. *Procedia Engineering*, 172, 441–448.
- Jayaraman, K. and Kortschot, M.T., 1996. Correction to the Fukuda-Kawata Young's modulus theory and the Fukuda-Chou strength theory for short fibre-reinforced composite materials. *Journal of materials science*, 31 (8), 2059–2064.
- Kalaprasad, G., Joseph, K., Thomas, S., and Pavithran, C., 1997. Theoretical modelling of tensile properties of short sisal fibre-reinforced low-density polyethylene composites. *Journal of materials science*, 32 (16), 4261–4267.
- Kaloush, K.E., Biligiri, K.P., Zeiada, W.A., Rodezno, M.C., and Reed, J.X., 2010. Evaluation of Fiber-Reinforced Asphalt Mixtures Using Advanced Material Characterization Tests. *Journal of Testing and Evaluation*, 38 (4).

- Kelly, A. and Macmillan, N.H., 1987. *Strong Solids (Monographs on the Physics and Chemistry of Materials)*. Oxford University Press, Cary, North Carolina, USA.
- Kelly, A. and Tyson, W.R., 1965. Tensile properties of fibre-reinforced metals: copper/tungsten and copper/molybdenum. *Journal of the Mechanics and Physics of Solids*, 13 (6), 329–350.
- Kelly, A. and Tyson, W.R., 1964. Fiber-strengthened materials.
- Kennedy, T.W., 1983. Tensile characterization of highway pavement materials.
- Khattak, M.J., Khattab, A., Rizvi, H.R., and Zhang, P., 2012. The impact of carbon nano-fiber modification on asphalt binder rheology. *Construction and Building Materials*, 30, 257–264.
- Kim, H., Wagoner, M.P., and Buttlar, W.G., 2008. Simulation of fracture behavior in asphalt concrete using a heterogeneous cohesive zone discrete element model. *Journal of Materials in Civil Engineering*, 20 (8), 552–563.
- Kim, K.W. and El Hussein, M., 1997. Variation of fracture toughness of asphalt concrete under low temperatures. *Construction and Building Materials*, 11 (7–8), 403–411.
- Kim, Y.-R., 2003. Mechanistic fatigue characterization and damage modeling of asphalt mixtures.
- Kim, Y.R., Baek, C., Underwood, B.S., Subramanian, V., Guddati, M.N., and Lee, K., 2008. Application of viscoelastic continuum damage model based finite element analysis to predict the fatigue performance of asphalt pavements. *KSCCE Journal of Civil Engineering*, 12 (2), 109–120.
- Klinsky, L.M.G., Kaloush, K.E., Faria, V.C., and Bardini, V.S.S., 2018. Performance characteristics of fiber modified hot mix asphalt. *Construction and Building Materials*, 176, 747–752.
- Krenchel, H., 1964. Fibre reinforcement; theoretical and practical investigations of the elasticity and strength of fibre-reinforced materials.
- Lackner, R., Spiegl, M., Blab, R., and Eberhardsteiner, J., 2005. Is low-temperature creep of asphalt mastic independent of filler shape and mineralogy?—arguments from multiscale analysis. *Journal of Materials in Civil Engineering*, 17 (5), 485–491.
- Lawler, J.S., Wilhelm, T., Zampini, D., and Shah, S.P., 2003. Fracture processes of hybrid fiber-reinforced mortar. *Materials and Structures*, 36 (3), 197–208.
- Laws, V., 1971. The efficiency of fibrous reinforcement of brittle matrices. *Journal of Physics D: Applied Physics*, 4 (11), 1737.
- Lee, H.-J. and Kim, Y.R., 1998. Viscoelastic continuum damage model of asphalt concrete with healing. *Journal of Engineering Mechanics*, 124 (11), 1224–1232.
- Lee, S.J., Rust, J.P., Hamouda, H., Kim, Y.R., and Borden, R.H., 2005. Fatigue cracking resistance of fiber-reinforced asphalt concrete. *Textile Research Journal*, 75 (2), 123–128.
- Li, F., 1998. Fracture characterization of fiber reinforced concrete in direct uniaxial tension.

- Li, V.C. and Maalej, M., 1996. Toughening in cement based composites. Part II: Fiber reinforced cementitious composites. *Cement and Concrete Composites*, 18 (4), 239–249.
- Li, V.C., Wang, Y., and Backer, S., 1990a. Effect of inclining angle, bundling and surface treatment on synthetic fibre pull-out from a cement matrix. *Composites*, 21 (2), 132–140.
- Li, V.C., Wang, Y., and Backer, S., 1990b. Effect of inclining angle, bundling, and surface treatment on synthetic fiber pull-out from a cement matrix.
- Li, V.C., Wang, Y., and Backer, S., 1991. A micromechanical model of tension-softening and bridging toughening of short random fiber reinforced brittle matrix composites. *Journal of the Mechanics and Physics of Solids*, 39 (5), 607–625.
- Li, X. and Marasteanu, M., 2004. Evaluation of the low temperature fracture resistance of asphalt mixtures using the semi circular bend test. *In: Association of Asphalt Paving Technologists-Proceedings of the Technology Sessions, AAPT 2004*. 401–426.
- Lim, I.L., Johnston, I.W., and Choi, S.K., 1993. Stress intensity factors for semi-circular specimens under three-point bending. *Engineering Fracture Mechanics*, 44 (3), 363–382.
- Löfgren, I., 2005. *Fibre-reinforced Concrete for Industrial Construction-a fracture mechanics approach to material testing and structural analysis*. Chalmers University of Technology.
- Mahrez, A., Karim, M.R., and bt Katman, H.Y., 2005. Fatigue and deformation properties of glass fiber reinforced bituminous mixes. *Journal of the Eastern Asia Society for Transportation Studies*, 6, 997–1007.
- Malekmohammadi, S., 2014. Efficient multi-scale modelling of viscoelastic composites with different microstructures.
- Mamlouk, M.S. and Zaniewski, J.P., 2006. *Materials for civil and construction engineers*. Pearson Prentice Hall Upper Saddle River, NJ.
- Marasteanu, M.O., Dai, S., Labuz, J.F., and Li, X., 2002. Determining the low-temperature fracture toughness of asphalt mixtures. *Transportation Research Record*, 1789 (1), 191–199.
- Maurer, D.A. and Malasheskie, G.J., 1989. Field performance of fabrics and fibers to retard reflective cracking. *Geotextiles and Geomembranes*, 8 (3), 239–267.
- Mcdaniel, R., 2015. *Fiber Additives in Asphalt Mixtures*. NCHRP Synthesis 475, National Cooperative Highway Research Program.
- Mcdaniel, R. and Shah, A., 2003. *Asphalt Additives to Control Cracking and Rutting*.
- Mera, H. & Takata, T., 1989. High-performance fibers. *Ullmann's Encyclopedia of Industrial Chemistry, Vol. A 13, Weinheim, Germany, VCH Verlagsgesellschaft mbH, pp. 1-23*.
- Van Mier, J.G.M. and Man, H.-K., 2009. Some notes on microcracking, softening, localization, and size effects. *International Journal of Damage Mechanics*, 18 (3), 283–309.
- Mobasher, B., 2011. *Mechanics of fiber and textile reinforced cement composites*. CRC press.

- Mohammed, M., Parry, T., Thom, N., and Grenfell, J., 2018. Investigation into the bond strength of bitumen-fibre mastic. *Construction and Building Materials*, 190, 382–391.
- Mohammed, M., Parry, T., Thom, N., and Grenfell, J., 2020. Microstructure and mechanical properties of fibre reinforced asphalt mixtures. *Construction and Building Materials*, 240, 117932.
- Motamedi, H., Fazaeli, H., Aliha, M.R.M., and Amiri, H.R., 2020. Evaluation of temperature and loading rate effect on fracture toughness of fiber reinforced asphalt mixture using edge notched disc bend (ENDB) specimen. *Construction and Building Materials*, 234, 117365.
- Mouritz, A.P. and Gibson, A.G., 2007. *Fire properties of polymer composite materials*. Springer Science & Business Media.
- Muftah, A., Bahadori, A., Bayomy, F., and Kassem, E., 2017. Fiber-reinforced hot-mix asphalt: Idaho case study. *Transportation Research Record*, 2633 (1), 98–107.
- Naaman, A.E., Namur, G.G., Alwan, J.M., and Najm, H.S., 1991a. Fiber pullout and bond slip. I: Analytical study. *Journal of Structural Engineering*, 117 (9), 2769–2790.
- Naaman, A.E., Namur, G.G., Alwan, J.M., and Najm, H.S., 1991b. Fiber pullout and bond slip. II: Experimental validation. *Journal of Structural Engineering*, 117 (9), 2791–2800.
- Nairn, J.A., 1997. On the use of shear-lag methods for analysis of stress transfer in unidirectional composites. *Mechanics of Materials*, 26 (2), 63–80.
- Nairn, J.A., 2004. Generalized shear-lag analysis including imperfect interfaces. *Advanced Composites Letters*, 13 (6), 096369350401300601.
- Nairn, J.A. and Liu, Y.C., 1997. Stress transfer into a fragmented, anisotropic fiber through an imperfect interface. *International journal of solids and structures*, 34 (10), 1255–1281.
- Nayfeh, A.H., 1977. Thermomechanically induced interfacial stresses in fibrous composites. *Fibre Science and Technology*, 10 (3), 195–209.
- Noorvand, H., Salim, R., Medina, J., Stempihar, J., and Underwood, B.S., 2018. Effect of synthetic fiber state on mechanical performance of fiber reinforced asphalt concrete. *Transportation Research Record*, 2672 (28).
- Obaid, N., 2018. Understanding and Predicting the Stress Relaxation Behavior of Short-Fiber Composites.
- Obaid, N., Kortschot, M.T., and Sain, M., 2017. Understanding the stress relaxation behavior of polymers reinforced with short elastic fibers. *Materials*, 10 (5), 1–15.
- Paipetis, A., Galiotis, C., Liu, Y.C., and Nairn, J.A., 1999. Stress transfer from the matrix to the fibre in a fragmentation test: Raman experiments and analytical modeling. *Journal of composite materials*, 33 (4), 377–399.
- Pan, P., Wu, S., Xiao, F., Pang, L., and Xiao, Y., 2015. Conductive asphalt concrete: A review on structure design, performance, and practical applications. *Journal of Intelligent Material Systems and Structures*, 26 (7), 755–769.
- Park, P., 2012. *Characteristics and Applications of High-Performance Fiber Reinforced Asphalt Concrete*. Thesis (PhD). Texas A&M University.

- Park, P., El-Tawil, S., and Naaman, A.E., 2017. Pull-out behavior of straight steel fibers from asphalt binder. *Construction and Building Materials*, 144, 125–137.
- Park, P., El-tawil, S., Park, S., and Naaman, A.E., 2015. Cracking resistance of fiber reinforced asphalt concrete at -20°C . *Construction and Building Materials*, 81, 47–57.
- Park, S.W. and Schapery, R., 1999. Methods of interconversion between linear viscoelastic material functions. Part I—A numerical method based on Prony series. *International journal of solids and structures*, 36 (11), 1653–1675.
- Partl, M.N., Vinson, T.S., and Hicks, R.G., 1994. Mechanical properties of stone mastic asphalt. *In: Infrastructure: New Materials and Methods of Repair*. ASCE. ASCE, 849–858.
- Peltonen, P. V, 1991. Characterization and testing of fibre-modified bitumen composites. *Journal of materials science*, 26 (20), 5618–5622.
- Piggott, M., 2002. *Load bearing fibre composites*. Springer Science & Business Media.
- Piggott, M.R., 1987. The effect of the interface/interphase on fiber composite properties. *Polymer Composites*, 8 (5), 291–297.
- Piggott, M.R., Sanadi, A., Chua, P.S., and Andison, D., 1986. Mechanical interactions in the interphasial region of fibre reinforced thermosets. *Composite interfaces*, 109–121.
- Putman, B.J. and Amirkhanian, S.N., 2004. Utilization of waste fibers in stone matrix asphalt mixtures. *Resources, conservation and recycling*, 42 (3), 265–274.
- Qian, S., Ma, H., Feng, J., Yang, R., and Huang, X., 2014. Fiber reinforcing effect on asphalt binder under low temperature. *Construction and Building Materials*, 61, 120–124.
- Rao, S., Jayaraman, K., and Bhattacharyya, D., 2012. Micro and macro analysis of sisal fibre composites hollow core sandwich panels. *Composites Part B: Engineering*, 43 (7), 2738–2745.
- Roque, R., Sankar, B., and Technologists, A.P., 1999. Determination of crack growth rate parameters of asphalt mixtures using the superpave IOT. *In: Proc., Annual Meeting of the Association of Asphalt Paving Technologists*. Washington, DC: Transportation Research Board.
- Saha, G. and Biligiri, K.P., 2016. Fracture properties of asphalt mixtures using semi-circular bending test: a state-of-the-art review and future research. *Construction and Building Materials*, 105, 103–112.
- Schapery, R.A., 1984. Correspondence principles and a generalized J integral for large deformation and fracture analysis of viscoelastic media. *International Journal of Fracture*, 25 (3), 195–223.
- Serfass, J.P. and Samanos, J., 1996. Fiber-modified asphalt concrete characteristics, applications and behavior (with discussion). *Journal of the Association of Asphalt Paving Technologists*, 65.
- Shah, S.P. and Ouyang, C., 1991. Mechanical Behavior of Fiber-Reinforced Cement-Based Composites. *Journal of the American Ceramic Society*, 74 (11), 2727–2953.
- Shaopeng, W., Qunshan, Y., Ning, L., and Hongbo, Y., 2007. Effects of fibers on the dynamic properties of asphalt mixtures. *Journal of Wuhan University of Technology--*

Materials Science Education, 22 (4), 733–736.

Simo, J.C. and Hughes, T.J.R., 2006. *Computational inelasticity*. Springer Science & Business Media.

Slebi-Acevedo, C.J., Lastra-González, P., Indacochea-Vega, I., and Castro-Fresno, D., 2020. Laboratory assessment of porous asphalt mixtures reinforced with synthetic fibers. *Construction and Building Materials*, 234, 117224.

Slebi-Acevedo, C.J., Lastra-González, P., Pascual-Muñoz, P., and Castro-Fresno, D., 2019. Mechanical performance of fibers in hot mix asphalt: A review. *Construction and Building Materials*, 200, 756–769.

Slebi-Acevedo, C.J., Pascual-Muñoz, P., Lastra-González, P., and Castro-Fresno, D., 2019. A multi-criteria decision-making analysis for the selection of fibres aimed at reinforcing asphalt concrete mixtures. *International Journal of Pavement Engineering*, 1–17.

Stakston, A.D. and Bahia, H.U., 2003. *The effect of fine aggregate angularity, asphalt content and performance graded asphalts on hot mix asphalt performance (Vol. 92, No. 45-98)*. Wisconsin Highway Research Program.

Stark, H.L. and Ibrahim, R.N., 1986. Estimating fracture toughness from small specimens. *Engineering fracture mechanics*, 25 (4), 395–401.

Stroeven, P. and Hu, J., 2006. Review paper–stereology: historical perspective and applicability to concrete technology. *Materials and structures*, 39 (1), 127–135.

Sueki, S., Soranakom, C., Mobasher, B., and Peled, A., 2007. Pullout-slip response of fabrics embedded in a cement paste matrix. *Journal of Materials in Civil Engineering*, 19 (9), 718–727.

Suuronen, J.-P., Kallonen, A., Eik, M., Puttonen, J., Serimaa, R., and Herrmann, H., 2013. Analysis of short fibres orientation in steel fibre-reinforced concrete (SFRC) by X-ray tomography. *Journal of Materials Science*, 48 (3), 1358–1367.

Tada, H., Paris, P.C., Irwin, G.R., and Tada, H., 2000. *The stress analysis of cracks handbook*. ASME press New York.

Takaikaew, T., Tepsriha, P., Horpibulsuk, S., Hoy, M., Kaloush, K.E., and Arulrajah, A., 2018. Performance of fiber-reinforced asphalt concretes with various asphalt binders in Thailand. *Journal of Materials in Civil Engineering*, 30 (8), 4018193.

Tapkın, S., 2008. The effect of polypropylene fibers on asphalt performance. *Building and Environment* 43, 43, 1065–1071.

Teklal, F., Djebbar, A., Allaoui, S., Hivet, G., Joliff, Y., and Kacimi, B., 2018. A review of analytical models to describe pull-out behavior – Fiber/matrix adhesion. *Composite Structures*, 201 (June), 791–815.

Toney, C.A., 1987. *Fiber Reinforced Asphalt Concrete Pavements-City of Tacoma*.

Tsai, C.-L. and Daniel, I.M., 1999. Determination of shear modulus of single fibers. *Experimental mechanics*, 39 (4), 284–286.

Tucker III, C.L. and Liang, E., 1999. Stiffness predictions for unidirectional short-fiber composites: review and evaluation. *Composites science and technology*, 59 (5), 655–671.

Underwood, B., Baek, C., and Kim, Y., 2012. Simplified viscoelastic continuum damage model as platform for asphalt concrete fatigue analysis. *Transportation Research Record: Journal of the Transportation Research Board*, (2296), 36–45.

Underwood, B.S., 2011. *Multiscale constitutive modeling of asphalt concrete*. Thesis (PhD). North Carolina State University.

Underwood, B.S., Kim, Y.R., Guddati, M., Pellinen, T., Rongzong, W., King, G., Kluttz, R., and Gibson, N., 2006. Characterization and performance prediction of ALF mixtures using a viscoelastoplastic continuum damage model. *In: Association of Asphalt Paving Technologists-Proceedings of the Technical Sessions 2006 Annual Meeting*. 577–636.

Underwood, B.S., Kim, Y.R., and Guddati, M.N., 2010. Improved calculation method of damage parameter in viscoelastic continuum damage model. *International Journal of Pavement Engineering*, 11 (6), 459–476.

Valenta, R., Sejnoha, M., and Zeman, J., 2010. Macroscopic constitutive law for mastic asphalt mixtures from multiscale modeling. *International Journal for Multiscale Computational Engineering*, 8 (1).

Vavrik, W.R., Pine, W.J., Huber, G., Carpenter, S.H., and Bailey, R., 2001. The bailey method of gradation evaluation: the influence of aggregate gradation and packing characteristics on voids in the mineral aggregate (with discussion). *Journal of the Association of Asphalt Paving Technologists*, 70.

Viel, Q., Esposito, A., Saiter, J.-M., Santulli, C., and Turner, J.A., 2018. Interfacial Characterization by Pull-Out Test of Bamboo Fibers Embedded in Poly (Lactic Acid). *Fibers*, 6 (1), 7.

Wang, Y.D., Keshavarzi, B., and Kim, Y.R., 2018. Fatigue Performance Prediction of Asphalt Pavements with FlexPAVETM, the S-VECD Model, and DR Failure Criterion. *Transportation Research Record*, 2672 (40), 217–227.

World Health Organization, 1993. Selected Synthetic Organic Fibres-Environmental Health Criteria 151.

Wu, J., Yuan, H., Li, L., Fan, K., Qian, S., and Li, B., 2018. Viscoelastic shear lag model to predict the micromechanical behavior of tendon under dynamic tensile loading. *Journal of theoretical biology*, 437, 202–213.

Wu, S., Ye, Q., and Li, N., 2008. Investigation of rheological and fatigue properties of asphalt mixtures containing polyester fibers. *Construction and Building Materials*, 22 (10), 2111–2115.

Xu, Q., Chen, H., and Prozzi, J.A., 2010. Performance of fiber reinforced asphalt concrete under environmental temperature and water effects. *Construction and Building Materials*, 24, 2003–2010.

Yang, H.H., 1993. *Kevlar Aramid Fiber*. New York: John Wiley & Sons.

Ye, Q., Wu, S., and Li, N., 2009. Investigation of the dynamic and fatigue properties of fiber-modified asphalt mixtures. *International Journal of Fatigue*, 31 (10), 1598–1602.

Yi, C.K. and Ostertag, C.P., 2001. Strengthening and toughening mechanisms in

microfiber reinforced cementitious composites. *Journal of materials science*, 36 (6), 1513–1522.

Yoo, P.J. and Al-Qadi, I.L., 2014. Pre-and post-peak toughening behaviours of fibre-reinforced hot-mix asphalt mixtures. *International Journal of Pavement Engineering*, 15 (2), 122–132.

Yoo, P.J. and Kim, K.-H., 2014. Thermo-plastic fiber's reinforcing effect on hot-mix asphalt concrete mixture. *Construction and Building Materials*, 59, 136–143.

Zeiada, W., Medina, J., Underwood, S., and Stempihar, J., 2017. *Fiber-Reinforced Asphalt Concrete Laboratory Procedure: Verification of Aramid Dispersion*. Arizona State University.

Zhandarov, S. and Mäder, E., 2005. Characterization of fiber/matrix interface strength: applicability of different tests, approaches and parameters. *Composites Science and Technology*, 65 (1), 149–160.

Zollinger, C.J., 2005. *Application of surface energy measurements to evaluate moisture susceptibility of asphalt and aggregates*. Thesis (PhD). Texas A&M University.

Zube, E., 1956. *Wire mesh reinforcement in bituminous resurfacing*.

APPENDIX A
TEST PROCEDURE

Dynamic Modulus

Temperature and frequency sweep tests were performed in general accordance with the AASHTO T342 protocol. The testing was performed to measure the dynamic modulus, $|E^*|$, at temperatures of 4.4, 21.1, and 37.8°C and frequencies of 25, 10, 5, 1, 0.5, and 0.1 Hz. In this project the -10°C temperature was omitted for two primary reasons; 1) eliminating this test temperature doubled the productivity of the testing and allowed the research team to evaluate more conditions during the allotted time and 2) previous research suggests that the benefits of fiber with respect to dynamic modulus were largest at intermediate temperature and less at extreme high and low temperature meaning that not having -10°C would not affect the conclusions for this project. A standard methodology can be used to extrapolate the measured data to -10°C for use in pavement analysis (AASHTO PP61-13).

Test samples were compacted to a height of 178 mm (7 in.) and a diameter of 150 mm (6 in.) via the Superpave gyratory compactor. After the samples had cooled from compaction they were cored and cut to a final testing geometry of 100 mm (4 in.) x 150 mm (diameter x height). The bulk density of these samples were then measured and used to calculate air void contents, which were $6.5 \pm 0.5\%$. Samples were instrumented with three linear variable displacement transducers (LVDT), which were used to monitor on-specimen deformation during the test. Lubricated membranes were placed between the sample and the loading platens prior to testing reduce any end effects. Load levels for these tests were determined by a trial and error process so that the resulting strain amplitudes were between 40 and 60 microstrains. The overall test setup for the dynamic modulus test is shown in Figure A-1 while a close-up view of the LVDTs is given in Figure A-2.

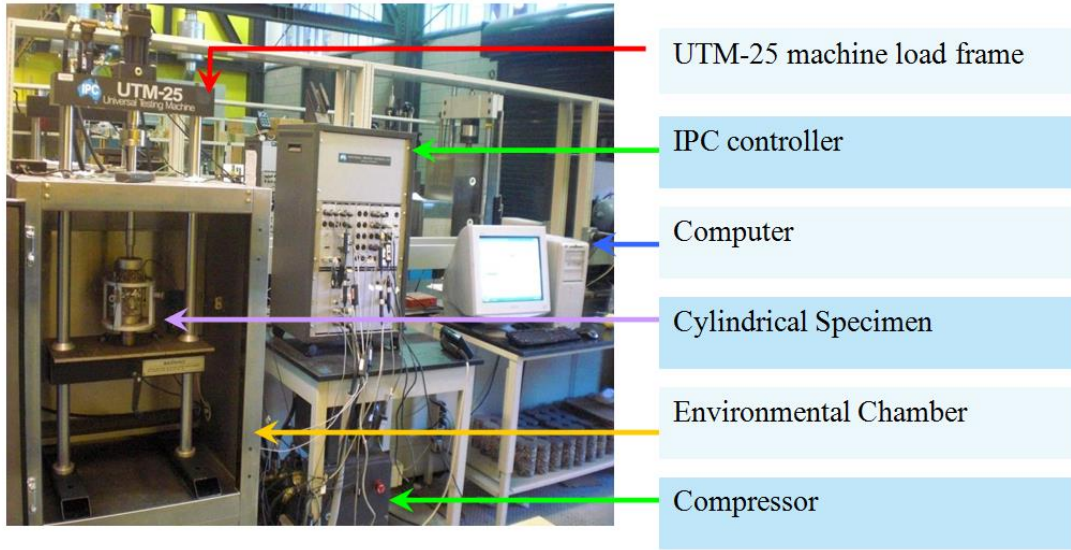


Figure A-1. Dynamic Modulus Test Set-up.

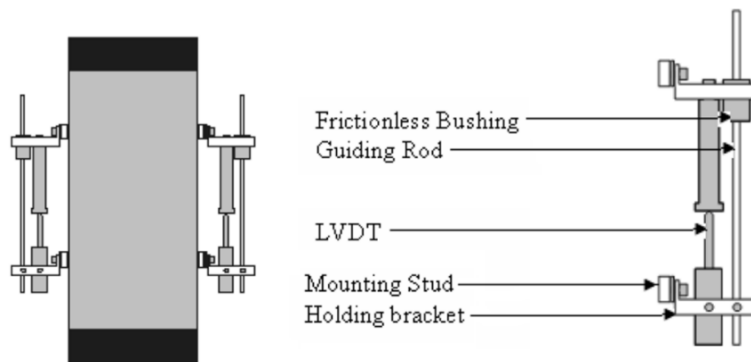


Figure A-2. Specimen Instrumentation in $|E^*|$ Testing.

The most common method to report dynamic modulus data is the mastercurve function, which is so named because it shows the joint effects of temperature and frequency on the modulus of asphalt concrete. The process of characterizing a mastercurve function is shown schematically in Figure A-3. A mastercurve is created by plotting the data at each temperature as a function of frequency in log-log space and then horizontally shifting the data for each temperature to produce a single, continuous and smoothly varying function. The amount of horizontal shift required to create such a curve is referred to as the *time-*

temperature shift factor (t-T shift factor) and varies according to temperature. Note that upon shifting, the x-axis is relabeled as reduced frequency to denote that the curve was not actually developed with measurements at a single temperature. The mathematical representation of reduced frequency is shown in Equation (A-1).

$$f_R = f \times a_T \quad (A-1)$$

where:

- f_R = reduced frequency (rad/s);
- f = test frequency (rad/s); and
- a_T = t-T shift factor for test temperature.

The common availability of desktop computers that have spreadsheet optimization tools makes this process more objective and often easier than was heretofore possible. With these tools, a functional form for the mastercurve and the t-T shift factor function can be assumed up front and the coefficients of these functions can be optimized to best match the experimental data. The sigmoidal model, Equation (A-2), is adopted to represent the mastercurve of asphalt mixture and the second order polynomial function, Equation (A-3), is utilized for the t-T shift factor function. Once characterized the $|E^*|$ mastercurve can be used to generate inputs for mechanistic pavement response analysis independently or in conjunction with the AASHTOWare Pavement ME Design software.

$$\log |E^*| = \delta + \frac{\alpha}{1 + e^{\beta + \gamma(\log f_r)}} \quad (A-2)$$

where:

- f_r = reduced frequency of loading (Hz);
- δ = minimum logarithmic value of $|E^*|$;
- $\delta + \alpha$ = maximum logarithmic value of $|E^*|$; and

β, γ = parameters describing the shape of the sigmoidal function.

$$\log a_T = \alpha_1(T^2 - T_R^2) + \alpha_2(T - T_R) \quad (\text{A-3})$$

where:

T = test temperature ($^{\circ}\text{C}$);

T_R = reference temperature (21°C); and

α_1, α_2 = fitting coefficients.

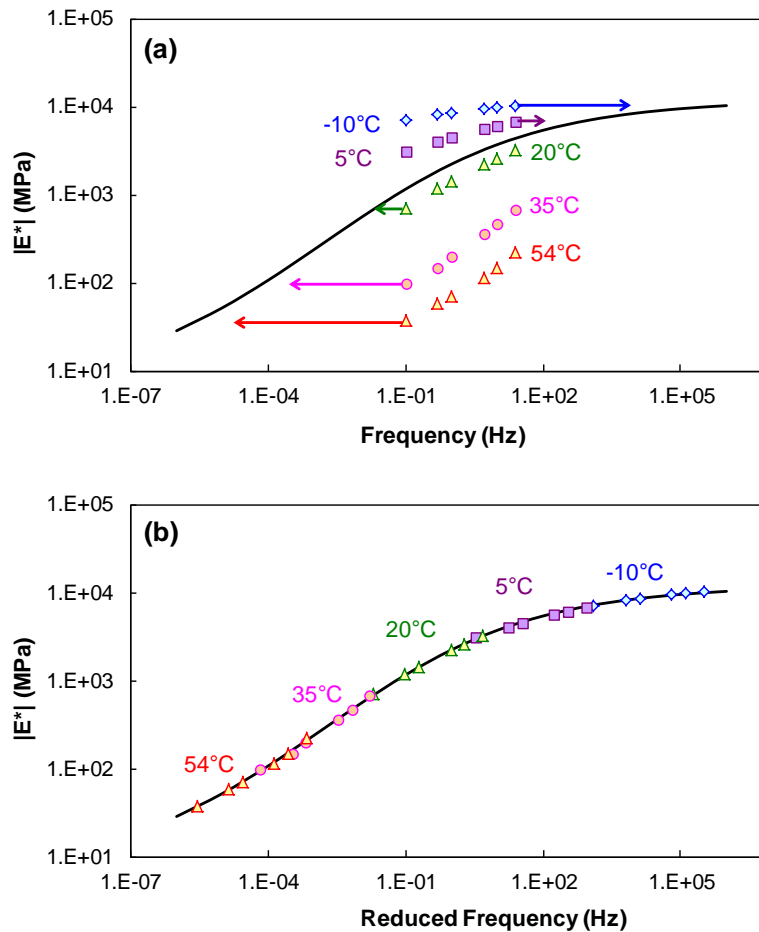


Figure A-3. Schematic Representation of Mastercurve Creation Process; (a) Unshifted Modulus Data and (b) Shifted Modulus Data.

Flow Number

The Repeated Load Permanent Deformation or Flow Number Test is used to determine the permanent deformation characteristics of paving materials. The test procedure used in this study generally followed the method suggested in AASHTO TP79 and applied repeated 0.1 s haversine load pulses that were each followed by a 0.9 s rest period. At the end of each rest period the cumulative permanent deformation was recorded. The deformations were measured using LVDTs mounted to the surface of the sample. The test was performed under atmospheric conditions, and prior to testing a thin and lubricated membrane was placed between the sample ends and the loading platens to create frictionless surface conditions and prevent end effects. This test was performed using the same IPC UTM-25 that was previously described with respect to the $|E^*|$ test. In the initial experiment, the flow number test was performed at 37.8°C (100°F) and using a stress level of 450 kPa. The reason that this temperature was chosen was to be consistent with the Dispersion study carried out in 2014. The stress level was selected so that the test would fail in a reasonable number of cycles. However, for the actual study the flow number test was performed at 50°C (120°F) and using a stress level of 100-120 kPa. To make sure that the test would fail in a reasonable number of cycles (5000-10000 cycles).

Figure A-4 shows the typical relationship between the total cumulative plastic strain and the number of load cycles during a flow number test. This relationship is generally defined by three regions: primary, secondary, and tertiary. In the primary region, permanent deformations accumulate rapidly. The incremental permanent deformations decrease reaching a constant value in the secondary region. Finally, the incremental permanent deformations again increase, and permanent deformations accumulate rapidly

in the tertiary region. The starting point, or cycle number, at which tertiary flow occurs, is referred to as the Flow Number (FN).

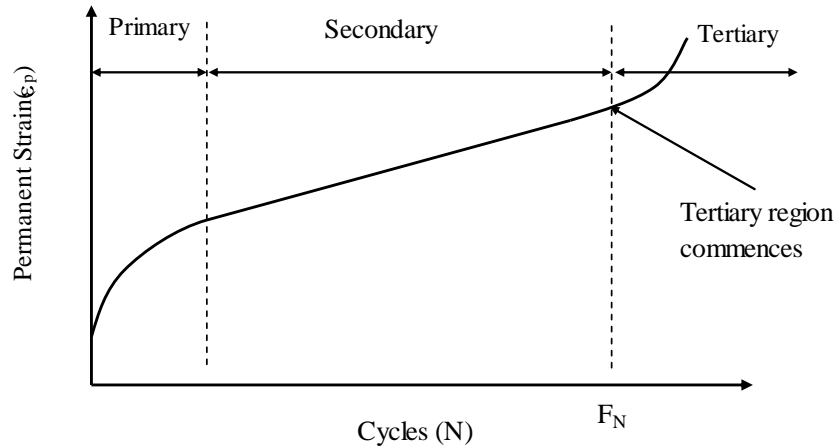


Figure A-4. Typical Relationship Between Total Cumulative Plastic Strain and Number of Load Cycles.

Two basic analyses are performed with the data in these tests; (1) identifying the FN and (2) establishing strain accumulation coefficients for structural performance assessment. To identify the FN value, a statistical analysis technique, the Francken model, is often utilized. This model structure, shown in Equation (A-4), has been selected because it combines both a power function, which characterizes the primary and secondary regions, and an exponential function that fits the tertiary region.

$$\varepsilon_p(N) = AN^B + C(e^{DN} - 1) \quad (A-4)$$

where:

- $\varepsilon_p(N)$ = permanent deformation or permanent strain;
- N = number of loading cycles; and
- A, B, C and D = regression constants.

The regression constants in this model are determined by optimization of Equation (A.4) against the measured permanent deformation in the repeated load test. In the above model, the regression constant C represents whether or not the material reaches the tertiary region. The FN can be determined by double differentiation of Equation (A-4) with respect to N , setting this expression equal to zero (e.g., solving for the cycle with a minimum slope), and then numerically solving for FN , Equation (A-5).

$$e^{D(FN)} - (FN)^{B-2} = \frac{AB(1-B)}{CD^2} \quad (\text{A-5})$$

Axial Fatigue

The axial fatigue test is performed by applying a repeating sinusoidal load or deformation along the long axis of a cylindrical test specimen until it fails. The test is performed using a servo-hydraulic loading frame and by controlling temperature in an appropriately conditioned test chamber. Figure A-5 provides an overall view of the testing system and mounted sample. Axial fatigue tests were performed in controlled actuator displacement mode. This test is like a controlled strain test, but was used because a controlled strain test with cylindrical specimens is difficult to conduct and can damage equipment if improperly performed. The controlled actuator test applies a cyclic tensile crosshead movement at some constant level at 10 Hz loading until the sample fails. Due to machine compliance issues, the actual on-specimen strain is significantly less than the programmed level and is not constant throughout the loading, as shown in Figure A-6. Even though the on-specimen strains remain tensile, both tensile and compressive stresses are applied on the specimen, with a decreasing mean stress, as shown in Figure A-6. All fatigue test samples were initially compacted to the same 150 mm diameter by 178 mm tall

dimensions as the dynamic modulus specimens. However, unlike the dynamic modulus specimens the fatigue samples were cored and cut to a cylindrical testing geometry 75 mm (3 in.) in diameter and 150 mm (6 in.) tall. The air voids for these fatigue tests were the same as the dynamic modulus samples ($6.5 \pm 0.5\%$). The test temperature for this study was 18°C intended to simulate fatigue crack initiation at intermediate pavement service temperatures.

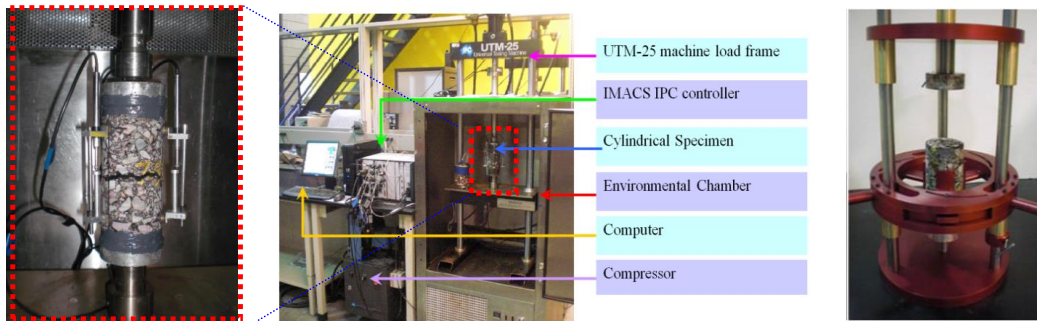


Figure A-5. Uniaxial Fatigue Test Setup and Gluing Jig.

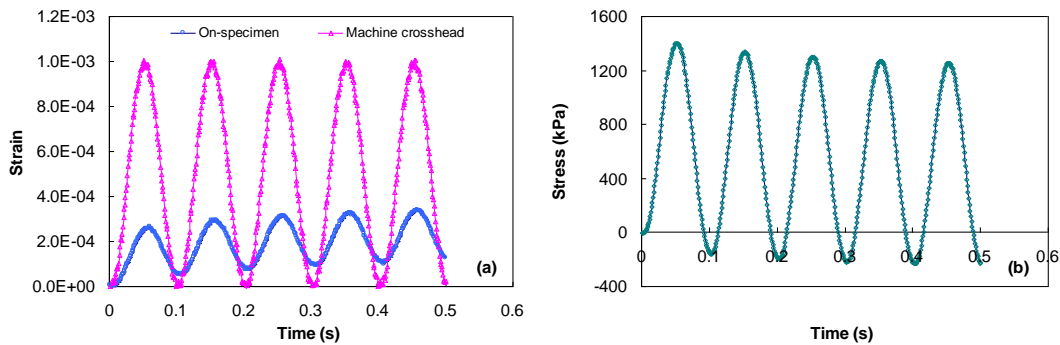


Figure A-6. Strain and Stress History for the First Five Cycles of a Typical Controlled Crosshead Cyclic Test.

The first step when performing the tests is to glue end plates to the specimen using the jig shown in Figure A-5. The specimen is then instrumented with four axial LVDTs to monitor the on-specimen deformation. The experiment is carried out using a closed-loop

servo hydraulic testing machine (UTM-25) in a temperature-controlled environment as shown in Figure A-5. This machine applies a continuous sinusoidal loading pattern based on output from the LVDT attached to the machine actuator. The load cell data and on-specimen deformation is recorded and used to calculate stress, strain, modulus, and phase angle throughout the fatigue test. These calculations are performed using research software developed by the PI.

The dynamic modulus and phase angle are tracked throughout the entire fatigue test. The traditional fatigue analysis method determines failure as the point where the material's modulus drops to 50% of its initial value. However, this method is purely empirical, and a different approach based on the change in the energy dissipation, indicated by the cycle at which the phase angle shows a sharp decrease is define as the failure cycle (N_f). Figure A-7 shows this failure definition from a typical test. It is believed that the drop of the phase angle is caused by macrocrack localization, which is normally caused by the coalescence of microcracks under repeated cycles of loading. When a macrocrack develops, all the work input is concentrated at the crack tip and the remaining body relaxes, thus causing the time dependence of the global stress-strain behavior to reduce. This reduction in the time dependence is physically measured as a reduction in the phase angle.

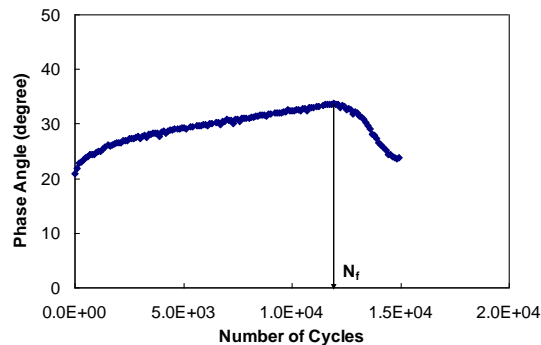


Figure A-7. Fatigue Life Definition of a Typical Axial Fatigue Test.

The test results are analyzed using the simplified viscoelastic continuum damage (S-VECD) approach for characterizing fatigue behavior. The first step in that approach is to establish the damage characteristic (*C-S*) curve. The *C-S* curve is a relationship unique to a given asphalt concrete mixture that is independent of test conditions including strain levels, temperatures, mode of loading (stress controlled or strain controlled), and loading history. This unique function exists as a fundamental characteristic of the material and is characterized by employing the work potential theory as incorporated into the S-VECD formulation and summarized in the following equations. The *C-S* relationship generally follows an exponential or power-law decay form as shown in Figure A-8.

$$C = \begin{cases} \frac{\sigma}{\varepsilon^R \times DMR} & \text{first cycle} \\ \frac{\sigma}{\varepsilon_{0,ta}^R \times DMR} & \text{rest of cycles} \end{cases} \quad (\text{A-6})$$

$$\varepsilon^R = \frac{1}{E_R} \int_0^t E(t-\tau) \frac{d\varepsilon}{d\tau} d\tau \quad (\text{A-7})$$

$$(\varepsilon_{0,ta}^R)_i = \frac{1}{E_R} \times \frac{\beta+1}{2} \left((\varepsilon_{0,pp})_i \times |E^*|_{LVE} \right) \quad (\text{A-8})$$

$$DMR = \frac{|E^*|_{fp}}{|E^*|_{LVE}} \quad (\text{A-9})$$

$$S_{N+1} = S_N + \left[-\frac{DMR}{2} (C_N - C_{N-1}) (\varepsilon^R)^2 \right]^{\frac{\alpha}{(1+\alpha)}} (\Delta \xi_i)^{\frac{1}{(1+\alpha)}} (K_1)^{\frac{1}{(1+\alpha)}} \quad (\text{A-10})$$

$$\alpha = \frac{1}{1+m} \quad (\text{A-11})$$

$$K_1 = \frac{1}{\xi_f - \xi_i} \int_{\xi_i}^{\xi_f} (f(\xi))^{2\alpha} d\xi \quad (\text{A-12})$$

where:

- C = normalized pseudo stiffness indicating the material integrity;
- S = internal state variable denoting the internal damage in the material;
- σ = measured stress;
- ε^R = pseudo strain;
- DMR = dynamic modulus ratio;
- $\varepsilon_{0,ta}^R$ = tensile pseudo strain tension amplitude;
- E_R = reference modulus;
- $E(t)$ = relaxation modulus and creep compliance, respectively;
- t = elapsed time from specimen fabrication and time of interest;
- τ = time when loading began;
- ε = measured strain;
- $\varepsilon_{0,pp}$ = peak-to-peak strain amplitude;
- β = stress wave shape factor (1 tension, 0 tension-compression, and -1 compression);
- $|E^*|_{fp}$ = fingerprint dynamic modulus;
- $|E^*|_{LVE}$ = linear viscoelastic dynamic modulus of the material;
- N = number of loading cycle;
- $\Delta\xi_i$ = change in the average reduced time between analysis cycles;
- K_1 = developed functional parameter to account for the analysis of cyclic data;
- α = material property;
- m = slope in the central part of the dynamic modulus master curve for the $\log E(t)$ - $\log(t)$;
- ξ_i = reduced starting time; and
- ξ_f = reduced ending time.

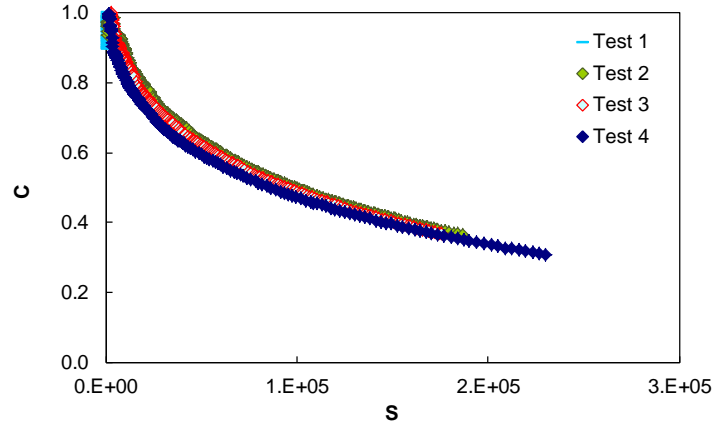


Figure A-8. Example of Damage Characteristic Curve.

At small levels of damage, the material integrity is high (close to 1), but as damage increases the material integrity is lost until eventually failure will occur. Thus, from characterization of this function two factors are important, the overall position of the C-S curve and also the material integrity level at which failure occurs, $C_{failure}$. All other factors being the same, materials with lower $C_{failure}$ values will exhibit superior fatigue performance. Once characterized, the C-S relationship can be fitted to an analytical form represented by Equation (A-13), where C_1 and C_2 are regression coefficients.

$$C(S) = 1 - C_1(S)^{C_2} \quad (A-13)$$

In order to gain useful information on fatigue cracking, simulated predictions of the fatigue life at specific conditions of interest can be performed using theoretically derived formulas for predicting the material response to fully reversed constant strain loadings as shown in the following formulations:

$$N_{failure} = \frac{(f_r)(2^{3\alpha})S_{failure}^{\alpha - \alpha C_2 + 1}}{(\alpha - \alpha C_2 + 1)(C_1 C_2)^\alpha \left[(\varepsilon_{0,pp}) (|E^*|_{LVE}) \right]^{2\alpha} K_1} \quad (A-14)$$

$$N_{failure} = \frac{f_r * 2^{3\alpha} |E^*|^{2\alpha}}{[(\sigma_{0,pp})]^{2\alpha} K_1} \int_0^{\hat{S}_{failure}} \left(\frac{(1 - \hat{C}_1 (\hat{S})^{C_2})^2}{\hat{C}_1 C_2 \hat{S}^{C_2-1}} \right)^\alpha (d\hat{S}) \quad (A-15)$$

$$\hat{S}_{failure} = \frac{S_{failure}}{|E^*|^{2\alpha/\alpha+1}} \quad (A-16)$$

$$\hat{C}_{11} = C_{11} (|E^*|^{2\alpha/\alpha+1})^{C_{12}} \quad (A-17)$$

where:

- $N_{failure}$ = predicted cycle number of cycles to failure;
- f_r = reduced frequency for the condition being simulated;
- $|E^*|$ = dynamic modulus for the condition being simulated;
- $\epsilon_{0,pp}$ = peak-to-peak strain level for simulation; and
- $S_{failure}$ = damage level at failure.

Verification of this modeling approach is given in the literature and summarized in the plot shown in Figure A-9. This figure shows the measured and predicted failure cycle for tests at different temperatures. The predictions were generated using the failure equations above and the damage function used in the predictions was characterized using only the results from the test that is circled.

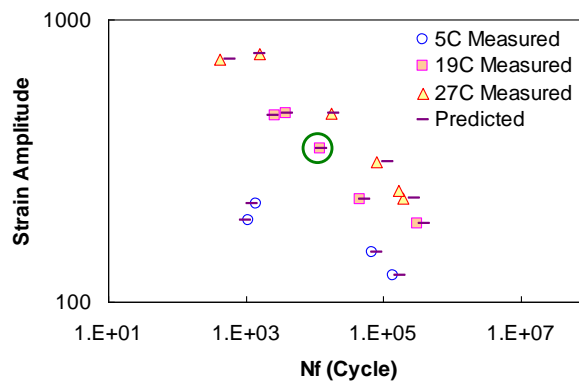


Figure A-9. Verification of Damage Modeling Approach to Fatigue Testing.

APPENDIX B
FIBER EXTRACTION PROCEDURE

Summary

The purpose of the test method is to determine the amount of recovered fiber from fiber reinforced asphalt concrete (FRAC). The test method utilizes ASTM D-2172 to extract the asphalt binder from FRAC samples. The amount of fiber remaining after extraction is measured by washing, sieving, manually removing the fiber, and recording total fiber mass. Due to the lightweight nature of aramid fiber and residual AC binder present on the fiber after extraction, the extracted fiber content will measure higher than the amount of fiber added at the time of mixing. The amount of extracted fiber is reported as a percentage of total sample size. CAUTION: Solvents used as part of ASTM D2172 are dangerous and specific safety concerns and procedures in ASTM D2172 must be followed. This document provides an overview of the procedure but more details and background involving the extraction process can be found elsewhere¹.

Sample

Samples shall be obtained from plant mixed FRAC. Sample size should be determined based on Table 1 of ASTM D2172. A minimum of three samples should be tested for each plant mixed FRAC sampled.

Solvent Type

The recommended solvent for this process is Trichloroethylene, which was found to yield no negative reaction with the fiber produce. If this solvent is not available then the chosen solvent should be verified for no reaction to reinforcing fibers. To test reactivity, soak a minimum 0.5 g sample of fibers in solvent overnight (12 hours minimum). Record the mass

of fibers before and after soaking to the nearest 0.01g. Fiber loss to solvent should be determined as a percentage loss compared to the original mass by Equation (B-1):

$$L = \frac{M_1 - M_2}{M_1} \times 100 \quad (\text{B-1})$$

M_1 = mass of the fibers prior to soaking (g),

M_2 = mass of the fibers after soaking (g), and

L = loss (%), must not exceed 1.0 percent of original mass.

Procedure

1. Complete extraction in accordance with ASTM D2172 with the exception that the ashing method, or any method that heats the sample above 400°F must not be used.
2. Dry and record the extract as directed in ASTM D2172. Transfer extract to a suitable sized mixing bowl and add sufficient water to immerse the extract. Add a few drops of soap to the extract and thoroughly agitate using hand methods for a minimum of 90 seconds. After agitation, wash the extract over a stacked No. 50 and No. 200 sieve for a minimum of 120 seconds until soap solution is removed. Pick up the extracted fibers manually using tweezers and store them in a clean can with a closed top.
3. Perform a sieve analysis of the washed and dried extract, utilizing sieve sizes from the original asphalt concrete mix design. Manually separate out fibers during weighing of separated sizes and add to fibers previously separated in step 4.2.
4. Soak the extracted fibers in the solvent for an hour at room temperature. Then remove the remaining solvent and dry the washed extract and separated fibers to a constant mass at $230 \pm 9^\circ\text{F}$. Record the mass of the separated fibers to the nearest 0.01 g.

5. Once fibers are extracted, the aramid dosage rate is determined, and the dispersed fiber state quantified by separating fibers into the bundles, agitated bundles, clusters and individuals.
6. Next, the amount of aramid fibers in the individual state are calculated using Equation (B-2). This calculation is defined as the Fiber Dispersion Percentage (*FDP*). *FDP* is used to quantify aramid dispersion in an asphalt concrete mixture. Increasing *FDP* signifies more fibers exist in the individual state thus better aramid dispersion. In comparison, lower *FDP* is an indicator of poor dispersion in the asphalt concrete mixture. Supplemental calculations for fibers in the cluster and agitated bundle states were also performed.

$$FDP = F_I = \frac{M_I}{M_a} \times 100 \quad (B-2)$$

Where;

FDP = aramid dispersion state ratio,

F_I = aramid fibers in the individual state (%),

M_I = mass of aramid fibers in the individual state (g), and

M_a = total extracted aramid mass prior to separation (g).

The extraction process is shown Figure B-1.

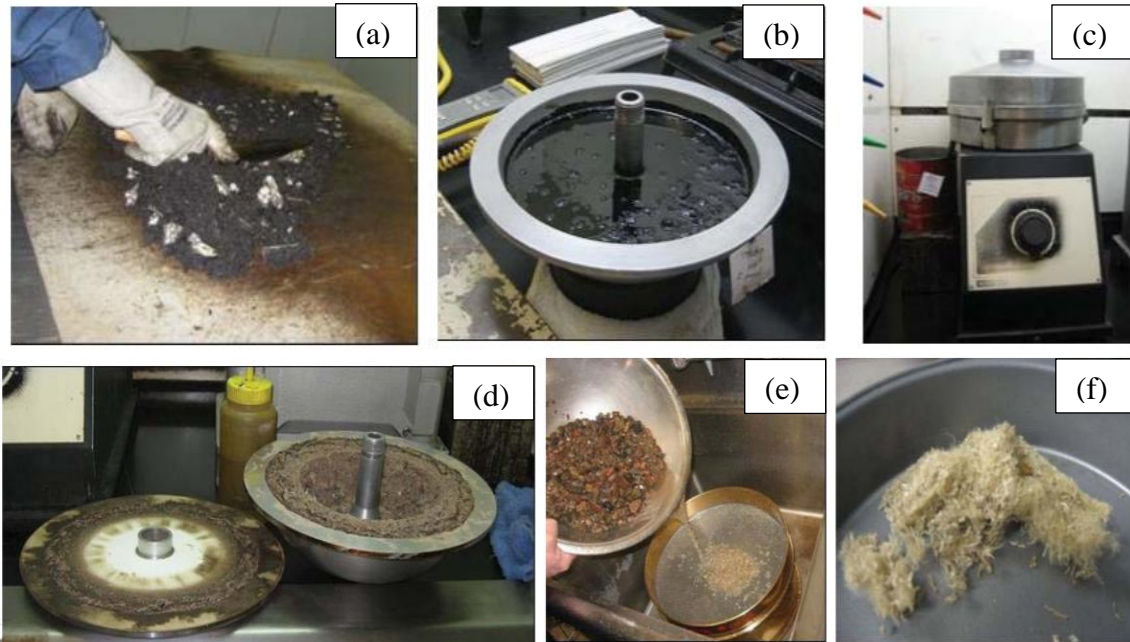


Figure B-1. The Process of Fiber Extraction

APPENDIX C
FIBER MIXING METHOD

Method A:

The mixing steps to use for the Polyethylene blend:

1. Calculate the amount of each aggregate size and the amount of asphalt cement required to make one gyratory sample using the mix design gradation.
2. Weigh and batch the aggregates in an appropriate container.
3. Weigh the appropriate amount of polyethylene and aramid fibers using an electronic analytical balance to make one gyratory sample. Place the polyethylene in a separate container.
4. Keep the metal container with the batched aggregates in the oven until thoroughly heated to the appropriate mixing temperature (preferably overnight but a minimum of 6 hours unless local laboratory practice suggests less time is sufficient).
 - If the mixing temperature is less than 165°C, heat the aggregates to a temperature between 165 and 175°C.
 - If the mixing temperature is at 165°C or above, heat the aggregate following local laboratory practices as long as this temperature is not above 185°C.
5. On the mixing day, keep the asphalt cement in the oven at mixing temperature and wait until the asphalt cement temperature reaches the mixing temperature.
6. Heat all mixing tools (bucket, blade, metal scoop, metal spoon and spatula) to the mixing temperature.
7. Once the asphalt cement reaches the mixing temperature, transfer the aggregates into the mixing bucket.
8. Create a crater in the middle of the aggregates.

9. If the aggregates have been heated above the allowable mixing temperature allow the aggregate to cool to the appropriate temperature. Do not continue to stir during this cooling period, which should not take longer than three minutes.
10. Place the bucket on the weighing scale.
11. Carefully pour the correct amount of heated asphalt cement into the blend. Pouring the asphalt binder into the bucket should not take longer than 20 seconds.
12. Take the container with the polyethylene and pour the fibers directly into the binder.
13. Sprinkle the aramid or aramid fiber dosage around the crater directly into the aggregate.
14. Place the mixing bucket into the mixing machine and run it for a minimum of 1.5 minutes. If at the end of the 1.5 minutes the aggregate and asphalt have not fully blended, then continue the mixer until all aggregates are completely coated with the asphalt cement.
15. Once mixing is completed, transfer the hot asphalt mixture to an aging pan and scrape the side of the bucket and the blade using a heated spatula. Add the material scraped from the bucket and blade and any material stuck to the spatula back into the aging pan.
16. Remove the metal scoop from the oven and stir the aging material thoroughly.
17. Continue stirring the material during the aging process according to AASHTO R30 and again prior to compaction.

Follow regular procedures for compacting asphalt mixtures being careful to use heated utensils at every step to prevent loss of mixture and fibers.

Method B and C:

Calculation of Fiber Dosage

Methods B and C are similar, and the only difference is the number of layers. The fiber dosage rate is calculated based on weight of the asphalt mix sample to be prepared in the laboratory. The typical fiber dosage rate is 0.05%.

Batching Aggregates and Mix Preparation (bucket mixer)

1. Calculate the amount of each aggregate size and the amount of asphalt cement required to make one gyratory sample using the mix design gradation.
2. Weigh and batch the aggregates in a single container.
3. Evenly divide (by mass) the batched aggregates into three suitable size metal containers for heating.
4. Keep the metal containers with the batched aggregates in the oven until thoroughly heated to 6 - 8°C higher than the mixing temperature (to compensate for heat lost while adding fibers). Preferably heat overnight but a minimum of 6 hours unless local laboratory practice suggests less time is sufficient.
5. Prior to mixing, heat asphalt cement in an oven at the mixing temperature and wait until the asphalt cement reaches the mixing temperature.
6. Heat all mixing tools (bucket, blade, metal scoop, metal spoon and spatula) to the mixing temperature.
7. Once the asphalt cement reaches the mixing temperature, transfer the aggregates and Bag #1 fibers to the mixing bucket according to the following steps (The entire process

of adding aggregate and fiber in the 3-layer system should be accomplished within 3 – 4 minutes).

- a. Add the first container of aggregate (1/3rd of total aggregate by mass) to the mixing bucket.
 - b. Evenly sprinkle the first portion of Bag #1 fibers onto the first layer of aggregate.
 - c. Slowly add (circular motion) the second container of aggregate (1/3rd of total aggregate by mass) to the mixing bucket so that the fibers do not become airborne.
 - d. Sprinkle the remaining portion of Bag #1 fibers (by mass) onto the second layer of aggregate.
 - e. Slowly add (circular motion) the third container of aggregate (1/3rd of total aggregate by mass) to the mixing bucket so that the fibers do not become airborne.
 - f. Create a crater in the middle of the aggregates without stirring the aggregate and fiber mixture.
8. If the addition of fibers and aggregate to the mixing bucket exceeds four minutes in duration, take appropriate steps to ensure the aggregate is at the appropriate mixing temperature.
 9. Place the bucket on the weighing scale.
 10. Carefully pour the correct amount of heated asphalt cement into the blend. Pouring the asphalt binder into the bucket should not take longer than 20 seconds.
 11. Take the container of pre-weighed Bag #2 fiber and sprinkle it directly into the binder.

12. Place the mixing bucket into the mixing machine and run it for a minimum of 1.5 minutes. If at the end of the 1.5 minutes the aggregate and asphalt have not fully blended, continue mixing until all aggregates are completely coated with asphalt cement.
13. Once mixing is completed, transfer the hot asphalt mixture to an aging pan and scrape the side of the bucket and the blade using a heated spatula. Add the material scraped from the bucket and blade and any material stuck to the spatula back into the aging pan.
14. Remove the metal scoop from the oven and stir the aging material thoroughly.
15. Continue stirring the material during the aging process according to AASHTO R30 and again prior to compaction.
16. Follow regular procedures for compacting asphalt mixtures being careful to use heated utensils at every step to prevent loss of mixture and fibers.

Method D:

Calculation of Fiber Dosage

The fiber dosage rate is calculated based on weight of the asphalt mix sample to be prepared in the laboratory. The typical fiber dosage rate is 0.05%.

Laboratory Pre-Dispersion of Fibers

A pre-dispersion process for lab mixing fibers has been developed to achieve similar fiber dispersion observed in plant-mixed asphalt concrete. The following steps describe the laboratory process:

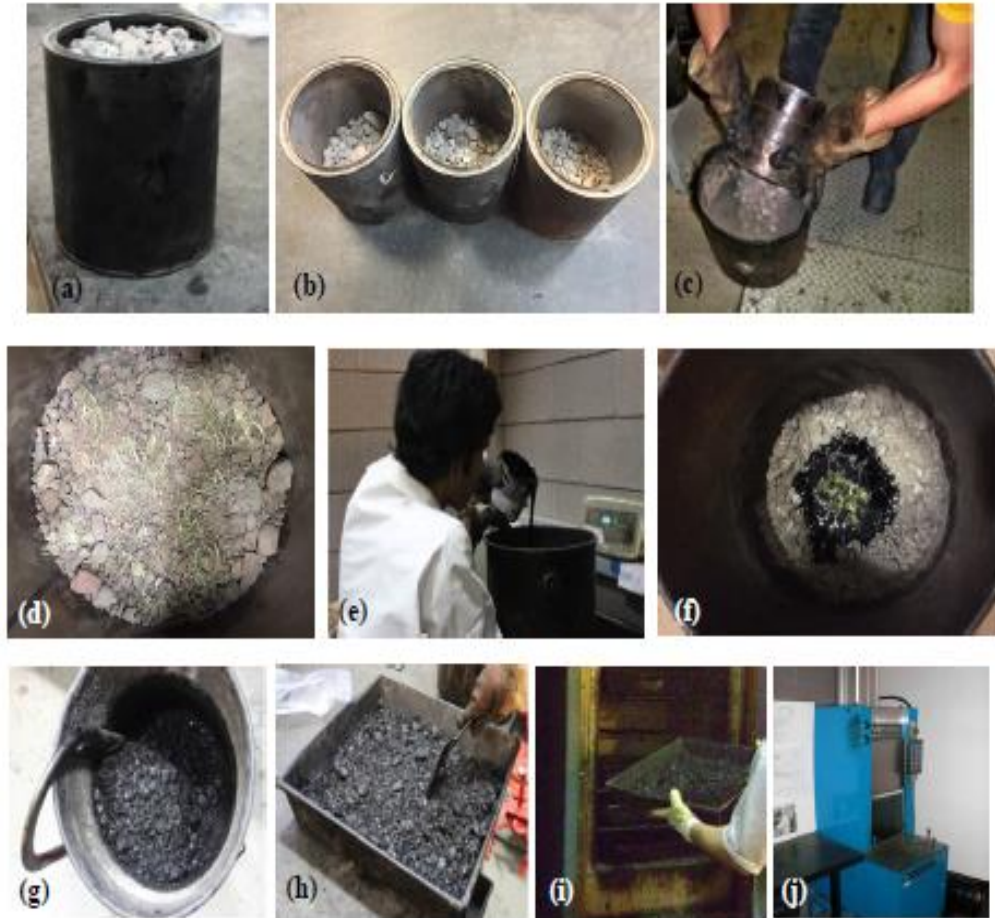


Figure C-1. Laboratory Mixing of Fiber-Reinforced Asphalt Concrete Mixture: a) Batched Aggregates, b) Batched Aggregate Divided into Thirds (By Mass), c) Pouring 1/3 of Aggregate into the Mixing Bucket, d) Evenly Spreading 1/2 of Bag #1 Fibers to Top of First 1/3 Layer of Aggregate (Repeat for the 2nd 1/3 of Aggregate And 2nd 1/2 of Bag #1 Fibers), e) Weighing Asphalt Binder, f) Bag #2 Fiber Added Directly into the Binder, g) Mixing of Asphalt-Fiber-Aggregate Blend, h) Transferred Hot Asphalt Mixture for Aging Process, i) Aging of Fiber Reinforced Asphalt Mixture, and j) Compaction of Fiber Reinforced Asphalt Mixture.

1. Divide Bag #1 fibers into two equal portions (by mass).
2. Add the first portion of Bag #1 fibers to a 1-quart (1-liter), wide mouthed glass canning jar (e.g. Mason jar).
3. Cover the opening of the jar with a non-cloth based mesh (equivalent to a No. 16 (1.19 mm) sieve size opening) and secure with a rubber band or equivalent.
4. Using a flexible hose (1/4 inch (6 mm) outside diameter x 0.04 inch (1 mm) wall thickness), apply compressed air at a pressure of 12 psi (82 kPa) vertically through the mesh opening and move the hose in a clockwise circle around the opening (1 rotation per second). Pressure should be applied for 3 – 4 seconds.
5. Transfer the pre-dispersed fibers into a suitable sized glass container for introduction to the aggregate. Take care to avoid additional agitation of the fibers.
6. Repeat steps 2-5 for the second portion of Bag #1 fibers (store in a separate container than the first portion).

Figure C and Figure C provide a pictorial summary of the laboratory pre-dispersion process of Bag #1 Fibers. After this process, fibers were added with the same procedure described in under Method C.

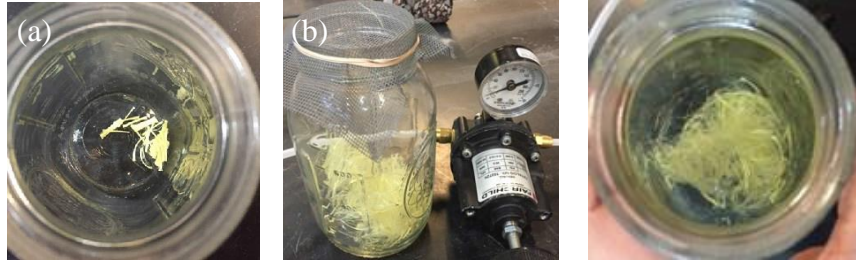


Figure C-2. Laboratory Pre-Dispersion of Bag #1 Fibers: a) One Portion of Bag #1 Fibers in A Glass Jar, b) Pre-Dispersion Setup, and c) Pre-Dispersed Fibers.

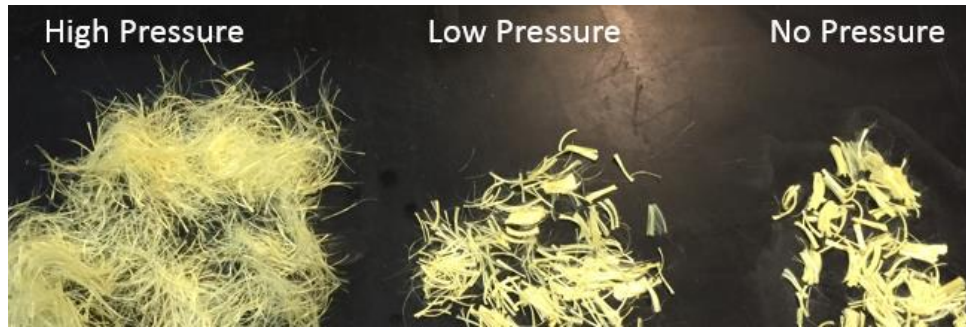


Figure C-3. Schematic of Pre-Dispersed Aramid Fibers Shown At Different Air Pressure.